SUSTAINABLE RESOURCE MANAGEMENT VIA D.C. THERMAL PLASMA TECHNOLOGY.

by

PETER MICHAEL KEELEY

UNIVERSITY OF BIRMINGHAM

A thesis submitted to the University of Birmingham for the degree of

DOCTOR OF ENGINEERING.

School of Chemical Engineering

College of Engineering and Physical Sciences

University of Birmingham

September 2017

Abstract.

The recovery of metals from secondary resources is increasing to alleviate supply risks associated with primary sources. This thesis presents a series of solutions to existing industrial problems which center on the use of plasma technology and that address the issue of sustainable resource management. Thermal plasma is widely used for platinum group metal recovery from automotive catalysts, but the mixing of various catalyst types makes their processing difficult. It was found that it was possible to separate silicon carbide based catalysts from cordierite based catalysts by a combination of magnetic and electrostatic separation processes resulting in a cordierite fraction of over 98% purity, which would result in a more consistent feed material to the plasma process enhancing metal recovery. The flexibility of plasma means that the operational conditions in the furnace can be controlled to suit the chemistry of less noble metals such as rhenium. The technology was used to recover platinum and rhenium from spent petrochemical catalysts via a novel pyrometallurgical process with over 98% recovery efficiencies of both metals. The plasma process produces a large amount of slag as a by-product which can be used in higher value applications to avoid waste and improve business models. Plasma derived slag was shown to be an effective, low carbon cement replacement which can potentially obtain a market value of £50/tonne. The increasing use of renewable energy to generate electricity means that plasma technology is becoming much greener and so it could be used to reform waste industrial gases such as steel plant gases, rich in CO_2, into high value synthetic gases for use around plants saving money and carbon emissions.

Acknowledgments.

I would like to thank the EPRSC for the funding which supported this EngD. The grant code for the project is EP/G036713/1. I would also like to thank everyone at Tetronics International for all their support and help through the four years, in particular Dr. David Deegan for his guidance and input as my industrial supervisor which have no doubt helped the completion of this work and also Dr. Tim Johnson for his input, thoughts and ideas along the way. This thesis would not have been completed without the help from many students and staff from the schools of chemical engineering, metallurgy and materials, chemistry and civil engineering. Dr. Richard Greenwood deserves many thanks for his friendship and encouragement throughout my EngD and special thanks go to Professor Neil Rowson for his role as academic supervisor, from whom I have learnt a great deal and whose input into this thesis has been invaluable.

To all, thank you.

Peter.

“The real voyage of discovery consists not in seeking new lands but seeing with new eyes.”

Marcel Proust, In Search of Lost Time.

Table Of Contents.

Table of Figures.

1. Thesis Introduction.

1.1. Introduction to Plasma Technology.

Formed when a gas becomes ionised, plasma is a highly flexible tool which has been exploited for many industrial applications. The ionisation of a gas only occurs at very high temperatures; at around 2000°C molecules dissociate into atoms and as the temperature increases, these atoms collide with each other more frequently which, at around 3000°C, causes electrons to be ejected from their shells forming plasma. Although electrically neutral, plasma contains electrons, positive ions and neutral species. Plasmas have different characteristics depending on their degree of ionisation which has led to two distinct categories of plasma; thermal and non-thermal plasma.

Non-thermal plasma has a low degree of ionisation (usually less than 1%). It is used to facilitate chemical reactions as it can produce highly reactive free radicals and it is also used for surface coating applications for example, ceramic coatings. Thermal plasma on the other hand, has a degree of ionisation around 99% so contains a large number of ejected electrons. These electrons have a high energy and they frequently collide with the heavier species in the plasma, causing the temperature of the heavier species to approach the temperature of the electrons. This results in a thermal equilibrium being established and a high plasma temperature which can vary between 2000 and 20,000 K, although the extreme temperatures are only found in small localised regions. Thermal plasma has found extensive use in pyrometallurgical and other high temperature furnace applications.

A plasma arc is generated using electricity meaning that high temperatures in a furnace can be produced without the reliance on combustion to produce and maintain heat. With the

plasma arc being chemically neutral, the chemistry in a plasma furnace can be closely controlled to suit the chemistry required for a particular application. Plasma furnaces can also operate at higher temperatures than traditional cupola or blast furnaces which rely on heat generated by combustion and are generally limited to a maximum temperature of 1500°C. Typically a plasma furnace would operate between 1500 to 1800°C, but it is possible to operate at higher temperatures. Although there are analogies between plasma furnaces and other electrically driven furnaces such as submerged arc furnaces, there are significant differences between the processes. Submerged arc furnaces pass a current between two electrodes which are submerged in a molten material. The power input for this process relies on resistive heating and so the power input is dependent on the conductivity of the melt pool. A plasma arc furnace on the other hand superheats the top surface of the melt which causes convection currents in the melt pool and this churning of molten material distributes heat around the furnace.

1.2. Tetronics International.

Tetronics International are a thermal plasma technology supplier initially founded in 1964 as a plasma research and development company with a grant from the British steel and coal research council. As of today they have installed over 90 plasma installations around the world and are a world leader in plasma technology. As of June 2017, Tetronics has 58 employees and has an annual turnover of just over £9,000,000. Tetronics International's DC thermal plasma technology has been used in numerous industrial applications with the most successful being precious and valuable metal recovery, hazardous waste treatment, synthetic gas production and Tundish heating. The technology has also been used in the production of nano-materials

and clean melting of metals such as titanium alloys. A summary of the major applications of Tetronics' plasma technology are shown in Table 1-1.

Table 1-1: Applications of Tetronics International's thermal plasma technology (2017).

Business Area	**Process**	**Number of plants**	**Average/Total Throughput (Tonnes Per year of feed material)**
Environmental	Treatment of municipal solid waste ashes	10	19,930/199,300
Environmental	Treatment of contaminated soils	1	N/A
Environmental	Treatment of inorganic and organic wastes	1	720
Metal Recovery	PGM recovery from spent automotive and chemical catalysts	11	2,400/26,500
Metal Recovery	Electronic waste smelting	1	7,000
Metal Recovery	Recovery of metal values from mixed stainless steel plasma waste	1	30,000
Metal Recovery	Recovery of stainless steel electric arc furnace dust	1	8,000
Clean Heat	Steel tundish heating	14	N/A
Clean Heat	Titanium melting	3	N/A
Clean Heat	Titanium sponge welding	1	N/A
Clean Heat	Silica glass melting	1	N/A
Clean heat	Glass melting	1	N/A
Gasplasma® (Energy from Waste)	Energy from MSW and commercial waste	2	17,000
Advanced Materials	Nanopowder production facility	3	N/A

1.3. The Recovery of Critical Raw Materials via Plasma Technology.

The recovery of metals from waste materials is currently the most successful application of Tetronics' plasma technology. There are currently 11 Tetronics built plants recycling platinum group metals (PGMs) with a combined installed PGM recycling capacity processing 26,500 tonnes per year of catalysts and recovering over 1.2 million troy oz (~ 37,000 kg) of PGMs per year.

Waste materials such as spent catalysts and electronic waste contain precious and valuable metals at concentrations greater than their primary ore (Table 1-2). The concentration of PGMs in catalysts are around 400 times greater than high grade ores making them important secondary resources. Platinum group metals are widely recovered from catalysts due to their high value but, their recovery from wastes is a more sustainable approach to their supply which is often stretched and vulnerable.

Table 1-2: Comparison of metal concentrations in primary and secondary resources.

Source	Metal	Concentration (g/t)
PGM Ore (Bushveld complex)	3PGM + Au	4.3
High grade WEEE	Au, Ag	22, 313
Industrial reforming catalyst	Pt, Re	3000, 3000
Automotive catalyst	Pt	1800

Critical raw materials are those which have a high economic importance, but have a significant supply risk. Critical raw materials lists have been made for states, markets and industries to highlight materials critical to their sector or economy. The critical raw materials list in the European Union (EU) has been created on the basis that the EU needs many specialised materials for its economy, but there are little or no natural resources of them inside the EU (European Commission, 2014). The rare earth elements (REE), the platinum group metals

(PGMs), cobalt, natural graphite and phosphate rock are all examples of materials required for electronics, renewable energy, chemical and materials production and are critical for the EU. For the aviation industry, rhenium is a critical metal due to its importance in nickel based super alloys used to increase the life span of jet engine turbine blades. Figure 1-1 shows the critical raw materials list for the EU with the economic importance along the x-axis and the supply risk on the y-axis. The highlighted block contains the materials which are deemed to be most critical to the EU.

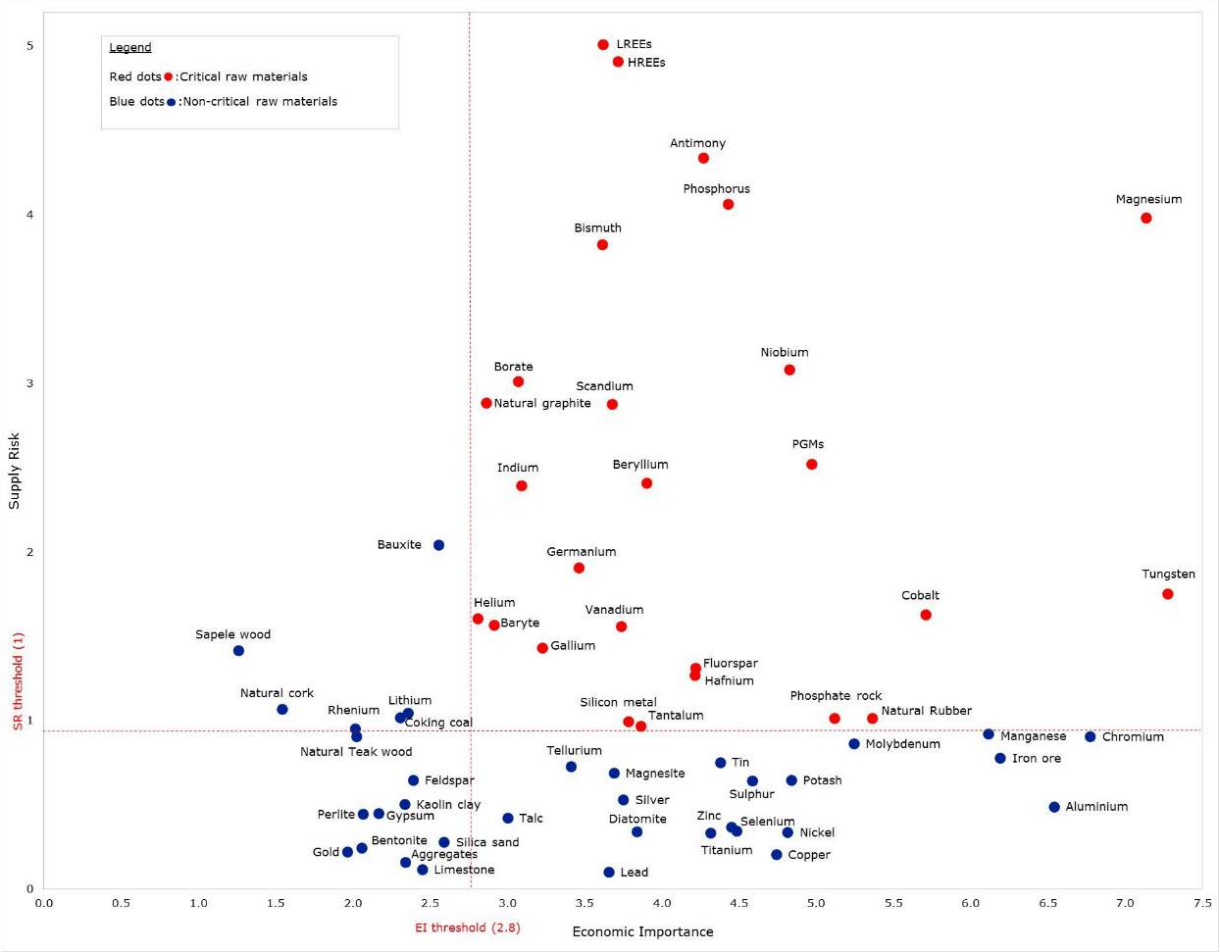

Figure 1-1: Critical raw materials list for the European Union (European Commission, 2017).

Raw materials can be supplied from primary or secondary sources, but it is the primary sources that are the root cause of supply risks. The supply risk associated with primary production is largely dependent on the distribution of the material's extraction around the world. Even though the ores of critical raw materials can be found all over the world, the high costs associated with their mining and processing means that for a mining venture to be economically feasible, very specific circumstances are required and these are found in just a handful of countries.

Mining is dominated by economics; some mines are doomed to failure because they are just too expensive to run. However, sometimes in an ore critical metals are co-associated with high volume, high demand materials such as iron, copper or nickel making them more economic to mine. If a material is produced in low volumes its production is very susceptible to price fluctuations which can potentially undermine a business model. Co-producing the material with iron ore for example, means that the price volatility of the critical metal can be absorbed. Platinum group metals extracted in Russia at the Norilsk mine in Siberia are co-extracted with nickel and copper and in China (Crundwell et al. 2011), REE extracted from the Bayan Obo mine are co-extracted with iron ore and these are examples of successful mining operations of critical raw materials (Kanazawa and Kamitani, 2006). When it may take up to twenty years for a mine to open, there is a high risk in opening a mine for just one material, especially when the prices of those materials are so volatile and long term market predictions are extremely difficult to make.

Mining and ore processing produces vast quantities of waste; the extraction processes for REE require the use of large quantities of concentrated acids and solvents which need to be treated

(Hague et al. 2014). The Bayan Obo mine and the rare earth processing plant at Baotou is associated with numerous environmental issues including a 'toxic lake' where chemical waste from the surrounding facilities is dumped (Maughan, 2015). The Norlisk mining area in Siberia is also extremely polluted which adversely affects the health of residents and plants in the area. Heavy pollution is an intrinsic problem for primary metal extraction processes and strict environmental legislation can make processes uneconomical and so mining ventures are more successful in countries with fewer environmental regulations.

As well as less stringent environmental regulations, reduced labour costs in certain areas of the world make mining cheaper and these countries are sometimes politically unstable, even suffering with violence and corruption leading to reduced rights for mine workers. This leads to their exploitation, leaving them with poor pay and unsafe working conditions. The PGM industry has recently suffered from numerous strikes from workers over pay and conditions which has led to significant production losses. Corruption and a lack of governance can lead to the loss of the control of mines and trade routes to gangs, rebels or militias fuelling repeated conflicts with devastating consequences. An example is the extraction of cobalt, used for batteries and electronics, in the Democratic Republic of Congo (DRC). A civil war took place there between 1994 and 2003, but gangs of militia still fight to control mines and trade routes in the Congo often using child soldiers (BBC, 2016). This fighting leads to uncertainty in the supply of the materials and also raises ethical concerns about how the consumption of these metals can inadvertently fund violence.

By relying on just a handful of countries to produce a material, end users are vulnerable to disruptions in the supply chain. The producers know the importance of these materials and

this can be exploited for economic and political gains. The Chinese dominate the REE market and so are able to control the market with mining quotas and withhold supply, which can artificially inflate the price (Massari and Ruberti, 2013).

Having alternative resources is the best contingency against volatile and uncertain supply of materials. Reduce, reuse, recycle are the fundamentals of the recycling hierarchy and they can be applied when thinking about critical raw materials. The recycling hierarchy is a holistic approach to recycling that covers industry, government and society and a holistic approach to critical material supply is also required.

Focusing on the PGMs, their major application as catalytic agents and automotive catalysts account for 37% of the total platinum demand. The catalytic properties of platinum and the other PGMs make them very effective catalytic agents and as the environmental regulations surrounding car emissions are becoming stricter, there are no real alternatives to PGM based catalysts which match their high performance. There is little room to reduce the amount of PGMs on catalysts without adversely affecting their performance and although the automotive industry has reduced its platinum consumption, it has only shifted its demand towards palladium because of its lower price.

Sustainability in material use and supply is essentially the core philosophy of the circular economy and although the circular economy may seem idealistic, the way in which PGMs are handled within the automotive and petrochemical industry is probably the best current example of it. The value of the PGMs and their concentration on end-of-life materials make their recycling desirable and consequently, these metals have high recycling rates. The PGMs are impregnated on ceramic supports and at the end of their life, the catalysts are collected

and the PGMs recovered to be reused in the manufacturing of new catalysts. Primary PGMs are only required to top up from losses in the supply chain and to meet differences in the supply and demand of the metals. In this way, the industry operates in a semi closed loop supply chain shown in the diagram in Figure 1-2. There is great efficiency in the recycling of PGMs from the collection of the catalysts (over 98% of autocatalyst are recovered from cars) to the technology used to recover them (Saurat and Bringezu, 2009, Hagelüken, 2012).

In most market assessments of platinum consumption, the petrochemical sector only accounts for about 1% of the Pt demand, but these assessments do not account for the recycling of the metal within the industry. Typical reforming catalysts operate in chemical reactors each containing around 25 tonnes of catalyst for between 1 to 2 years before they are removed and sent for metal recovery. Typically, the recovery rate of the metals is around 96% and so the petroleum industry contains a large stock of PGMs estimated to be around 5 m troy oz (155,000 kg) equating to approximately $4.8 billion based on the price of platinum in 2017. In this market, the catalysts would be removed from the reactor and sent to a refiner who would recover the PGM as a salt and then be sent to a catalyst producer. Typical PGM salt producers are Johnson Matthey, Umicore, Tanaka Kikinzoku and Heraeus, the catalyst suppliers include Criterion Catalysts, UOP, Axens, Haldor Topsoe and Akzo and the end users would be major petrochemical companies such as Shell, BP and Exxon Mobil.

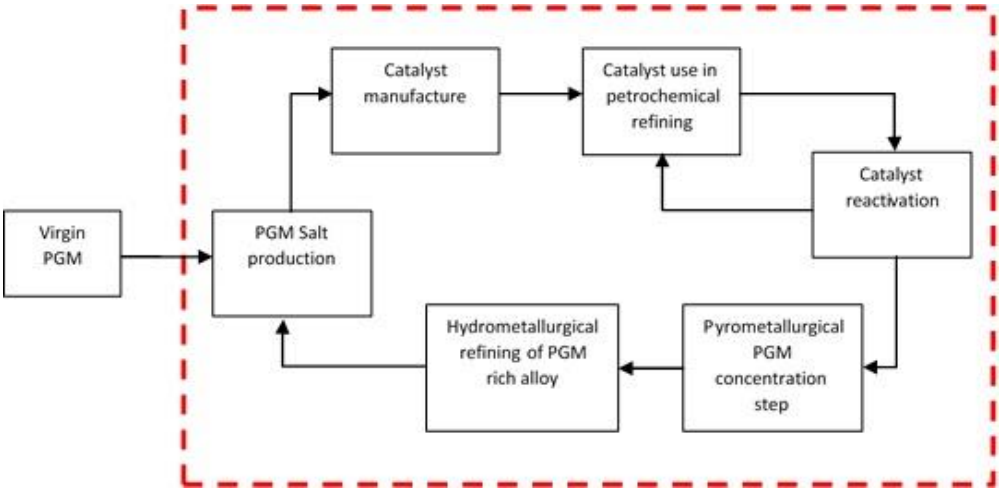

Figure 1-2: Semi closed loop recycling system in the PGM catalyst industry (Keeley, 2017).

The growth of the recycling of PGMs has been evident over the past ten years, as shown in Figure 1-3 and recycled PGMs from automotive catalysts now account for over 25% of the total supply (Thompson Reuters, 2014) although in the petrochemical industry it is much higher, but the exact figure is not known.

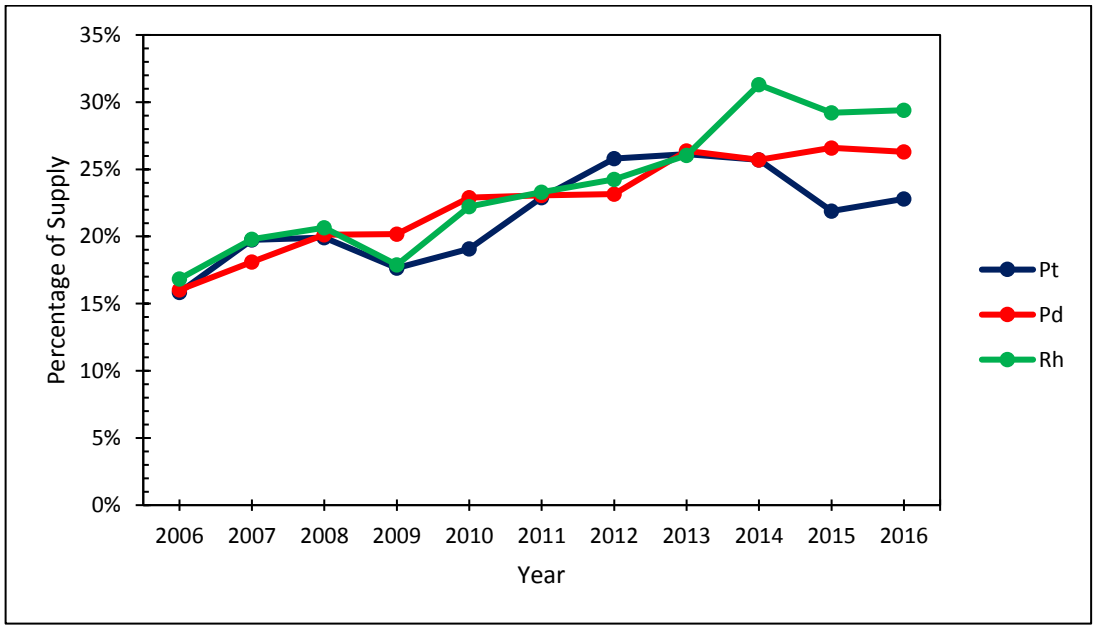

Figure 1-3: Platinum group metal recycling as a percentage of total supply (Johnson Matthey, 2016).

The increase in the amount of PGM recycling has already positively impacted their supply chain. The EU first released a critical raw materials list in 2010, which can be seen in Figure 1-4 and the PGMs had a much greater supply risk then than they do today. This shows that the recycling of critical metals does have a positive impact on resource sustainability even within a short time.

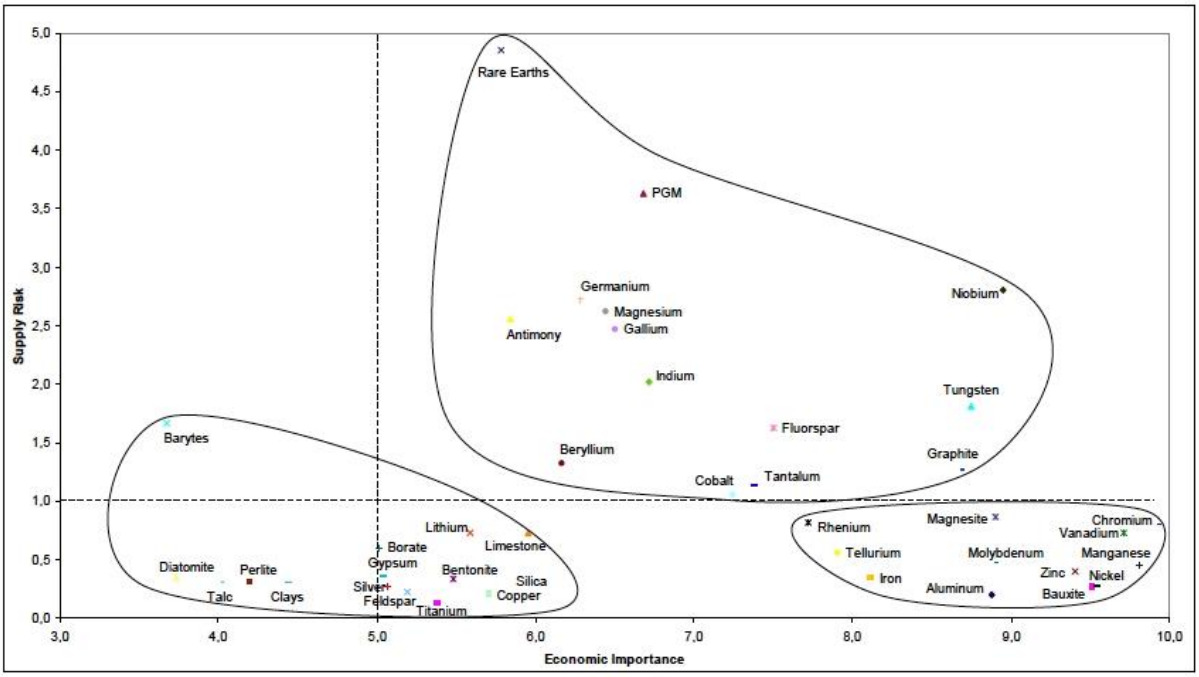

Figure 1-4: The European Union's first critical raw materials list released in 2010. (European Commission, 2010).

The amount of PGMs recycled from automotive catalysts has risen by around 350% in 10 years. The introduction of automotive catalysts was only made mandatory for all transport in the UK in the 1990s, whereas in the USA, automotive catalysts were required by law since the 70s and so PGM recycling is more established there. In the UK, there are 31.5 million cars on the road which all have platinum group metal based catalysts. Therefore, a PGM stock of a value around £1.4 billion exists and can be exploited as cars reach their end of life. The average lifespan of a car is 14 years (SMMT, 2015) and each year around 1.8 million cars reach their

end of life in the UK creating a PGM value stock of around £173 million pounds. Therefore, there is an enormous incentive to recover these metals from the scrap. However, the slight dip in the recycling rate of platinum shown in Figure 1-3 has been linked to the dip in the price of steel. If the steel price is low then fewer cars are scrapped meaning less catalytic converters are removed from the cars for recycling (Johnson Matthey, 2016).

There are various methods to recover PGMs from catalysts. The methods can be broadly split into hydrometallurgical and pyrometallurgical processes, hydrometallurgical processing routes use wet chemistry to extract the materials. This is usually achieved by solvent extraction techniques exploiting the differences in the solubility and chemical behaviour of the various components in the material to produce crystalline salts. Pyrometallurgical processing routes are high temperature processes which separate the materials due to either their thermal behaviour (vapour pressures) or their density when molten. Hydrometallurgical routes are very selective processes with can recover metals to very high purities. However, they are sensitive to the composition of the input material and not flexible enough to deal with compositional or mineralogical variabilities of the feed which can result in poor recovery efficiencies. Pyrometallurgical routes on the other hand, can process a variety of feed materials and are not as sensitive to variations of the input and can also achieve high throughputs. However, they are not usually selective enough to recover metals to very high purities especially when the feed contains various metals. So, in reality, both routes are used in conjunction with each other for PGM recovery; pyrometallurgical routes are used as a raw material upgrading process, producing a material of sufficient quality and consistency to enable highly efficient hydrometallurgical final extraction of the metals.

The plasma smelting process extracts precious or valuable metals from their initial material into what is known as a collector metal via a pyrometallurgical route. The collector metal is a base metal alloy, usually iron, which contains the target metals (PGMs for example). The iron alloy is easily refined and the target metals can be extracted with high purities. Figure 1-5 shows a simplified diagrammatic description of the plasma process.

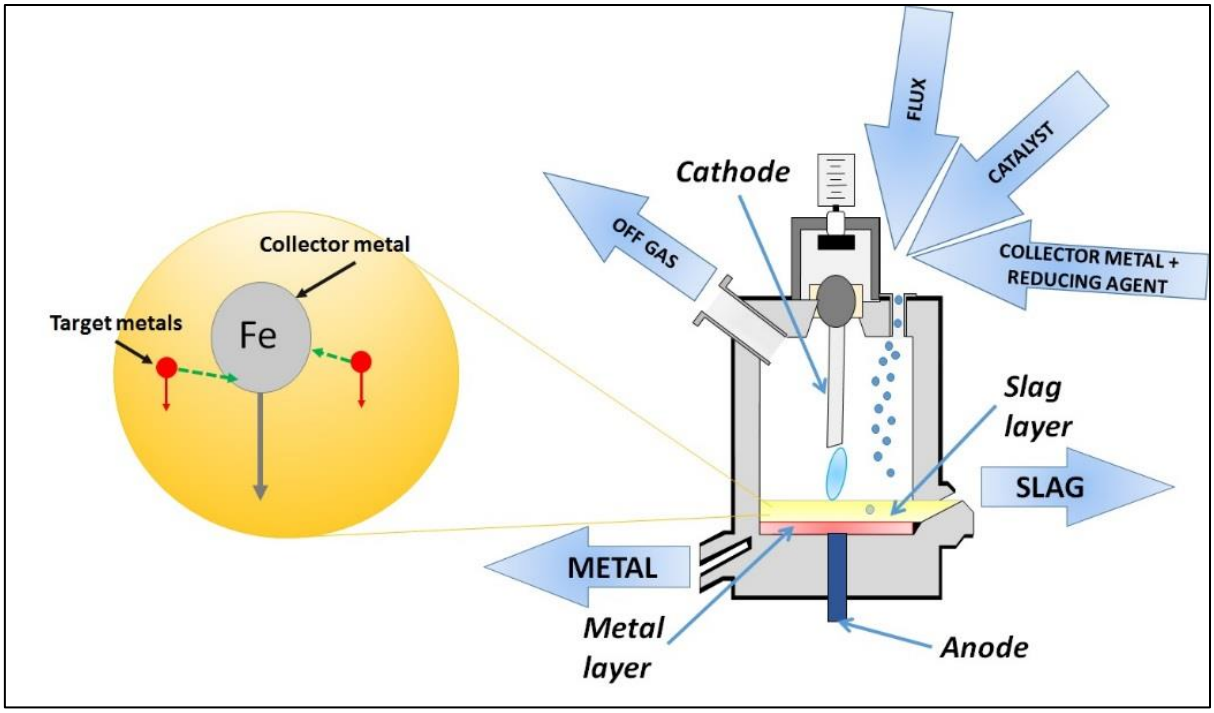

Figure 1-5: Simplified diagram showing the plasma smelting process (Keeley, 2017).

Platinum group metals are impregnated onto ceramic supports from which they need to be separated. The ceramic supports tend to have high melting temperatures and so are blended with fluxing agents to reduce the energy required to melt the feed (plasma power input). The blend is fed into the furnace where it is melted and the ceramic components and the fluxing agents form a molten slag. With the blend a collector metal precursor, usually iron oxide, and a reducing agent, metallurgical coke, are added. The coke reduces iron oxide to metallic iron

via the carbothermic reduction (Equation 1-1) reaction which forms discrete droplets in the melt.

$$Fe_3O_4(s) + 2C(s) \rightarrow 3Fe(s) + 2CO_2(g) \qquad \text{Equation 1-1}$$

These metallic droplets are denser than the slag and so fall through it to form a discrete metal phase beneath the slag. As the collector metal falls through the slag, it alloys with the target metals and by doing so recovers them from the slag. The slag and the metal are tapped separately from the furnace from which they can be sent to downstream refining.

The use of plasma based systems to recover PGMs from catalysts is a well-established technology with companies such as Texasgulf and Johnson Matthey using the technology for this application since the mid-1980s. Benson et al. (2000) described the plasma process and in particular discussed the importance of the collector metal in recovering the PGMs. The group described the settling of the PGMs using Stokes' law (Equation 1-2) for the terminal settling velocity of a particle through a fluid (Equation 1-3). Stokes' law is highly dependent on the diameter of the settling particle and so they concluded that the settling rate of PGMs through a slag is too slow to occur in an economic time frame and so the process requires a 'collector metal' which forms larger droplets, that fall through the slag at a faster rate, alloying with the 'target' PGM metals and forming a metal layer beneath the slag.

$$u_T = \frac{(\rho_p - \rho_L)d_p^2 g}{18\mu}$$ Equation 1-2

$$t_s = \frac{H}{u_T}$$ Equation 1-3

Where u_T is the terminal settling velocity of a particle (m/s), ρ_p and ρ_L are the densities of the particle and the liquid respectively (kg/m^3), d_p is the particle diameter (m), g is acceleration due to gravity (m/s^2), μ is the viscosity of the fluid (kg/m.s), t_s is the settling time of a particle (s) and H is the height of the slag bath (m).

Using Stokes' law the group developed a model to determine the concentration of PGMs remaining in slag as a function of time (Equation 1-4). This equation was to be used to determine the minimum operating time in the plasma furnace required to achieve a high recovery of PGMs.

$$C_t = C_0 e^{-DAkt}$$ Equation 1-4

C_t is the concentration of PGMs in the slag after time t, C_0 is the initial concentration (mg/m^3), D is the migration coefficient of PGM particles (m^2/s), A is the surface area of iron (m^2), k is an efficiency coefficient (m^{-4}) and t is time (s).

The use of Stokes' law to describe the settling of the metal particles is an over simplification as Stokes' law is only valid for fluid systems with very a low Reynold's number. The superheating of the surface of the slag layer causes a circulation of the slag due to convection currents and the generation of carbon monoxide and carbon dioxide as products of the carbothermic reduction process causes agitation of the melt which both create complex flow

patterns in the slag. The experiments used to develop this model were performed in muffle furnace based crucible trials which would have resulted in a static slag and more idealistic conditions. Although equation 4 includes a migration coefficient it only assumes that the PGM particles move by Brownian motion and does not account for their movement by advection in the slag. However, despite the model being an over-simplification of the process, it is a useful way to imagine the settling of the PGM particles and how to understand why a collector metal is necessary.

One of the major issues with recycling of PGMs from catalysts is the collection and sorting of the material. The mixing of automotive catalyst scrap and diesel particulate filters (DPF) during manual removal is common and the DPFs which are usually made of silicon carbide cause a processing problem during the process. The high melting point of silicon carbide causes an increase of the viscosity of the slag melt pool reducing the PGM recovery efficiency. Chapter 3 in this thesis is dedicated to separate silicon carbide from the cordierite based automotive catalyst to facilitate the PGM recovery and widen the scope of acceptance of raw material for end users of the plasma technology.

Although the plasma process is well established for the recovery of PGMs from spent automotive catalysts, there are a wide variety of catalysts which are in use particularly within the petrochemical and industrial chemical industries. Many of these catalyst contain metals other than the PGMs for example one of the chapters of this thesis deals with the recovery of both platinum and rhenium from spent petrochemical catalysts. Rhenium is a metal whose chemical behaviour is different from platinum and is easily oxidised at high temperatures. This has made the recovery of rhenium difficult via pyrometallurgical processes and has not

previously been reported. However, the flexibility of the plasma process means that operating conditions can be optimised to suit the chemistry of rhenium and promote its recovery into a collector metal for further hydrometallurgical refining. This work can be found in chapter 4.

The plasma process also produces large quantities of slag as a by-product in metal recovery processes and as the main product from hazardous waste treatment. Although this material is chemically inert, it is not currently used in any higher value applications other than landfilling or as a construction aggregate. Increasing the value of this material would have a significant impact on all the plasma processes, but in particularly those environmental processes which treat hazardous waste. The use of the slag as a cement replacement has been another focus of the research presented in this thesis which aims to understand the suitability of the plasma derived slag as a raw material for alkali-activated slag binders and also as a pozzolan and this work can be found in chapters 5 and 6.

Finally, similarly to the use of plasma as a clean heat source to optimise the process chemistry for rhenium recovery, plasma can be used to facilitate chemical reactions. The final chapter of this thesis discusses the potential use of plasma as a tool for carbon dioxide abatement and the valorisation of siderlurgical (iron and steel making) waste gas streams. The blast furnace and coke ovens in iron making produce large quantities of gases which contain high concentrations of carbon dioxide and other compounds associated with global warming. However, especially in continental Europe there are large amounts of excess renewable energy available for industrial use and so using plasma powered by renewable electricity a clean and environmentally sustainable method of reutilising these waste gas streams could be achieved. Blast furnace top gas can be reformed to produce high quality synthetic gas and

coke oven gas can also be reformed to produce a gas with high reducing potential to be used in the blast furnace as a substitute for coke. This work can be found in chapter 7.

The layout of the thesis is a traditional one which includes an overview of methods and materials, literature review and experimental results and discussion. However, due to the broad nature of the thesis the literature review will not be a single piece of work, but spread over the chapters. This is to help the reader through the thesis by improving the flow of the work.

2. Methods and materials.

2.1. Introduction.

Technical and analytical methods were used to produce data for this thesis. This chapter outlines the most prevalent techniques in the thesis and details of experiments used in isolation for specific sets of data will be given in the relevant section for ease of reading and understanding for the reader.

2.2. Tetronics Pilot Scale Plasma Plant.

2.2.1. Plasma Furnace.

Tetronics' pilot plant in Swindon, UK was used to demonstrate the recovery of platinum and rhenium from spent petrochemical reforming catalysts. The plant consists of a plasma furnace and an emissions gas 'off-gas' treatment system.

The plasma furnace used was a twin spout, steel vessel with an internal diameter of 650 mm and lined with an alumina spinel refractory (91% Al_2O_3, 7% MgO and 2% CaO). The upper section and roof of the furnace were water cooled to maintain a stable furnace temperature. A plasma arc was produced by passing an electric current between a graphite electrode acting as the cathode and a graphite disk present at the base of the furnace acting as the anode. Argon passed through the graphite electrode stabilized the arc avoiding the arc behaving unpredictably and attaching to other conductive pathways inside the furnace. During the process, the raw materials form a conductive melt pool which acts as the anode maintaining the electrical pathway. A direct current (DC) is supplied by a plasma power supply (PPS) which transforms alternating current (AC) to DC current and regulates the voltage, current and power. The plasma arc supplies heat to the process and the operational temperature is

maintained at around 1500°C. The graphite electrode is manipulated by a robotic arm moving it up or down increasing or decreasing the arc length. The length of the plasma arc influences the power input to the process. By increasing the arc length the resistance of the circuit, due to air, increases which in turn increases the voltage. For a given current, increasing the voltage of the process would increase the power input into the furnace shown in Equation 2-1 and Equation 2-2.

$$P = IV \qquad \text{Equation 2-1}$$

$$V = IR \qquad \text{Equation 2-2}$$

Where P is power (W), I is current (A), V is voltage (V) and R is resistance (Ω).

Figure 2-1 is a schematic is of a typical plasma furnace and is essentially the same as the furnace used in the trials except that the trial furnace had a twin spout configuration. A twin spout furnace has two tap holes, one located above the other, which can be seen in Figure 2-2. The highest tap hole is designed to remove slag from the furnace whilst the lowest tap hole is to remove the metal which sits below the slag. This configuration allows for the intermittent removal of slag from the furnace allowing for a significant accumulation of metal.

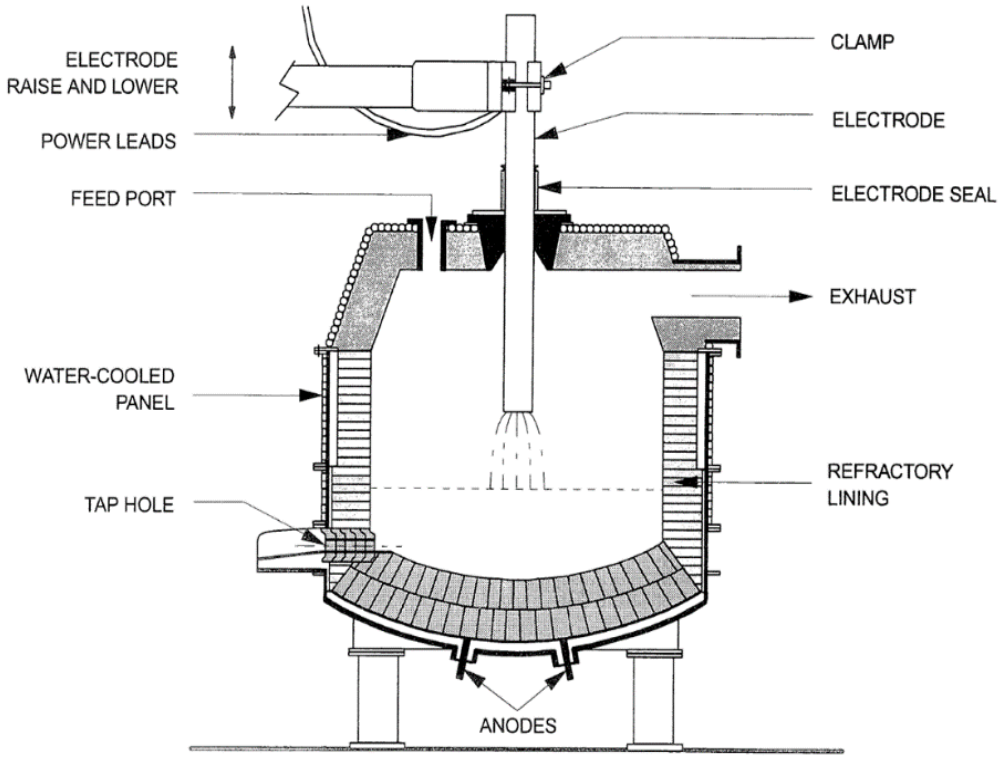

Figure 2-1: A schematic of a typical plasma furnace. Furnace internal diameter 650 mm. (Tetronics, 2012).

The tap hole is plugged with refractory that requires piercing using a thermal lance which is a tube through which oxygen is piped to remove material. The oxygen burns through the refractory releasing the molten mass inside which is then collected in a ladle or a 'slag pot' and allowed to cool.

In the pilot trials, the catalysts were blended with fluxing agents, a collector metal and reducing agents inside a rotating intermediate bulk container (RIBC). The blended material was placed into a hopper from which it was feed to the furnace by a screw feeder. The feedrate was controlled remotely and gradually increased to 100-120 kg/h. The furnace was operated at a controlled temperature around 1500°C and at a pressure of between 50 and

100 Pa controlled by an inverter driven induced draft (ID) fan which also controlled the gas flow into the off-gas system.

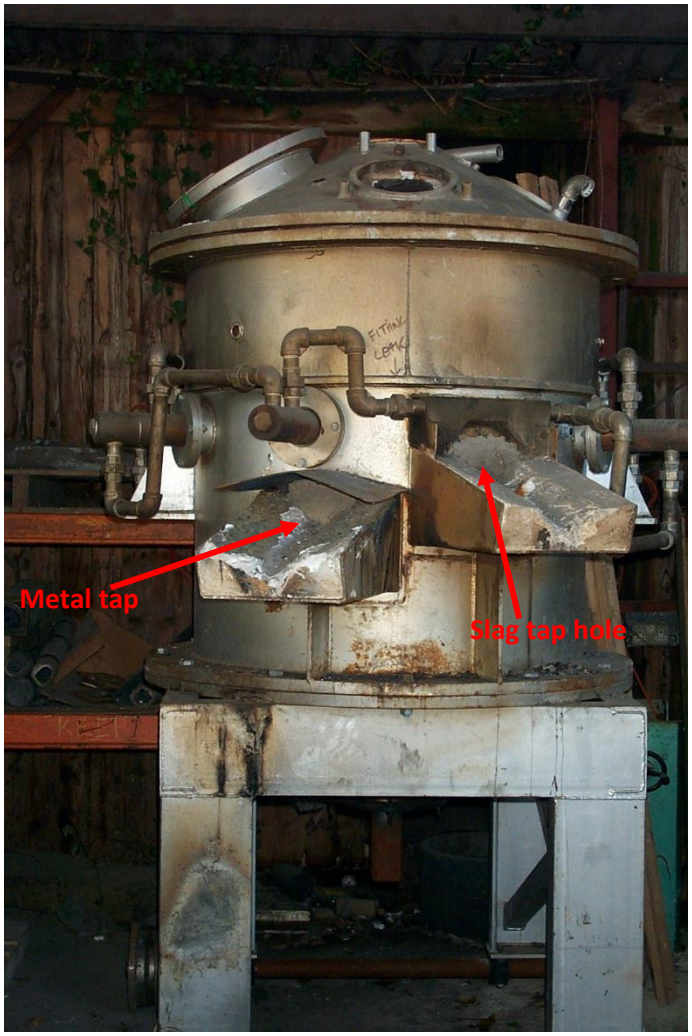

Figure 2-2: A photograph of a twin spout plasma furnace with an internal diameter of 650 mm (Tetronics, 2017).

2.2.2. Off Gas System.

The off gas system consists of emissions control equipment designed to reduce emissions to the environment. From the furnace the gaseous compounds and particulate matter enter a refractory lined combustion chamber where volatile components are combusted. Afterwards they enter a cooling chamber which lowers the temperature to below 200°C so that the material can enter a baghouse, lined with a polytetrafluoroethylene (PTFE) filtration membrane, to trap particulate matter. A wet scrubber follows the baghouse which uses a caustic solution to neutralise any acidic gases before the final emissions stack. In the plasma trials to recover Pt and Re from the reforming catalysts, the composition of the off-gas was monitored at two sample points (A and B) to ensure that the emissions were compliant with the site's environmental permit and also to measure the concentration of rhenium in the off-gas. The sampling and measurements were performed by a third party analytical team due to licence requirements.

Sample point A was located immediately at the furnace exhaust to determine the rhenium content in the gas before it interacted with the emissions control system. Particulate phase rhenium was trapped using a heated glass cyclone and glass fibre filter. The vapour phase rhenium was collected when the filtered gas was passed into solution containing nitric acid/hydrogen peroxide. The procedure used to analyse the components conformed to BS EN 14385 and the typical measurement technique employed to analyse the components is inductively coupled plasma optical emission spectroscopy (ICP-OES).

Sample point B was located at the emissions stack to measure the composition of the gas. At this sample point the particulate matter concentration was determined using a quartz filter and measuring the gas velocities and temperature. The gas was also analysed for hydrochloric

acid (HCl) and sulphur dioxides (SO_2) based on BS EN 14791, volatile organic compounds (VOCs) following BS EN 12629, combustion gases (CO, CO_2 and O_2) following BS EN 15058 and NO_x following BS EN 12629. The sample points A and B are shown in Figure 2-3 which is a schematic outlining the complete plasma process.

The process was controlled using a supervisory control and data acquisition (SCADA) system and was used to collect process data (temperatures, heat losses etc.). The trial campaign consisted of five, ten hour, trials and after each trial the material generated in all parts of the process was collected, weighed and sampled for analysis.

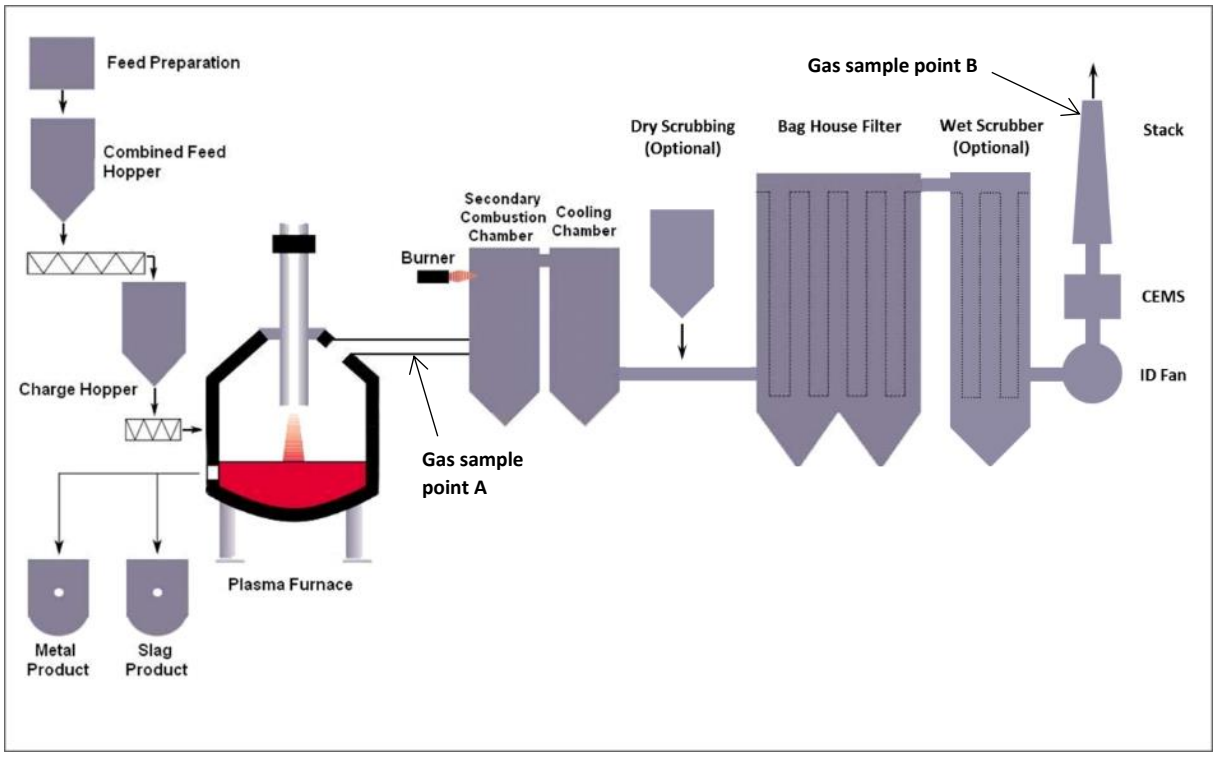

Figure 2-3: A schematic of the plasma pilot plant, including the furnace and the off gas system. Sample points A and B represent the locations were gas analysis took place.

2.3. X-Ray Fluorescence (XRF).

X-ray fluorescence (XRF) was used to determine the composition of samples. It is a technique used to obtain the bulk composition of a material by taking advantage of the unique electron configuration of an element.

When an X-ray is directed at an atom, it can cause the ejection of an electron from its inner shell. This vacancy leaves the atom in a high state of excitement and this causes an outer-shell electron to relax and fill this vacancy. As the electron relaxes it releases energy, in the form of an X-ray, due to the inner-shell electrons having less energy than those in the outer-shell. The energy can be detected and is characteristic of a particular element. The number of X-rays of a certain energy collected per unit time is then related to the concentration of the element in the sample. As each element has a number of different electron shells, many vacancies are created and are filled by electrons from the K, L or M shells creating a 'finger print' of the element used for its identification.

Elements lower than sodium (Na) in the periodic table cannot be detected using XRF due to their electron configuration and so XRF is only a semi-quantitative technique and must be used with other complementary techniques to determine a full composition. This is particularly important for carbon which cannot be detected using XRF and so XRF is usually used in conjunction with loss on drying and loss of ignition to determine the moisture and carbon content of a material. Nevertheless, the speed and ease of XRF analysis makes it a powerful technique.

A limitation of XRF is its lower limit of detection (LLD). A rule of thumb is that XRF analysis can be considered accurate up to 100 parts per million (ppm) or 0.01 wt%. Therefore, for accurate

trace metal analysis, particularly for precious metal analysis, alternative techniques such as ICP-OES are used which has a LLD from between 1 – 10 ppm.

The machine and measurement technique affects the accuracy of XRF analysis. Wavelength dispersive (WD) XRF is generally more accurate than energy dispersive (ED) XRF. In WDXRF, the X-rays emitted from the material are directed onto a crystal which are then dispersed in different directions depending on their wavelength which are then measured by a detector moving through different angles, effectively scanning for each element. EDXRF machines have a static detector and the X-rays are all directed onto it at once which can result in distortion of the data or spectral overlap. WDXRF machines can typically achieve a resolution of between 5 to 20 eV whereas EDXRF resolutions are between 150 to 300 eV. However, EDXRFs are able to perform their analysis faster than WDXRFs, can be portable, require minimal sample preparation and when properly calibrated are very useful tools.

XRF analysis is a surface analytical technique and so requires a representative surface composition for accurate results. Samples can be prepared as pressed pellets or more complex fused beads. A pressed pellet is made by mixing the sample with an 'XRF invisible' binder, usually cellulose or carbon based wax, at a 5:1 sample to binder ratio and then compacted using a die press to make a pellet usually with usually an 8 mm diameter, although larger sizes can be made. Achieving a representative surface is of vital importance, otherwise erroneous results will be obtained. A finer particle size increases the number of particles present on the surface allowing for a more representative sample and more accurate results.

However, sometimes the X-rays released by one element may be strong enough to cause secondary excitation in another and causing it to appear to be present in a greater

concentration. Making glass beads of the sample is one way to avoid this problem. To make a glass bead, the analyte is melted with lithium metaborate and lithium tetraborate at 850°C before being cooled into to form a glass. This procedure breaks up the structure of the analyte and produces a glass with the components randomly distributed on the surface. This method is able to produce more homogenous samples, but is more complex and time consuming than producing pressed pellets.

However, in this research it was found that unless the slag was ground to less than 65 µm, the XRF results were not accurate and resulting in them displaying a higher calcium content than that was present in reality.

Figure 2-4 illustrates the differences obtained from the compositions of the slags from the plasma trials due to their sample preparation techniques. The normalised compositions are plotted on the phase diagram and it is seen that the fused bead sample compositions are very close to the designed slag composition and the pressed pellet samples are shown to be higher in calcium. However, once the particle size of the slag was reduced to below 65 µm, the fused bead compositions were almost identical to the composition from the pressed pellet.

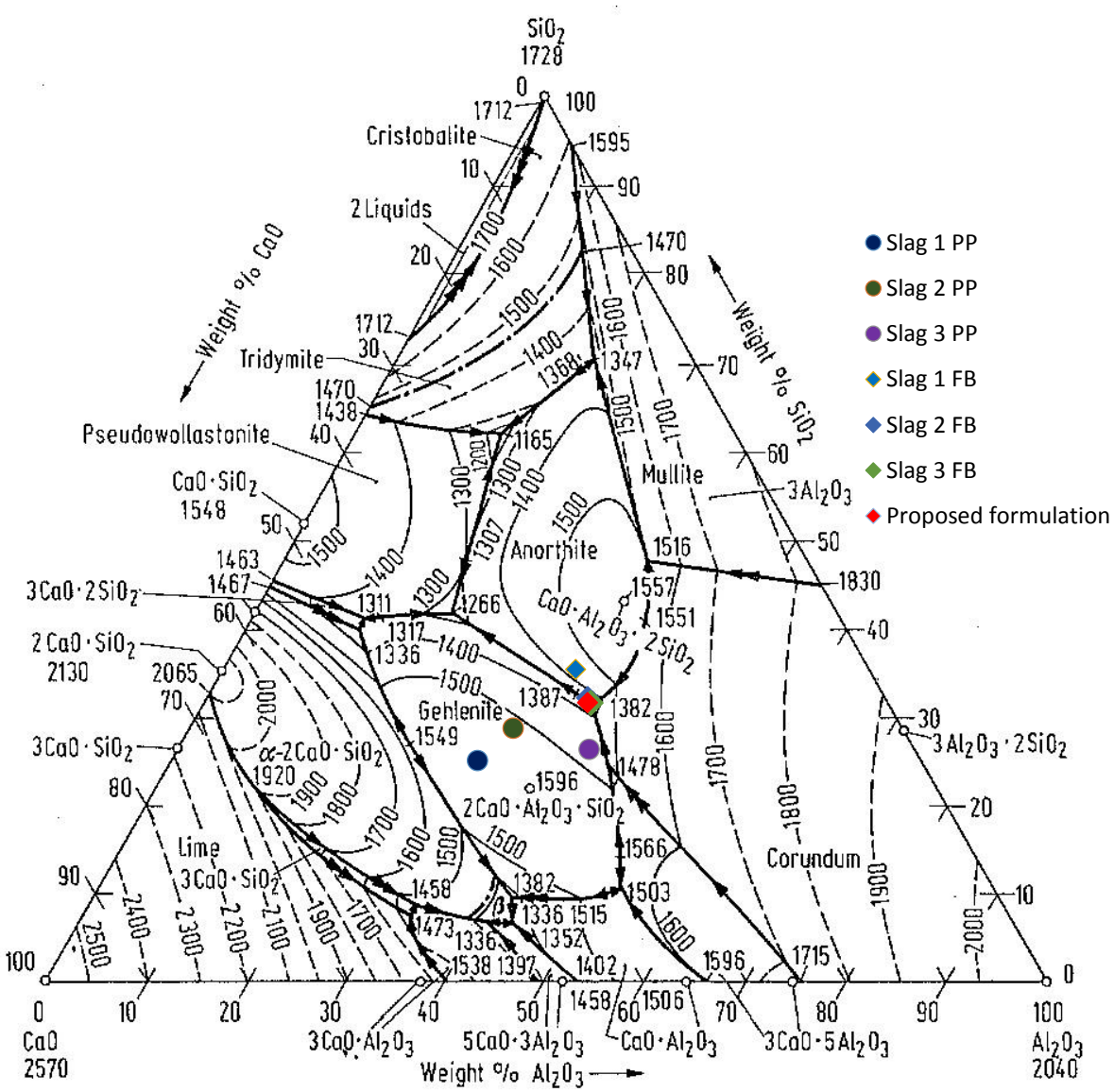

Figure 2-4: Comparison between the slag compositions obtained using the pressed pellet and fused bead sample preparation techniques.

Unfortunately, even though each element has a unique fingerprint, there can be an overlap of the peaks of certain elements which can make analysis difficult. Therefore, it is useful for the user to have an idea of what they would expect to be present in the material to properly analyse the data and not be over reliant on the computer software. A particular problem which was encountered during this work was an overlap between rhenium's $L_{\alpha 1}$ peak and

zinc's $K_{\alpha 1}$ peak which occurs at 8.637 and 8.652 respectively. The overlap of these particular peaks, shown in Figure 2-5 caused the software to assign the peak to zinc because it is the more common element. However, in this material which was the particulate from the off-gas system both zinc and rhenium was present and so this required software manipulation to determine both their contents.

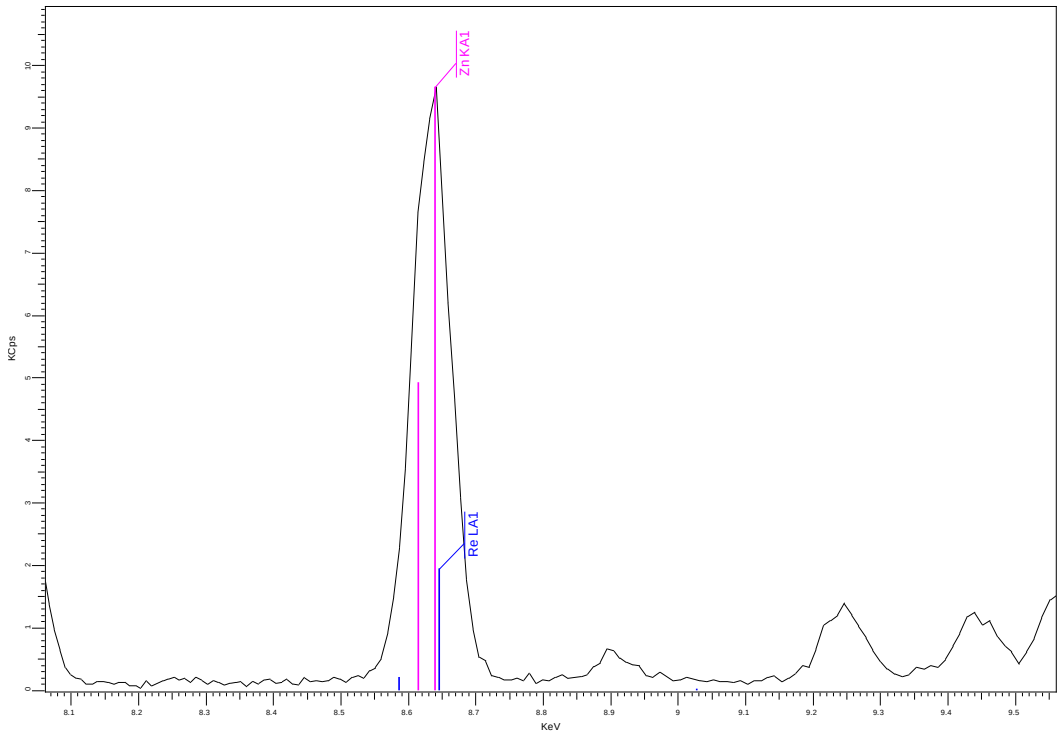

Figure 2-5: XRF peak overlap between zinc Kα and rhenium Lα peaks.

Manipulating the software to analyse for rhenium's L_{α} peak and for zinc's L_{α} it was possible to obtain a concentration of both these elements show in Table 2-1. Comparing the analysis of the rhenium content in the particulate using the XRF with software manipulation with the results obtained from ICP-OES of the material in Table 2-2 shows that similar results could be obtained which leads to confidence in the method.

Table 2-1: Comparison between Zn and Re analysis results depending on XRF software manipulation.

XRF analysis method	Zn (wt%)	Re (wt%)
Analyse for default peaks	2.98	Not detected
Zinc not present	Not detected	8.17
Analyse for Zn-$L_{\alpha1}$ and Re-$L_{\alpha1}$	1.8	2.84

Table 2-2: Comparison between Re content in the particulate using XRF and ICP techniques.

Rhenium content in the total particulate	T3	T4
XRF (g)	8.4	6.2
ICP-OES (g)	8	6

In this work XRF was used to determine the bulk composition of materials and used as a first basis to determine the change in composition of a material after experimentation. The majority of the XRF data, unless otherwise stated, was obtained using a Bruker S8 Tiger WDXRF machine with a rhodium X-ray source.

2.4. Inductively Coupled Plasma Optical Emission Spectroscopy (ICP-OES).

Inductively coupled plasma optical emission spectroscopy (ICP-OES) was used throughout the work to determine trace metal analysis with the emphasis on the PGM content of materials. The concentration of PGMs in the material was expected to vary between 10 ppm and 3000 ppm making ordinary XRF analysis inaccurate. ICP-OES is commonly used for trace metal analysis due to its capability of achieving a very high analytical resolution up to 5 ppm. The analysis was performed by a third party laboratory either the Birmingham Assay Office or AMG analytical services in Rotherham.

ICP-OES detects photons emitted by elements after they have been excited by a radio frequency discharge plasma. A liquid sample is injected into a nebuliser which converts it to

an aerosol and is then directed towards the plasma. The argon plasma vaporises the sample and liberates all the elements contained in it. Electrons are emitted from the atoms causing them to become excited and when they return to a relaxed state, photons of an energy specific to the element are emitted. The photons are detected and the analysis is made.

The sample must be in solution for the analysis to occur and so solid samples need to undergo digestion into solution. Strong acids such as hydrochloric (HCl), nitric (HNO_3) or hydrofluoric (HF) acids are used to digest the solid and ensure that there is complete decomposition of the solid matrix to ensure proper analysis of the sample.

ICP-OES was used to determine the platinum and rhenium concentration in the raw materials and products produced during the thermal plasma trials for their recovery and also to determine the PGM concentration in automotive catalyst scrap.

2.5. X-Ray Diffraction (XRD).

X-ray diffraction (XRD) was used to discover and identify crystalline phases present in a sample. It was used to determine the extent of crystallisation of slag samples which is an important factor in their ability to be used as a cement replacement. It was also used to determine the phases present in samples, for example the components contained in mixed automotive scrap. When used in conjunction with XRF, it was used to identify minerals and phases present in the material.

During XRD analysis, X-rays are directed at a sample which are scattered by the sample over different angles. Crystalline materials have a unique structure, which is symmetrical and displays long range periodic order, meaning that the lattice planes of a crystalline material are separated by a regular spacing (d-spacing). The scattering of X-rays from successive

crystallographic planes causes the diffracted radiation to be in phase with each other. This is known as constructive interference and is known as Bragg diffraction which satisfies Bragg's Law (Equation 2-3):

$$n\lambda = 2d\sin\theta \qquad \text{Equation 2-3}$$

Where n is an integer, λ is the wavelength of the incident X-ray, d is the lattice spacing between crystallographic planes and θ is the angle between the incident rays and the surface of the crystal.

By scanning a range of 2θ angles a diffraction pattern can be obtained and using Bragg's law the wavelength of the X-ray can be related to the diffraction angle and the d spacing which can be used to identify the crystalline component.

The XRD patterns of purely crystalline substances show sharp diffraction peaks, but if the material is amorphous there is no long range periodic order due to the asymmetric distribution of components meaning that constructive interference cannot occur. This causes the diffraction pattern of an amorphous material to show a broad, diffuse halo. Although this halo cannot be used to identify materials, it is useful in determining the nature of the material. This is particularly interesting for slag analysis; when slags are cooled quickly they form a glassy amorphous structure which has different properties than slowly cooled, crystalline slags. A comparison between the XRD patterns of an amorphous and a crystalline material is shown in Figure 2-6.

In this work, powdered XRD analysis was used to analyse samples using a Bruker D2 Phaser with a molybdenum target for the X-ray source. Powdered XRD requires the materials to be

finely ground, homogenous powders to produce high quality data and so samples were milled in either a planetary disc mill or with a pestle and mortar, depending on how hard the material was.

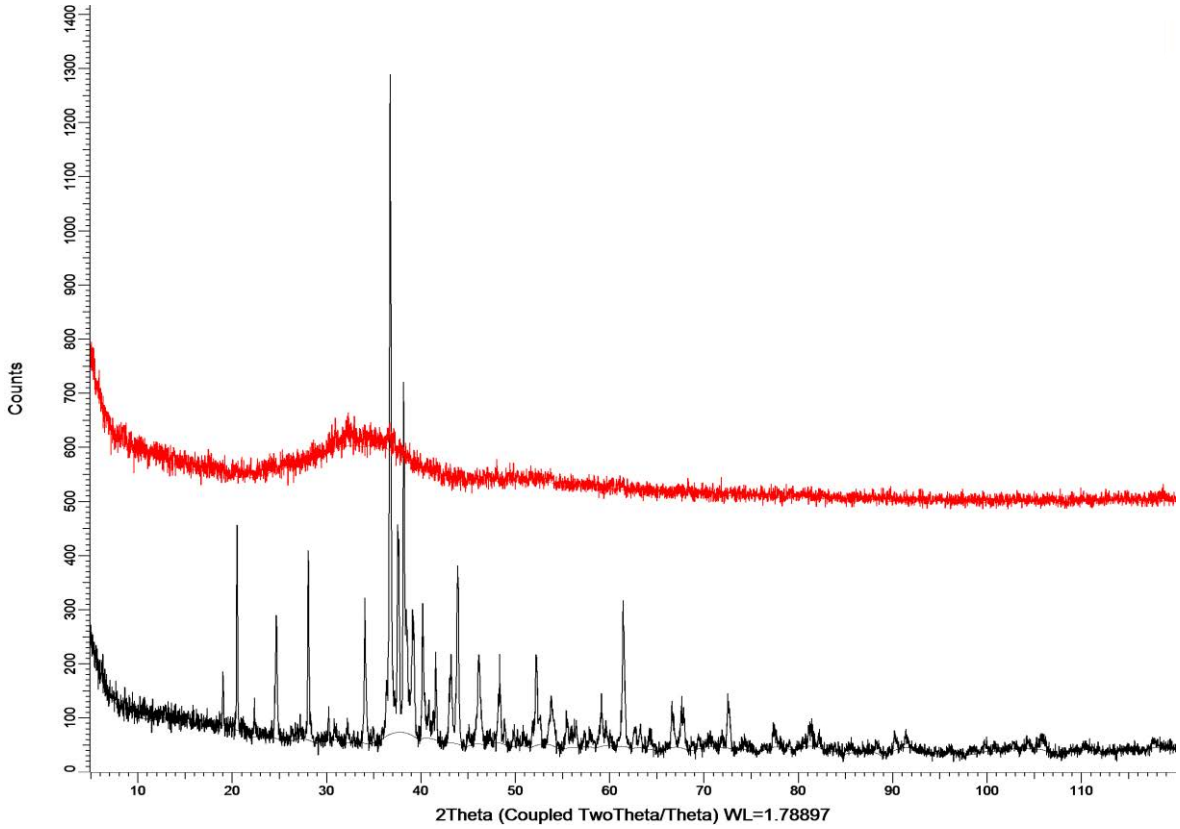

Figure 2-6: A comparison between the XRD pattern of an amorphous slag in red and a crystalline slag in black. The amorphous slag shows a diffuse halo characteristic of non-crystalline materials.

2.6. Scanning Electron Microscopy (SEM).

Using microscopic analysis to examine a material's microstructure can give an insight into its properties. An SEM image is generated by focusing an electron beam using condensing lenses on a sample. The electron beam interacts with the atoms in the sample producing secondary electrons, backscattered electrons and X-rays; all three of these can be used to analyse the samples in different ways.

Secondary electrons are produced by the electron beam knocking electrons from the shells of an atom in the sample. These electrons are detected and are used to create a topographic image. The number of electrons detected is related to the topography of the point on the sample. Electrons are more easily 'recaptured' by the sample on flat areas than they are on higher areas and so more electrons are detected from higher areas giving the appearance of a raised section show in a diagram in Figure 2-7.

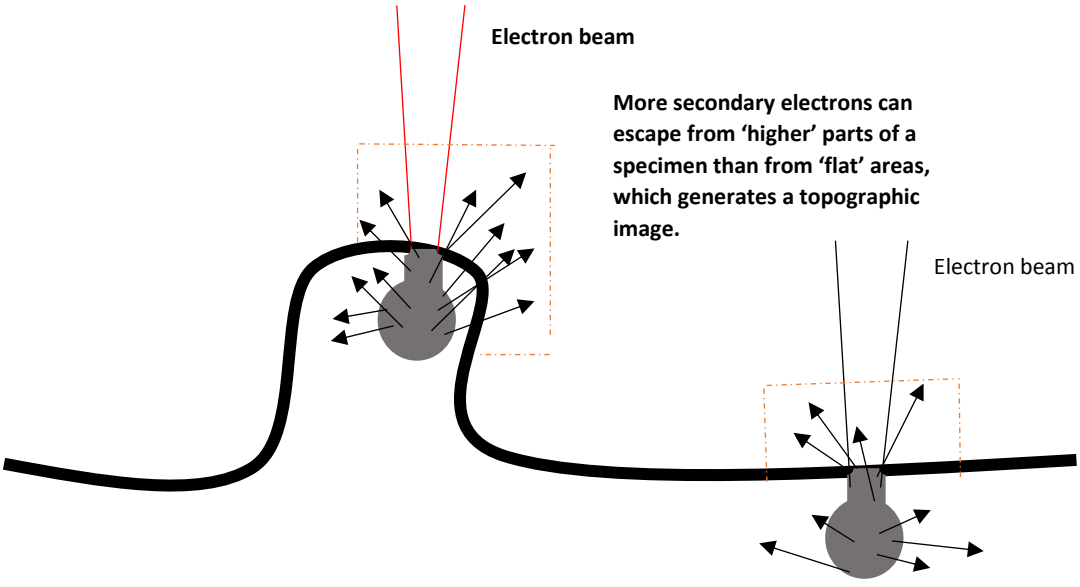

Figure 2-7: A diagram representing the mechanism of the production of topographical images using an SEM (Keeley, 2017).

A backscattered electron (BSE) is one which has collided with an atom in the sample causing it to 'bounce backwards' in an elastic process. These backscattered electrons are detected and an image of the sample can be formed. As the atomic mass of an atom in the sample increases, more electrons are backscattered and so elements with a higher atomic mass appear brighter than elements of a lower atomic mass in a sample. Therefore, an image is created with varying contrasts dependent on the relative concentration of heavier or lighter atoms in a specific area. BSE images can be interesting to see the changes in composition and distinct phases in a sample. In this work BSE images were useful in understanding how platinum and rhenium were distributed in a base metal alloy produced plasma smelting. An example of a back scattered image is seen in Figure 2-8 which is an image of the Pt-Re rich collector metal alloy. The bright phases are where the precious metals are located.

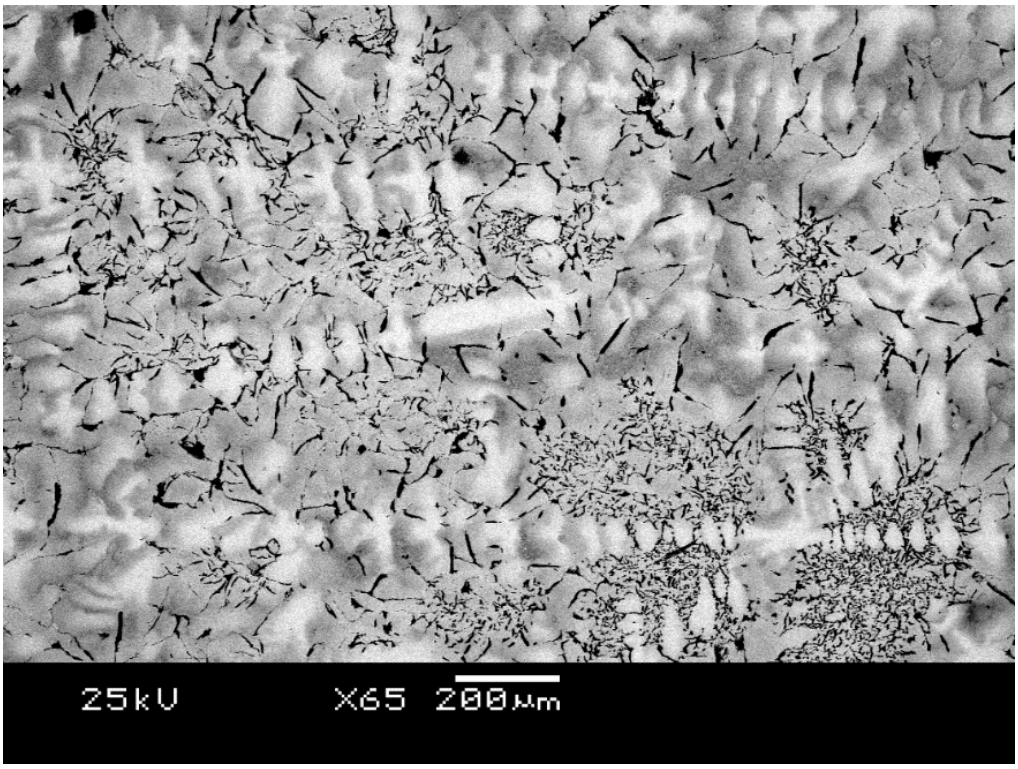

Figure 2-8: A back scattered electron image of the collector metal alloy showing the Pt and Re rich bright sections of the alloy.

When electrons are knocked out of the atoms in the sample characteristic X-rays are emitted. This means with an X-ray detector equipped to the SEM, element analysis can be made. By focusing the electron beam at small sections of the sample it is possible to determine the composition and this technique is known as energy dispersive X-ray spectroscopy (EDX).

A JEOL 6060 SEM equipped with an Oxford Instruments EDX with INCA software was used to examine samples for this work. For SEM analysis, the sample preparation is of great importance in being able to obtain good images and data. Obtaining flat, polished samples for metal analysis is best for BSE and EDX analysis. The collector metal samples were polished to a 1 µm finish with diamond polishing fluid using a metal lapping machine and then etched using natal which brought out the microstructure of the material. Nital was prepared by slowly adding 2 ml of 70% nitric acid to 98% ethanol whilst stirring. For high vacuum SEM analysis, samples must be conductive and non-conductive samples such as alkali-activated pastes were coated with gold and attached to a stub with carbon tape and silver paint to give a good conductive pathway. This avoids charging on the surface of the sample which distorts the image. Surface coating the material with gold means BSE imaging is not possible, but EDX analysis is still possible due to the user being able to manipulate the acquired data.

2.7. Raman Spectroscopy.

XRD is a very powerful technique, but the lack of long range order of amorphous materials makes XRD analysis limited. Although glassy slags are not crystalline, they do contain structural units which can be studied using light spectroscopy such as Raman spectroscopy and Fourier Transform Infrared Spectroscopy. These structural units lack long range periodic order making the material X-ray amorphous, but they do play an important role in determining the properties of the slag. Similarly, cement pastes and alkali-activated pastes are also X-ray

amorphous, but also have a structure which influences the properties of the material. Using both these techniques it is possible to examine the bonds present in a sample and from that gain an understanding of the structures which are present.

Raman spectroscopy is a technique which detects Raman scattering caused by a sample when it interacts with light. Light can be reflected, absorbed, transmitted or scattered by a material. When light is scattered most of the light is unchanged, but when a tiny proportion of light interacts with molecular vibrations, its frequency changes because it has either gained or lost energy. The change in energy is dependent on the frequency of the molecular vibrations which is dependent on the type of bonding. If there are strong bonds present in the molecule then there is a high frequency change, whereas weaker bonds cause only a low frequency change. Therefore, by looking at the type of bonds present in the sample, an idea of the structure can be gained.

In this work, Raman spectroscopy was used to identify the structural units present in slags. Slags can be considered to have a network structure composed of interconnected silicon tetrahedra. The structural units present in the slag cause vibrational frequency peaks between 850 – 1190 cm^{-1} with a shift to a higher frequency with a greater number of bonded oxygens; the Q_{Si}^{n} notation describes a silicate structural unit with n number of bridging oxygens from 0 to 4. The frequency assignments can be seen in Table 2-3.

The Raman spectrum which is obtained from slag samples is a broad and diffuse spectrum because the material is non-crystalline and also because of the presence of a number structural units. The Raman spectra can be deconvoluted from a broad diffuse peak to a series

of individual peaks which show the presence of various species. The deconvolution was performed using a peak fitting software Fityk shown in Figure 2-9.

Table 2-3: The Raman frequencies of silicate structural units in slag (Mysen 1980).

Q^n_{Si}	Structural Unit	NBO/Si	Frequency (cm^{-1})
Q^0_{Si}	SiO_4^{4-}	4	850-880
Q^1_{Si}	$Si_2O_7^{6-}$	3	900-920
Q^2_{Si}	$Si_2O_7^{4-}$	2	950-980
Q^3_{Si}	$Si_2O_5^{2-}$	1	1050-1100
Q^4_{Si}	SiO_2	0	1060-1190

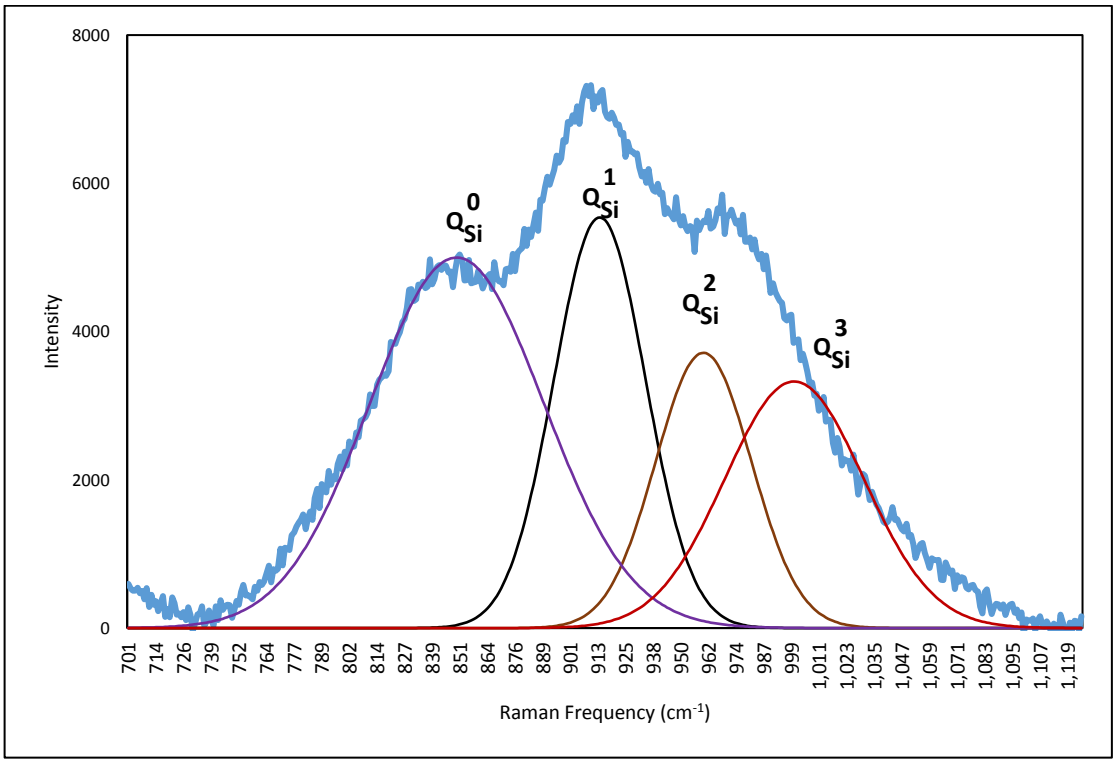

Figure 2-9: The diffuse Raman spectrum of a slag and the deconvolution of the spectrum using Fityk peak fitting software (Keeley et al. 2017).

In this work a Renishaw inVia Raman microscope with a 532 nm edge laser with a 50 cm filter was used. The frequencies obtained for a given vibrational transition are the same for Raman spectroscopy as they are for FTIR, but the method through which these frequencies are obtained is different meaning that the intensities of the peaks are different. FTIR was used to analyse the bonds present in the alkali-activated pastes which were produced from the slag samples due to the data obtained from the Raman microscope not being sufficient.

2.8. Fourier Transform Infra-Red Spectroscopy.

Fourier transform infrared spectroscopy (FTIR) is a technique which measures the amount of light of a certain wavelength is absorbed by a sample. A light source will shine a beam of light containing many different frequencies at a sample. The frequencies of light which are absorbed by the sample are measured and the process will be repeated numerous times with various combinations of light frequencies. The data is then converted by a computer using a Fourier transformation to produce a spectrum.

FTIR was used to study the structure of the alkali-activated slag binders. Like the slag, these pastes have an aluminosilicate chain structure and the extent of the interconnectivity of the chains determines the structure of the paste which in turn gives the material certain properties. Identifying the structure can be used to determine the presence of phases such as calcium-silicate-hydrate (CSH), calcium-aluminium-silicate-hydrate (CASH) and sodium-aluminium-silicate-hydrate (NASH) which have a short chain silicate structure (low tetrahedral connectivity), silicate sheet structure (intermediate tetrahedral connectivity) and three dimensional silicate structure (four-fold tetrahedral connectivity).

The silicon units frequencies are the same as they are for Raman spectroscopy, but it has been reported in the literature that the substitution of aluminium for silicon in the structure causes

a slight shift to lower frequencies. The spectrum can be used to determine the presence of other bonding present such as O-H bonds at 3200 – 3700 cm^{-1}, H-O-H at 1650 cm^{-1}m and carbonate at 1470 and 870 cm^{-1}. However, the assignment of peaks can be slightly confused as some bonds produce vibrational frequencies at the same point for example Al-O stretching can cause a peak at 870 cm^{-1} which is the same as carbonate and so complementary analysis can be required to gain confidence in the data. A combination of EDX and FTIR was used to determine the presence of the multicomponent nature of the alkali-activated slag paste highlighting the complex microstructure of the material. A Varian 660-IR FTIR Spectrometer was used during this work.

2.9. HSC Modelling.

Thermodynamic modelling was used in this work to calculate equilibrium compositions from a mixture of raw materials and to predict the behaviour of elements to determine optimum operating conditions. HSC Chemistry is software developed by Outotec which uses a thermochemical database to make chemical reaction and equilibrium calculations based on the Gibbs energy minimization method. This calculates the mixture of reaction products, from what can be several simultaneous chemical reactions that gives the lowest Gibbs free energy under either isothermal or isobaric conditions.

The version of HSC used in this work is HSC Chemistry 7.0 and this software is used extensively at Tetronics as a first basis to design plasma processes and determine the operating conditions for trials. The software can be used to predict the partitioning of components during the process at a given operating temperature and determine energy input requirements by conducting mass and energy balances across process units.

The software calculates chemical compositions on a thermochemical basis and does not involve kinetic data such as reaction rates and heat or mass transfer effects. However, at the high operating temperatures during the plasma process, reactions are expected to happen very quickly so kinetics effects are assumed to be less important. Also the high temperatures in the furnace also allow for the assumption that the components display ideal behaviour. Therefore, HSC offers a good platform for the modelling of the plasma process which can be refined using empirical trials.

HSC requires the user to specify the reaction system by inputting the amount of raw materials, the phases present and the species which could be formed from the reactions and it then makes thermochemical calculations based on the enthalpy (H), entropy (S), heat capacity (C_P) and Gibbs free energy (G) of the chemical species. The database contains enthalpy and entropy data for chemical species and the heat capacity constants A, B, C and D. When required, the software will calculate the enthalpy (H), entropy (S), heat capacity (C_p) and Gibbs free energy (G) at a specific temperature using the relationships given in Equation 2-5 to Equation 2-8.

$$dH = c_P dT \text{ (at constant P)} \qquad \text{Equation 2-4}$$

$$H_{(T)} = H_{f\,298.15} + \int_{298.15}^{T} C_P\, dT + \sum H_{tr} \qquad \text{Equation 2-5}$$

$$S_{(T)} = S_{298.15} \int_{298.15}^{T} \frac{C_P}{T}\, dT + \sum \frac{H_{tr}}{T_{tr}} \qquad \text{Equation 2-6}$$

$$C_P = A + B \cdot 10^{-3} \cdot T + C \cdot 10^{5} \cdot T^{-2} + D \cdot 10^{-2} \cdot T^{2} \qquad \text{Equation 2-7}$$

$$G = H - T \cdot S \qquad \text{Equation 2-8}$$

Where T is temperature in Kelvin, $H_{f\,298.15}$ is the enthalpy of formation of the substance at 298.15 K, H_{tr} is the enthalpy of transformation the substance. $S_{298.15}$ is the standard entropy of the substance.

The change in enthalpy, entropy or Gibbs energy of reaction is given by the sum of the enthalpy, entropy or Gibbs energy of the products minus the sum of those properties of the reactants, an example of which can be seen in Equation 2-9 and Equation 2-10 and it is on this basis on which the software makes its calculations.

$$\Delta H_r = \sum n_i H_i(\text{products}) - \sum n_i H_i(\text{reactants}) \qquad \text{Equation 2-9}$$

$$\Delta G_r = \sum n_i G_i(\text{products}) - \sum n_i G_i(\text{reactants}) \qquad \text{Equation 2-10}$$

By calculating the Gibbs free energy, the equilibrium constant, K, can be obtained via Equation 2-11. The equilibrium constant is related to the extent of reaction, via Equation 2-12 and this can be used to determine the composition of a mixture of reaction products.

$$\ln K = \frac{\Delta G_r}{-RT} \qquad \text{Equation 2-11}$$

For the reaction $\mathbf{aA} + \mathbf{bB} + \cdots \rightarrow \mathbf{cC} + \mathbf{dD} + \cdots$

$$K = \frac{[C]^c \times [D]^d \times \ldots}{[A]^a \times [B]^b \times \ldots} \qquad \text{Equation 2-12}$$

Where R is the universal gas constant 8.314 J mol^{-1} K^{-1}; [A] is the activity or partial pressure of species A, B, C etc. and a is the stoichiometric coefficient of A in the reaction. If the reaction system is assumed to not deviate from ideal behaviour, the activity of the species can be substituted for its concentration.

When a reaction reaches equilibrium the change in Gibbs free energy, dG is 0 and the Gibbs minimization method calculates which composition of reactants and products would achieve the lowest Gibbs free energy whilst obeying the law of conservation of mass.

The user must ensure that they have sufficient knowledge of what species may be present in the system and what phases they would occur in. This must be done manually and the software is very much dependent on what the user inputs to be able to give accurate results.

The change in enthalpy of the process allows for the determination of the energy input into the process to be able to melt the material and it also indicates what impact fluxing agents will have on the process in reducing the plasma power input reducing operating costs.

2.10. Closing Remarks.

The methods outlined above are those which have been used extensively throughout the research presented in this thesis. The following text may refer to this section so the reader can refresh their mind over the plant layout for example. There are various other experiments which have been performed during the work, but are presented alongside the results to help the reader through this thesis.

3. The Removal of SiC From Mixed Automotive Catalyst Scrap.

3.1. Introduction.

3.1.1. Processing issues caused by silicon carbide.

Plasma technology is successfully used to recover platinum group metals (PGMs) from cordierite based end-of-life automotive catalysts. However, not all catalysts are cordierite based and cars can contain silicon carbide (SiC) based catalysts or SiC based diesel particulate filters (DPFs) which become mixed with cordierite based catalysts during collection and sorting.

DPFs are used in diesel engine exhaust systems to trap particulate matter emitted from the engine and are located immediately before or after the catalytic converter in a car's exhaust system. In the UK there are 12.1 million diesel cars representing 39% of the total number (Department for Transport, 2017), so there are high volumes of DPFs in end-of-life recycle chains. When a car reaches its end of life, the catalytic convertor is removed from the car so valuable PGMs can be recovered, but the DPF is also removed and often mixed with the catalytic convertor although, some catalysts are combined DPF and oxidation catalysts which are SiC based. A photograph of a SiC based catalyst from an Audi car is shown in Figure 3-1 (right) alongside a DPF (left). Typically a SiC catalyst would contain platinum as the catalytic agent in similar concentrations to a cordierite based catalyst (between 700 to 2000 ppm), but a diesel particulate filter would contain a lower concentration of platinum as it is only catalyses the regeneration process (around 100 to 300 ppm).

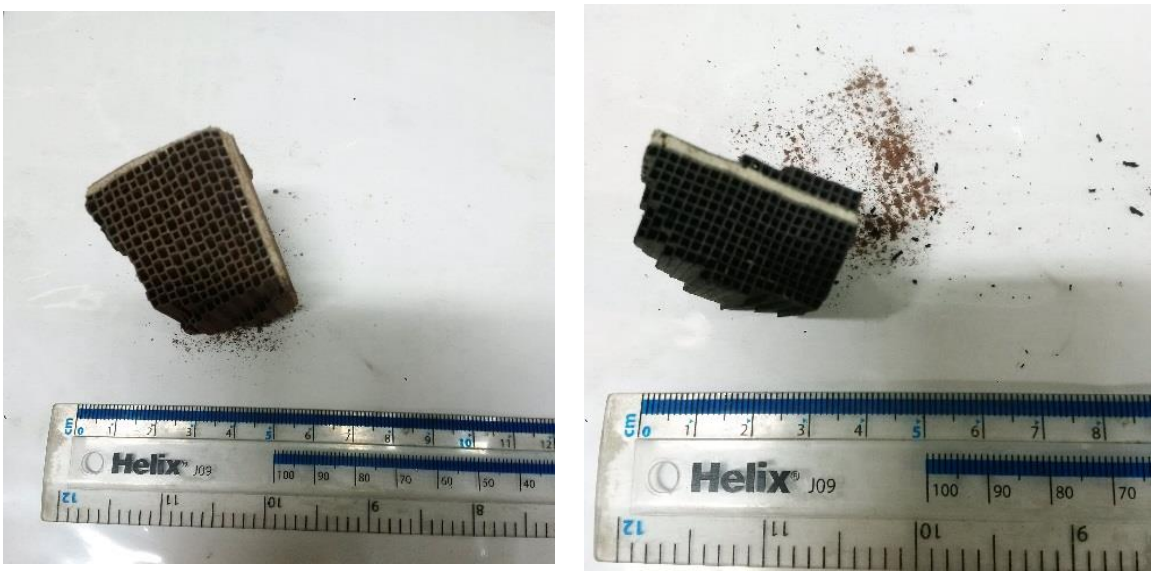

Figure 3-1: Photographs of pieces of a SiC diesel particulate filter (left) and a SiC combined catalyst (right).

The SiC content in the raw automotive catalyst scrap sent for PGM recovery is variable and can range from less than 1 wt% to almost 40 wt% (Table 3-1) and these inconsistencies in the composition of raw materials produce processing headaches. Generally, a SiC content over 5 wt% becomes problematic for plasma processes.

Table 3-1: Silicon carbide content in automotive catalyst raw material analysed over 27 different batches (data from Solar Technologies).

Parameter	SiC Content
Mean	10.18%
Maximum	0.88%
Minimum	37.19%
Standard deviation	7.5%

The viscosity of the slag during the plasma process is increased when silicon carbide is present due to its high melting temperature. A highly viscous slag is not desired because it inhibits the separation of metallic phases from the slag as the movement of metal droplets is dependent

on the viscosity of the slag (Huaiwei et al. 2012). An inefficient separation of the metal and slag causes a reduction in the recovery efficiency of the PGMs during the process. In the melt silicon carbide is conductive and for submerged arc processes this causes great difficulties as submerged arc furnaces rely on resistive heating to input power to the process. The lower resistivity of silicon carbide means the process requires more current to compensate for the lower resistance of the melt and at high SiC levels the current required to melt the material cannot be supplied (Johnson and Deegan, 2015). Tetronics' plasma process can tolerate SiC content of up to 5% because plasma furnaces rely on superheating the surface layer of the slag causing convection currents in the melt which is the major heat distribution mechanism (Johnson and Deegan, 2012). Nevertheless, the increased slag viscosity caused by SiC is the major issue for plasma processes and is a significant limitation on its operation.

Currently, the method employed at Tetronics to alleviate the problems associated with SiC in the plasma process is to increase the magnetite (Fe_3O_4) addition which oxidises SiC by the reaction between carbon and oxygen producing iron and silicon. However, the additional iron produced dilutes the PGM containing bullion, reducing its value and because the silicon is not oxidised, it partitions to the alloy increasing the silicon content of the bullion, which according to refiners such as Johnson Matthey makes final hydrometallurgical refining of the alloy difficult.

Removing SiC from the cordierite prior to it being added to the furnace would reduce variations in the raw material and widen the acceptance criteria of material which can be processed. This would help to improve PGM recovery by creating a more controllable and consistent feed.

The separation of materials from others relies on the exploitation of differences in material properties and silicon carbide's electrical conductivity differs from cordierite's. SiC is a semi-conductor whereas the cordierite is non-conductive (Table 3-2) and it is possible to exploit this difference in electrical conductivity using electrostatic separation.

Table 3-2: Electrical properties of silicon carbide and cordierite. (Kingon and Davis (1991); Shaffer (1991); Mahajan and Kimerling (2013)).

Material	**Dielectric constant (25°C, 1 MHz)**	**Electrical resistivity (Ω cm @25°C)**
Cordierite	4.7	10^{14}
Silicon carbide	10.2	10^{8}
Phlogopite	5-6	$10^{10} – 10^{13}$

During electrostatic separation, the particles acquire a surface charge which can pass through conductive particles to earth, but the charge remains on non-conductive particles. Therefore, the differences in how the charge can dissipate through particles is the key to their separation. The relaxation time (s) of a particle during electrostatic separation depends on its dielectric constant (the measure of the ability of a material to store electrical energy) and its resistivity. The relaxation time constant is calculated by Equation 3-1:

$$\tau = \varepsilon_r \varepsilon_o \rho \qquad \text{Equation 3-1}$$

Where ε_r is the dielectric constant of the material, ε_o is the permittivity of free space (8.85 x 10^{-12} F/m) and ρ is the electrical resistivity of the material (Ω/m). Cordierite has a greater electrical resistivity than silicon carbide and so opposes the flow of an electric current more strongly than silicon carbide. Therefore, the relaxation time constant for cordierite is several

orders of magnitude greater (41595s) than silicon carbide (0.09s) and phlogopite, the third phase present in the material has a relaxation time constant of 487s.

3.2. Electrostatic separation.

3.2.1. Particle size analysis.

Automotive catalyst raw material was obtained from Platinum Recoveries Limited (PRL) and crushed to a size range which 80% of the material was between 2000 and 100 µm. The particle size distribution of the material is shown in Figure 3-2.

Around 20% of the crushed material was below 90 µm, but typically, in electrostatic separation the optimum size range for recovery is between 2000 µm and 100 µm. At fine particle sizes below 100 µm, interparticle forces such as electrostatic attraction and repulsion forces as well as van der Waals forces become more dominant over gravitational forces and the force generated by the electric field. These interparticle forces can reduce the efficiency of the separation process because the particles can either agglomerate or not be affected by gravitational forces which are required to throw off the particles from the drum. At sizes above 2000 µm the gravitational forces become too strong and so the particles are more easily thrown off the drum despite their charge.

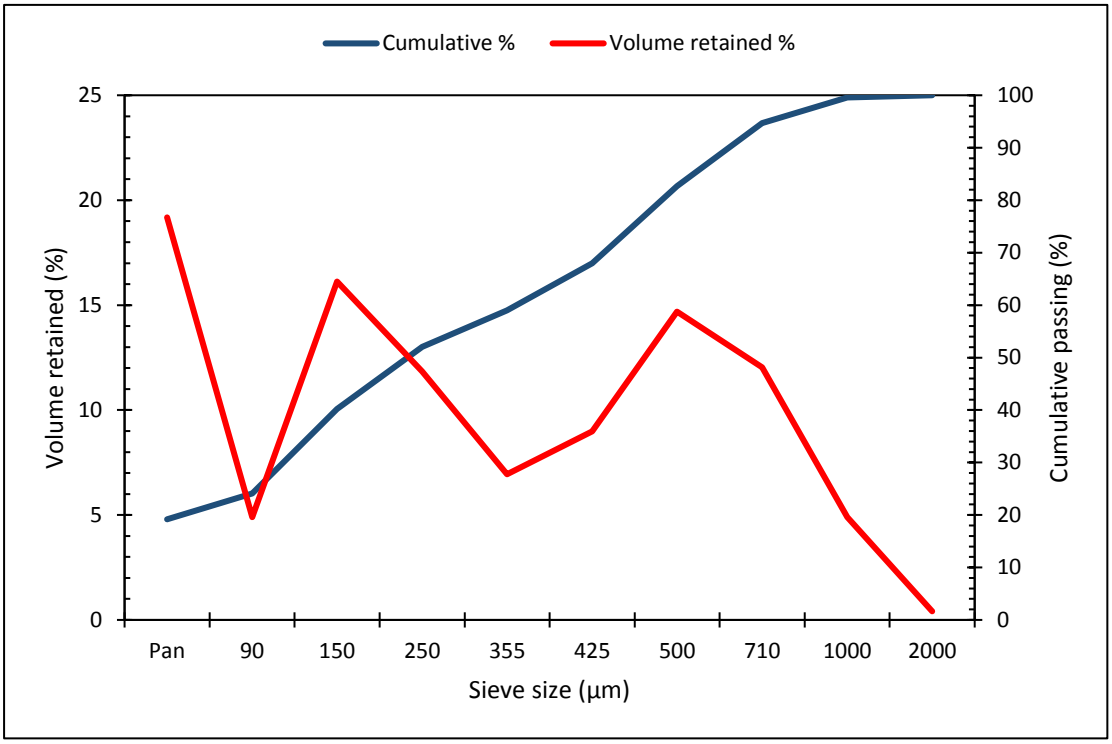

Figure 3-2: Particle size distribution of the autocatalyst feed material. The graph shows a bi-modal distribution which suggests two materials are present with different particle sizes after crushing. This can be related to Figure 3-16 where the SiC content in the experimental groups with a finer particle is lower than in the groups with coarser fractions.

To investigate the effect of particle size on the efficiency of the process the material was split into different particle size fractions show in Table 3-3. Most size ranges were tested, but the very fine particle sizes (< 90 µm) were not used due to safety concerns (dust generation etc.). Having a close size range for the electrostatic separation process is beneficial to optimise the operating conditions in the unit as forces such as centrifugal forces are strongly affected by particle size and so different roll speeds may be required for various particle sizes.

Table 3-3: Particle size ranges used in the experiment.

Experiment number	Maximum particle size	Minimum particle size	Mass processed in each experiment (g)
3	500	355	38
4	2000	710	28
5	850	710	29
6	650	500	40
7	250	150	37

3.2.2. Material characterisation.

XRD analysis (Figure 3-4) of the raw material shows it is composed of a mixture of cordierite ($Mg_2Al_4Si_5O_{18}$) and SiC and also a third minor phase which is a mica mineral. The major SiC peaks appear at 42° 2θ and 71° 2θ. The SiC content of this particular sample was 28 wt%. Figure 3-4 shows the XRD spectrum of the mixed catalyst material is dominated by the cordierite and SiC phases, the characteristic cordierite phases are at 12, 25, 31, 33, 34 and 39° 2θ. The minor peak on the XRD spectrum at around 10° 2θ is of the mica. The mica mineral phase is most likely phlogopite indicated by XRD analysis after it had been isolated (Figure 3-5). The material has a metallic lustre and SEM images show is has a plate like structure (Figure 3-6) and EDX analysis shows it is a K-Mg-Si-Al-Fe containing mineral (Figure 3-8) all consistent with phlogopite, a member of the biotite group, which has a mineral composition of $KMg_3(Si_3Al)O_{10}(OH)_2$. Phlogopite can have Fe/Al tetrahedral substitution which explains its iron content. The composition determined by EDX analysis is similar to XRF analysis of Norwegian phlogopite which was also examined (see Table 3-5). Mica is often used in corrosion and heat resistant paintwork for car components and so it is possibly used as a protective coating of the catalyst canister. The paintwork is shown in Figure 3-3 which shows catalysts canisters with flaked mica (left) and a canister after it has been opened by a hydraulic

saw during the removal of the catalyst (right). As the saw cuts the canister the paintwork chips off and becomes mixed with the catalyst. The low intensity of the peak in the XRD spectrum of the mixed raw material suggests that it is present only as a minor phase probably around 5 to 10%.

Figure 3-3: Automotive catalyst canisters showing mica paintwork.

The XRF data combined with the silicon carbide analysis supports the XRD data in showing that the raw material is a mixture of SiC, cordierite, mica and other components such as ceria, phosphorous oxide, iron oxide and sulphur oxide. Ceria is present as an oxygen stabiliser in the catalyst washcoat and the other components may be impurities from the catalyst lifetime or in the ceramics themselves. An overview of the composition of the raw materials from the experiments is shown in Table 3-4.

The SiC content in feed material varied with particle size from 4.3% in the finer material to 28% in the coarse material. The phlogopite content also varied with there being around 11%

in the coarse material to 35% in material size range of 500 to 335 µm and so the cordierite content in the feed material varied from 55% to 76%.

Table 3-4: Mineralogical composition of the automotive catalyst feed material in each of the experiments.

Component	Experiment 3	Experiment 4	Experiment 5	Experiment 6
Cordierite ($Mg_2Al_4Si_5O_{18}$) and phlogopite	87.2%	70.7%	75.2%	85.5%
Silicon carbide (SiC)	10.8%	27.5%	22.9%	12.9%
LOI @ 800	2.0%	1.8%	1.9%	1.7%

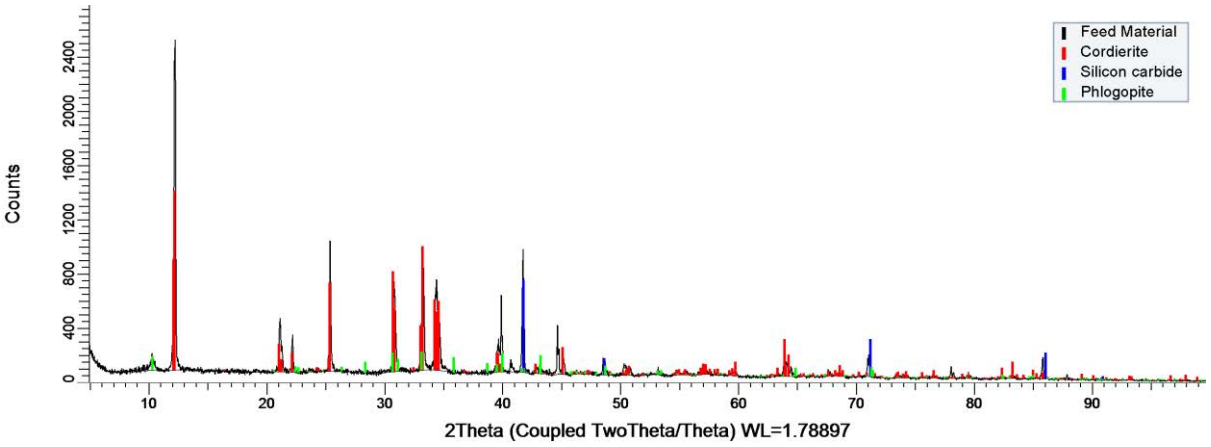

Figure 3-4: XRD pattern of the autocatalyst raw material showing a mixture of cordierite and silicon carbide.

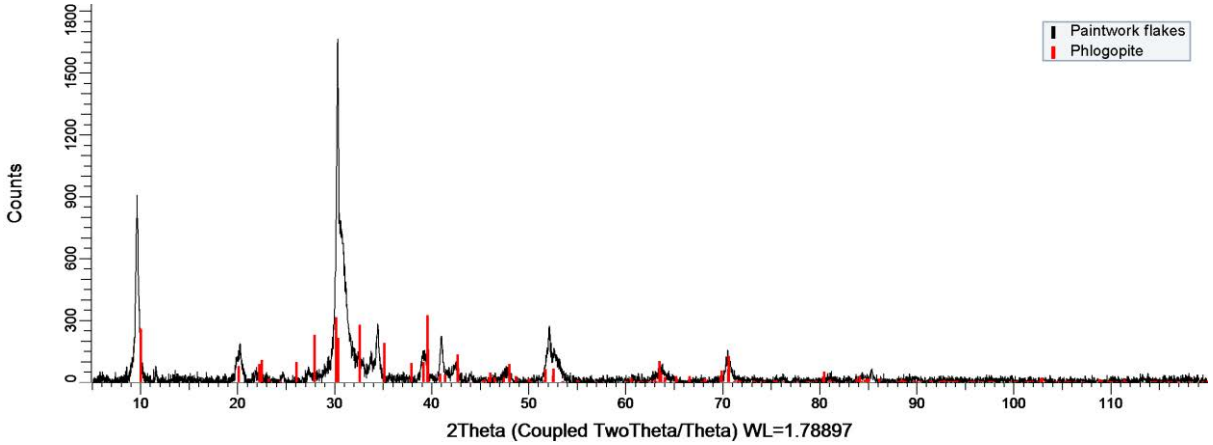

Figure 3-5: XRD spectrum of the third mineral phase present in the mixed automotive catalyst material suggesting this material is phlogopite.

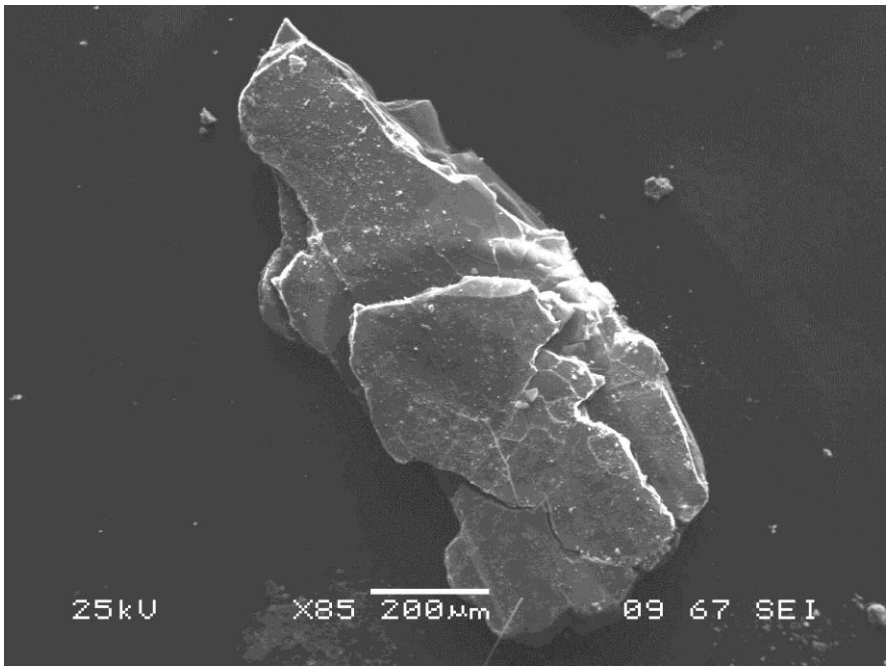

Figure 3-6: SEM image of the mica phase in the mixed raw material. The image shows its distinct plate like structure typical of mica.

SEM images of the raw material shows an interesting insight into the different materials present. The three components have different morphologies which can be seen in Figure 3-7. The cordierite has a smother morphology than silicon carbide although both can be seen as

either pieces or parts of a honeycomb structure. The mica phase looks as if it is almost metallic and has a very distinct layered plate structure.

EDX analysis was used to analyse the surface composition of the materials and can be seen in Figure 3-8 to Figure 3-10. The EDX and XRD analysis of the mica phase was used to help identify it. The results show the molar ratios of the components are similar to the stoichiometric composition to phlogopite seen in Table 3-5. The iron content in phlogopite is what probably causes its paramagnetic behaviour seen later in this report. Tetraferriphlogopite is a similar mineral, but which has a complete substitution of Al by iron. The presence of aluminium in the analysis suggest either that there is only a partial substitution of Al by Fe or there is perhaps solid solution between two phases, phlogopite and tetraferriphlogopite.

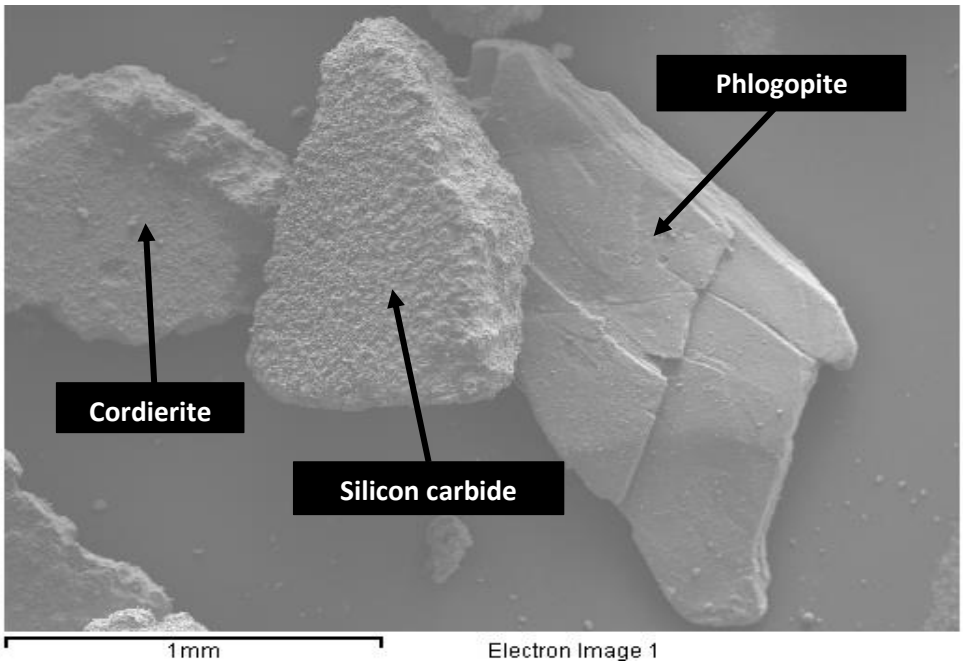

Figure 3-7: SEM image of the three components present in the mixed automotive catalyst mixed material.

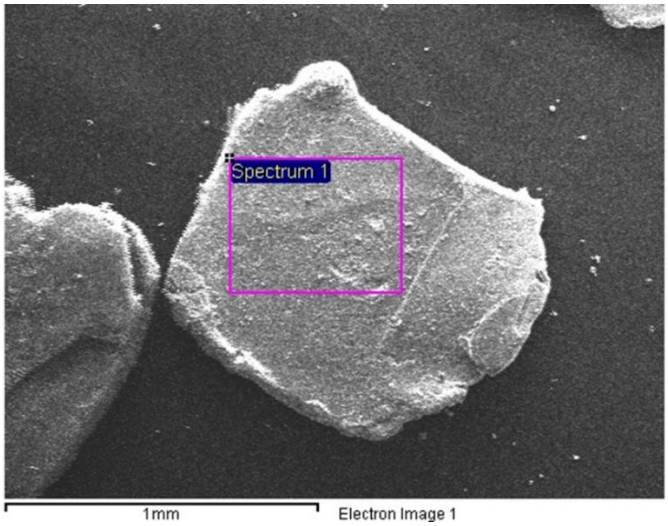

Element	Weight %	Atomic %
O	28.83	43.22
Mg	14.40	14.20
Al	9.01	8.01
Si	28.06	23.96
K	9.66	5.92
Ca	1.27	0.76
Ti	2.06	1.03
Fe	6.73	2.89
Total	100.00	

Figure 3-8: EDX analysis of the mica phase present in the mixed raw material.

Table 3-5: Comparison of phlogopite compositions from around the world.

Element	Origin of phlogopite				
wt (%)	EDX	Norwegian	Finnish	Brazilian	Canadian
Si	28	22	20.2	18.6	19.3
Ti	2.1	2	0.2	0.1	0.1
Al	9	3.4	5.4	8.0	5.5
Fe	6.7	3.9	6.3	2.1	10.5
Mg	14.4	4.2	14.4	15.7	11.0
K	9.7	8	8.3	8.5	8.0

The cordierite particles can be determined from the aluminium, silicon and magnesium content seen from the EDX analysis (Figure 3-9). The Si:Al ratio in these results is around 1 which is correct for cordierite confirming its identification and also differentiating these particles from SiC particles. In the analysis of the cordierite particles the presence of cerium and platinum is detected which is due to their presence in the washcoat.

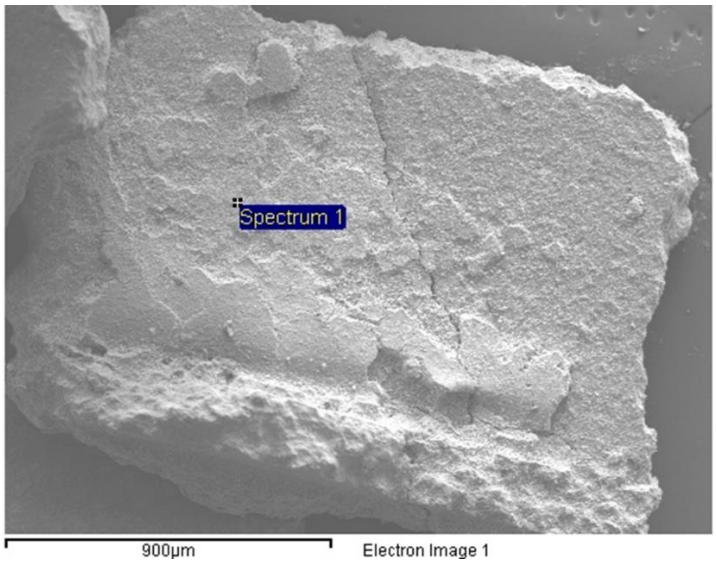

Element	Weight %	Atomic %
C	9.47	27.41
O	14.57	31.67
Al	7.52	9.69
Si	8.24	10.20
Ti	17.51	12.71
Fe	1.36	0.85
Ce	2.29	0.57
Pt	27.22	4.85
Hg	11.83	2.05
Total	100.00	

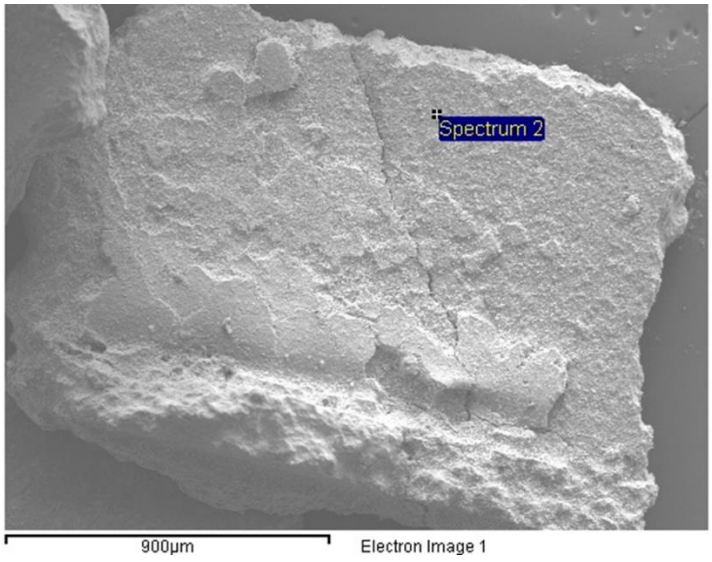

Element	Weight %	Atomic %
C	7.89	16.63
O	18.99	30.06
Mg	5.07	5.28
Al	16.92	15.88
Si	28.56	25.76
Ti	5.49	2.90
Fe	0.71	0.32
Sr	5.97	1.73
Ce	1.84	0.33
Pt	8.56	1.11
Total	100.00	

Figure 3-9: Elemental analysis of a cordierite particle in the mixed automotive catalyst material.

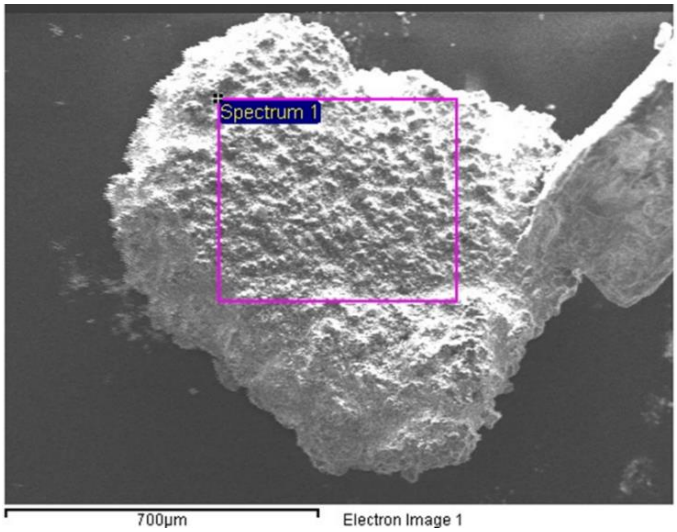

Element	Weight %	Atomic %
C	16.3	29.2
O	17.9	24
Al	7.6	6
Si	51.2	39.2
S	0.5	0.3
Ti	0.3	0.1
Fe	0.5	0.2
Ce	5.7	0.9
Total	100	

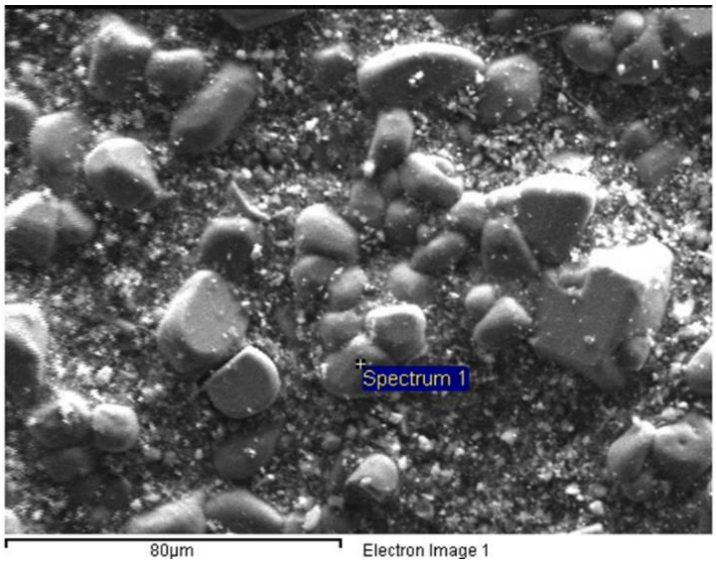

Element	Weight %	Atomic %
C	12.3	24.5
O	4.9	7.3
Si	78.6	67
Sr	4.2	1.1
Total	100	

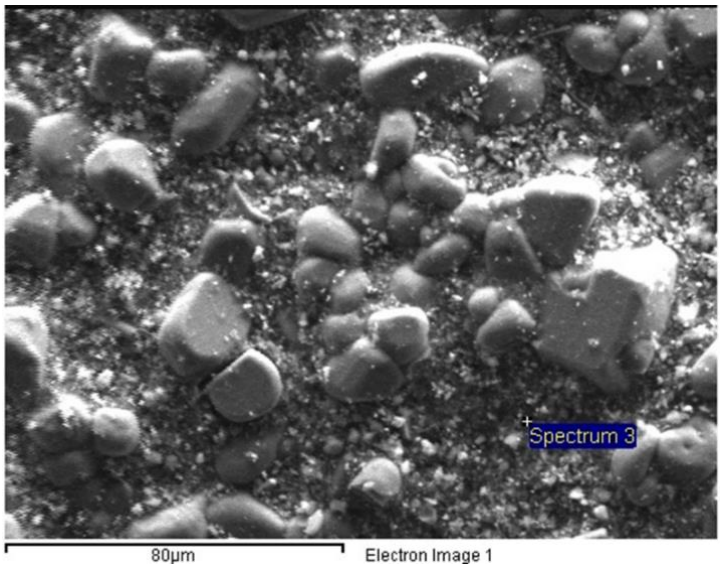

Element	Weight %	Atomic %
C	9.3	22.1
O	5.8	10.5
Al	13.6	14.5
Si	41.8	42.8
Ti	5.8	3.5
FeK	5	2.6
Sr	4.6	1.5
CeL	7.54	1.55
Pt	6.53	0.96
Total	100.00	

Figure 3-10: EDX analysis of silicon carbide particles in the mixed automotive catalyst.

The SiC particles have a rougher morphology than the cordierite ones. These particles can be identified by their greater Si:Al ratio than the cordierite particles (Figure 3-10). The overall spectrum shows the presence of aluminium which was not initially expected, but on closer inspection of the surface of the material it can be seen that the surface consists of what could be described as islands of pure silicon carbide surrounded by silicon carbide coated in a washcoat. The washcoat for these catalysts appears to be an alumina based, which is common, and also containing titanium, iron, cerium and platinum. The presence of the platinum indicates that there will be some PGM value associated with the SiC fraction, because of Pt use in catalytic regeneration of DPFs or the SiC being oxidising catalysts, but the platinum content appears to be lower than the catalyst content of the cordierite. Both the cordierite and the SiC contain a significant amount of carbon, but in the SiC this is most likely chemically

bound carbon, whereas in the cordierite the carbon may be soot deposited during its operational life.

3.3. Experimental results.

The materials were passed through a Boxmag Rapid High Tension Electrostatic Separator and the products from the process were collected into three bins; an insulator bin, a conductive bin and a middling bin. The mass of the material in the bins was recorded and samples taken for analysis.

The electrostatic separator consisted of a hopper, a vibrating feed tray, an earthed rotating drum and an electrode shown in Figure 3-11.

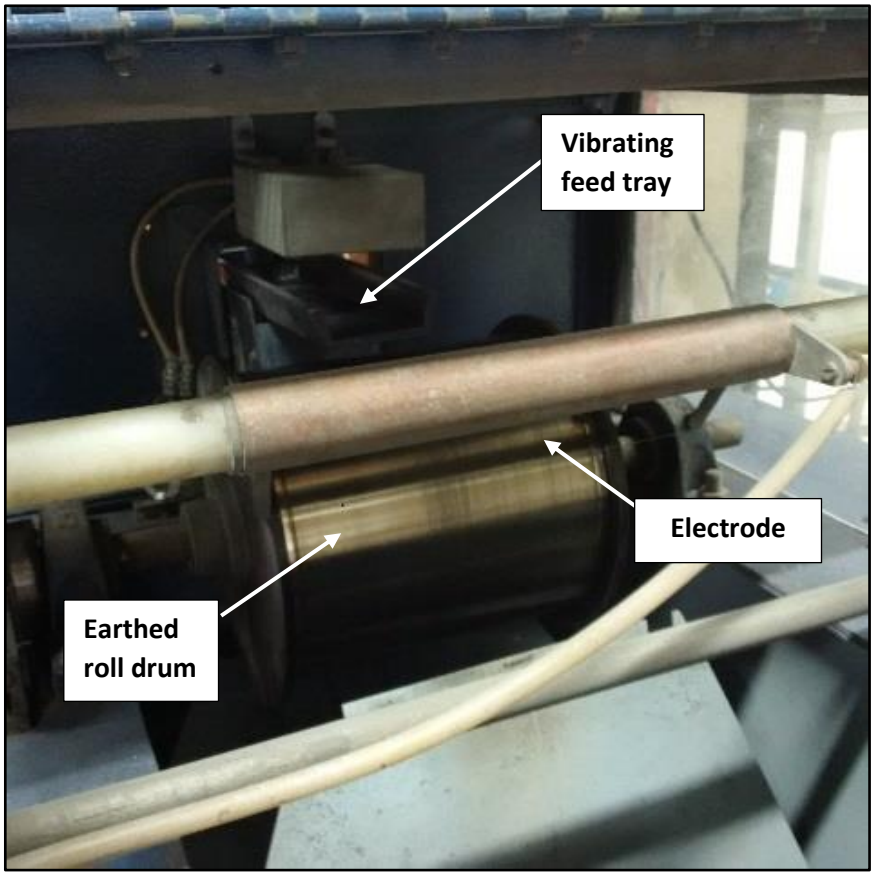

Figure 3-11: Components of the electrostatic separator.

The variables of the electrostatic separation unit which can be controlled are the corona voltage (kev) and the drum roll speed (RPM). The variables were changed until there was an obvious physical separation between the conductive material and the insulating material.

At voltages higher than 20 keV there was a visual separation of the components meaning that the electric field was strong enough to sufficiently charge the particles. The voltage could be increased further to improve the separation of the components, but this also risked causing sparking from the electrode as seen in Figure 3-12. Sparking is undesirable because during the moment of the spark the electric field is lost and so results in a lower separation efficiency. The sparking was promoted by a higher corona voltage and also a greater mass of material on the drum. Therefore, sparking can be reduced by either reducing the corona voltage or lowering the feedrate or increasing the drum speed, both of which reduce the amount of material in the electric field at one point of time.

Figure 3-12: Example of sparking in the electrostatic separator.

The results show that most the material passed to the insulating bin and between 3% and 30% of the material partitioned to the combined middling and conductive bins (Table 3-6). However, this is consistent with the silicon carbide content of the material. The material which was collected in the conductive and middling bins was of a much darker colour than the cordierite which appeared a light brown colour as opposed to the darker grey/black of the conductors and middle fractions. This is shown in a photograph in Figure 3-13.

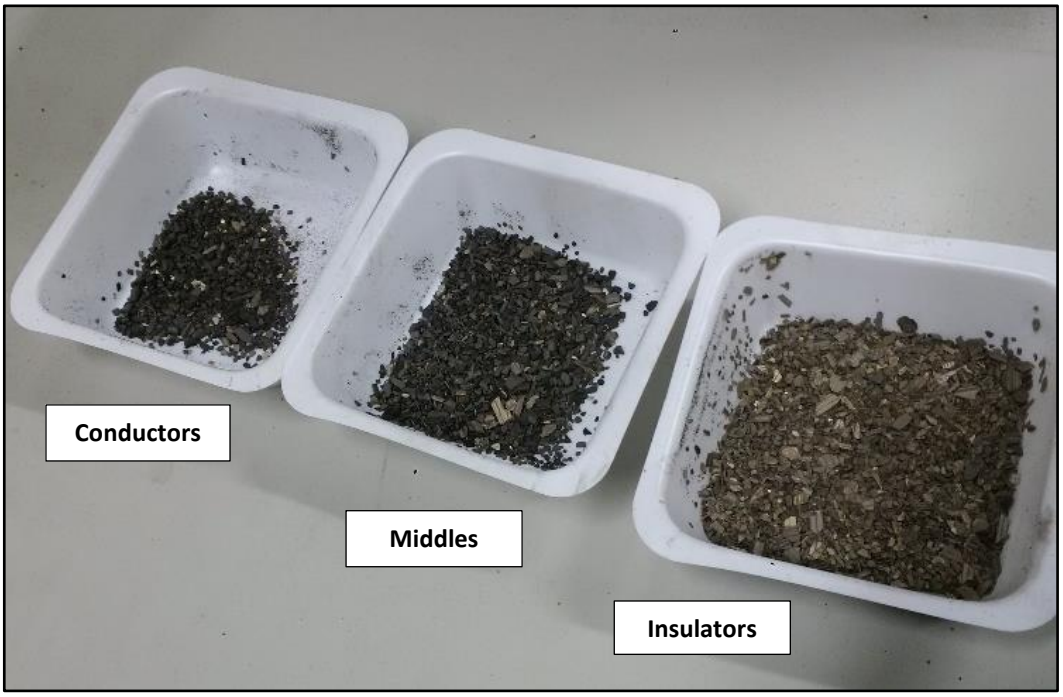

Figure 3-13: Material collected in the product bins.

Table 3-6 shows the mass of material processed and recovered from each bin during the experiment. During experiments 5 and 6, the insulating material was recycled through the separator twice and so there was a total of three passes for these experiments (this is indicated by 2p and 3p). After pass 2 and 3 the conductive and middle fractions were combined due to the small mass obtained from them individually.

The silicon carbide analysis was performed on some of the products which were obtained from the experiment. The analysis for SiC was done, at a third party laboratory by igniting the material in oxygen below 800°C to combust and remove unbound carbon from the sample and which was detected using infra-red in a LECO instruments carbon analysis machine. The sample was then ignited at 800°C to remove chemically bound carbon, which was assumed to be SiC and which was measured in the same way as the unbound carbon.

Table 3-6: Mass of material recovered from the insulator, middle and conductor bins in the experiments.

Experiment #	Feed material (g)	Insulators recovered (g)	Middles recovered (g)	Conductors recovered (g)
3	38	32	3	3
4	28	17	7	4
5	29	21	6	2
5 2p	21	20		1
5 3p	21	19		2
6	40	34	5	1
6 2p	37	33		4
6 3p	31	30		1
7	37	35	1	1

Table 3-7: Silicon carbide content in the products.

Experiment #	Feed	Insulator	Middle	Conductor	SiC Reduction over whole experiment
3	10.8 %	3.2 %	63.8 %	49.0 %	75 %
4	28.0 %	5.4 %	76.4 %	81.3 %	88 %
5 3p	23.4 %	0.5 %			98 %
6 3p	13.1 %	0.6 %			96 %
7	4.3 %	3.8 %			17 %

Experiment #	Feed material (g)	Insulators recovered (g)	Middles recovered (g)	Conductors recovered (g)
3	38	32	3	3
4	28	17	7	4
5	29	21	6	2
5 2p	21	20		1
5 3p	21	19		2
6	40	34	5	1
6 2p	37	33		4
6 3p	31	30		1
7	37	35	1	1

Table 3-7 shows the SiC content of the samples sent for analysis. The SiC content in the insulators for experiments 5 and 6 were after the 3rd pass through the process. The table also shows the SiC reduction over the entirety of each experiment which ranges from 17% for experiment 7 and 88% for experiment 4 these results were after one pass through the separator. After three passes through the separator the SiC removal was increased to 98%. After one pass through the separator, the SiC content of the insulting material is between 3 to 5 wt% and after three passes the SiC content is reduced to 0.5 wt%. The results show that the electrostatic separation process is an effective way to reduce the SiC content of automotive catalyst raw material prior to it being added to the plasma furnace and Table 3-8 shows the SiC content across the products. However, it must be noted that the target SiC is 5 wt% due to the plasma process being able to cope with 5 wt% SiC content in the feed material. For some of the finer size fractions, for example in experiment 7, this target is met by crushing alone. This means that finer particle sizes may not require further separation after they are crushed. Silicon carbide still contains Pt and so it is an economically valuable material and so after the separation process, the removed SiC can be blended back into the cordierite to levels of 5 wt% or below to recover the Pt via the plasma smelting process.

The XRD analysis in Figure 3-14 shows a clear reduction in the SiC content in the insulating material and most the conductive material is composed of SiC. Figure 3-15 shows that even though most of the material in the conductive fraction is SiC there is still some cordierite present. The SiC content in this sample is 81.3% and the cordierite and mica content was estimated by combined XRF, XRD and SiC analysis to be 13.2%.

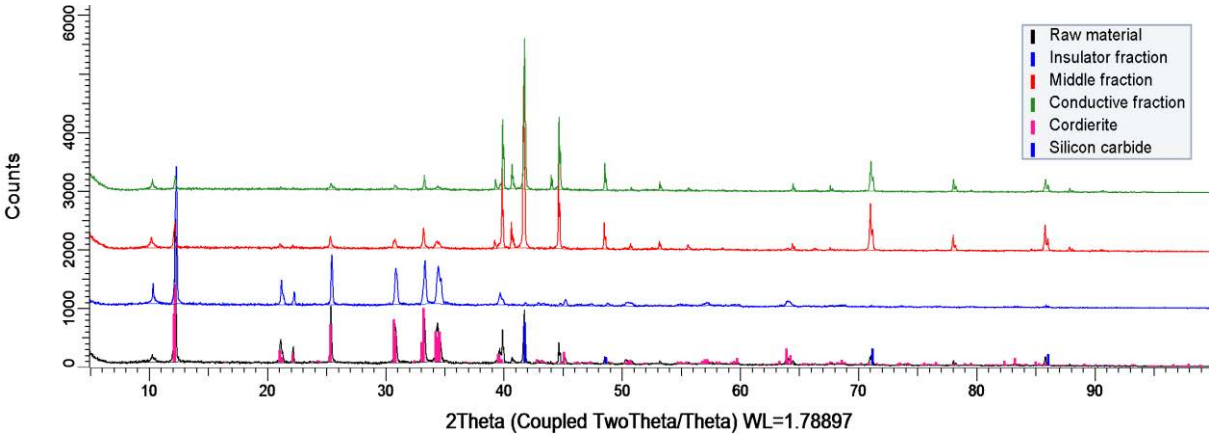

Figure 3-14: XRD analysis of the raw, insulating and conductive materials obtained from the electrostatic separation.

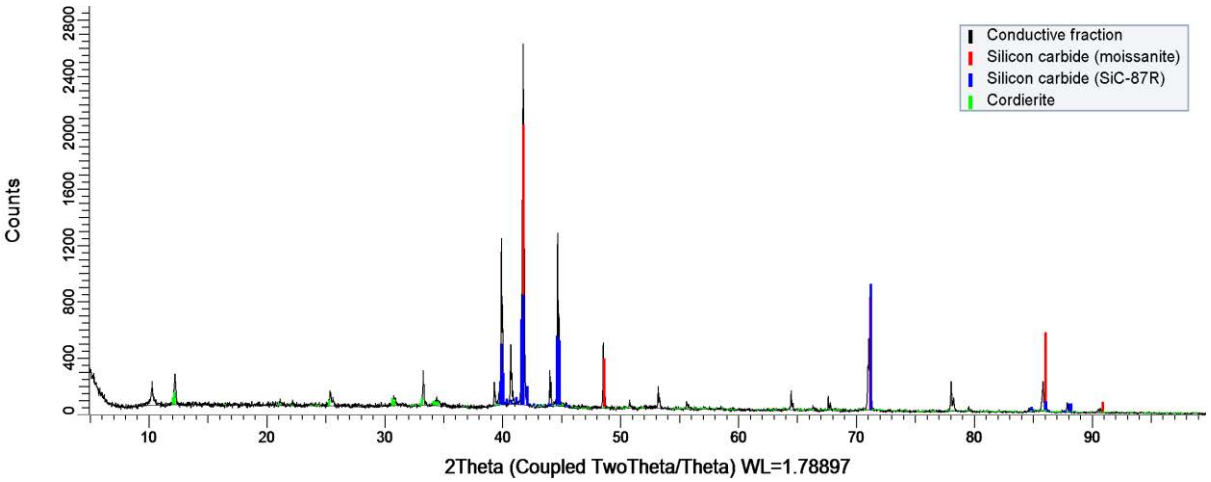

Figure 3-15: XRD analysis of the conductive material.

Table 3-8: % Cordierite and SiC in the products from the electrostatic separation (Loss of ignition (LOI) was performed at 800°C).

Experiment		3	4	5	6	7
Feed	Cordierite and mica	87.3	70.3	74.6	85.3	92.7
	SiC	10.8	28.0	23.4	13.1	4.3
	LOI	2.0	1.8	2.0	1.7	3.0
Insulators	Cordierite and mica	95.0	92.4	97.2	97.6	93.2
	SiC	3.25	5.4	0.5	0.6	3.8
	LOI	1.8	2.2	2.3	1.8	3.0
Middle	Cordierite and mica	34.5	22.8	-	-	-
	SiC	63.8	76.4	-	-	-
	LOI	1.6	0.8	-	-	-
Conductors	Cordierite and mica	43.5	18.2	-	-	-
	SiC	49.0	81.3	-	-	-
	LOI	7.5	0.5	-	-	-

3.4. Discussion of results.

A clear separation of the SiC from cordierite is obtained with SiC reporting to both the middle and conducting fractions. There seems to be little difference between the composition of the

middle fraction and the conducting fractions and so it is possible to combine these two fractions and this may be optimised by the positioning of the splitter plate.

Figure 3-16 suggests that differential grinding between the cordierite and the silicon carbide occurs during the milling process. Differential grinding occurs due to differences in the material properties such as their brittleness and hardness. SiC may require more energy to reduce its size than cordierite, but the reasons for this may require more investigation. Due to the differential grinding, it may be possible to blend in dust with a low SiC content to the coarser material which had gone through the electrostatic separator.

The sieve sizes shown in Figure 3-16 were chosen to investigate the effect of the particle size of the material on the separation efficiency of silicon carbide and cordierite and also to investigate the particle size range. This is why there is a 2000-710 μm and a 850-710 μm where there was a hypothesis that a narrower particle size range may make the separation process more efficient.

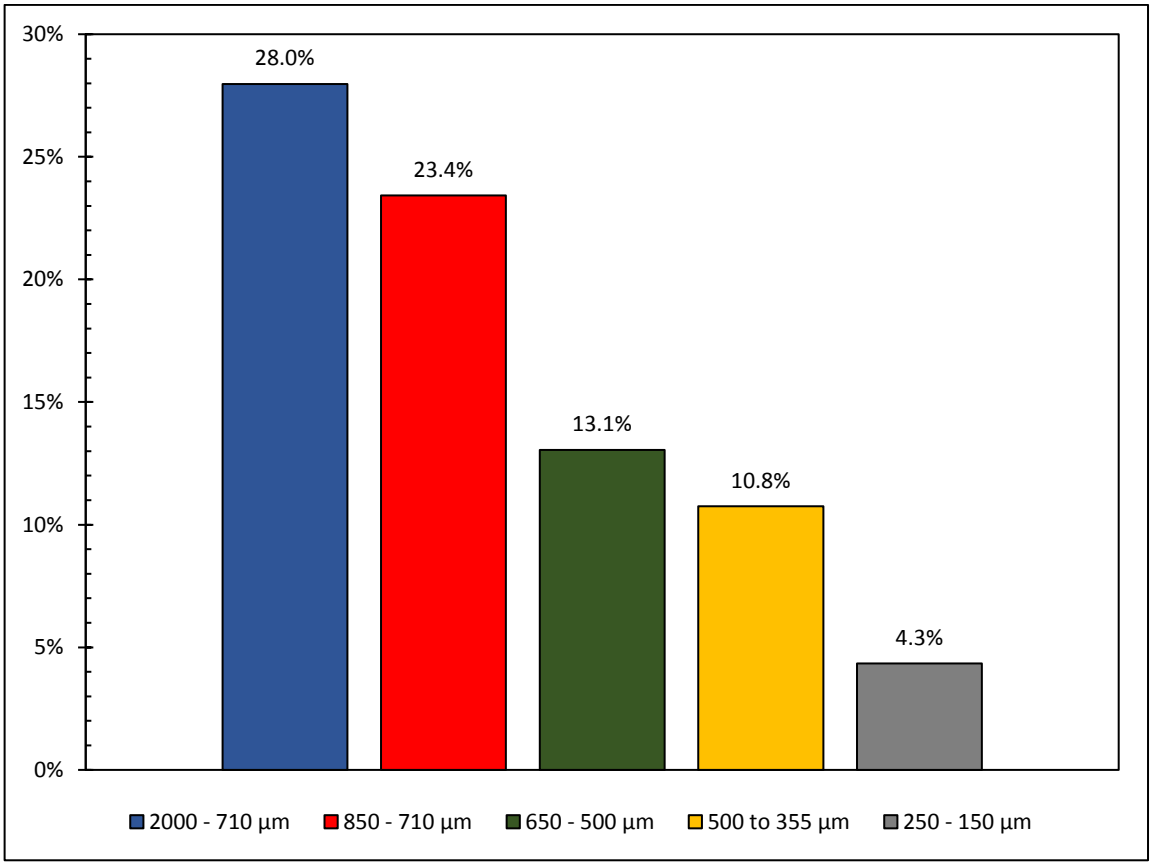

Figure 3-16: Silicon carbide content of the raw material at different particle sizes.[1]

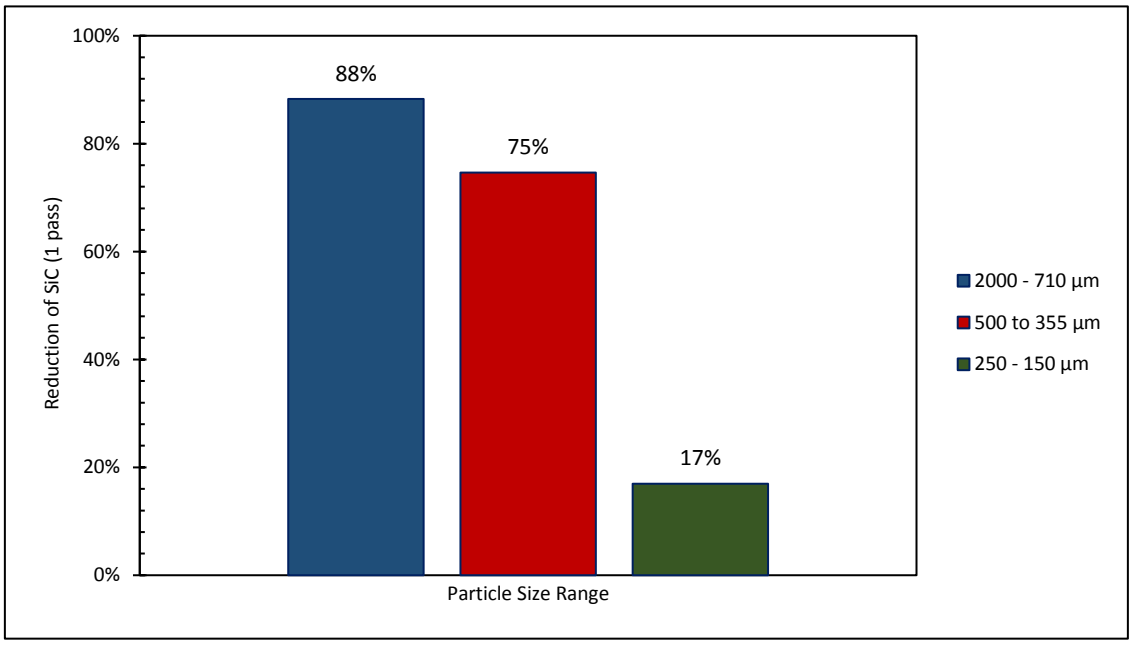

[1] In this chapter, error bars do not appear on the SiC analysis due to the high cost of the SiC test meaning only one test per sample could be performed.

Figure 3-17: % Reduction of silicon carbide from the raw material after one pass through the electrostatic separator.

The % removal of SiC from the raw material is reduced as the particle size reduces. The removal at coarse fractions where the particle size ranges from 2000 to 710 µm after one pass is 88% but drops to just 17% when the particle size range is fine at 250 to 150 µm. Therefore, the crushing of the autocatalyst raw material should be controlled to reduce the generation of dust and fine particles.

The major constituent of the conductive and the middle fractions is SiC, but there is also a considerable amount of cordierite and mica present. It may be possible to reduce the cordierite and the mica loss to the conductive fractions by optimising the processing conditions and variables which is discussed later in this section. The conductive and middle fractions could also be recycled to try and further separate the SiC from the other components of the material.

3.4.1. Recycling of the conductive fraction.

The conductive and middle fractions were recycled through the electrostatic separator to attempt to increase the SiC content in the conductive fraction and reduce the cordierite and other phases. The experiment was conducted under the following conditions: particle size of between 2000 and 710 µm, a corona discharge of 25 keV, a roll speed of 90 RPM and a feed-rate of 70%.

The raw material fed into the electrostatic separator had a SiC content of 27.7% and the SiC content in the combined conductive and middle fractions after the first pass through the

machine was 72.3%. This means that there was a cordierite and mica content of approximately 27.7%.

As expected, after the second recycling pass the silicon carbide content was increased to 80.7%, but after a third pass the SiC content was only able to be increased to 82%. The results can be seen in Table 3-9 and Figure 3-18.

Table 3-9: Silicon carbide and other content of the recycled mixed middle and conductive fractions.

Sample	SiC (%)	Cordierite and mica (%)	LOI @ 800 (%)
Raw	27.7	70.9	1.5
1st Pass	72.3	27.3	0.4
2nd Pass	80.7	19.0	0.3
3rd Pass	81.8	17.9	0.2

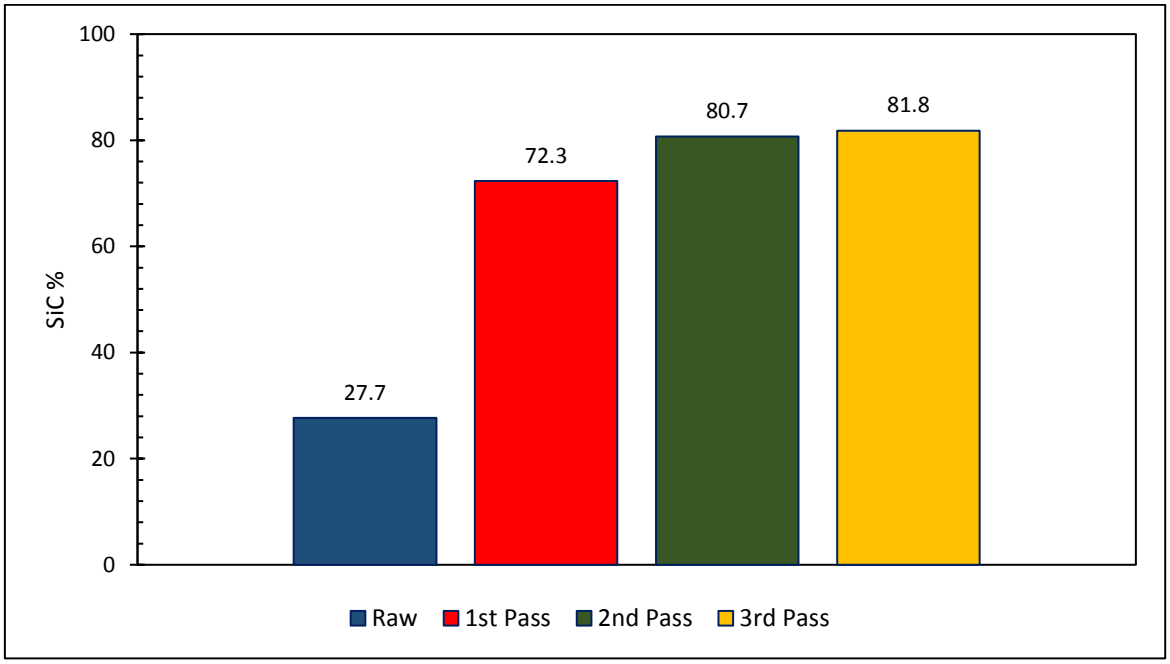

Figure 3-18: Silicon carbide content in the recycled mixed and conductive fractions after 1, 2 and 3 passes.

The recycling of the conductive fraction quickly reaches a plateau after a 2nd pass through the separator. There appears to be little benefit for further recycling passes as the SiC content is not raised significantly. Therefore, the removal of cordierite and other fractions cannot be achieved simply by recycling alone. It may be required that various process parameters need to be optimised for further removal of the cordierite and mica fractions i.e. roll speed etc.

3.4.2. Operational parameters.

The effect of changing the roll speed, corona voltage and the feed rate on the SiC separation was investigated to attempt to determine the optimum operating conditions at lab scale.

The experiments were conducted with a particle size of 1600 to 710 µm the effect of the roll speed was investigated at 50, 75 and 100 RPM with the corona voltage at 20 keV and the feed rate at 10 kg/h.

The mass portioning of the material to the conductive fractions increased as the roll speed increased as shown in Table 3-10. The partitioning of the material to the conductive and middle fractions increases from 33% to 53% as the roll speed increases from 50 to 100 RPM. The raw material contained 28% SiC and although the silicon carbide content drops from 7.8% in the insulating fraction at 50 RPM to 4.31% at 100 RPM, representing an increase from 81% reduction to 93% reduction, the silicon carbide content in the conductive fractions decreases from 75% at 50 RPM to 56% at 100 RPM. This can be seen in Figure 3-19 and it shows that as the roll speed increases a greater amount of insulators will partition to the conductive fractions. As the roll speed increases the centrifugal forces which are acting on the particles become greater than the electrostatic forces (image forces) which cause the non-conductive

particles to stick to the drum and causes some of these particles to be thrown from the drum into the conductive bins.

Table 3-10: Mass balance of the components to the different bins with varying roll speed.

Roll Speed (RPM)	% Mass Balance		
	Conductors	Middle	Insulators
50	1%	32%	68%
75	3%	41%	57%
100	4%	49%	47%

Increasing the corona voltage increases the SiC content in the conductive fractions (Figure 3-20). There is little effect of increasing the strength of the electric field on the SiC content in the insulating fraction, but the stronger electric field reduces the amount of insulators partitioning to the conductive fraction. Increasing the field strength ensures that the image forces attracting the non-conductive particles to the drum are greater than the centrifugal forces throwing the particles from the drum. The limitation of increasing the electric field is the generation of sparks but, increasing the drum speed or reducing the feedrate would reduce the mass of material on the drum which in turn reduces sparking. Therefore, it is possible to operate with an increased voltage at higher drum speeds. Sparking can also be reduced by working in a dust free environment and so having an extraction device on a commercially operational unit would also enable operation at higher voltages.

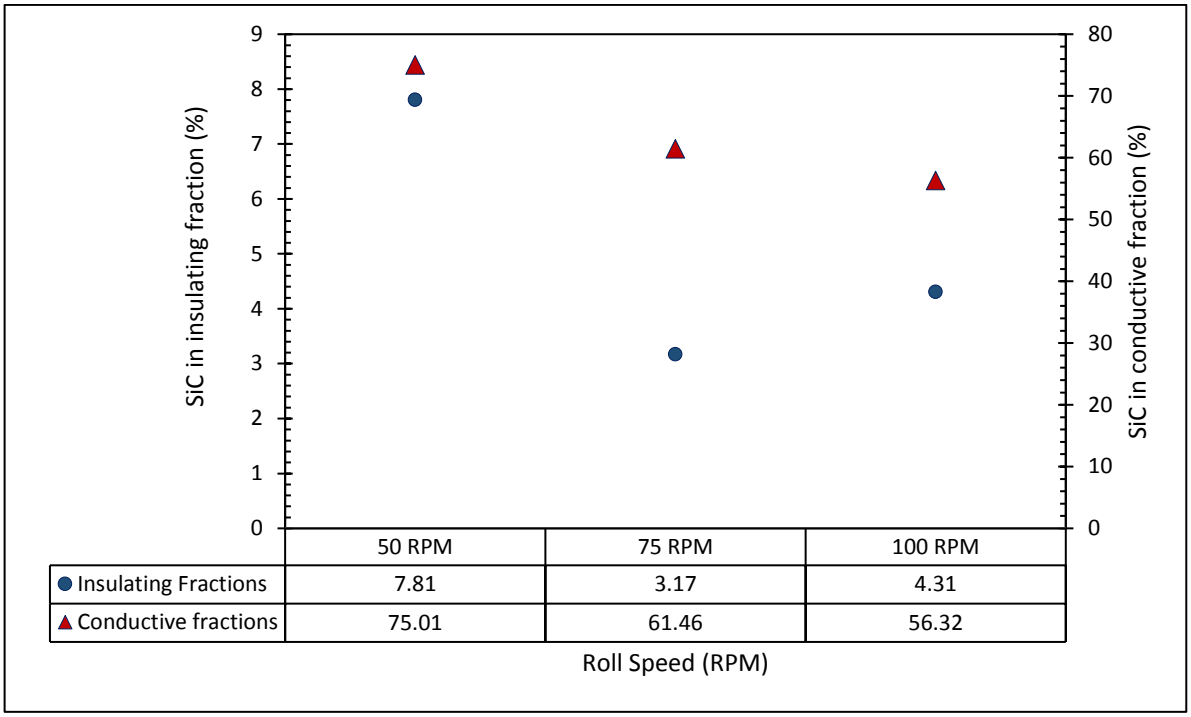

Figure 3-19: Effect of roll speed on the silicon carbide content of the insulating and conductive fractions.

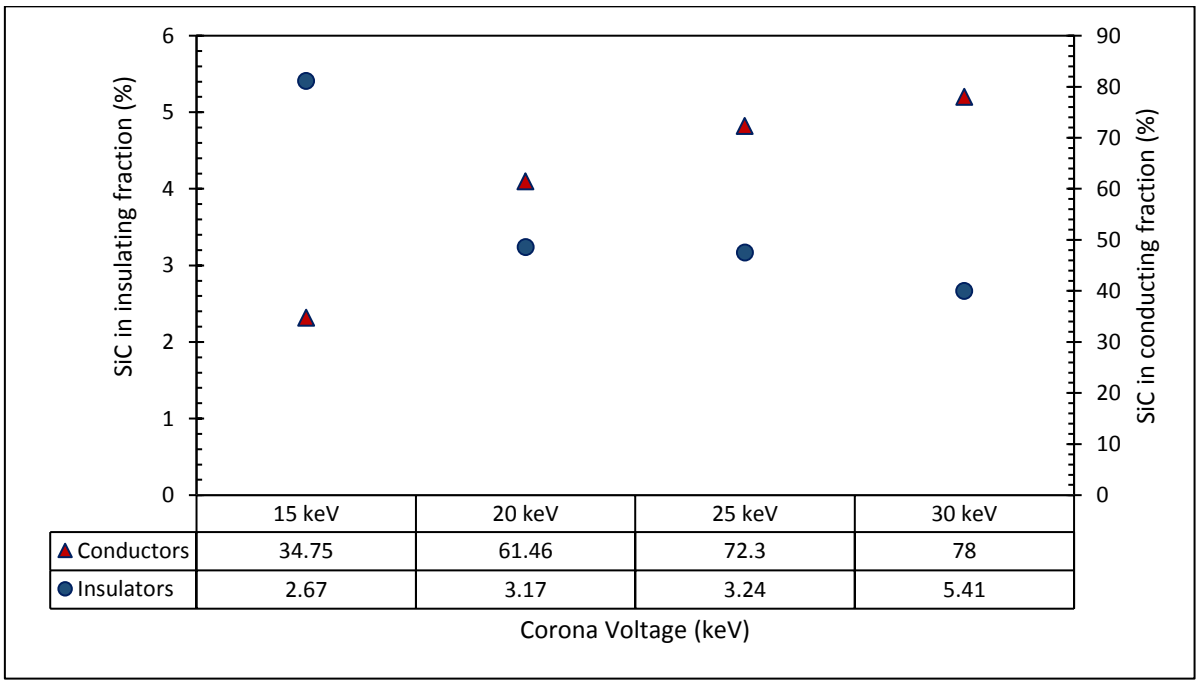

Figure 3-20: The effect of the strength of electric field on the silicon carbide content in the various fractions.

A summary of the process variables is shown in Table 3-11. The proposed operating conditions for the lab scale process to maximise SiC removal would be; a particle size distribution between 2000 and 710 µm, a corona voltage as high as possible between 25 and 30 keV and a roll speed high enough to reduce sparking, which should be between 75 and 100 RPM. It was found that the corona voltage was one of the most significant variables in producing greater separations where an increased voltage would cause more efficient separation. However, an increased voltage would lead to sparking, but it was found that sparking was also caused by a large mass of material on the drum. If the roll speed was increased and the feed rate reduced, there would be less material on the drum at a single point in time allowing for a higher corona voltage leading to better separation.

Table 3-11: Summary table of the effect of changing variables on the SiC removal and cordierite partitioning in the process.

Variable	Modification	Effect
Particle size	Reduction	Reduces SiC removal from mixed material.
Corona voltage	Increase	Increases the silicon carbide content in the conductive fractions.
Roll Speed	Increase	Increases the cordierite and washcoat content in the conductive fractions.

Table 3-12: Platinum and palladium concentrations in the raw material and products from the separation process.

Experiment #4	Raw	Insulator	Middle	Conductor

Pt (ppm)	359	380	297	347
Pd (ppm)	281	359	112	100

Table 3-13: Partitioning of platinum and palladium to the products of the electrostatic separation process.

Fraction	Pt (g)	Pd (g)	Pt (%)	Pd (%)
Raw material	1.01	0.79		
Insulator	0.65	0.61	64.3%	77.6%
Middle	0.21	0.08	20.7%	10.0%
Conductor	0.14	0.04	13.8%	5.1%

Analysis of the platinum content and the palladium content of the raw materials and the products was performed using inductively coupled plasma optical emission spectroscopy (ICP-OES) and the partitioning of Pt and Pd calculated. Table 3-12 and Table 3-13 show that there is a distribution of platinum and palladium throughout all the fractions of the process and it must be noted that the raw material seems to be of a low grade (combined PGM content 640 ppm whereas high grade material would typically be around 2000 ppm Pt, Pd and Rh). There seems to have been some upgrading of the concentration of both platinum and palladium in the insulating material as both the concentration of the Pt and Pd increases. The concentration of Pd in the middle and conductive fractions drops, but the concentration of Pt does not drop significantly in the conductive and middle fractions.

The platinum partitioning indicates that there is Pt associated with the SiC components which may be due to their use in DPF regeneration and as some catalysts being silicon carbide based. Palladium is not typically used as the catalytic agent in diesel catalysts or filters and so gives some explanation to its reduction in the conductive fractions. Optimising the process operating conditions can reduce the loss of insulators to the conductive fractions as well as

some recycling of the conductive fractions after an initial pass through the separator. The intrinsic PGM content of the SiC fraction means that there would be a commercial benefit to process it through the plasma furnace to recover the valuable metals. The benefit of removing the SiC and then putting it back in to the furnace would be that it still could be used as a reductant and it could be added at controlled levels (below 5%) in a consistent feedstock. This would mean that any residual PGM containing cordierite in the conductive fractions would still be processed through the furnace and not lost.

3.4.3. Feedrate and throughput.

Timed tests were carried out at lab scale to determine the throughput of the electrostatic separator and to aid the scale up of the design.

The throughput of the separator is determined by the feeder rate which feeds the material onto the roller and by the ratio of the feed-tray width to roller width (F/R ratio). The dimensions of the electrostatic separator used in the lab scale tests are as follows; feed tray width: 50 mm and the roller width is 165 mm (Figure 3-21). Therefore, the F/R ratio was 0.3, but in commercial applications the ratio can be increased to 1.

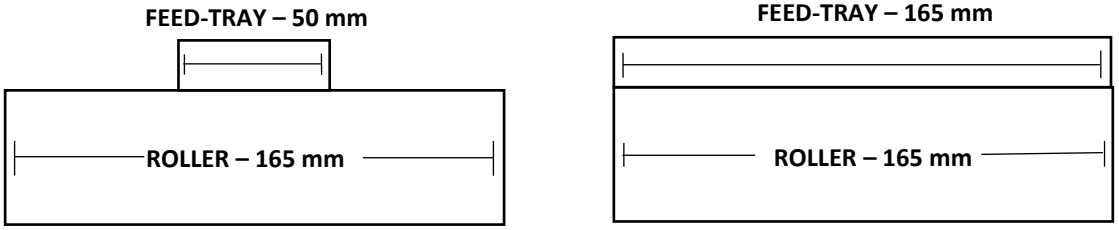

Figure 3-21: Feed-tray and roller configurations of the lab scale separator. F/R ratio 0.3 (left) F ratio 1 (right).

320 g of mixed autocatalyst was passed through the separator and the time taken to pass that material was recorded. The feeder speed control on the machine was a percentage based controller i.e. 10% maximum, 30% maximum and so on. The experiment calibrated these set points to a mass per unit time (kg/h) figure.

The feeder speed control was set to three speeds, 60%, 70% and 80% to determine the throughput. At speeds lower than 60% the feedrate was visibly slow and the data shown in Figure 3-22 suggests that only mid-range to high end speeds would give reasonable through-puts with speeds lower than that being unrealistic for any meaningful operation.

The lab scale feeder can achieve around 20 kg/hr at 80% feeder speed in its current configuration, but the throughput of the separator can be increased if the F/R ratio is increased and at an F ratio of 1 the throughput would be 63 kg/hr at 80% based on extrapolating this data.

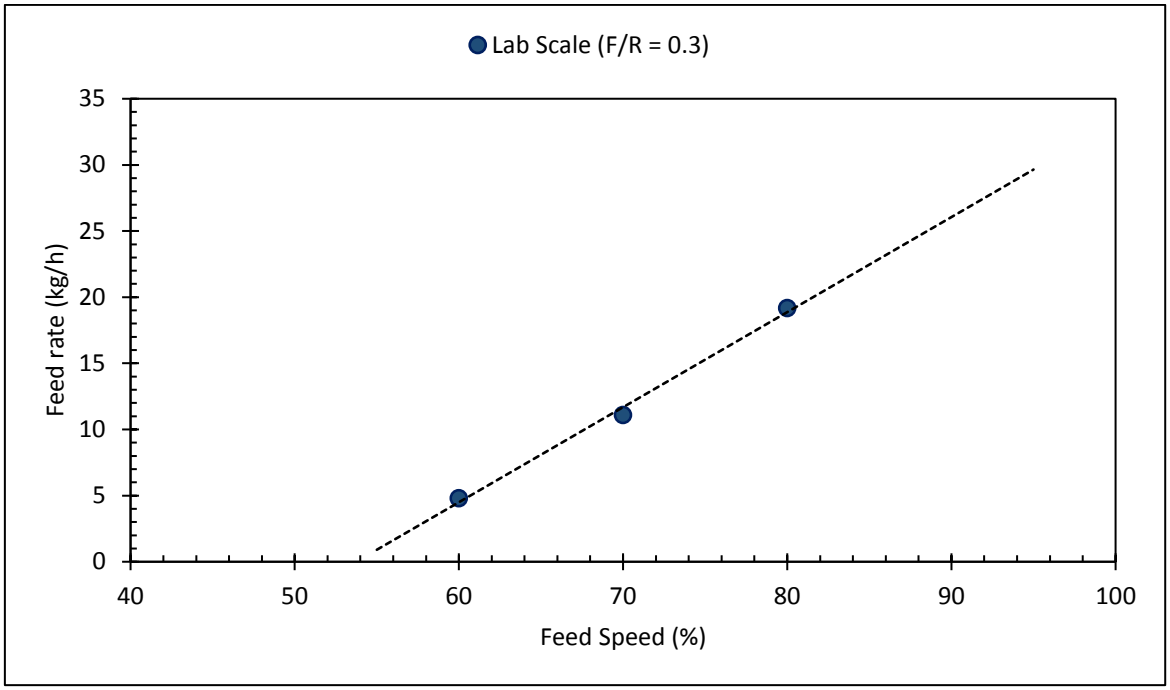

Figure 3-22: Lab scale throughput with particle size range between 2000 and 710 µm.

A design basis with an F/R ratio of 1 would enable a higher throughput of the material and a wider feed tray may facilitate the formation of a monolayer distribution of material across the feed-tray improving operational conditions by avoiding particles overlapping.

A commercial scale electrostatic separator typically has a roll width of 750 mm or 1000 mm. To achieve around a 300 kg/h throughput a roller width of 750 mm would be sufficient as shown in Figure 3-23. Throughputs of around 400 kg/h could be achieved at a controller speed of 100% and so the commercial scale units could process a large amount of material without having an enormous footprint. However, the throughput may be a factor in determining the separation efficiency which needs to be determined and may limit the maximum throughput for the unit.

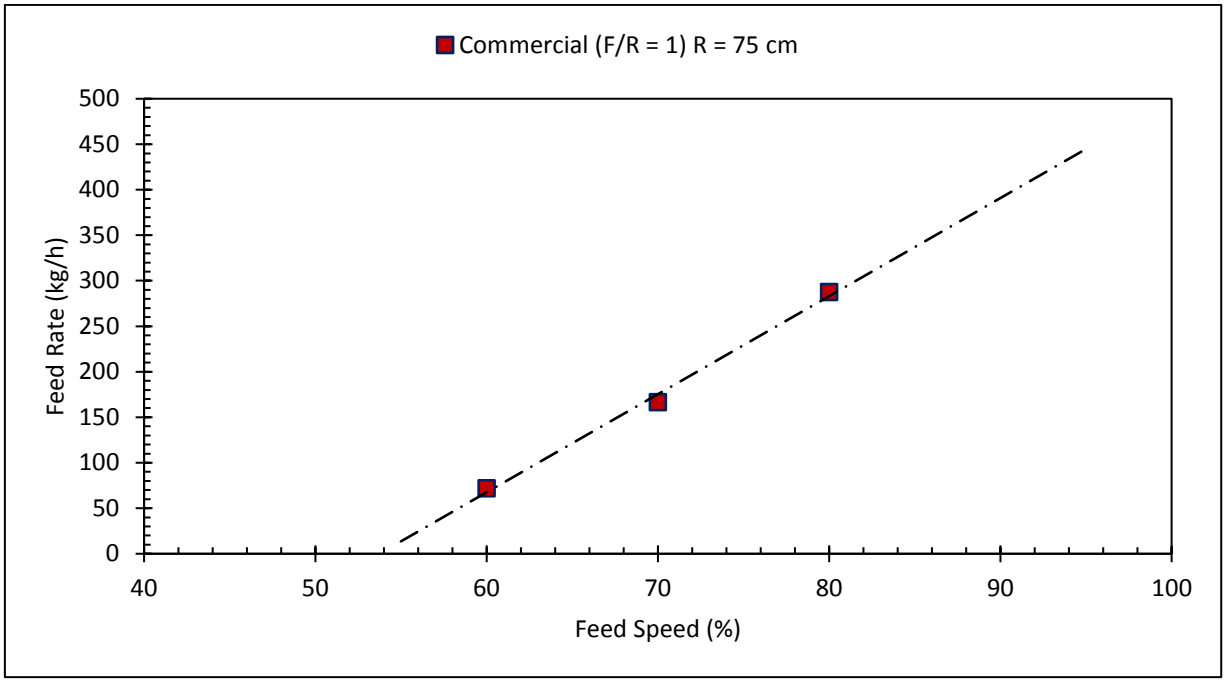

Figure 3-23: Calculated throughput of a commercial scale electrostatic separator with a roller width of 750 mm.

Figure 3-24 shows that the feed rate of the material does not seem to have a significant effect of the separation efficiency of the silicon carbide from the material. As the feed rate varied from 60 to 80% the SiC content in the insulating fraction was similar in all the tests at between 3.17 and 4.34%. All these tests showed a good separation efficiency of between 91 to 93%. The feed rate would be limited by the size of the rotating drum and the production of sparking at a given corona voltage.

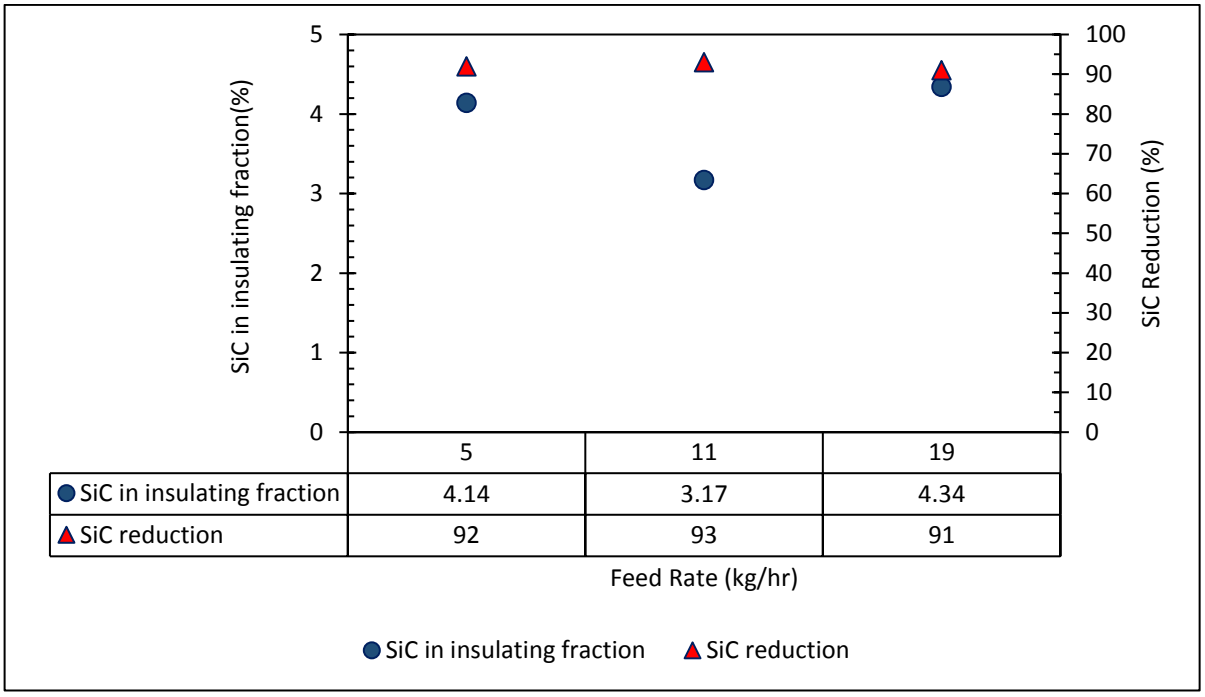

Figure 3-24: The effect of feed-rate on the SiC reduction of mixed automotive catalyst.

The multicomponent nature of the mixture may be a cause for the low grade SiC conductive fraction recovered from the electrostatic separator and also the presence of impurities in the cordierite fraction obtained. It was discovered that it was possible to also separate the components in the mixture using magnetic separation due to the differences between the magnetic properties of silicon carbide, phlogopite and cordierite. Magnetic separation prior to an electrostatic separation could be used to improve the grade of the products and increase the flexibility of the process to handle greater variations in the raw material.

3.5. Magnetic Separation.

3.5.1. Magnetic properties of the components in the mixed material.

The magnetic properties of the components was investigated using a vibrating sample magnetometer (VSM) and the results are presented in Figure 3-25. From the VSM data it can be seen that the cordierite, silicon carbide and phlogopite all show ferromagnetic properties, but phlogopite and silicon carbide have a greater magnetic susceptibility than cordierite and is why, as discussed later in this chapter are able to be magnetically separated from cordierite.. The ferromagnetic nature of phlogopite is possibly due to its iron content which is around 5 to 6%.

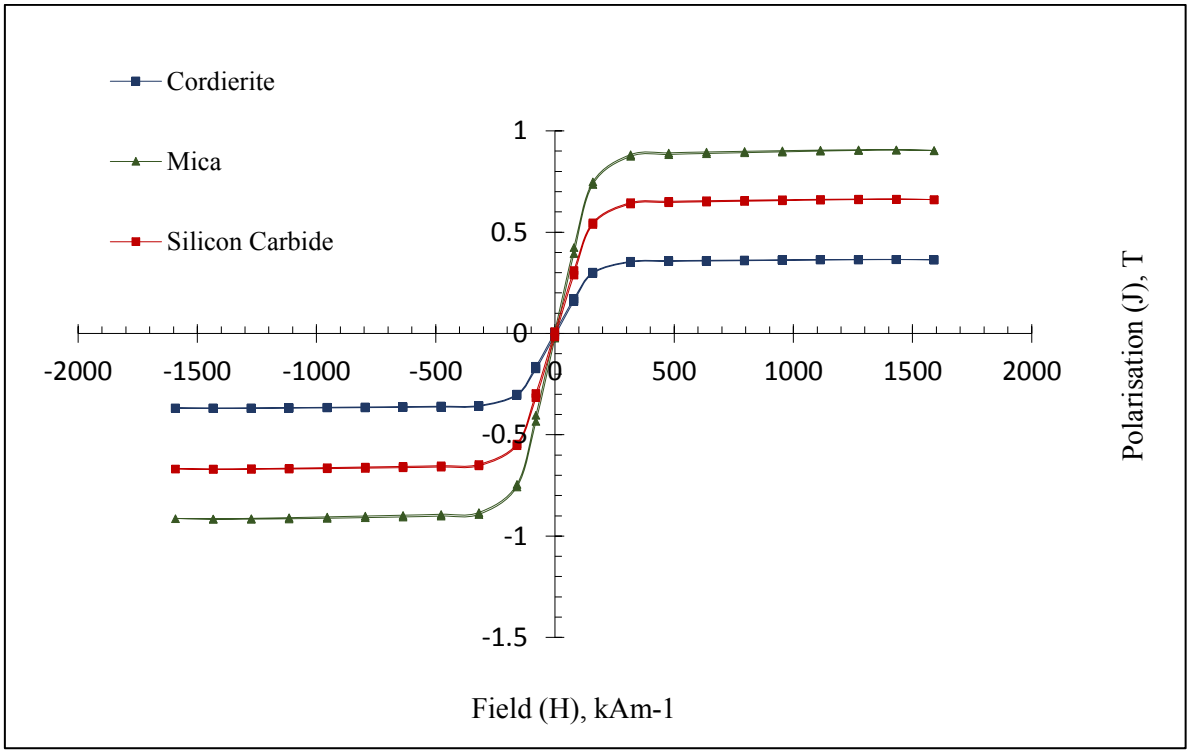

Figure 3-25: The magnetic properties of silicon carbide, phlogopite and cordierite from a vibrating sample magnetometer (VSM).

3.6. Experiment into the magnetic separation of the mixed automotive catalyst components.

After an initial proof of concept using a lab based induced roll magnetic separator, the material was screened to two size fractions; a coarse fraction between 2000 µm and 710 µm and a mid-size fraction between 710 µm and 250 µm and fed onto a two pilot scale magnetic separators at Master-Magnets in Redditch. The two separators were used in series and the first of the separators was a low intensity magnetic (LIM) drum separator and the second was a high intensity rare earth magnetic (HIM) separator, both are shown in Figure 3-26. The LIM separator used a barium-ferrite magnet producing a magnetic field of around 0.1 Tesla, and the HIM separator uses a neodymium-iron-boron magnet which would produce a magnetic field around 10 times stronger at about 1 Tesla. The LIM separator was used to remove ferromagnetic materials from the feed and the HIM separator was used to remove the paramagnetic materials.

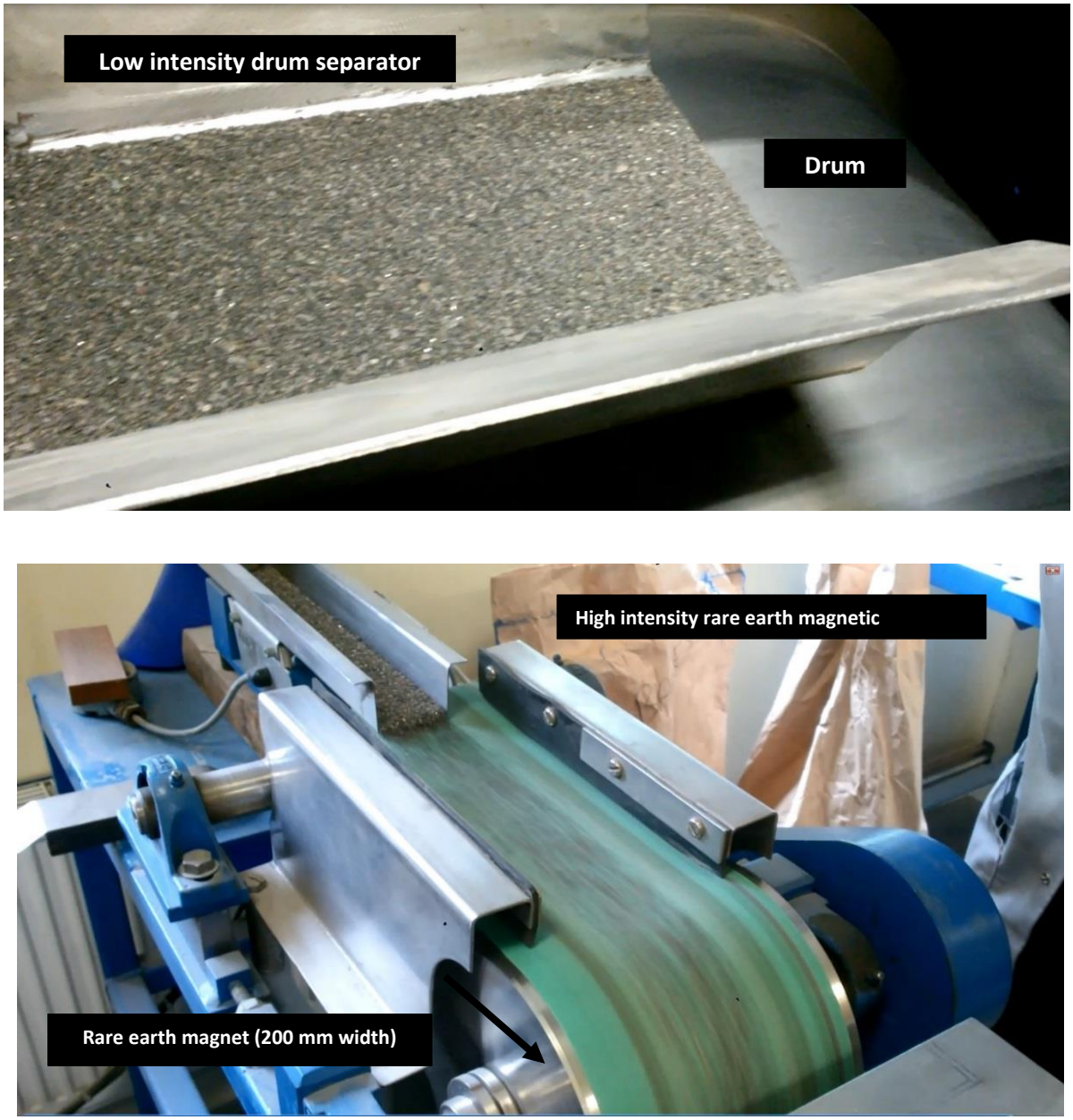

Figure 3-26: Magnetic separators. Top low intensity drum separator. Bottom rare earth high intensity magnetic separator.

Table 3-14 and Table 3-15 show the mass balances of material when passed through a low intensity magnetic field and a high intensity magnetic field. There was little highly magnetic material removed during the low intensity separation. However, there was a significant partitioning of material during the high intensity separation; 23.7% and 30.9% of material

partitioned to the magnetic fraction for the coarse and finer particle size fractions. This partitioning is positive as in this material the silicon carbide content of the mixed material is around 21%. The importance of having a low intensity separation prior to the high intensity separator is to ensure that highly magnetic material is removed, such as tramp metal, as it can cause damage to the high intensity separator by ripping the belt.

Table 3-14: Mass balances during low intensity magnetic separation.

Low intensity separator fractions	2000 – 710 µm		710 – 250 µm	
	Mass (kg)	Partitioning (%)	Mass (kg)	Partitioning (%)
Magnetic	0.003	0.24%	0.075	1.7%
Non-magnetic	1.256	99.76%	4.232	98.3%

Table 3-15: Mass partitioning during high intensity magnetic separation.

High intensity separator fractions	2000 – 710 µm		710 - 250 µm	
	Mass (kg)	Partitioning (%)	Mass (kg)	Partitioning (%)
Magnetic fraction	0.294	23.7%	1.268	30.9%
Middle fraction	0.156	12.6%	1.61	39.2%
Non-magnetic fraction	0.789	63.7%	1.229	29.9%

Table 3-16: Portable Niton XRF data of the samples taken from the magnetic separation tests.

Sample	Element wt%			
	Al	Si	Fe	Si/Al
Feed	3.4	12.4	0.5	3.6
LIM				
Magnetics coarse	4.4	13.1	2.9	3
Magnetics fine	4.9	12.8	1.6	2.6
HIM Coarse				
Non magnetics	4.1	7.3	0.4	1.8
Middles	3.4	14.1	0.5	4.1
Magnetics	2.9	22.8	1.6	7.9
HIM Fine				
Non magnetics	4.7	7.8	0.5	1.7
Middles	4.5	8.1	0.5	1.8
Magnetics	3.9	13.0	1.7	3.3

Table 3-16 shows handheld XRF analysis of the samples obtained from the magnetic separators. The table only shows the major components and in particular silicon and aluminium as the Si/Al ratio is a good method of analysing the cordierite and silicon carbide content. As the Si/Al ratio approaches unity, the cordierite amount in the material should be increasing, whereas when the Si/Al ratio is greater, the silicon carbide content should be increasing. The results show a clear increase of the Si/Al ratio in the LI magnetic fractions and a decrease of the non-magnetic fraction. This is a positive indication of separation of silicon carbide and cordierite. There was an upgrading of iron in the LI magnetic material and the XRD spectra of the magnetic materials obtained from the LIM separator in Figure 3-28 show that the material consists of a mixture of all three phases. This may mean that the presence of iron in all these fractions may be enough to make them magnetic. However, the tiny fraction of the material which was removed from this separator means that there are no significant losses.

Table 3-17: Silicon carbide content of the fractions obtained from magnetic separation.

	SiC (wt%)
Coarse material	
Feed material	21
Non-magnetic material from magnetic separation.	5.1
Non-magnetic material from magnetic separation followed by electrostatic separation.	1.8
Fine material	
Feed material	12
Non-magnetic material from magnetic separation.	1.4

Table 3-18: Silicon carbide reduction from magnetic separation.

	SiC reduction (%)
Coarse material	
Magnetic separation	85
With subsequent electrostatic separation	95
Fine material	
Magnetic separation	97

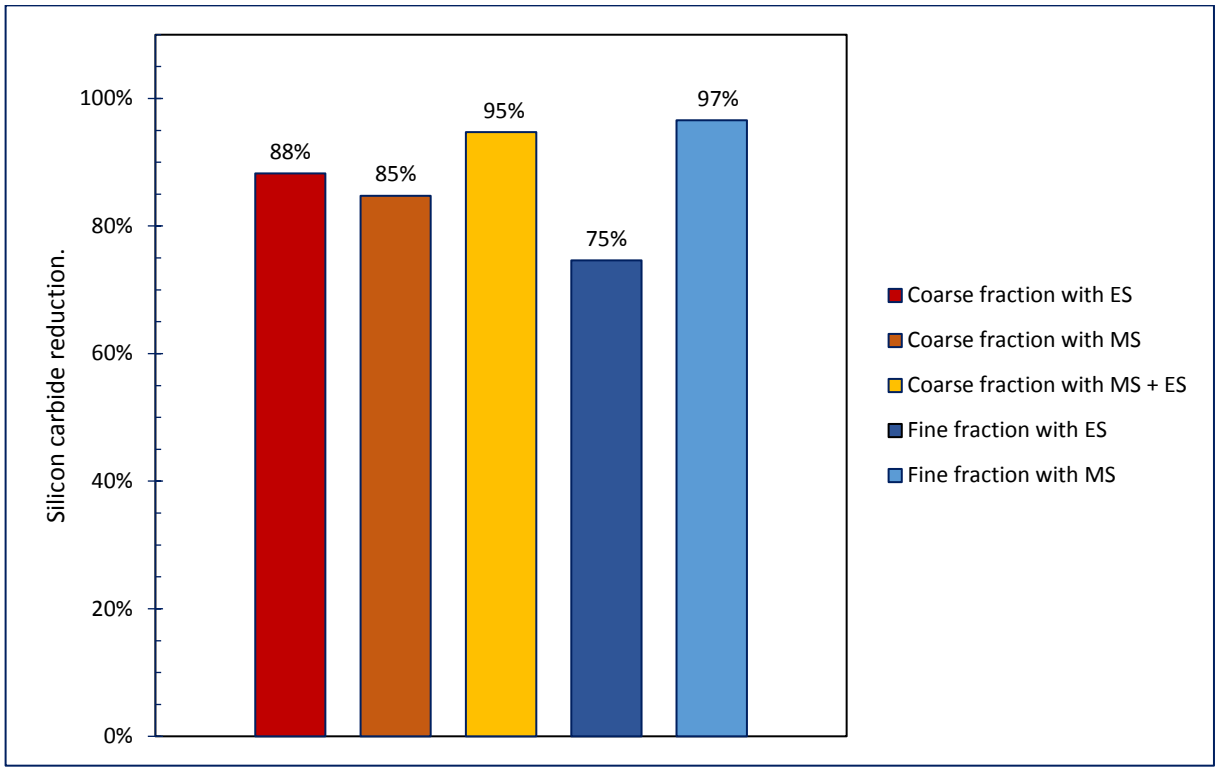

Figure 3-27: Comparison of silicon carbide reduction via electrostatic (ES) and magnetic (MS) separation.

The SiC content of the fractions obtained from the magnetic separation is shown in Table 3-17. The SiC is reduced in all non-magnetic fractions representing a 85% reduction in the SiC for the coarse material (2000 to 710 µm) and a 97% reduction for the finer material (710 – 250 µm), shown in Table 3-18. Subsequent electrostatic separation of the non-magnetic fraction reduced the SiC content from 5.1% to 1.8% which represented a total 95% reduction in SiC.

This was all achieved after one pass through each separator. A comparison between the SiC reduction of the materials via electrostatic and magnetic separation is shown in Figure 3-27 and it can be seen that for the coarser fraction similar SiC reductions are achieved after one pass through an electrostatic separator and a magnetic separator, 88% and 85% respectively. However, an improvement in the reduction is made with a combination of magnetic and electrostatic separation which is equivalent to multiple passes through an electrostatic separator. There is a clear improvement in the SiC reduction of the finer material using magnetic separation rather than electrostatic. The SiC removal efficiency of finer material using magnetic separation is greater than electrostatic separation.

The SiC content of the magnetic fraction varies as the particle size varies (Table 3-19). The finer material produces a magnetic fraction with a much lower SiC content than the coarser fraction, but this is due to the increased mica presence in the finer grade material which is supported by the XRD spectra in Figure 3-31. Electrostatic separation of the magnetic fraction is possible because of the mica being an electrical insulator. There is an upgrading of the SiC grade in the magnetic fraction of the coarse material after it was passed through the electrostatic separator from 64.9% to 79.6% and this may be improved by optimising the operating conditions of the electrostatic separator.

Table 3-19: The silicon carbide content of the magnetic fractions from magnetic separation.

	SiC (wt%)
Coarse material	
Magnetic fraction	64.9
Magnetic fraction after ES	79.6
Fine Material	
Magnetic fraction	27.4

The XRD spectra of the fractions collected from the experiment clearly show a separation between SiC and cordierite. Figure 3-29 to Figure 3-31 shows the differences between the magnetic and non-magnetic fractions from the process. The SiC and phlogopite partition to the magnetic fraction whilst the cordierite partitions to the non-magnetic fraction.

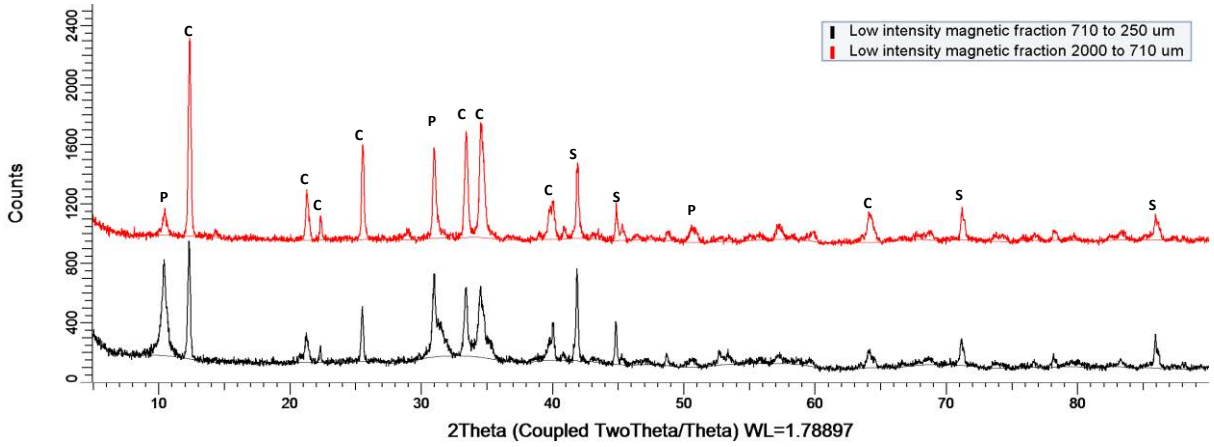

Figure 3-28: XRD spectra of the samples taken from the low intensity magnetic material.

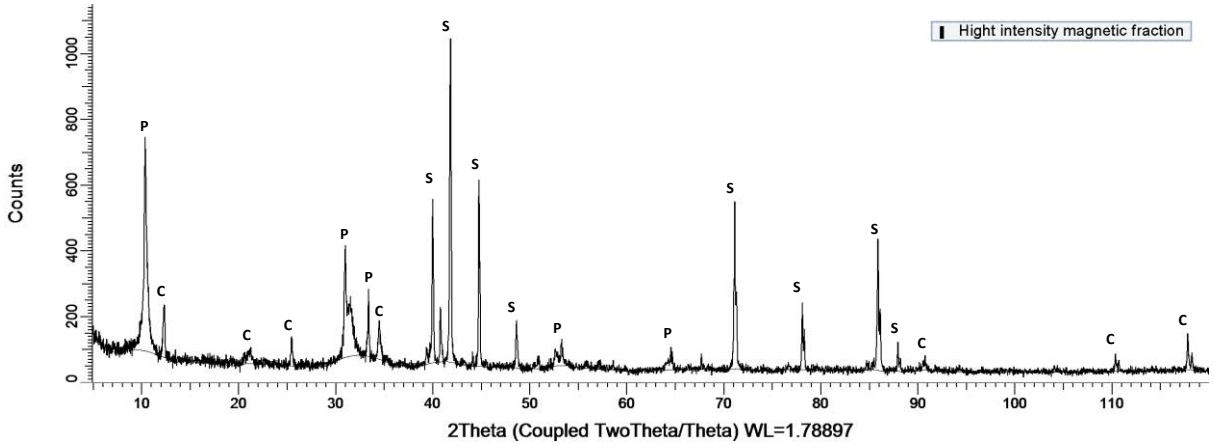

Figure 3-29: XRD spectrum of the magnetic fraction from HIM separation.

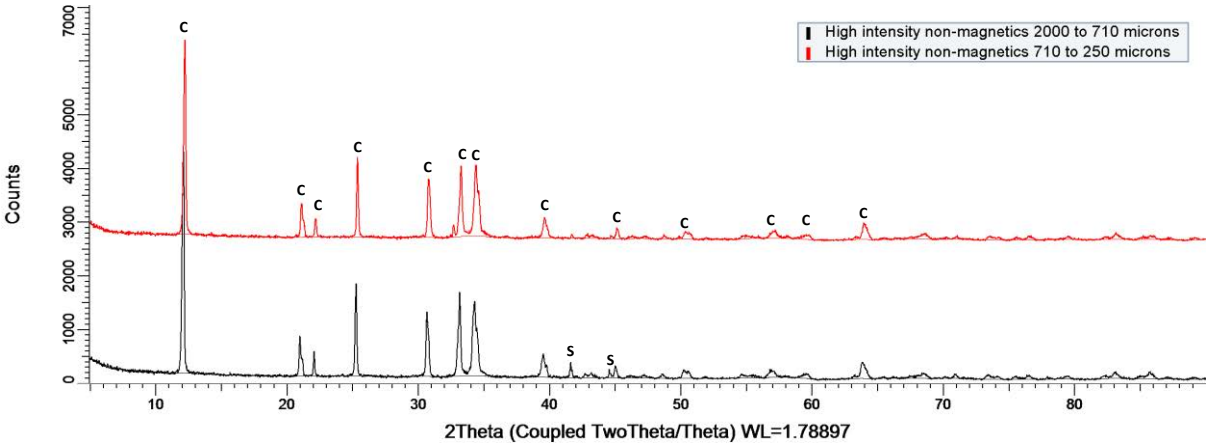

Figure 3-30: XRD spectra of the non-magnetic fractions from the HIM separator.

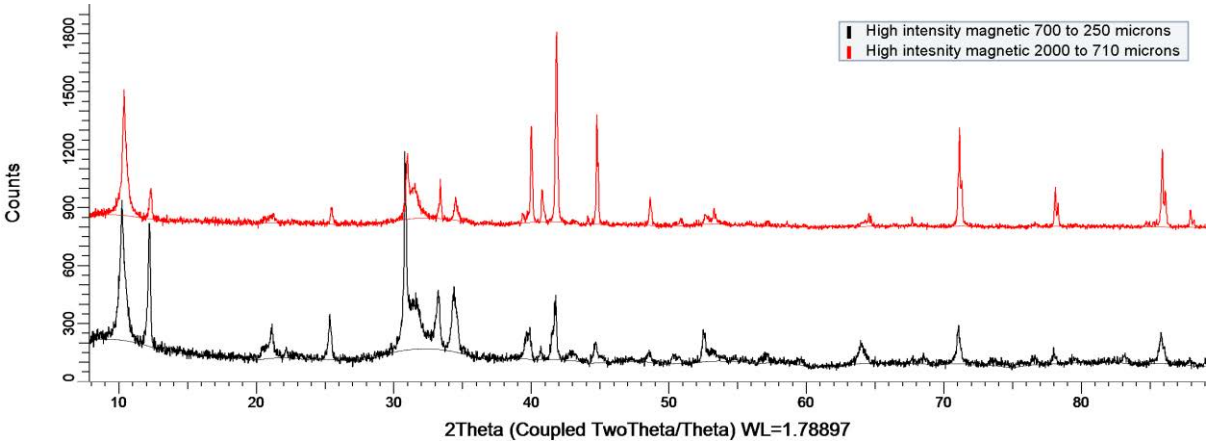

Figure 3-31: A comparison of the XRD spectra of the magnetic fractions from the HIM separator.

There is a high similarity between the non-magnetic fractions obtained from the two particle sizes (Figure 3-30). Both are rich in cordierite with little evidence of the presence of other phases. The coarser sample shows a minor silicon carbide peak at about 42 ° 2θ, but this does not seem to be present in the finer fraction. This is in line with the SiC analysis being 1.44 wt% for the fine fraction and 5.4 wt% for the coarse fraction.

Figure 3-31 compares the magnetic material collected from HIM separator for the coarse and finer particle sizes. There is a similarity between the products which are collected i.e. rich in both SiC and phlogopite, but there does appear to be a difference in the relative concentrations of the two materials. The intensity of the phlogopite peaks for the finer particle size is greater than it is for the coarser size range and the SiC peaks are less intense for the finer particle size. This indicates that the SiC/phlogopite ratio is different for the particle sizes and this could be due to:

- A greater concentration of phlogopite in the finer particle size fraction.
- A lower concentration of silicon carbide in the finer fraction (as indicated by data presented above).

Both these reasons may contribute to the differences in the peak intensity. Nevertheless, there is little evidence of the presence of cordierite in this fraction which is a positive indication of minimal cordierite losses to the magnetic fraction.

Comparing the products of the magnetic separation with the products of the electrostatic separation in Figure 3-32 and Figure 3-33 shows that the products are similar, i.e. SiC rich product and a cordierite rich product, but, there are subtle differences between the two products. The phlogopite phase at 10° 2θ is absent in the non-magnetic phase containing

cordierite but present in the insulating phase from electrostatic separation in Figure 3-33. The magnetic phase shows a greater phlogopite presence, but also seems to have a lower cordierite content.

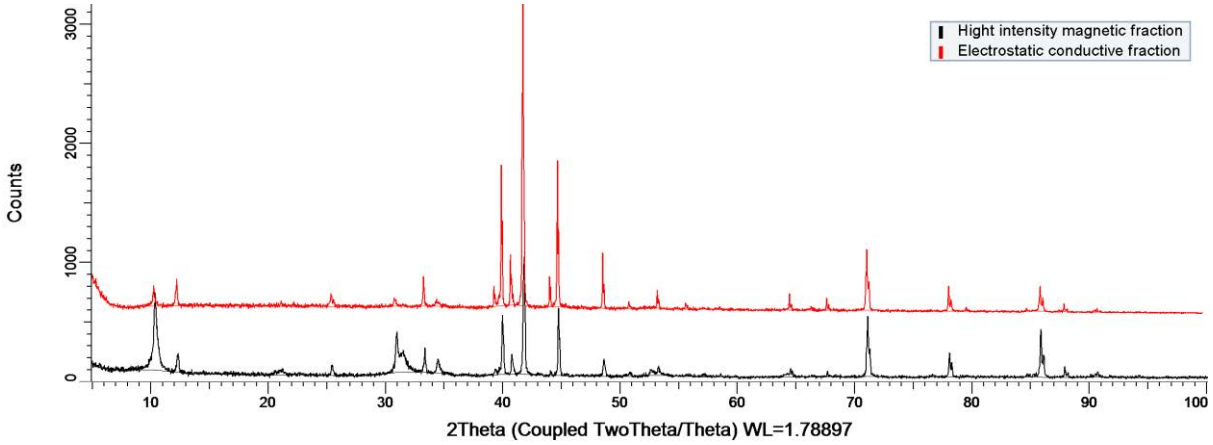

Figure 3-32: A comparison between the conductive fraction obtained via electrostatic separation and the magnetic fraction obtained after HIM separation.

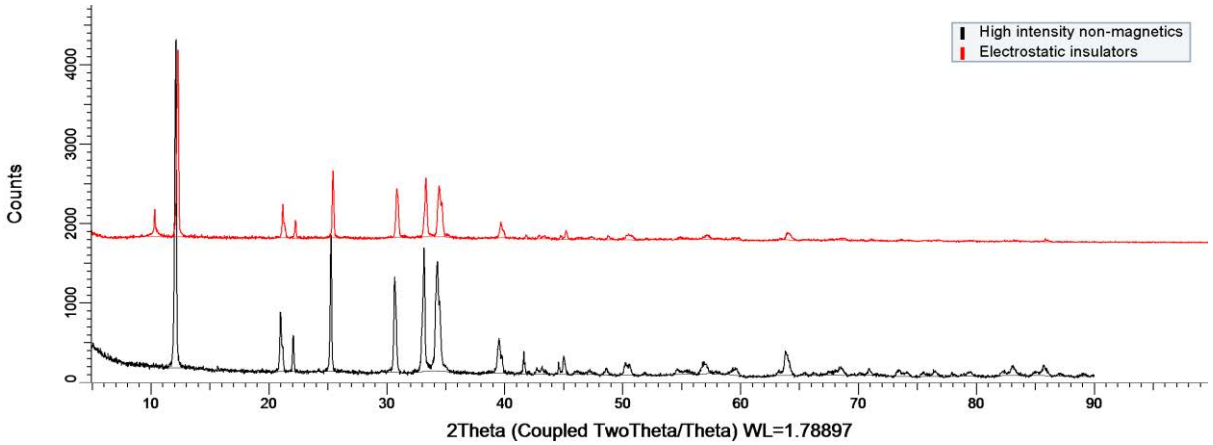

Figure 3-33: A comparison between the insulators obtained from electrostatic separation and the non-magnetic fraction obtained from HIM separation.

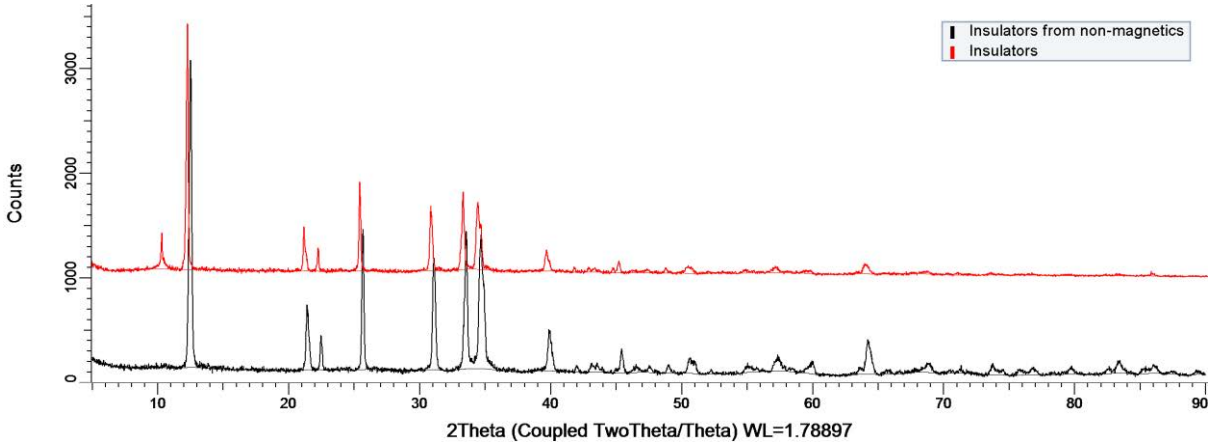

Figure 3-34: A comparison between the electrostatic insulators collected with and without prior magnetic separation.

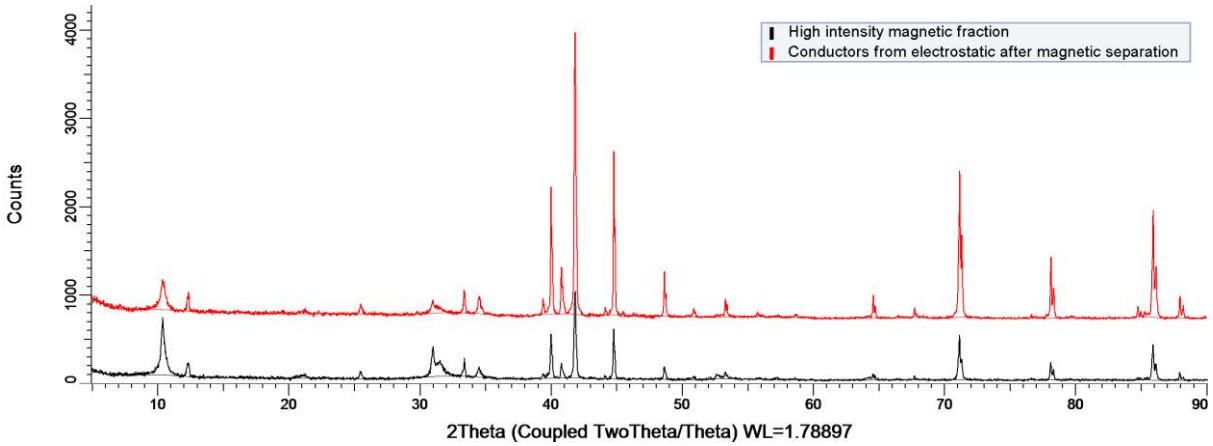

Figure 3-35: Comparison of XRD spectra for the magnetic fraction with and without subsequent magnetic separation.

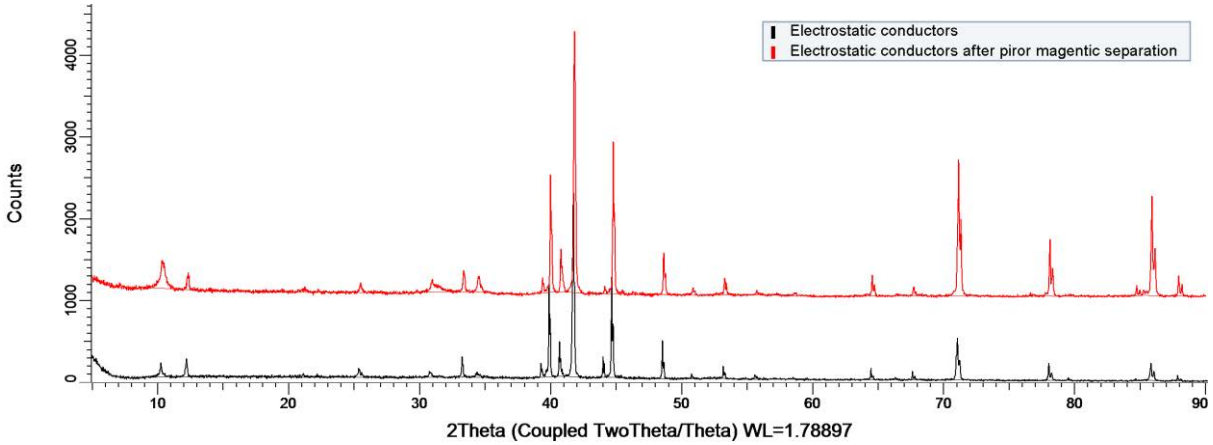

Figure 3-36: Comparison of XRD spectra of electrostatic conductive fractions with and without prior magnetic separation.

Combining the two processes together to obtain a greater grade of both cordierite and silicon carbide may be possible. Figure 3-34 shows a spectra two insulating fractions recovered from the electrostatic separator. The black spectra was obtained from the non-magnetic fraction which was then passed through the electrostatic separator. It shows a high grade cordierite which has no mica or silicon carbide peaks. The cordierite grade of this fraction is over 98% whereas the cordierite grade with just electrostatic separation was 88% with approximately 12% phlogopite content.

The magnetic fraction from LIM separation contains SiC and phlogopite. This fraction can also be processed through the electrostatic separator to remove phlogopite from SiC as phlogopite is not conductive. It is possible to achieve a high grade SiC from the process alongside a high grade cordierite. This would facilitate the downstream use of SiC as either a reductant or for alternative processing. Figure 3-35 compares the XRD spectra of the magnetic fraction obtained from LIM and the same fraction which has undergone subsequent electrostatic separation. It can be seen from this figure that there is a reduction in the phlogopite phase

and although this is still present in the final fraction this should be able to be improved by process optimisation. Figure 3-36 shows that the characteristics of the electrostatic conductive fractions with or without prior magnetic separation are similar.

The advantage of having a magnetic separator in the process alongside an electrostatic separator is that the process becomes more flexible to other impurities in the mixed material. Tramp iron or shredded steel present could be removed as well as other materials which may be present. This allows a user to process a wider range of materials through the process whilst still maintaining a consistent feed into the furnace. The combination of magnetic and electrostatic separators also has the advantage that it would be able to cope with silicon carbide catalysts from a wide variety of manufactures. The literature suggests that silicon carbide is non-magnetic, but in this work it has displayed magnetic susceptibility. This may be due to the sintering aids which are used to produce the ceramic such as nickel which may enhance the material's magnetic properties. Other manufactures may use different routes to produce SiC with different properties. Observations in the laboratory showed that some SiC had greater magnetic susceptibility than other SiC and so an electrostatic separator after the magnetic separator would allow for the removal of any residual, non-magnetic SiC.

3.7. Proposed process.

Figure 3-37 is process flow diagram showing a proposed process for the preparation of mixed automotive catalysts prior to it being fed to the plasma furnace. The process can be split into three parts; a milling stage with screening, magnetic separation and then electrostatic separation.

It should be possible for the process to operate as a batch process and thereby allowing for the separate treatment of different particle size fractions and compositions.

The first stage would be to crush or mill the raw material prior to treatment after which the raw material would be screened to two specified size fractions; 2000 to 700 µm and 700 to 250 µm. The crushing should be done in a way so as to attempt to reduce the formation of particles lower than 250 µm and avoid dust as best as possible. The presence of dust would cause difficulties in processing the material in the magnetic or electrostatic separation units due to safety concerns and cause inefficient separation in the electrostatic separator. In all the process units there should be dust extraction which would reduce the presence of airborne dust. The extracted dust should be collected in a hopper and due to its PGM content could be added to the plasma furnace. The data presented in this chapter suggests that this dust should have a low SiC content and therefore not require magnetic or electrostatic separation. The dust may need to be pelletized before being added to the plasma furnace to avoid the dust short circuiting to the off-gas system due to the suction in the furnace.

The two size fractions would be processed separately during the magnetic separator. This is because a large particle size range may cause inefficiencies in the process as the operating conditions for each size fraction could be optimised, for example drum roll speed, to ensure a more efficient separation.

The magnetic separation step would consist of firstly a LIM separator which would remove any ferromagnetic material from the mixture which may cause damage to the HIM. The mixed automotive material may be from various sources and it is possible that it could contain residual metal fractions which would be removed at this stage. The non-magnetic material would then be passed through the HIM separator which would separate the silicon carbide and the mica phases from the cordierite. The magnetic and the non-magnetic materials would

be collected and stored in hoppers and passed through the electrostatic separator separately and the operating conditions of the electrostatic separator can be optimised for each material.

The resulting materials from the electrostatic separator should be a high grade cordierite and a high grade silicon carbide. They can then be passed to the furnace feed hoppers where they can be blended prior to their addition to the furnace.

Figure 3-37: A schematic showing the proposed process.

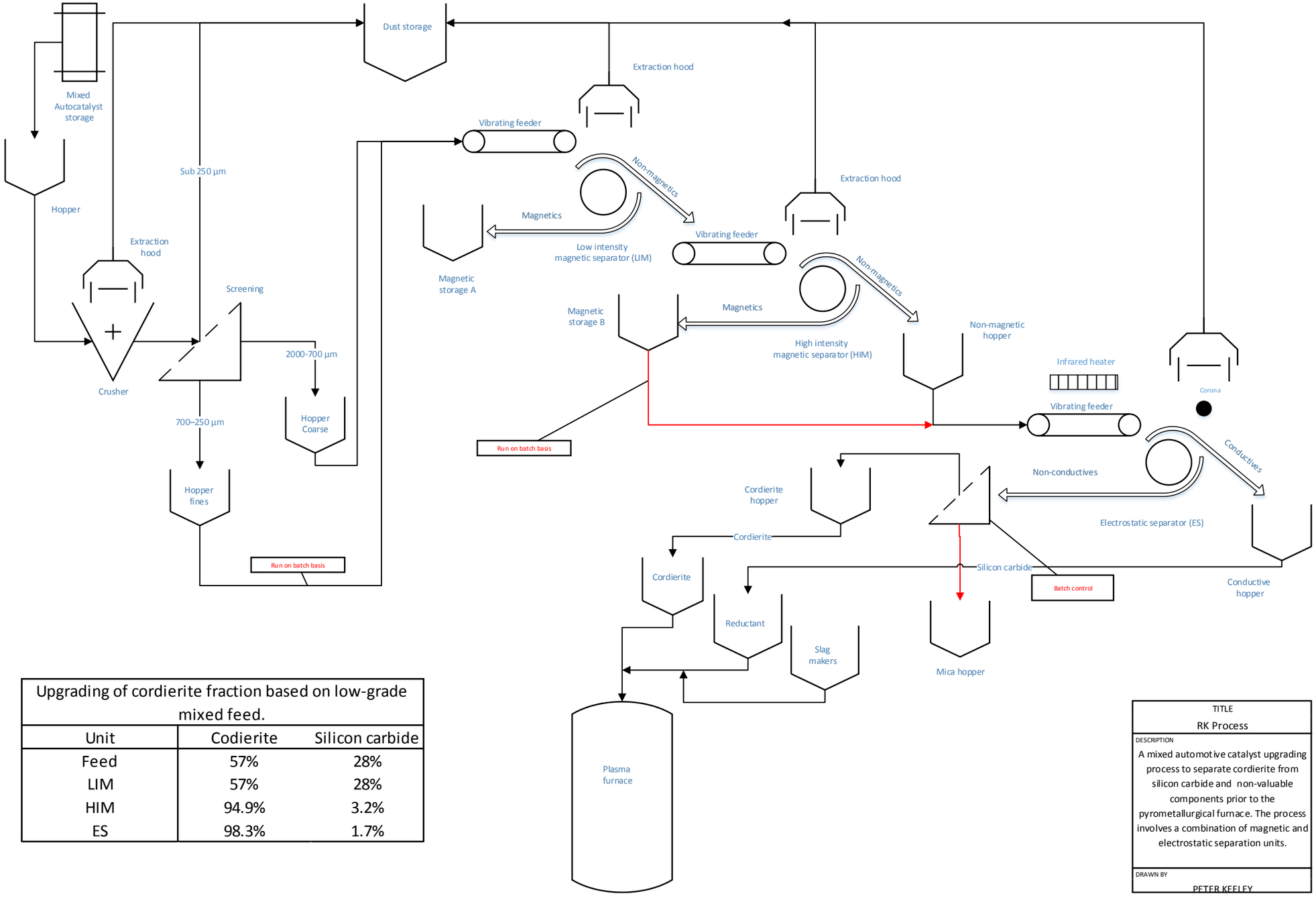

Upgrading of cordierite fraction based on low-grade mixed feed.		
Unit	Codierite	Silicon carbide
Feed	57%	28%
LIM	57%	28%
HIM	94.9%	3.2%
ES	98.3%	1.7%

3.8. Conclusions and Further Work.

A combination of magnetic and electrostatic separation allows for high grade SiC and cordierite to be produced from low grade mixed automotive catalyst scrap. The processes used on their own would not result in materials of such high grades and this would result in a less consistent feed to the furnace which may result in reduced PGM recovery efficiencies. The combined magnetic separation and electrostatic separation can achieve a SiC reduction of over 95% and a cordierite grade of over 98%. The benefits of a magnetic separation process are that it is flexible enough to remove many unwanted phases such as ferrous metals which may be present (springs or pieces of canister) and that there seemed to be excellent separation of both coarse and fine fractions which was a disadvantage of the electrostatic separator. The magnetic separator is also able to remove the mica phases from the cordierite which is not possible from electrostatic separation alone as both these materials are insulators.

The recommendations for further work for this project would be to analysis a wider range of raw materials to determine to variability of their composition and the different phases present. This would help to justify the use of the upgrading equipment.

A final use for the recovered silicon carbide should be investigated. It has been proposed that it could be used as a reducing agent, but this should be compared with the current reducing agents and determine if there are any detrimental effects of its use for example increased energy requirements or processing difficulties. Alternative end uses should be investigated, but the PGM content of the SiC should be kept in mind.

A costing exercise of the process should be made and an initial CAPEX and OPEX drawn up. A meeting with a supplier of the equipment may help to facilitate this. An initial design into a

pilot scale process should be considered to test the process against a variety of material mixtures to fine tune the process to be as flexible as possible. The intellectual property of the process should be protected before further work is done.

4. Platinum and Rhenium Recovery from Spent Petrochemical Reforming Catalysts via Plasma Arc Technology.

4.1. Introduction.

Platinum-rhenium reforming catalysts are used in the petrochemical industry in the reformation of low octane naphtha to reformates which form the blending stocks for high-octane petroleum. Many complex reactions occur during the reformation process, including dehydrogenation, isomerisation and aromatization reactions and examples of them are shown in Equation 4-1 to Equation 4-3. Equation 4-1 shows the dehydrogenation of methlycyclohexane to toluene, Equation 4-2 shows the isomerisation of octane to 2,5-Dimethylhexane and Equation 4-3 shows the aromatization of heptane to toluene. These reactions take place in vessels containing Pt-Re/Al_2O_3 catalysts at temperatures between 495 – 525°C and at pressures of between 5-45 atm (507 kPa- 4.5 MPa). Pt-Re catalysts can operate under increased temperatures and reduced pressures than Pt based catalysts, they can also produce higher C5 yields and increased petroleum octane numbers, whilst maintaining the catalyst's selectivity at high levels of coking (Jorthimurugesan et al. 1985; Kasikov and Petrova, 2009; Drobot et al. 2009). For these reasons, platinum-rhenium reforming catalysts are among the most common petrochemical catalysts and are typically 2 mm diameter, 1 cm length, Al_2O_3 pellets seeded with the catalytic agents shown in Figure 4-1 and their typical composition is shown in Table 4-1. These catalysts operate in reactors containing around 25 tonnes of catalysts for between one and two years before being sent for refining to recover the precious metals.

The concentration of platinum and rhenium on these catalyst varies with supplier, but the typical concentration of each metal is 0.3 wt%. There have been a number of reported techniques for the recovery of both platinum and rhenium from these catalysts, with most of the published and patented research focusing on hydrometallurgical processing and originating from Russia.

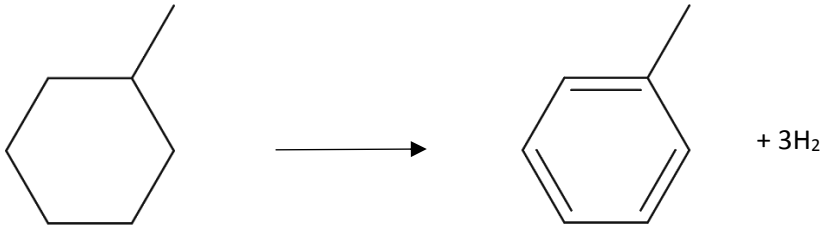

Equation 4-1

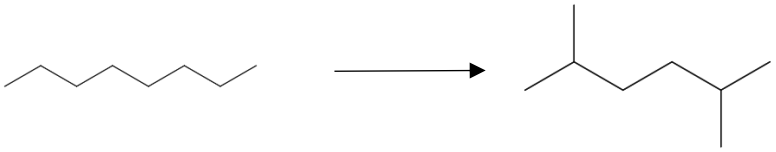

Equation 4-2

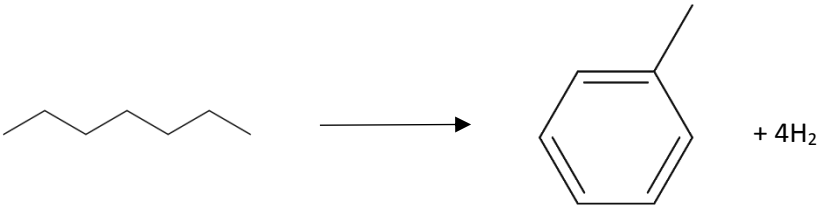

Equation 4-3

Figure 4-1: Photograph of the aluminium oxide pellet catalysts containing platinum and rhenium next to a 1p coin.

Table 4-1: Typical composition of the catalysts.

Component	**Typical content (wt%)**
Pt	0.2-0.5
Re	0.2-0.5
Al_2O_3	95
Other	4-5

4.1.1. Hydrometallurgical processing of Pt-Re/Al2O3 catalysts.

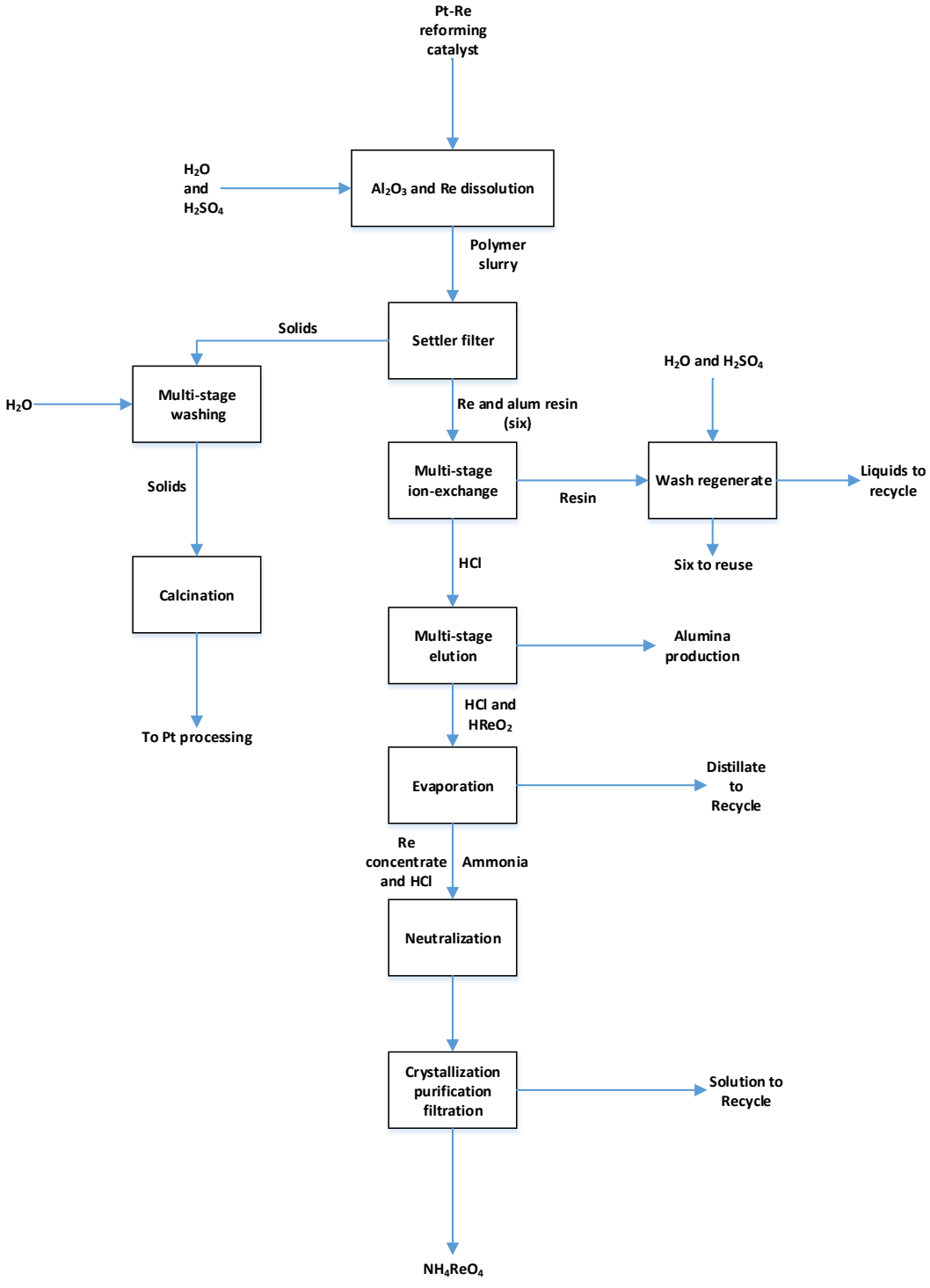

Figure 4-2: A flowsheet of a conventional rhenium recovery process from spent reforming catalysts via a hydrometallurgical route (Angelidis et al, 1999).

A traditional hydrometallurgical process for the recovery of Pt and Re from the spent reforming catalysts is shown in Figure 4-2. The first stage involves the dissolution of the catalyst support in sulphuric acid. The Al_2O_3 and Re would move into solution whilst the majority of the Pt remains in the slurry. The solids containing Pt and the liquids containing Re are separated via a filter and the Pt containing material is sent to Pt processing facilities. The Re is recovered from solution via ion exchange resins and then is passed through various processing units and reacted with ammonia to produce ammonium perrhenate (NH_4ReO_4) which is the form of rhenium primarily traded (Angelidis et al. 1999).

The major disadvantage of hydrometallurgical processing of these catalysts is the difficulty in dissolving the alumina support. The catalyst support is α-Al_2O_3, but during its lifetime it can undergo a phase change to the more stable γ-Al_2O_3. This phase is stable and difficult to dissolve resulting in very viscous solutions. To facilitate the dissolution of the catalysts either concentrated hot acids are used or the catalysts undergo a sintering process prior to the dissolution.

4.1.2. Hydrometallurgical processing with a prior sintering stage.

The catalysts are sintered with an alkali such as sodium carbonate at around 1000°C forming a residue which can be dissolved in weak hydrochloric or sulphuric acid. The thermal treatment is carried out in a reducing atmosphere to avoid the loss of rhenium due to evaporation. However, the reducing conditions do not remove coke on the catalyst and so the resulting sinter can be rich in carbon which is detrimental to the recovery of Pt and Re. During the dissolution, Pt and Re move into the solution from which they can be recovered using electrolysis. This sintering method is reported to increase the dissolution of the spent catalyst to 98% and it is able to obtain a Pt and Re recovery into a concentrate of over 99% (Borbat et

al. 1998; Novikov et al. 1986; Brobat et al. 2000). This concentrate requires further processing and even though high dissolution rates can be achieved, the alkali-sintering process still results in a viscous solution which is difficult to process (Kasikov and Petrova, 2009).

Calcining the catalysts at a lower temperature, about 500°C, in an oxidising atmosphere to removes the coke deposited on the catalysts, but risks rhenium losses due it to becoming volatilised. After calcination, the catalysts can be dissolved in H_2SO_4, HCl or aqua-regia (HCl and HNO_3). Strong acids (9 M/l) are preferred over alkaline solutions because of the greater dissolution of the catalysts achieved. The platinum and rhenium move into solution where rhenium is removed using selective sorption usually using an anion ion exchange resin and platinum is recovered by cementation with aluminium, an example of which is shown in Equation 4-4.

$$H_2PtCl_{6(l)} + 2Al_{(s)} \rightarrow Pt_{(s)} + 2AlCl_{3(l)} + H_{2(g)} \qquad \text{Equation 4-4}$$

Rhenium is desorbed from the resin using HNO_3 and is passed through various processes to produce ammonium perrhenate salt, the form in which rhenium is usually sold (Kasikov and Petrova, 2009). Although around 98% of the Pt and Re can be recovered at each processing step, due to the complex multi-stage process the ultimate recovery rate is between 80-90% (Bukin et al. 2002).

4.1.3. Pyrometallurgical Processing of reforming catalysts.

Hydrometallurgical processing requires a complex multi-stage process and the use of large volumes of solutions result in the production of large volumes of waste fluids which need to be treated. The combination of pyrometallurgical and hydrometallurgical processes is common in many PGM recovery chains, but the oxidation of rhenium makes recovering it by

a pyrometallurgical process demanding as volatile species are formed or rhenium oxides partition to the slag phase. Re_2O_7 forms in oxidising conditions at 500 – 700°C, seen in Equation 4-5.

$$2Re_{(s)} + 3.5O_{2(g)} \rightarrow Re_2O_{7(g)} \qquad \text{Equation 4-5}$$

However, some pyrometallurgical processes for these catalysts involve the oxidative stripping of rhenium by heating the catalysts in an oxidising atmosphere to form volatile Re_2O_7 which can then be captured in solution. Re recovery increased from 80% to 99% as the process temperature increased from 400 to 1180°C (Belov et al. 1986), but platinum was not recovered and still remained in the catalysts to undergo further treatment. Another thermal treatment to recover Pt and Re from the catalysts is a chlorination process (Drobot et al. 2009). Here the catalysts are exposed to chlorine gas whilst in water or HCl. The process relies on platinum and rhenium forming chloride complexes which can be recovered from solution after drying and filtration. However, the recovery efficiencies of both metals is poor achieving 91 – 96% rhenium recovery and only 52% Pt recovery. The Pt recovery can be improved to 72 – 94% by calcining the residue from the first chlorination stage at 500°C to remove coke and repeating the process.

There have been no reported investigations into the pyrometallurgical smelting of these catalysts to recover both platinum and rhenium into a base metal alloy suitable for final refining, like those produced in the plasma process.

Most commercial processes focus on the recovery of platinum from the catalysts and it can be the case that rhenium recovery is often sacrificed to optimise platinum recovery due to its

higher value. However, there have been historical peaks in the price of rhenium which has caused greater interest in its recovery and with it being highlighted as a critical metal by the aviation industry, its recycling is becoming more important. A review of the rhenium market can be seen in Appendix A.

Rhenium is only extracted as a by-product of molybdenum mining because there are no ores of rhenium economic to mine due to its rarity in the earth's crust and mantle. Like platinum (Pt), palladium (Pd) and gold (Au), rhenium is classed as a highly siderophillic element (HSE) (Ertel et al., 2008). A HSE has a high affinity to iron and in geological studies rhenium has shown a low solubility in silicate melts consequently making Re unlikely to be found in the earth's crust or mantle (Ertel et al., 2001, Righter and Drake, 1997 and Mallmann and O'Neil 2007). There are parallels with geology and plasma smelting, indicating that Re should form an alloy with iron and not partition to the silicate based slag phase. The solubility of rhenium in silicate melts is dependent on its oxidation state and as rhenium becomes increasingly oxidised, experiments show, it moves from an iron alloy to a molten silicate phase. This oxidation of the rhenium occurs when the partial pressure of oxygen increased in the system (Mallmann and O'Neil (2007)) and so as the partial pressure of oxygen increases, the more likely it is that rhenium would oxidise and partition to the slag phase during plasma smelting.

Although smelting processes have not been used to recover rhenium, Tetronics plasma technology has been used to recover ruthenium (Ru) from petrochemical catalysts used to remove hydrogen sulphide (H_2S) from gas streams. The concentration of ruthenium on these catalysts is high (1.8 wt%) and although ruthenium is a platinum group metal, it is less noble than platinum and can form ruthenium oxides which are volatile. The operation of the plasma

process can be controlled to reduce this oxidation and achieve 98% recovery efficiencies of ruthenium producing an iron based collector metal with a Ru content of 5 wt%. This process has been operating on a commercial scale in Japan since 2013 with a throughput of 1,000 tonnes per year of catalysts. The plant is operated by Furuya Metals and reportedly generates $2m of process credits annually. The success of this process indicates that the recovery of both platinum and rhenium can be achieved via a plasma smelting route.

4.2. Pt-Re/Al_2O_3 Catalyst Characterisation.

1 tonne of spent reforming catalysts were supplied by Ekaterinburg Non-Ferrous Metals Processing Plant (EZOCM) to be used in pilot plant trials at Tetronics' trials facility in Swindon, UK. The catalysts were sampled and analysed for material bulk composition and for the concentration of Pt and Re. The material was in 38 barrels each containing between 26 to 27 kg of catalysts. Several spear samples were taken to obtain around 500 g of catalysts from a random selection of five barrels and then blended and samples taken for analysis.

The catalyst support is a highly porous material with the pore sizes being nanoscale shown by the electron microscope image in Figure 4-3. The bulk oxide composition of the catalysts was determined using X-ray fluorescence (XRF) and the Pt and Re content was determined using inductively coupled plasma mass optical emission spectroscopy (ICP-OES). The composition of the catalysts is shown in Table 4-2, the major component being Al_2O_3 although there are other minor components for example Fe_2O_3 (1.11 wt%) and a loss on ignition of 1.9 wt% which may account for the coke content and other volatile components (chlorine for example).

Table 4-2: Composition of the Pt-Re reforming catalysts.

Component	(wt%)
Loss on ignition	1.9
Al_2O_3	94.4
SiO_2	0.19
TiO_2	0.06
Fe_2O_3	1.11
ZrO_2	0.59
ZnO	0.05
S	0.08
Pt	0.366
Re	0.21

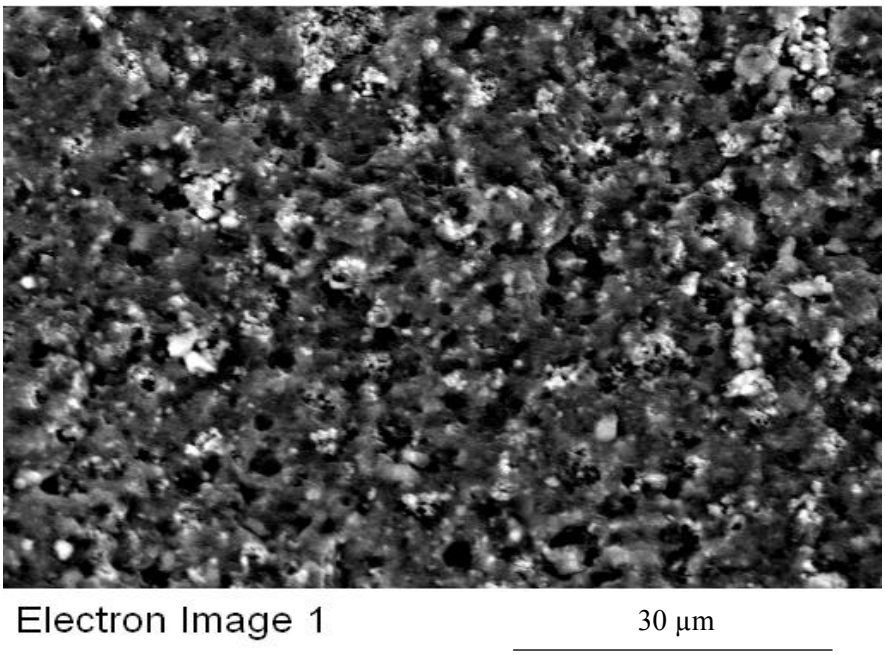

Figure 4-3: SEM image of the Pt-Re catalyst showing the Al_2O_3 porous microstructure.

The concentration of the platinum and rhenium on these catalysts was 3600 ppm and 2100 ppm respectively which is typical for this type of catalyst. The platinum and rhenium are finely dispersed over the catalyst support and transmission electron microscope (TEM) images (Figure 4-4) of the catalyst show that the catalytic metals are present as spheres between 20-50 nm in diameter. The consequence of this small size is emphasised by the need the collector metal in the plasma process.

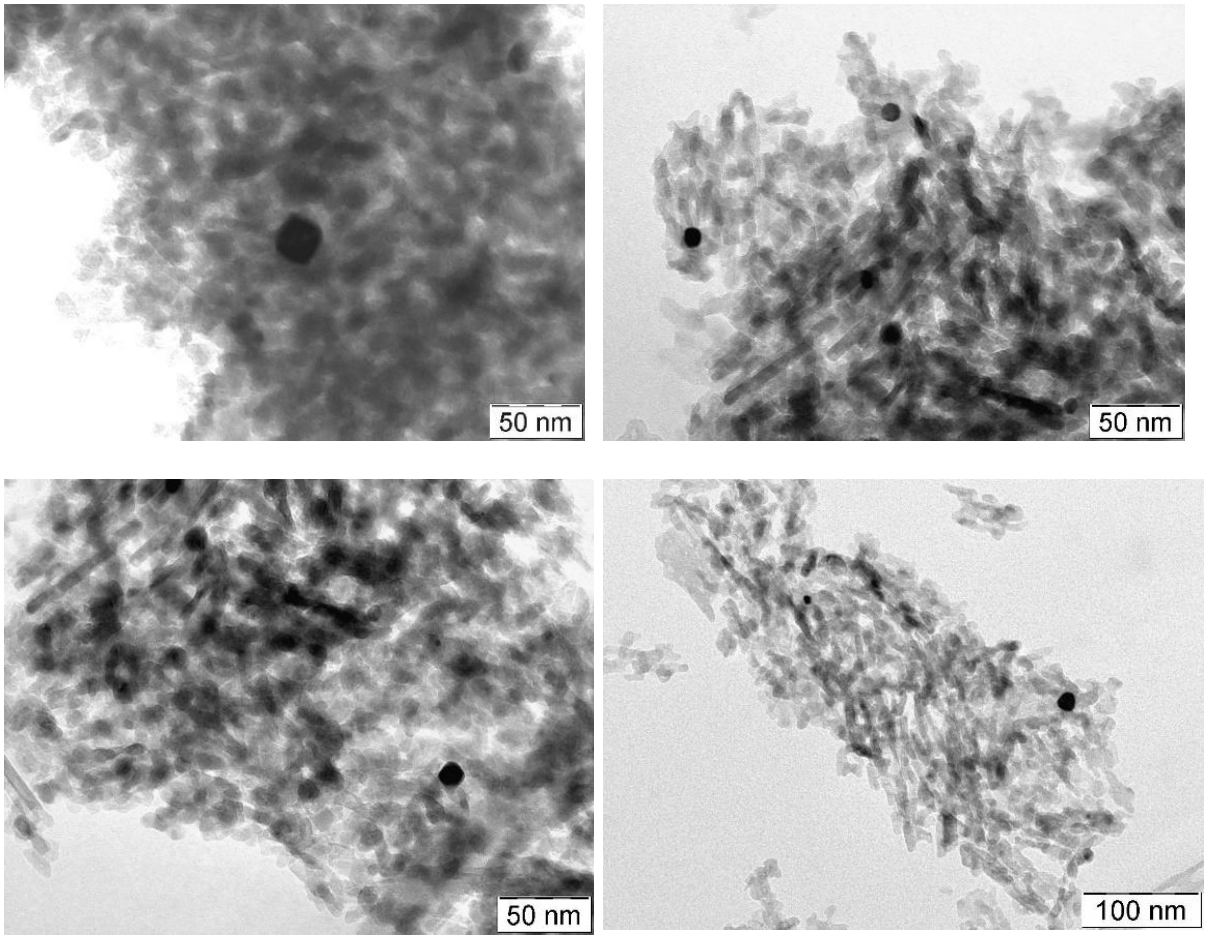

Figure 4-4: Transmission electron microscope (TEM) images of the spent Pt-Re catalysts showing small circles which are believed to be the catalytic particles.

4.3. Thermodynamic Modelling.

Thermodynamic modelling was performed to determine the energy requirements for the process and the operating conditions required to optimise the recovery efficiency of platinum and rhenium.

The calculation of the energy requirement of the process is performed by calculating the change of enthalpy between the products and reactants. In this way, the plasma power input can be determined and in this case, it would be the energy input required to melt the material and maintain a temperature of 1500°C in the furnace. The heat losses from the furnace can be accounted for manually. The steady state heat losses from the pilot plant plasma furnace which was used in these trials have been empirically determined from previous trial operations and are taken as 90 kW in the model.

The modelling was performed on the basis of 100 kg of blend assuming that platinum and rhenium are present in the catalyst in metallic form. The nobility of platinum suggests that this is a valid assumption and although rhenium has seven oxidation states and can form compounds with a variety of elements. There is little information on the state of rhenium in the catalysts in literature so several models were made varying rhenium's oxidation state to determine the effect of the oxidation state on the recovery efficiency of rhenium.

To recover rhenium via a pyrometallurgical process, there must be a highly reducing atmosphere inside the furnace which must be maintained. Figure 4-5 shows that as the oxygen concentration inside the furnace increases, HSC predicts that the oxidation of rhenium will occur and so by keeping the oxygen concentration low, rhenium will remain in the metallic phase and form an alloy with iron.

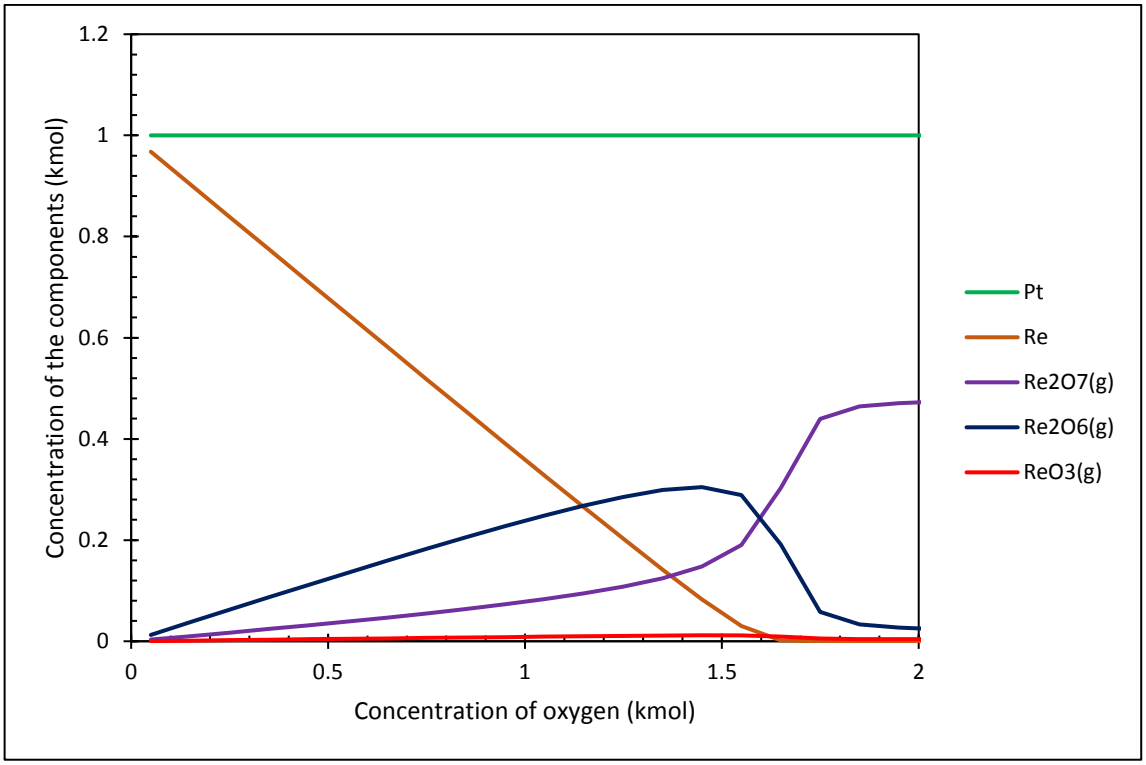

Figure 4-5: Ease of oxidation of rhenium compared to platinum at 1500°C.

The advantage the plasma arc being powered by electricity produces a heat source independent from the process chemistry so a reductive atmosphere can be maintained by the excess addition of coke to minimise the oxidation of rhenium.

The catalysts were blended with the fluxing agents, calcium oxide (CaO) and silicon dioxide (SiO_2), a collector metal precursor, magnetite (Fe_3O_4) and a reducing agent, coke (C). The fluxing agents were required to alter the energy requirements for melting, the chemistry of the slag and its viscosity. The formulation used in the trials is shown in Table 4-3.

Al_2O_3 has a melting temperature of approximately 2020°C and so fluxing agents reduce the energy requirements for the process by reducing the overall melting temperature of the blend. The CaO-Al_2O_3-SiO_2 (CAS) phase diagram was used to determine the fluxing additions required to ensure that the material in the furnace would be molten at approximately 1500°C,

the typical plasma operating temperature. There are several options for the slag composition, but the choice of the final composition was based on the economic addition of raw materials and Tetronics' previous experience in melting these three components.

Figure 4-6 shows the chosen slag composition which falls on a eutectic point of the phase diagram with a melting temperature of approximately 1380°C. The slag composition is also shown in Table 4-4.

Table 4-3: Formulation for the pilot plant trials.

Component	Trial 1	Trial 2	Trial 3	Trial 4	Trial 5
Catalyst	35%	36%	36%	36%	37%
SiO_2	29%	26%	26%	28%	29%
CaO	26%	30%	30%	28%	29%
Fe_3O_4	7%	5%	5%	5%	4%
C	3%	3%	3%	3%	2%

Table 4-4: Designed slag composition for pilot plant trials.

Component	Wt%
Al_2O_3	39
SiO_2	31
CaO	30

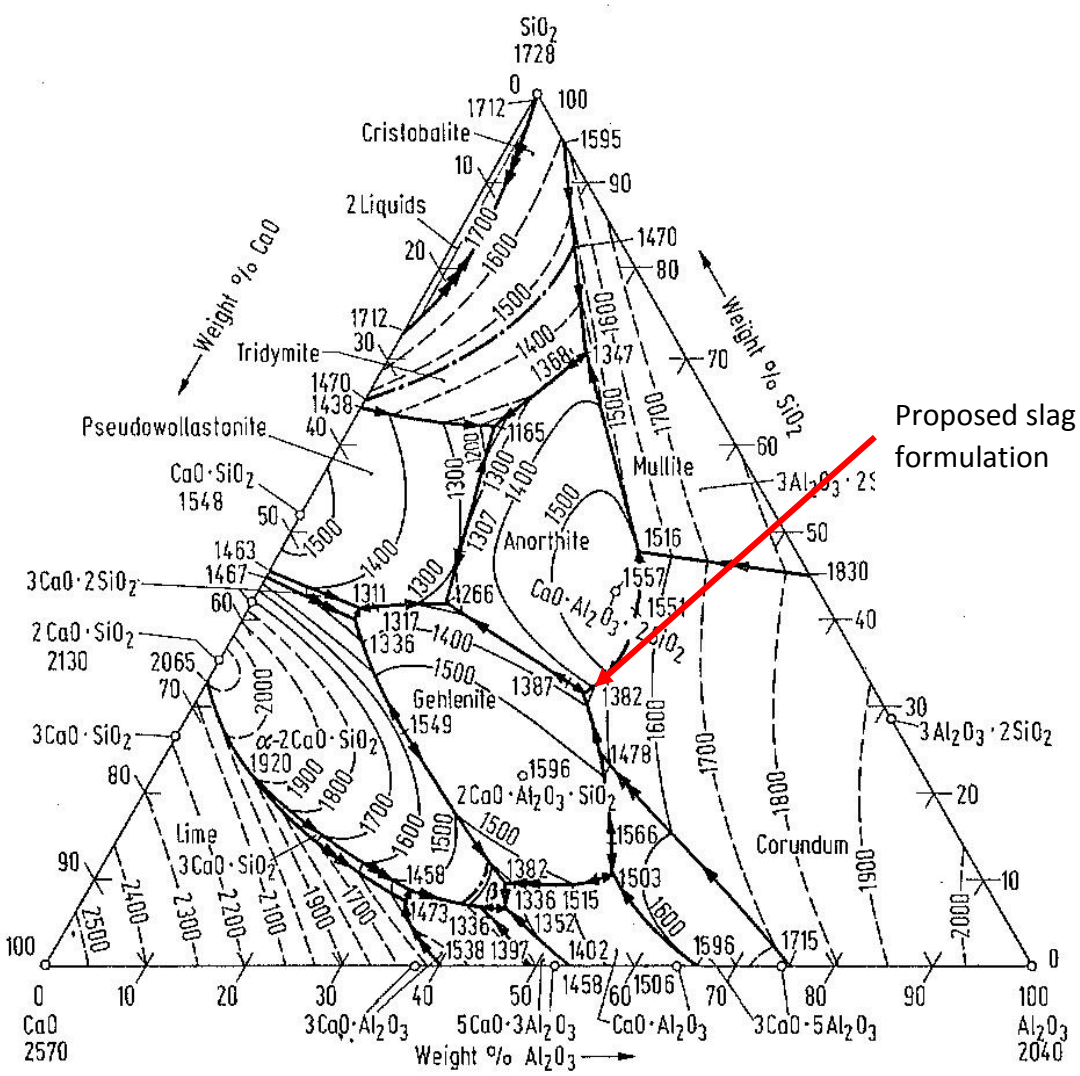

Figure 4-6: $CaO\text{-}SiO_2\text{-}Al_2O_3$ phase diagram and slag formulation.

The collector metal addition required for the recovery of Pt and Re from the melt was initially set at 7% of the total blend for the first trial and gradually lowered to 4% to determine an optimum collector addition for the process. A greater addition of the collector metal would increase the PGM recovery efficiency, but this would result in a dilution of the PGM content of the final alloy which would reduce its value. Therefore, optimising the collector metal addition for the PGM recovery and metal value is an objective for plasma smelting operations, but is usually something which is developed over many trials. The reducing agent addition (3

wt%) is based on the required carbon contain to reduce the magnetite to iron and maintain the reducing conditions within the furnace. This addition of carbon is also helps to reduce the melting temperature of the alloy. The final alloy is designed to have a carbon content between 3-5 wt% which as shown in the Fe-C phase diagram in Figure 4-7. As the carbon content of the alloy increases, the melting temperature of the alloy decreases making it closer to the melting temperature of the slag. When the slag and the metal have similar melting temperatures there is better heat transfer between the two phases which reduces problems in the operation of the furnace.

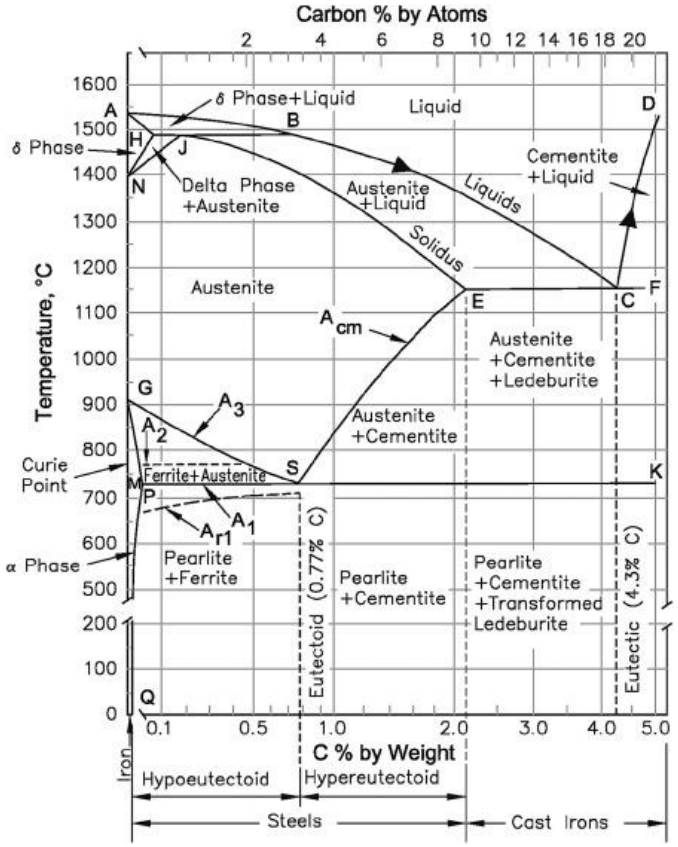

Figure 4-7: Fe-C phase diagram. (Sing, 2016).

Increasing the carbon content in the alloy causes the iron to become more brittle. This makes it easier to break the alloy into smaller fragments which aides final refining.

Figure 4-8 and Figure 4-9 show the predicted behaviour of the components during the process. The slag makers are expected to form a slag whilst the carbon reduces the iron oxide. Pt and rhenium are predicted to be recovered as metals from the process. Table 4-5 shows that the oxidation state of rhenium on the catalysts should not affect the recovery efficiency of the rhenium in the process providing the reducing conditions are maintained. The theoretical recovery efficiency of the rhenium from the catalysts is 100% showing that the reduction of rhenium to the metallic phase is feasible and the production of volatile species can be avoided. The amount of reducing agent (coke) required for this process does slightly change depending on the nature of the rhenium on the catalyst. This is shown in Table 4-6 and from Figure 4-10 to Figure 4-12. There is a slight increase in the reducing agent (coke) requirement if the rhenium is present on the catalyst as ReO_2 due to the preferential reformation of ReO_2 under low coke additions which is not predicted in models where rhenium is present at Re or Re_2O_7.

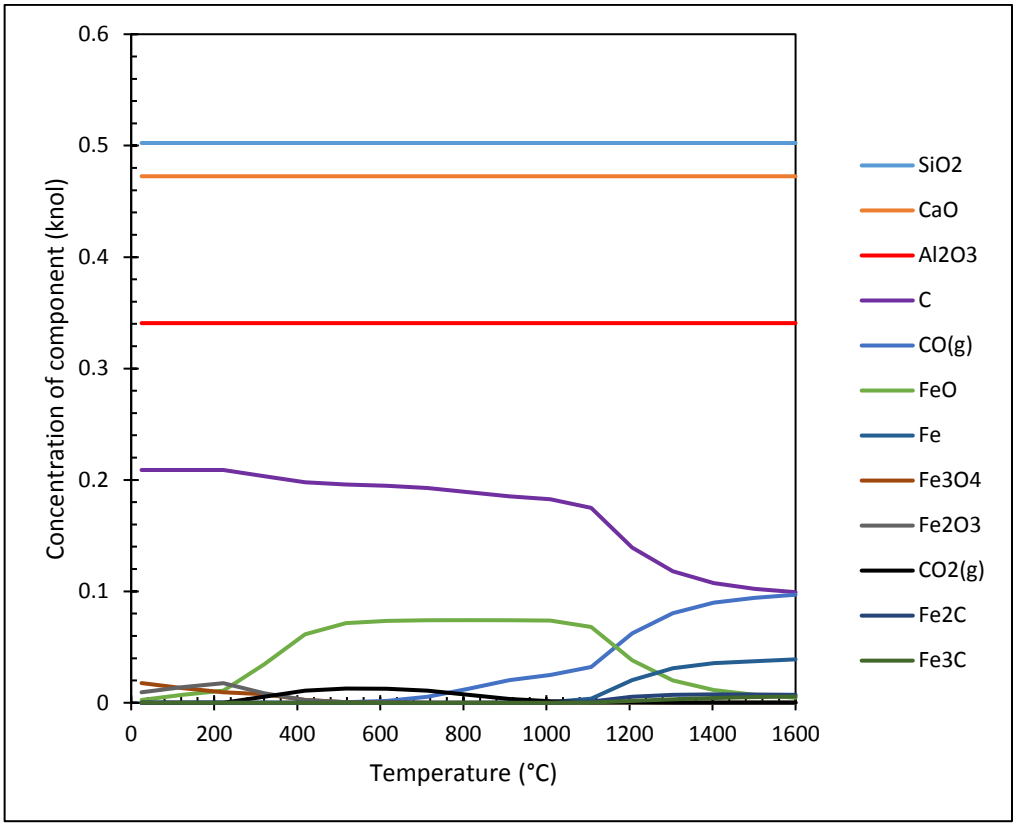

Figure 4-8: HSC modelling result of the behaviour of the bulk components in the plasma process.

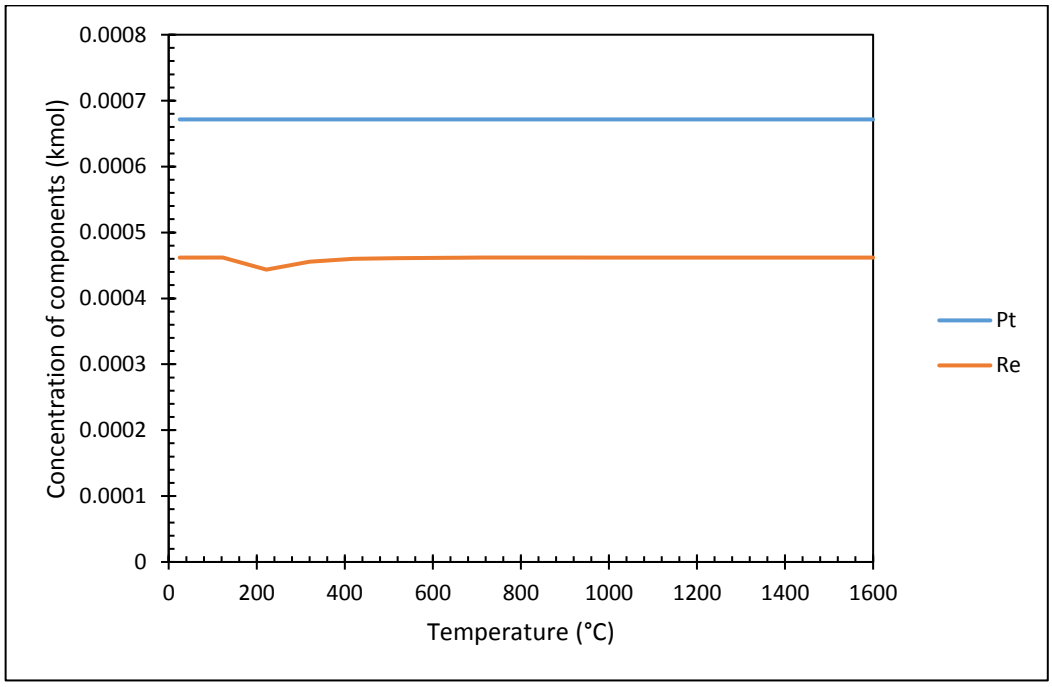

Figure 4-9: HSC model of the behaviour of platinum and rhenium (metallic rhenium) at the designed operating conditions.

Table 4-5: Theoretical rhenium recovery based on rhenium's oxidation state under reducing conditions.

Rhenium oxide present in catalyst	**Rhenium recovered to metallic phase**
Re	100%
ReO_2	100%
Re_2O_7	100%

Table 4-6: Theoretical amount of carbon required to reduce rhenium to metallic rhenium during the plasma process at 1500°C.

Rhenium oxide present in catalyst	**Carbon required to reduce Re to metallic phase (kg/t catalyst)**
Re	12.5
ReO_2	17.5
Re_2O_7	12.5

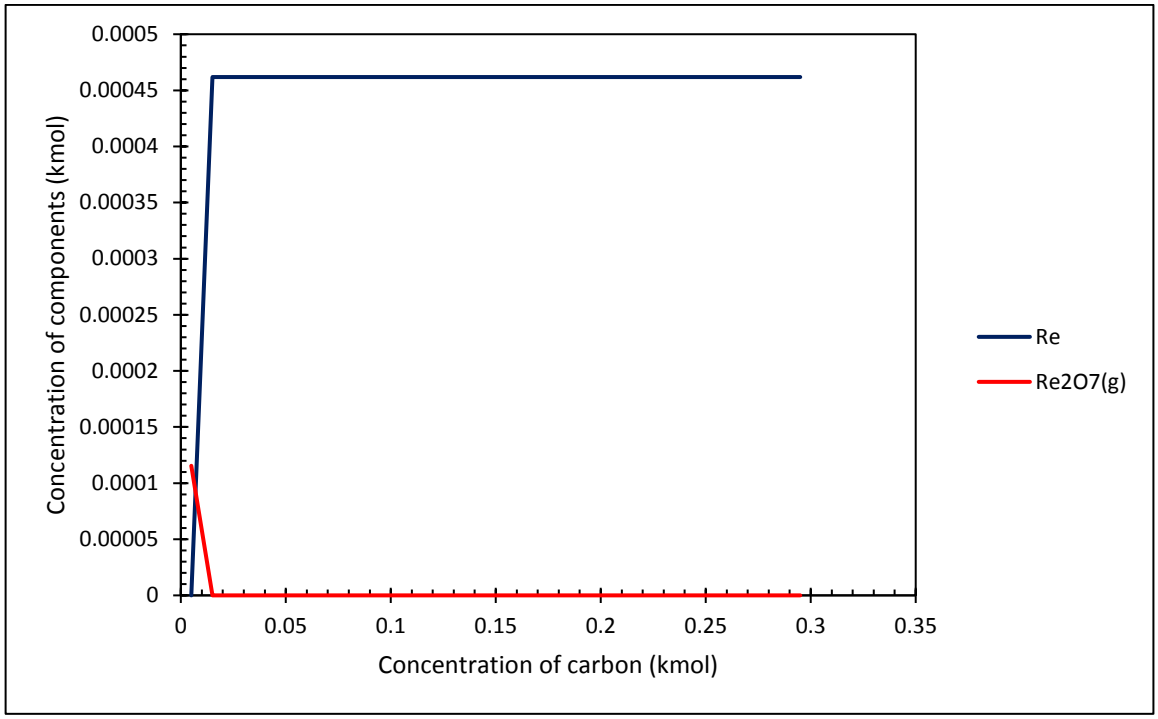

Figure 4-10: Carbon input required to recover rhenium in the metallic state.

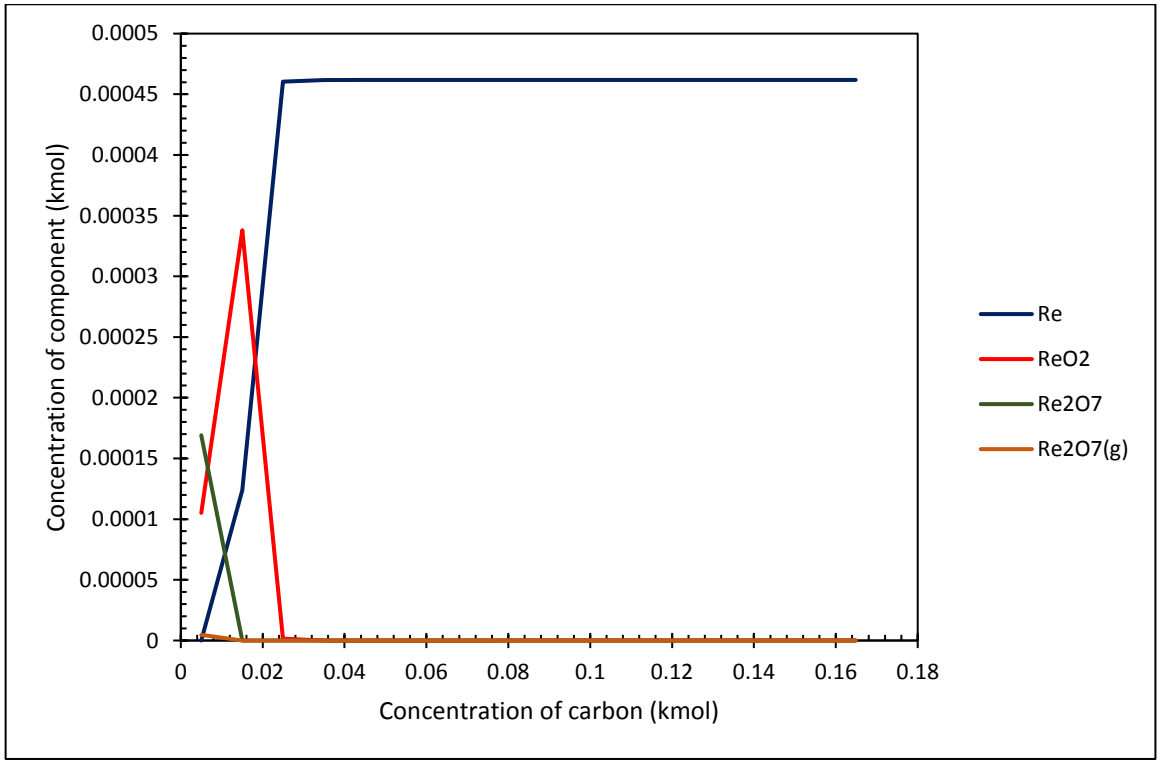

Figure 4-11: Carbon required to recovery rhenium in the metallic state from ReO_2.

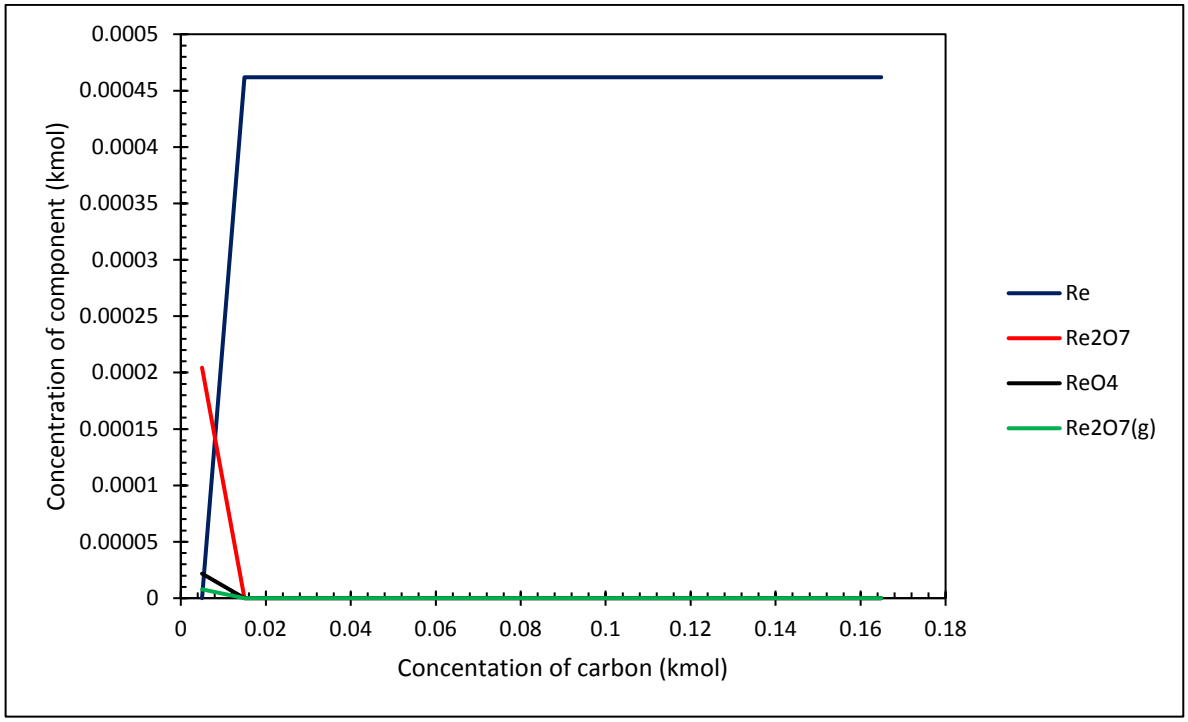

Figure 4-12: Carbon required to recover rhenium in the metallic state from Re_2O_7.

The variations in the carbon requirement to recover the rhenium in the metallic form are not so significant when it is seen that the carbon requirement to reduce the magnetite is much higher and so the reducing conditions in the furnace would be sufficient to avoid the oxidation of rhenium and reduce magnetite to iron.

The model (Figure 4-13 and Table 4-13) predicts that the magnetite (Fe_3O_4) would be reduced to FeO and Fe and that the Fe/FeO ratio increases as more carbon is added to the process producing more metal. The maximum Fe production occurs at 0.3 kg coke addition per 1 kg magnetite addition, (1.5 kg coke addition per 100 kg blend). When the addition of coke is increased above this amount the formation of iron carbide is predicted producing a carbon rich iron alloy.

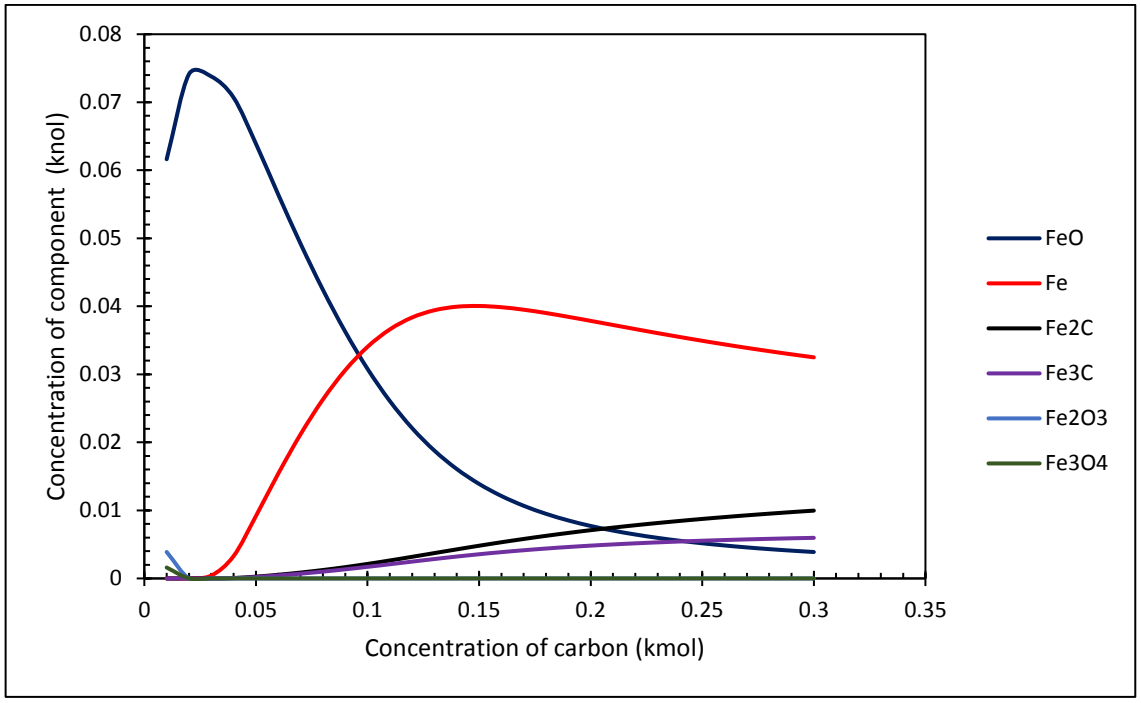

Figure 4-13: Carbon required for the reduction of magnetite to iron in the plasma smelting process.

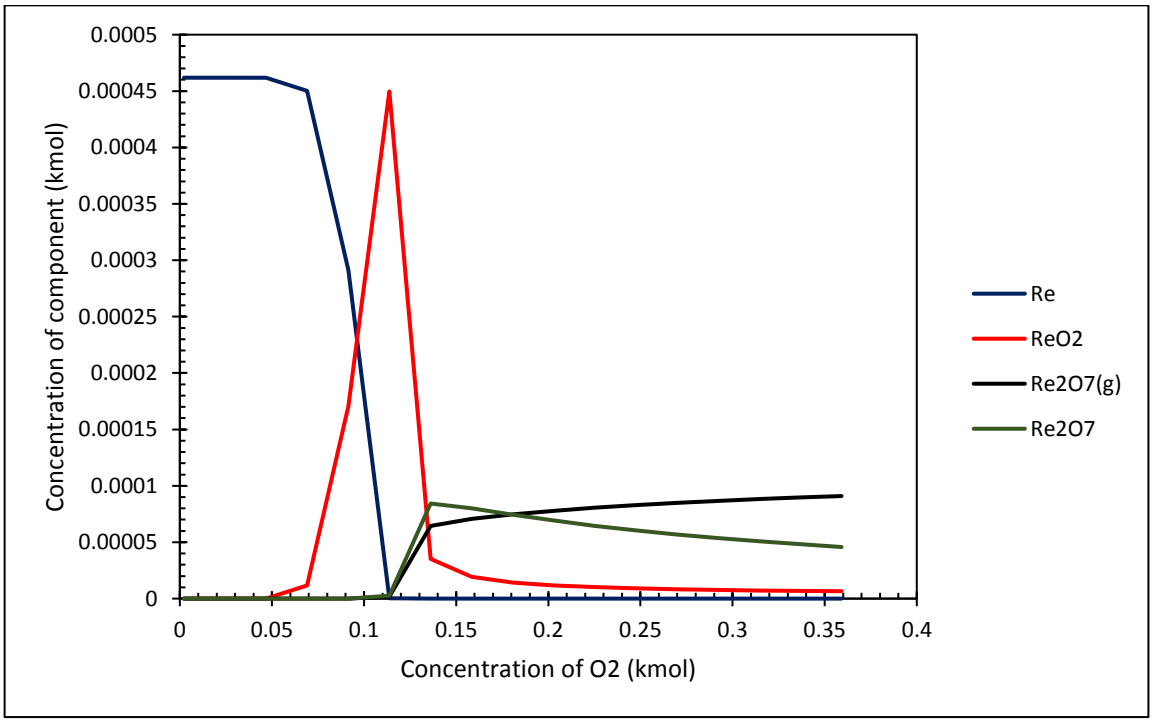

Figure 4-14; The effect of oxygen in the plasma process on the behaviour of rhenium at 1500°C with 1.5kg coke addition per 100 kg of blend.

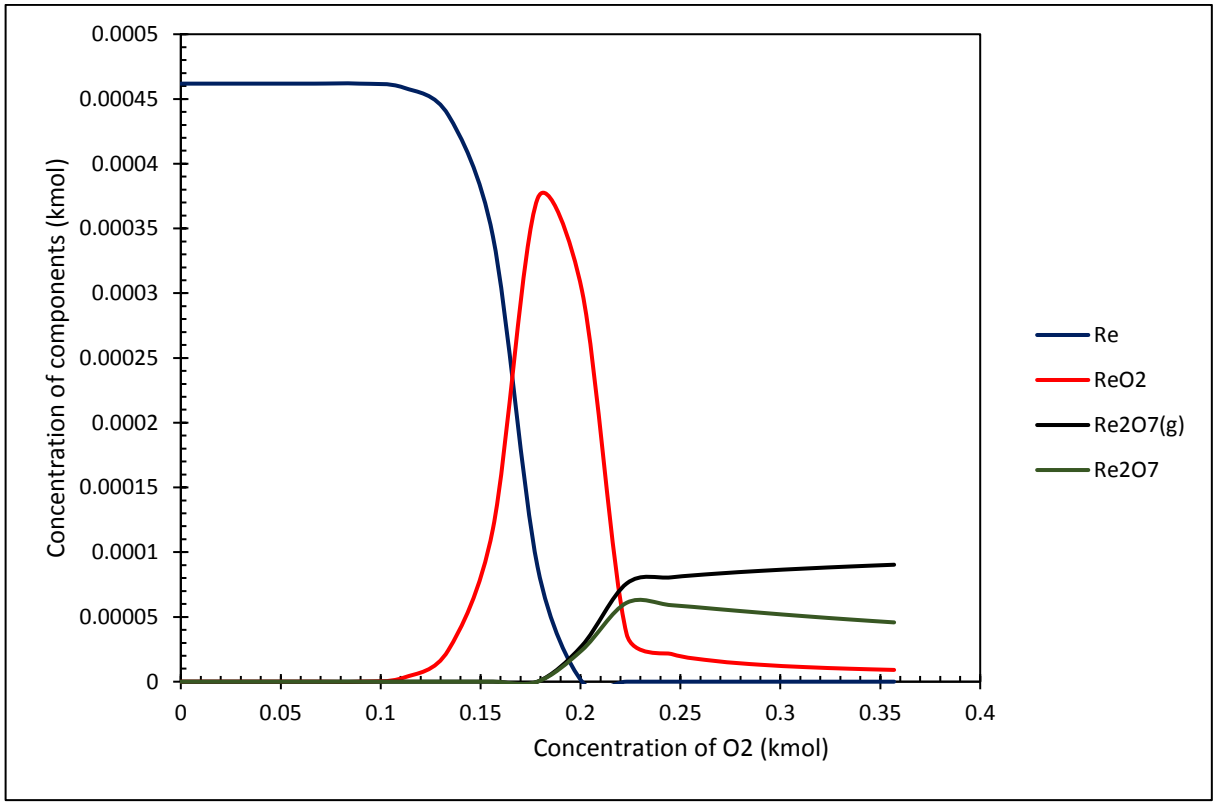

Figure 4-15: The effect of oxygen in the plasma process on the behaviour of rhenium at 1500°C with 2.5 kg coke addition per 100 kg blend.

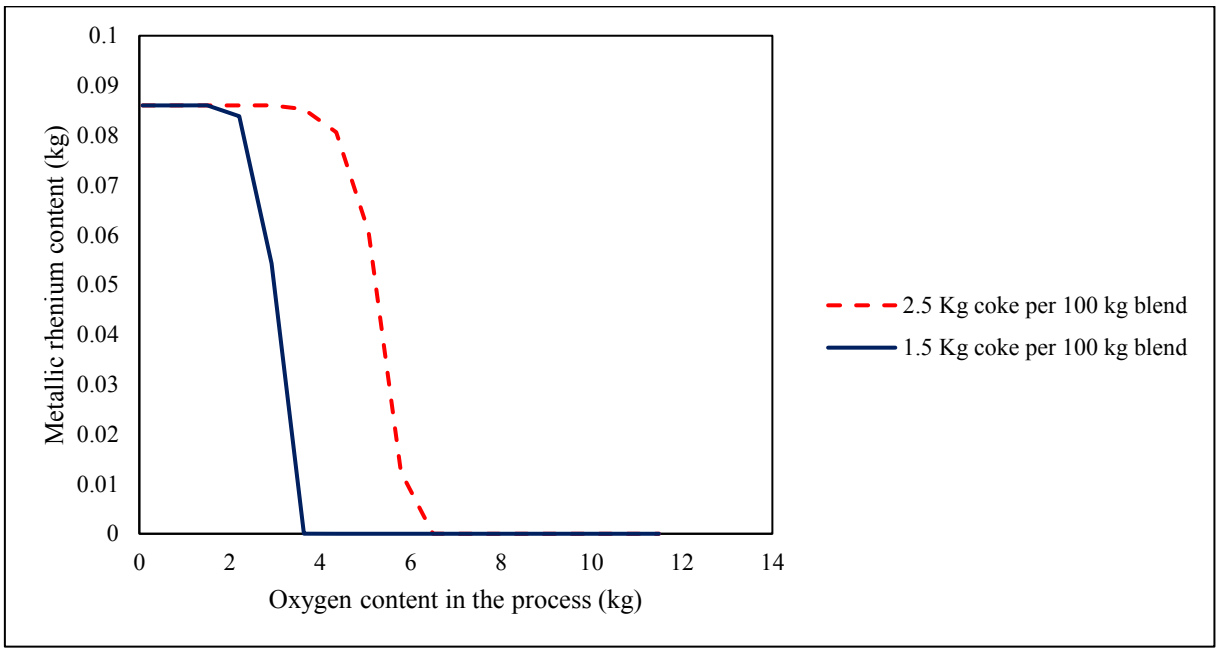

Figure 4-16: Comparison between the coke addition and the effect of oxygen on the recovery of rhenium in the metallic phase during the plasma process at 1500°C.

The modelling assumes that no oxygen would be present in the furnace. Although the process would be sealed and run under negative pressure to minimize oxygen ingress into the furnace, there is likely to be at least some oxygen which may either be produced via chemical reactions in the melt, or by some ingress from the surrounding environment. Therefore, excess carbon can be added to the process to help to avoid the formation of rhenium oxides shown by Figure 4-14 and Figure 4-15 when the coke addition is increased, rhenium is less susceptible to oxidation at the same oxygen concentration.

The addition of excess carbon into the process allows for a greater flexibility on the oxygen concentration in the furnace. The excess carbon allows for higher concentration of oxygen in the process before the formation of rhenium oxides (either volatile gaseous specious or oxides which would partition to the slag phase) and the difference can be seen in Figure 4-16.

Table 4-7 to Table 4-9 show the mass balance of the species across the process for a basis of 100 kg of total input feed. The 'output' streams from the process are a gaseous phase (off-gas), a slag phase and an alloy phase.

The slag phase mainly consists of aluminium oxide, calcium oxide and silicon dioxide at the desired composition although there will also be minor additions of partly reduced magnetite in the form of iron oxide (FeO), some chromium oxide and small fractions of $CaCl_2$ formed via chemical reactions between CaO and the Cl found in the catalysts.

The off-gas stream would consist of the inert gases argon and nitrogen, the argon being the gas used as the plasma stabilising gas. The other components of the off-gas were predicted to be carbon monoxide and carbon dioxide formed from the reduction of magnetite and also steam produced during the process. These gases enter the off-gas compound where they are

passed through a combustion chamber to reduce the final CO content of the final emission stream to the environment.

The melting of the components and the reduction reactions (and other chemical reactions) require an energy input to drive the process which is shown by the energy balance in Table 4-10. The overall process is endothermic and so the plasma power input is calculated by the difference between the enthalpy of the products (output stream) minus the enthalpy of the reactants (input stream) and so the plasma power is the energy required to overcome this difference, which for the modelled basis of 100 kg/h input is 55 kW. Table 4-11 shows the scaled up theoretical energy requirement for a tonne of the blended material to be 778 kWh/t of blend. This is known as the theoretical energy requirement because this does not consider furnace heat losses to the environment. The furnace heat losses to the environment are known from empirical data collected from previous Tetronics trials and are typically between 80 and 100 kW. Heat losses of 90 kW are assumed in this model and so the gross energy requirement for the process is 868 kWh/t blend.

Table 4-7: Input species for process model.

Catalyst components	**Temperature (°C)**	**(kmol)**	**(kg)**	**(Nm^3)**
Pt(s)	25	$4.3x10^{-4}$	0.084	$3.9x10^{-6}$
Re(s)	25	$3x10^{-4}$	0.06	$2.6x10^{-6}$
C(s)	25	$5x10^{-4}$	0.006	$2.7x10^{-6}$
Cl_2(s)	25	0.001	0.05	0.017
Al_2O_3(s)	25	0.24	24.1	0.006
SiO_2(s)	25	0.001	0.05	$1.7x10^{-5}$
Cr_2O_3(s)	25	$7x10^{-5}$	0.01	$2.1x10^{-6}$
Fe_2O_3(s)	25	0.003	0.4	$7.7x10^{-5}$
H_2O(s)	25	0.013	0.24	$2.6x10^{-4}$
Fluxes	**Temperature (°C)**	**(kmol)**	**(kg)**	**(Nm^3)**
SiO_2(s)	25	0.35	20.9	0.008
CaO(s)	25	0.33	18.4	0.006
Magnetite	**Temperature (°C)**	**(kmol)**	**(kg)**	**(Nm^3)**
Fe_3O_4(s)	25	0.023	5.21	0.001
Coke	**Temperature (°C)**	**(kmol)**	**(kg)**	**(Nm^3)**
C(s)	25	0.22	2.6	0.001
Plasma Gas	**Temperature (°C)**	**(kmol)**	**(kg)**	**(Nm^3)**
Ar(g)	25	0.54	21.4	12
Air Leaks	**Temperature (°C)**	**(kmol)**	**(kg)**	**(Nm^3)**
O_2(g)	25	0.05	1.7	1.2
N_2(g)	25	0.2	5.5	4.4
Total		**(kmol)**	**(kg)**	**(Nm^3)**
		2	100.7	18

Table 4-8: Modelled output species for the plasma process.

Off-gas	**Temperature (°C)**	**(kmol)**	**(kg)**	**(Nm^3)**
CO(g)	1200	0.98	2.73	2.2
CO_2(g)	1200	$4.5x10^{-5}$	0.002	0.001
Ar(g)	1200	0.54	21.4	12
N_2(g)	1200	0.20	5.5	4.4
H_2O(g)	1200	0.01	0.24	0.3
Slag	**Temperature (°C)**	**(kmol)**	**(kg)**	**(Nm^3)**
Al_2O_3(l)	1500	0.24	24	0.006
SiO_2(l)	1500	0.35	21	$2.1x10^{-17}$
CaO(l)	1500	0.33	18	0.005
$CaCl_2$(l)	1500	0.001	0.08	$3.9x10^{-5}$
Cr_2O_3(l)	1500	$1.5x10^{-7}$	$2.4x10^{-5}$	$4.5x10^{-9}$
FeO(l)	1500	0.002	0.15	$2.5x10^{-5}$
Excess coke forming CO	**Temperature (°C)**	**(kmol)**	**(kg)**	**(Nm^3)**
CO(g)	1500	0.1	2.9	2.4
Alloy	**Temperature (°C)**	**(kmol)**	**(kg)**	**(Nm^3)**
Pt(l)	1500	$4.3x10^{-4}$	0.08	$3.96x10^{-6}$
Re(l)	1500	$3x10^{-4}$	0.06	$2.62x10^{-6}$
Cr(l)	1500	$1x10^{-4}$	0.007	$1.04x10^{-4}$
Fe(l)	1500	0.04	1.93	$2.5x10^{-4}$
Fe_2C	1500	0.008	1.1	$1.05x10^{-18}$
Fe_3C	1500	0.006	1.1	$1.5x10^{-4}$
Total		**(kmol)**	**(kg)**	**(Nm^3)**
		2	100.7	21

Table 4-9: Total predicted mass balance for the process.

Stream	(kmol)	(kg)
Input	2	100.7
Output	2	100.7
Balance	0	00

Table 4-10: Modelled energy balance for the process.

Stream	Latent Heat (kWh)	Total Enthalpy (kWh)
Input	0.00	-264.9
Output	44.4	-209.4
Balance	44.4	55.5

Table 4-11: Calculated energy requirements for the trials.

Power requirement	Power (unit)
Theoretical plasma power input required (kWh) (at model basis)	55.5
Furnace losses (kWh)	90
Gross plasma power required (kWh) (at model basis)	146
Theoretical energy requirement (kWh/t blend)	778
Gross energy requirement (kWh/t blend)	868
Theoretical energy requirement (kWh/t catalyst)	2240
Gross energy requirement (kWh/t catalyst)	2330

4.4. Trials Data.

Five pilot plant trials were conducted with each trial lasting around 10 hours. They consisted of an initial pre-heating stage where the furnace was heated until the heat losses were around 80 kW and then the feeding of the material would begin. The feeding of the material was increased up to a maximum feed-rate of 100-120 kg/h.

The plasma power requirement vs feedrate is shown in Figure 4-17, the smelting power is the theoretical power requirement and the total power is the theoretical energy requirement (TER) plus the furnace losses.

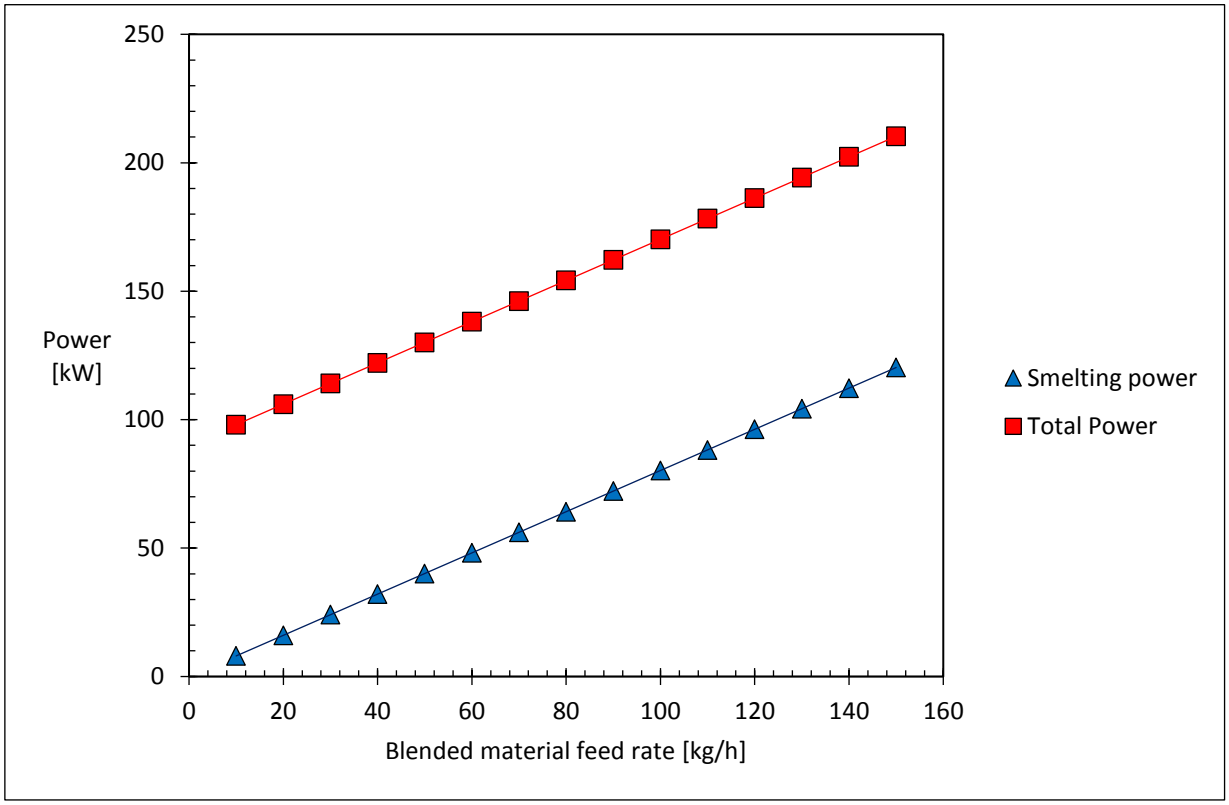

Figure 4-17: Calculated feedrate vs power requirement chart. The smelting power is the theoretical energy requirement for the process and the total power is the smelting power plus the furnace losses which were modelled at 90 kW.

Before the trials began, the furnace was pre-charged with pig iron, slag and carbon granules (Figure 4-18) which were required to protect the anode from direct exposure to the plasma arc, the pig iron acts as an initial conductive pathway and as material becomes molten a conductive melt is formed into which the feedstock can be added.

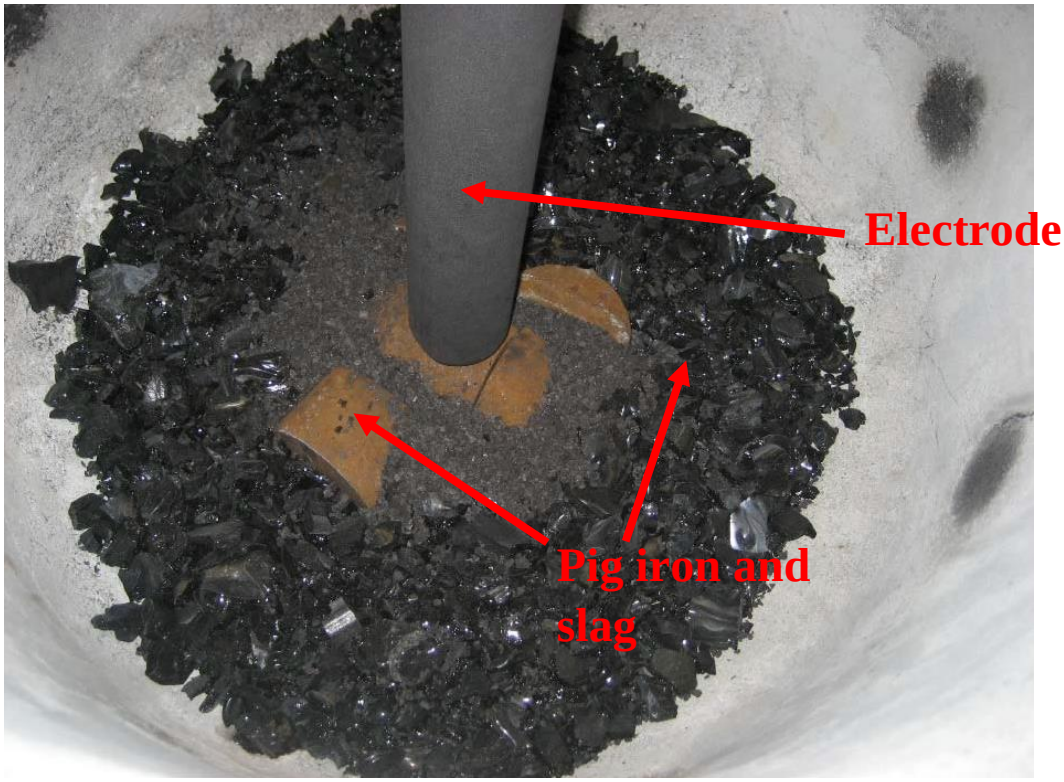

Figure 4-18: Image of the furnace after pre-charging.

The feeding of the material into the furnace began after the furnace losses reached 80 kW by which the furnace temperature was deemed to be around 1500°C. This took about 4 hours to reach from the start of preheating. As the feeding of the material progressed to between 100-120 kg/h there was an accumulation of molten material in the furnace, the majority of it being slag. This slag had to be removed periodically from the furnace to allow for more material to be added via a process called 'tapping'. In each trial there were two 'overflow taps' to remove the accumulated slag and one 'main tap' to remove the slag and the metal from the furnace.

Therefore every trial had the following stages:

- Initial heating stage;
- Initiation of feeding;
- Soaking period;
- Overflow tap 1;
- Re-initiation of feeding;
- Soaking period;
- Overflow tap 2;
- Re-initiation of feeding;
- Soaking period;
- Main tap.

The 'soaking' period before a tapping is a period where the feeding of the material into the furnace is stopped but the power input is still maintained, this allows the for the completion of the reduction of the iron oxide in the melt and the settling of the metal phase so that it is not removed from the furnace during the overflow tap. The soaking time before the tapping of the furnace was an hour.

Furnace tapping is performed by using an oxygen lance which breaks through the refractory plug in the tap hole allowing for the molten material to flow out. In the twin spout furnace, during the overflow taps the slag is removed from the top spout (which above the upper limit of the metal) and the bottom spout is tapped during the main tap to remove both the metal and the slag.

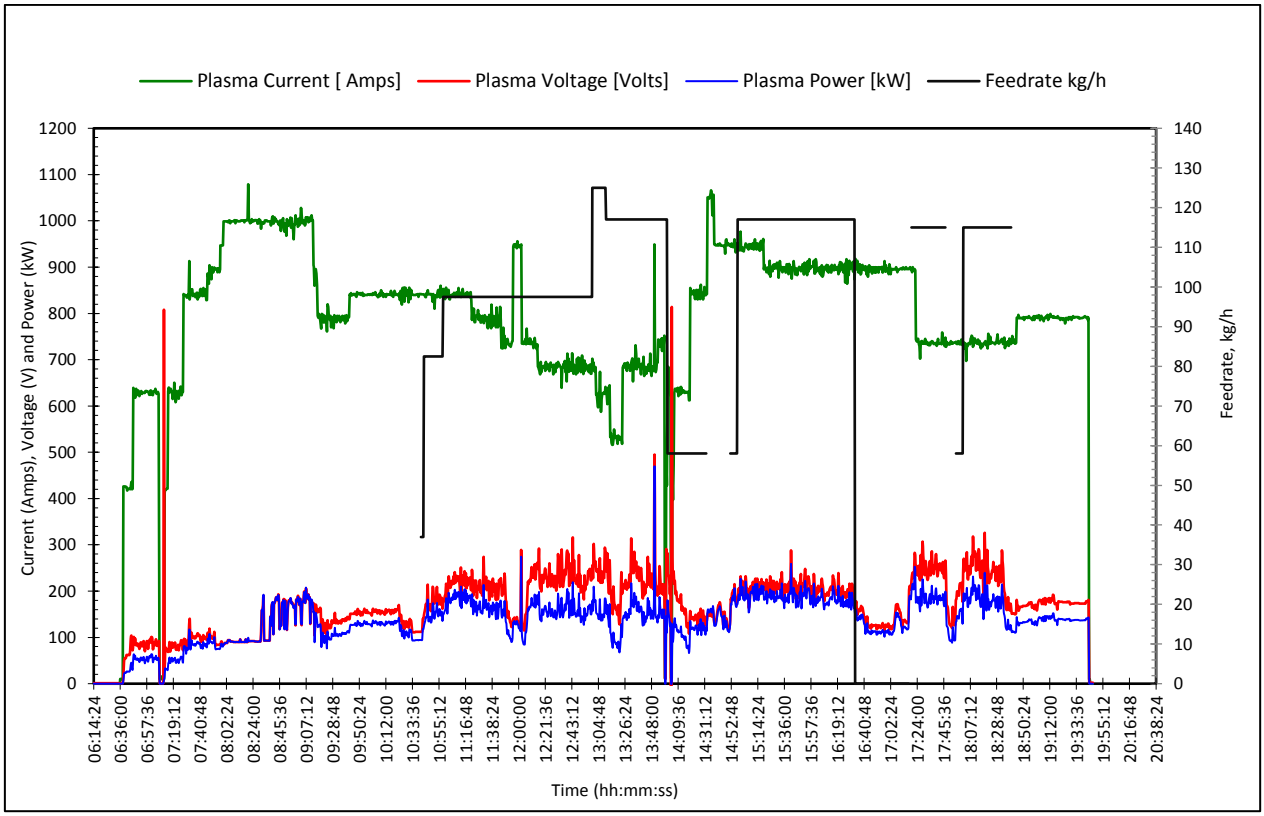

Figure 4-19: Example of the SCADA data obtained from trial 2 (4/12/2013).

Figure 4-19 is an example of the SCADA data which was obtained from the trails. This figure shows the plasma characteristics represented by the plasma current, voltage and power. The feedrate is also given and the time feeding started is seen at around 10:40. The stoppage in the feeding seen at just after 14:00 and 16:30 shows the stoppages for the soaking periods before an overflow tap. This corresponds with a drop in the plasma power just to maintain the heat in the furnace as additional power is not required for melting.

The SCADA data can also record the furnace temperatures. Figure 4-20 shows the furnace temperatures recorded from a mid-section thermocouple. Although the thermocouple gives a temperature colder than the actual furnace temperature due to its positioning, it does give a good insight in the energy input into the furnace and allows for the comparison between the

temperatures of each run. It can be see that generally, the furnace temperatures were similar for each run although trial 3 was colder. This is coupled with the lower energy input in this trial compared to the other trials (Table 4-14). This lower energy input did not result in any significant differences in the recovery of Pt or Re in the process.

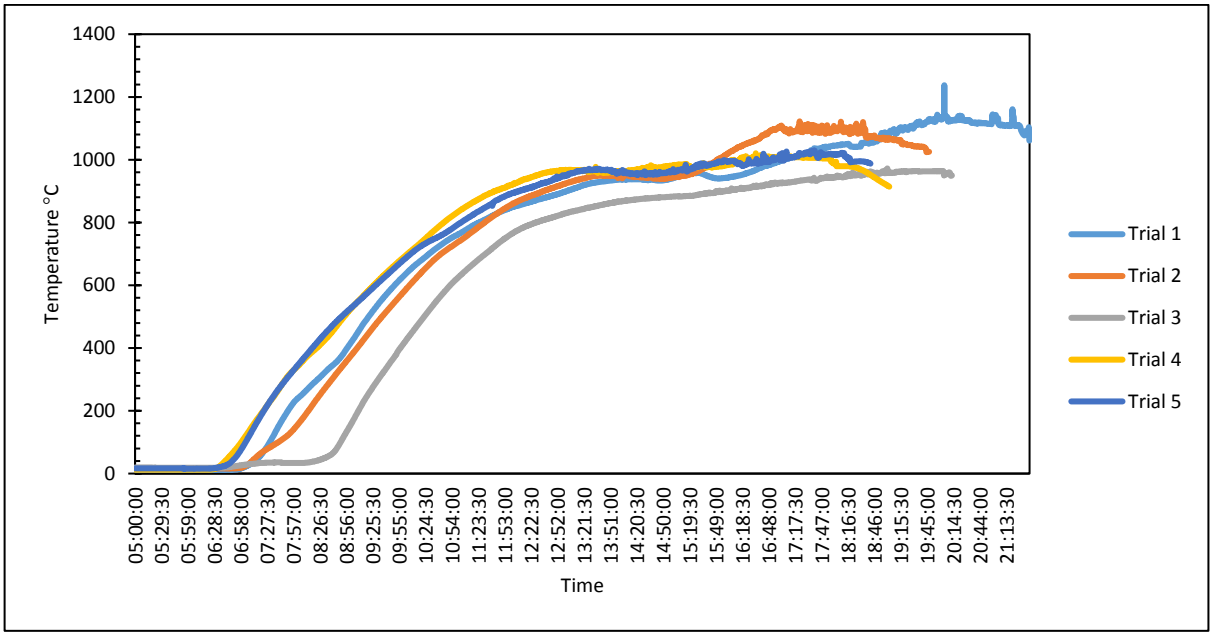

Figure 4-20: Furnace temperatures recorded with the SCADA system.

Table 4-12 shows the mass of material fed over the five pilot plant trails. A total of just over one tonne of catalysts was fed and a total of almost 2.8 tonnes of blended material. Each trail lasted approximately 10 hours during which around 3 hours was required for the heating of the furnace. This is not representative of a commercial plasma process which would maintain its operation over a 24-hour period running for several days at a time whereas in these trials each was conducted on a batch basis. The materials produced during the trials were collected and weighed to perform a mass balance across the process. The materials where analysed for chemical composition and Pt and Re content to understand the partitioning of the

components through the process and to validate the process model. The data and the partitioning of the elements was then able to be used in the design and operational costs of a commercial scale plant required for this application. Summaries of the energy input and the mass of material produced during the trails is shown in Table 4-13 and Table 4-14.

Table 4-12: Summary of the mass of material fed during the trials.

Mass Fed (Kg)	Trial 1	Trial 2	Trial 3	Trial 4	Trial 5	Total
Catalyst Fed	200	214	215	188	184	1001
Total Blend Fed	572	595	601	523	504	2795

Table 4-13: Summary of the operational data for the trials.

Trial	Feed-rate (kg/h)	Total trial time (hh:mm)	Feeding time (hh:mm)	Average gross power (kW)	Average net power (kW)	Net Energy requirement (kWh/t blend)	Net Energy requirement (kWh/t catalyst)
1	112	9:50	5:21	179	85	795	2274
2	103	10:15	5:45	176	89	859	2390
3	113	9:54	5:20	154	75	666	1858
4	117	9:10	4:30	184	99	842	2347
5	108	9:15	4:40	171	89	820	2246

Table 4-14: Summary of the mass of material produced during the trials.

Trial	Alloy (kg)	Overflow slag 1 (kg)	Overflow slag 2 (kg)	Main tap slag (kg)	Off-gas residue (particulate) (kg)
1	0	138	140	226	16
2	26	181	162	177	8
3	38	160	154	197	7
4	16	123	135	214	5
5	27	142	163	157	7
Recovered from Furnace	50[2]	-	-	-	-
Total	157	743	753	971	43

The average net energy requirement for the trials (total plasma power minus the furnace losses) was 796 kWh/t blend was similar to the energy requirement predicted by the model 769 kWh/t blend. Trial 3 was run at a lower temperature because of an issue with the high temperature of the material removed from the furnace during trial 2 which burnt a hole through a ladle. However, there did not seem to be any detrimental effects on the recovery of Pt or Re because of this.

There amount of metal recovered from each trial was variable and there was no metal recovered from the first trial. However, this was due to the furnace design as the volume of metal which was produced was not sufficient to reach the tap hole of the furnace. The metal from trial 1 remained at the base of the furnace during the trials and was removed manually

[2] This material was recovered from the furnace after the trial. Due to the configuration of the furnace taphole not all the metal can be recovered from the furnace during tapping and can only be recovered manually. In these trials a 50 kg heal was left in the furnace crucible and was only able to be recovered manually after the trials were completed. The majority of this metal was produced during trial 1 as the volume of metal produced in this trial was not sufficient to be removed during tapping. Although the majority of this metal was produced during trial 1, the inevitable mixing of the metals produced in all trials means that this recovered metal has been treated separately and not wholly assigned to trial 1.

afterwards, a photograph of this alloy can be seen in Figure 4-21. This does mean that the analysis of the metal from each trial was probably a mixture from the metal produced from all the previous trials.

Figure 4-21: A photograph showing the alloy in produced during trial 1 and retained in the furnace.

The metal retained in the furnace was manually removed and weighed 49.6 kg. A photograph of the alloy disc is shown in Figure 4-22. Although a large volume of it is from trial 1, it is a mixture of the alloy produced in all five trials and so cannot be attributed wholly to trail 1.

The metal recovered from the furnace accounts for 30% of the metal produced during the process. The theoretical mass of alloy which was to be produced was 165 kg and the actual metal recovered from the trials was 157 kg which represents 95%. The metal accountability can be seen in Figure 4-23. There are several possible reasons for the lower than anticipated metal production in this process which include:

- Incomplete reduction of iron oxide to iron.
- Metal trapped in the slag in the form of metal prills.
- Metal infiltration into the refractory.

Metallic prills are small spherical-like particles, typically 2 to 5 mm in diameter, which have not settled through the slag by the time the melt is tapped. Most of the metallic prills can be separated from the slag using magnets, but the efficiency of their separation is increased when the slag is crushed which did not happen during these trials. Therefore, some prills may have remained in the slag.

The composition of the slag recovered from the furnace has an iron oxide content of up to 3 wt% which does indicate the incomplete reduction of iron oxide. The green colour of the slag also indicated the presence of iron oxide as this is a typical colour of glasses containing Fe^{2+}. The incomplete reduction of iron oxide may be caused by an insufficient reaction time, which may be improved by increasing the soaking period or the reaction of carbon with other species in the melt.

Figure 4-22: Alloy disc of the metal retained in the furnace and manually removed after the trials.

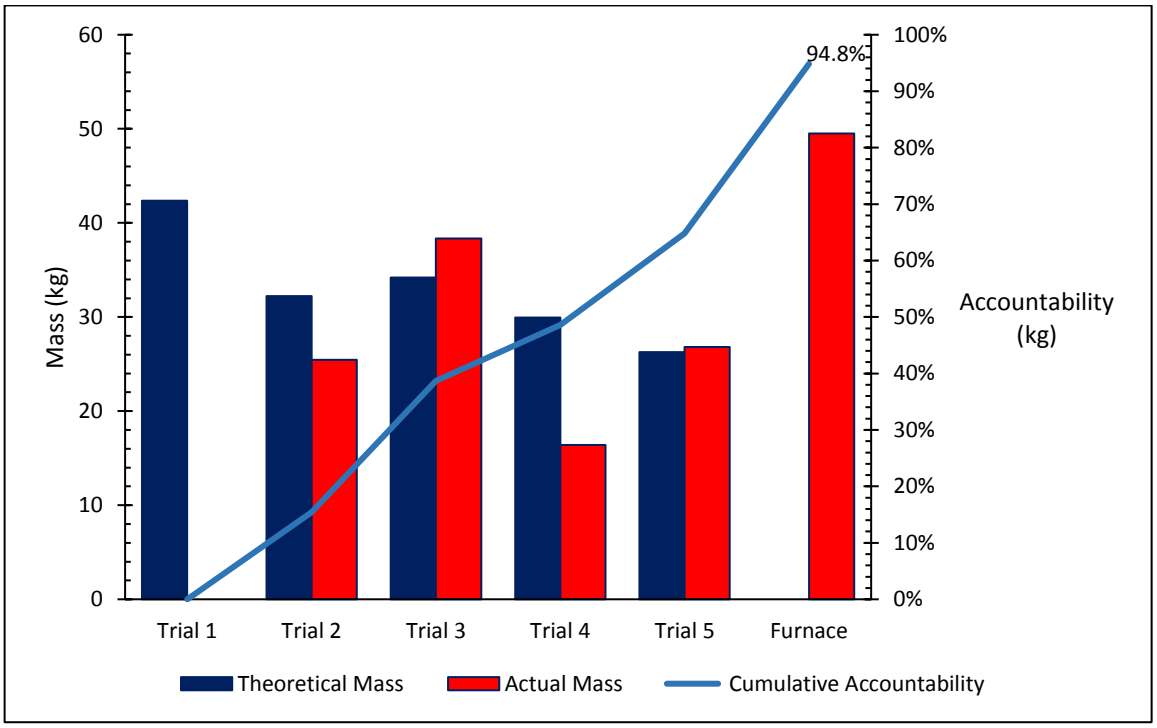

Figure 4-23: Metal mass accountability across the five trials.

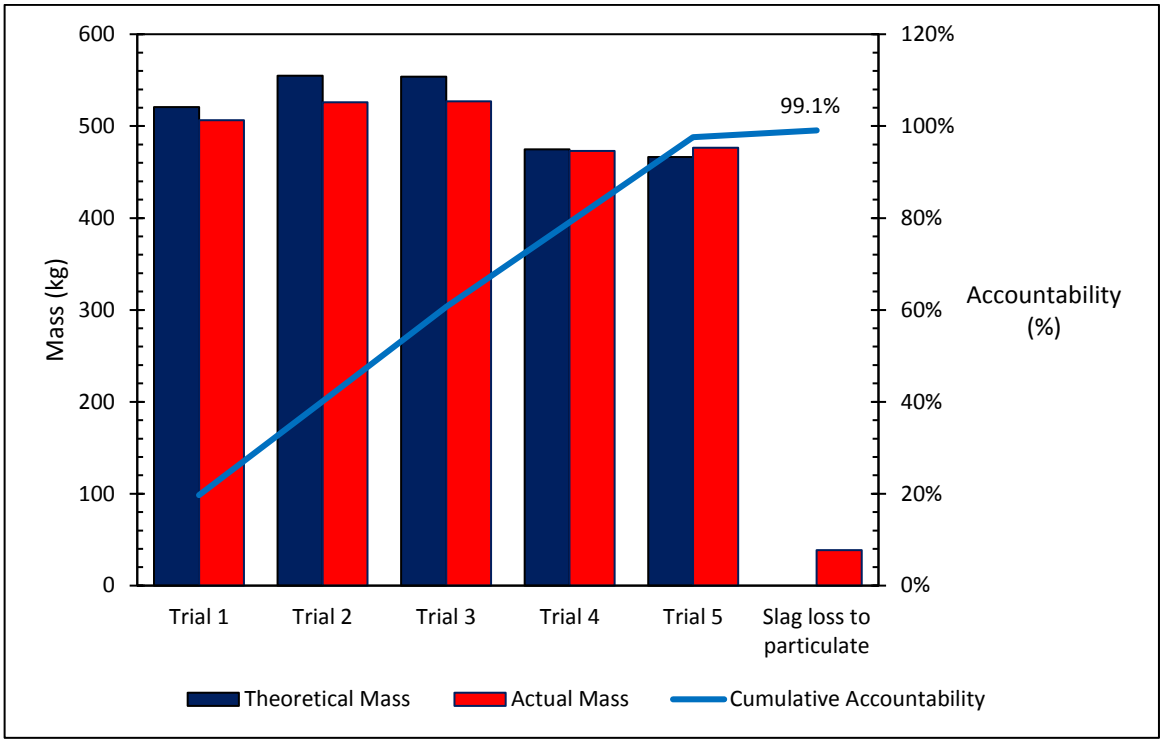

Figure 4-24: Slag mass accountability across the five trials.

The slag accountability in each five trials was high and the cumulative accountability of the mass of slag generated was 99.1%. The mass of slag collected from the overflow and main taps was 2500 kg which accounts for 97.6% of the theoretical mass. It was assumed that some of slag makers would have been lost to the off-gas and there is an assumed 'slag generation rate' of the feed material of 0.91 which means that 91% of the feed material will form the slag and the rest forming off-gas particulate. A total of 43 kg of particulate was collected over the trials and it is then estimated that 38.6 kg of this was from slag making components (raw material and fluxes) lost to the particulate as 'carry over'. The remaining components of the particulate would have been condensed volatile components from the furnace.

A table of unusual events is shown in Table 4-15. These unusual events may have had an impact on the Pt and Re recovery rates. For example, the lower temperatures recorded during

trial 3 were caused by a lower power input designed to avoid an incident seen in trial 2. This lower temperature input may have caused the lower Pt recovery during this trial due to an increased slag viscosity which also could be why a significant amount of metal prills were found entrained in the slag.

Table 4-15: A table showing unusual events during the trials.

Trial	Unusual Events
1	No unusual events during operation, but the metal could not be removed from the furnace.
2	The molten material from the main tap broke through the ladle due to its temperature and fell onto the floor.
3	Reduced energy input to the process due to the wish to avoid a similar incident to trial 2. Metal prills were found in the slag and a fused slag layer on the furnace walls indicated insufficient power input.
4	No unusual occurrences during the trial.
5	No unusual occurrences during the trial but metal prills found in the slag.

4.5. Platinum and Rhenium Partitioning.

The total analysis of platinum and rhenium in the output streams is shown in Table 4-16 and Table 4-17. Although both platinum and rhenium could be found in all products of the process, the majority of both metals partitioned to the collector metal. However, the nature of the loss of platinum and rhenium to other products in the process was different. The platinum which was not recovered to the collector metal was more likely to remain in the slag whereas the rhenium which was not present in the collector metal was more likely to be found in the off-gas particulate.

Table 4-16: Pt concentration in products.

Trial	Alloy (ppm)	Overflow slag 1 (ppm)	Overflow slag 2 (ppm)	Main tap slag (ppm)	Particulate (ppm)
1	-	13.7	4.4	10.1	380
2	16500	28.1	46.2	17.8	389
3	19600	121.7	64.6	50.5	450
4	21600	194.7	57.8	38.9	590
5	22300	64.4	63.9	27.3	400
Recovered from furnace	22300	-	-	-	-

Table 4-17: Rhenium concentration in products.

Trial	Alloy (ppm)	Overflow slag 1 (ppm)	Overflow slag 2 (ppm)	Main tap slag (ppm)	Particulate (ppm)
1	-	3.3	6.6	6.3	1090
2	9220	17.9	18.6	10.9	1017
3	11500	18.2	12.7	16.3	1690
4	12200	27.2	8.7	11.3	2040
5	12800	37.3	16.5	14.7	1950
Recovered from furnace	13200	-	-	-	-

The calculation of the recovery efficiencies of the metals can be approached on a mass balance basis and calculated either using a slag based recovery (SBR) equation (Equation 4-6) or a metal based recovery equation (MBR) (Equation 4-7). The difference between the two approaches lie in the SBR equation analyses the slag and particulate materials for the target metals and assumes the rest would be found in the metal. The MBR approach analyses the metal for the concentration of the target metals and uses these results directly for the mass balance.

$$SBR = 100 - \frac{(m_s \times C_{Ts}) + (m_P \times C_{Tp})}{m_C \times C_{TC}} \times 100$$ Equation 4-6.

$$MBR = \frac{m_{AL} \times C_{TAL}}{m_C \times C_{TC}} \times 100$$ Equation 4-7.

Where m_s, m_p, m_c and m_{AL} is the mass of the slag, particulate, catalyst and alloy produced or used in the process and C_T is the concentration of the target metal in the material.

Table 4-18: Platinum partitioning during the trials.

Trial	Overflow slag (%)	Main tap slag (%)	Particulate (%)	Alloy (SBR) (%)	Alloy (MBR) (%)
1	0.34	0.31	0.41	98.9	-
2	1.6	0.40	0.39	98	54
3	3.7	1.3	0.09	94.9	96
4	4.6	1.2	0.41	94	51.9
5	2.9	0.63	0.31	96	89.2
Overall	2	1	0.3	97	88.7

Table 4-19: Rhenium partitioning during the trials.

Trial	Overflow slag (%)	Main tap slag (%)	Particulate (%)	Alloy (SBR) (%)	Alloy (MBR) (%)
1	0.23	0.24	2.22	97.3	-
2	0.1	0.31	4.58	94	52.2
3	0.9	0.5	1.32	97.4	97.4
4	0.77	0.41	1.06	98	50.7
5	1.47	0.41	3.27	95	88.5
Overall	1	0.4	2	97	89

Table 4-18 and

Table 4-19 show the partitioning of platinum and rhenium throughout the products in the process and the recovery efficiencies using the SBR and MBR equations. The discrepancies lie in the calculation of the partitioning of the metals to the collector metal. The limitation of using the metal based recovery equation arises from the method of sampling the metal and obtaining a representative sample. The distribution of the platinum and rhenium is not uniform across the collector metal; this can be seen in microscope analysis presented later in this chapter. The sample from the metal was taken by drilling various areas of the collector metal disc and obtaining a swarf which was blended and sampled. By drilling at various points, it would be more likely to drill over areas which contains the target metals, but it may also be possible to miss them. This is shown in by the variation in the SBR and MBR in trail 2 (98% and 54% respectively for Pt and 94% and 52% for Re) and the similarity between the two results in trial 3 (95% and 96% respectively for Pt and 97% and 97% for Re). It is assumed that the concentration of the target metals across the other products of the process are more uniform and the nature of these products makes sampling easier. The particulate is a dust which enables good mixing of the material and easier to take representative samples and samples of the slag are taken from the molten slag as it flows from the furnace during tapping. Three to four 'spoon samples' of the molten slag are taken each containing between 300-500 g of slag which can then be ground and samples taken. Therefore, there is more confidence that the samples taken from the slag and the particulate are more representative allowing for confidence in the SBR equation.

Despite the discrepancies between the two methods of calculating the recovery efficiencies, both show that the majority of the platinum and rhenium both partition to the metal alloy and

so it can be deemed that the trials for the recovery of the two metals via a collector metal were successful and the behaviour of rhenium was able to be controlled.

The overall recovery efficiencies, using the SBR method, for platinum and rhenium was both 97% which are very high and could potentially be improved on a commercial basis as the process was not able to achieve a steady state operation for prolonged periods of time on a batch trial basis which would aid settling and recovery. A graphical view of the overall partitioning of platinum and rhenium can be seen in Figure 4-25 and Figure 4-26 where the differences in the behaviour of platinum and rhenium can be seen.

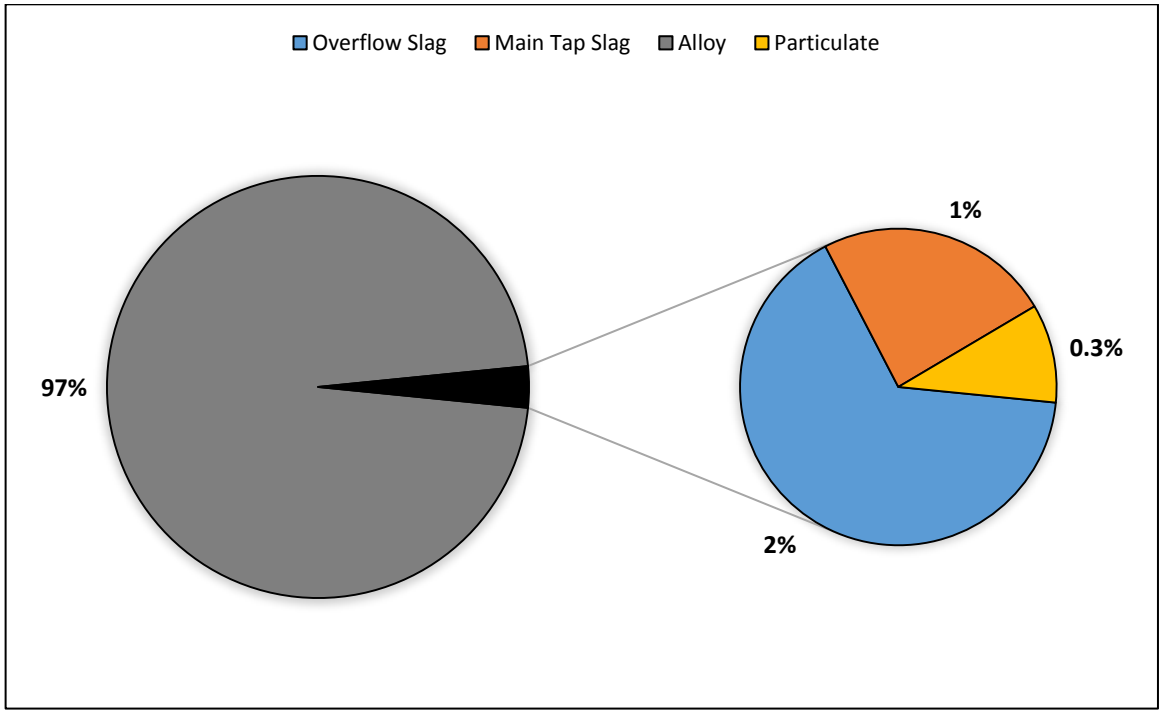

Figure 4-25: Overall partitioning of platinum during the trials 1 to 5.

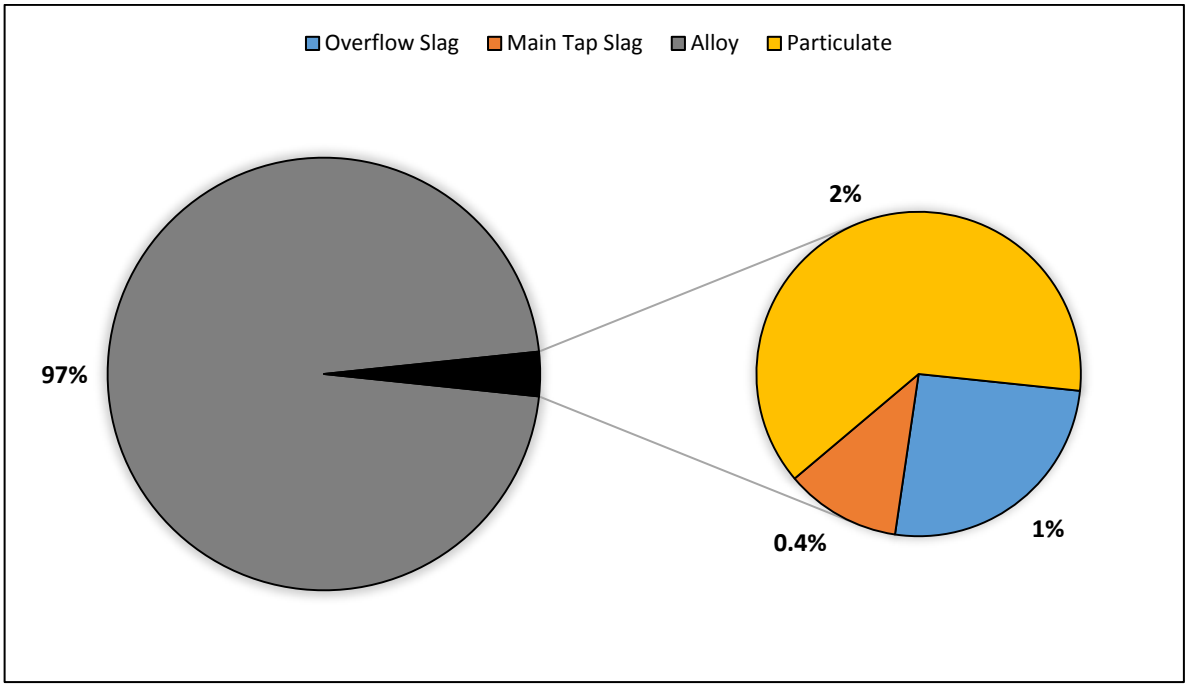

Figure 4-26: Overall rhenium partitioning during the trials 1 to 5.

The off-gas analysis is shown in Table 4-20. The results show that practically no rhenium was detected in the vapour phase during the sampling at point B, which is the emissions stack. There is a small amount of rhenium detected at sample point A (19.24 mg/Nm^3) which is higher than the rhenium recorded at sample point B (0.0143 mg/Nm^3) (

Table 4-21). This indicates that some rhenium would have been volatilised during the process which is supported by the higher concentration of rhenium than platinum in the off-gas particulate. The rhenium that is volatilised is captured in the off-gas compound and it may be possible that this dust could be reprocessed to increase rhenium recovery as the results of the modelling in Table 4-5 show that oxidation state of rhenium should not affect its recovery. However, the fine particle size of the dust may mean it would need to be pelletized before it is reprocessed. Much of this dust would have been 'carry over' from the feed where the finest particles are essentially sucked out of the furnace before they hit the melt pool and pelletizing

the material would reduce this from happening. Also an accumulation of volatile components may occur with excessive reprocessing of the dust. This material would contain a higher concentration of volatile components such as chlorine which may be detrimental to the process. Chlorine forms volatile complexes with both platinum and rhenium and so may have a negative effect on the recovery efficiency the target metals. Therefore, although reprocessing is possible care must be taken to reduce any detrimental effects and so blending small amounts of the dust with the raw material may be a method to process the material successfully.

Table 4-20: Off gas analysis recorded at sample point B.

Pollutant	**Mass Emission Rate ($g\ s^{-1}$)**	**Concentration at: 273K, 101.3 kPa, dry gas ($mg(N)m^{-3}$)**	**Estimate of Error 2σ (95%) %[3]**	**Release Limit ($mg(N)m^{-3}$) (WID - ELV)**
Total particulate matter	0.0004	8.87	±50	10
Rhenium	6.31E-07	0.01	±50	-
VOC (as carbon)	0.0001	3.39	±10	10
NOx (as NO_2)	0.0015	32.9	±10	400
Carbon Monoxide	0.0063	142.7	±10	50

Table 4-21: Rhenium concentration recorded at sample point A and sample point B.

Position of rhenium measurement	**Concentration (mg/Nm^3)**
Position A	19.24
Position B	0.0143

[3] These measurements were performed by a third party analytical company. The large error was stated by the company on their analysis certificate.

Despite the recorded rhenium in the off-gas, most the rhenium is recovered via the collector metal. Only a small percentage of rhenium is volatilised in the process and because of the difficulties in totally removing oxygen, it may be inevitable that some rhenium would be oxidised but nevertheless, as most of the rhenium reported to the metallic phase the initial modelling is still justified.

4.6. Analysis of the Products.

4.6.1. Collector Metal Analysis.

XRF was used to determine the oxide composition for the slag and particulate products and the bulk metal composition for the alloy. XRF analysis of the metal showed similar Pt and Re results to the ICP-OES analysis of the metal (Table 4-22), although the ICP-OES analysis was slightly higher.

Table 4-23 shows the collector metal to be a multicomponent alloy with the dominant component being iron which makes up approximately 90% of the alloy. Platinum and rhenium have a combined concentration of between 2 to 3 wt% and the other components of the alloy are those also reduced by the carbon during the process for example silicon and aluminium. The high calcium content seen in trial 5 may have been the presence of slag inclusions on the metal surface rather than as a component of the alloy due to the difficulty in being able to reduce calcium oxide.

Table 4-22: Comparison between XRF and ICP results for platinum and rhenium concentrations from the alloy obtained in trial 2.

Metal	XRF (wt%)	ICP (wt%)
Platinum	1.23	1.72
Rhenium	0.77	0.92

Table 4-23: Bulk composition of the collector metal alloy generated in the plasma process via XRF.

Element	Trial 2	Trail 3	Trial 4	Trail 5	Alloy from furnace
Fe	90.1	92.1	91	87.9	91.3
Pt	1.2	1.5	1.8	1.5	1.9
Re	0.8	0.8	1.0	0.9	1.2
Si	1.9	0.7	0.9	0.5	0.6
Cl	0.1	0.3	0.3	0.2	0.3
Ca	1.6	0.2	0.6	4.2	1.4
Al	0.9	0	0.9	1.2	0.4
Cu	0.1	0.2	0.1	0.1	0.2
Na	1.2	1.6	1.7	1.3	1.2
Loss on drying	0.1	0.6	0.2	0.2	0.5
Loss on ignition	0	0	0	0	0
Total	98.1	97.8	98.3	98	98.9

The XRF analysis cannot determine the carbon content of the metal due to carbon being a light element and so this is one reason for the total composition not reaching 100%. Carbon is present in the alloy as can be seen from XRD and microscope images but there was no loss of mass during loss on ignition which can indicate carbon content. The loss in mass would indicate free carbon and not chemically bound carbon i.e. in iron carbide. However, microscope images do reveal that the metal does have carbon phases including graphite and also iron carbide. An average of EDX analysis over various points of metal showed the carbon

content of the alloy to be 5.3 wt%, but with the limitations of the accuracy of the EDX analysis means that the carbon content is probably between 3-7 wt%. However, as mentioned above, the carbon content of the alloy is engineered to be in this region.

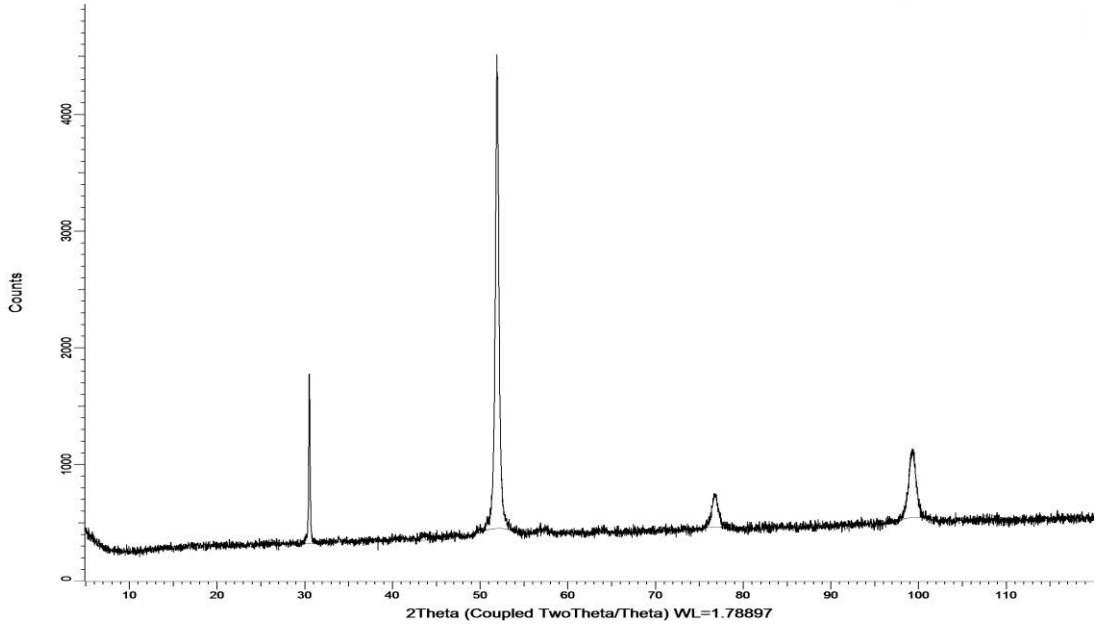

Figure 4-27: XRD spectrum of collector metal alloy removed from the furnace.

The XRD pattern shown in Figure 4-27 shows that the alloy is a multiphase system which is composed of an iron phase and a graphite phase. The peak at 30° 2θ is characteristic of graphite and the peaks at 52°, 77° and 100° 2θ are representative of iron.

Figure 4-28 shows the XRD spectra for all the alloys which were recovered over the trials. The spectra are consistent for all the metals although there are small peaks at approximately 34° 2θ for the alloys from trials 3 and 5 and this peak indicates a calcite phase. This is likely to be slag inclusions on the metal and would account for the high calcium content in the composition of the alloy from trial 5 (4.2 wt%) although this is not the case for trial 3.

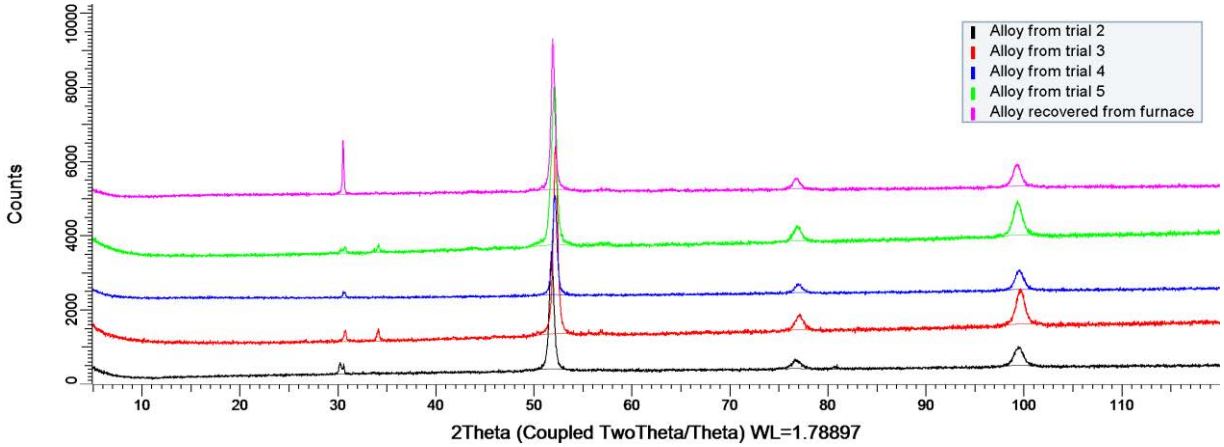

Figure 4-28: XRD spectra for the alloys recovered from all the trials.

SEM images show an interesting picture of the microstructure of the collector metal. The backscattered electron image in Figure 4-29 shows the graphite phase which are the black flakes surrounded by the brighter metal phase. This graphite phase resembles kish graphite which is found in cast iron which has a high carbon content (Walker & Imperial, 1957). These graphite flakes are confirmed by energy dispersive x-ray analysis of the collector metal in Figure 4-29 which show that these dark phases are carbon rich and combined with the XRD analysis can be thought to be graphite.

The metal phase which surrounds the graphite phase has a non-homogenous distribution of components in the material. The brighter regions in Figure 4-30 show the presence of dendrites in the microstructure of the metal. Brighter areas in back scattered electron (BSE) images are characteristic of the presence of heavier elements and it is in these brighter phases where the platinum and rhenium can be found and the darker grey areas are depleted of these heavier species. This is confirmed in Figure 4-31 and Figure 4-32 which show microprobe elemental analysis of the bright phases being rich in the platinum and rhenium whereas the

grey phases are depleted of these metals. This emphasises the difficulties in sampling the collector metal to obtain a representative sample of the alloy for the target metal analysis.

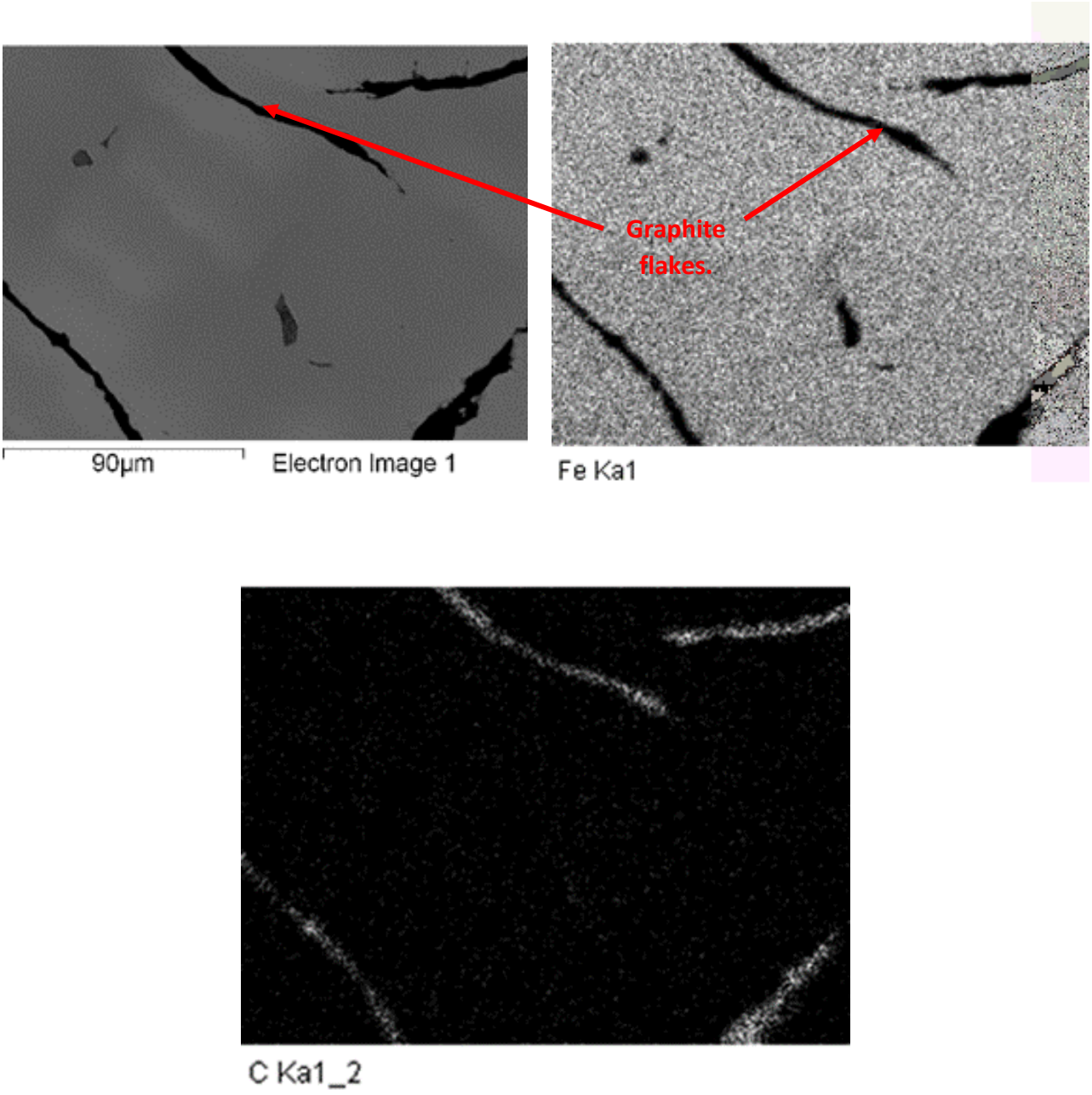

Figure 4-29: EDX analysis showing the graphite phases in the collector metal. These can be seen as the black veins surrounded by an iron matrix. The bottom image confirms these veins are carbon.

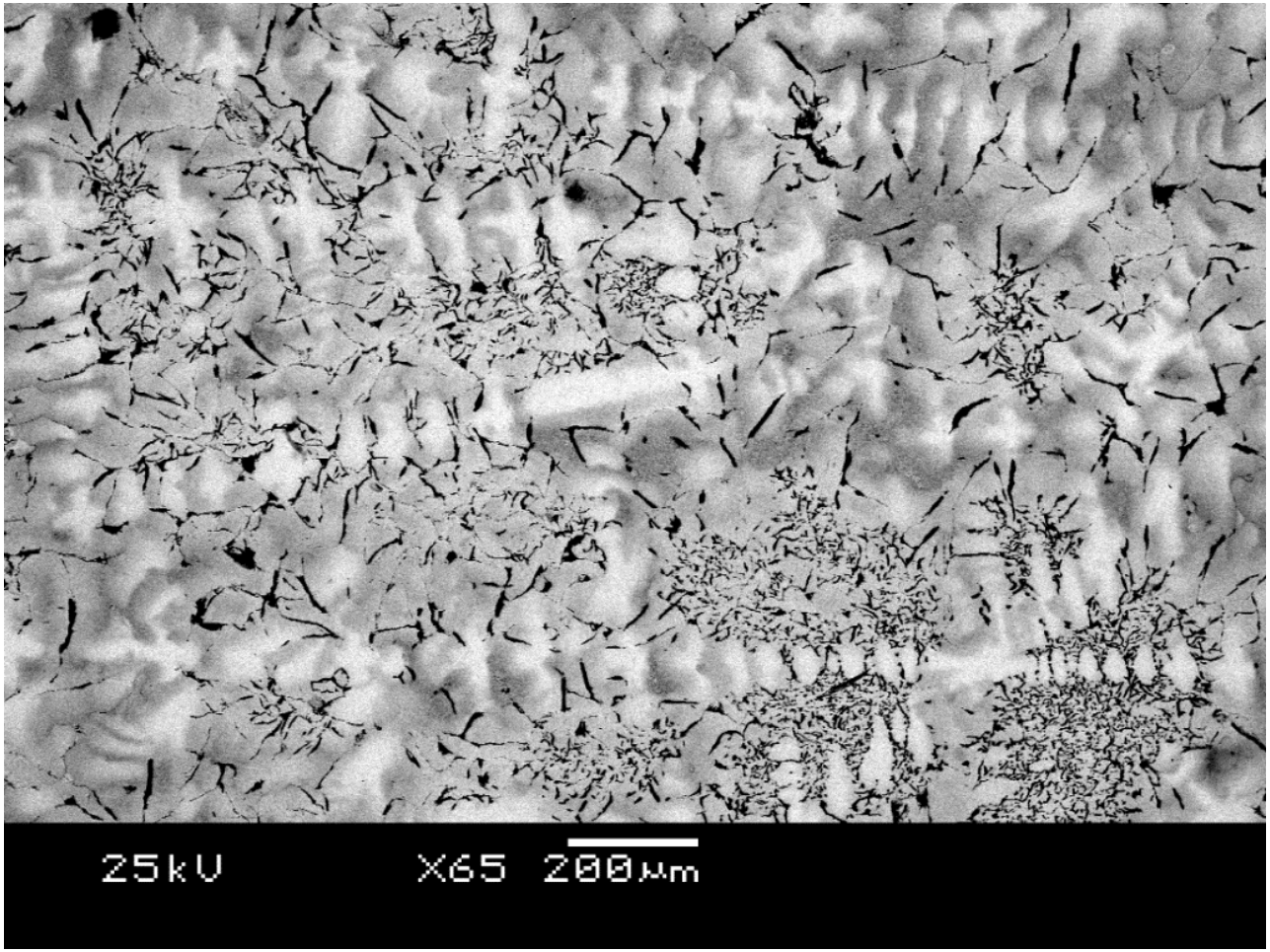

Figure 4-30: Back scattered electron image of the collector metal.

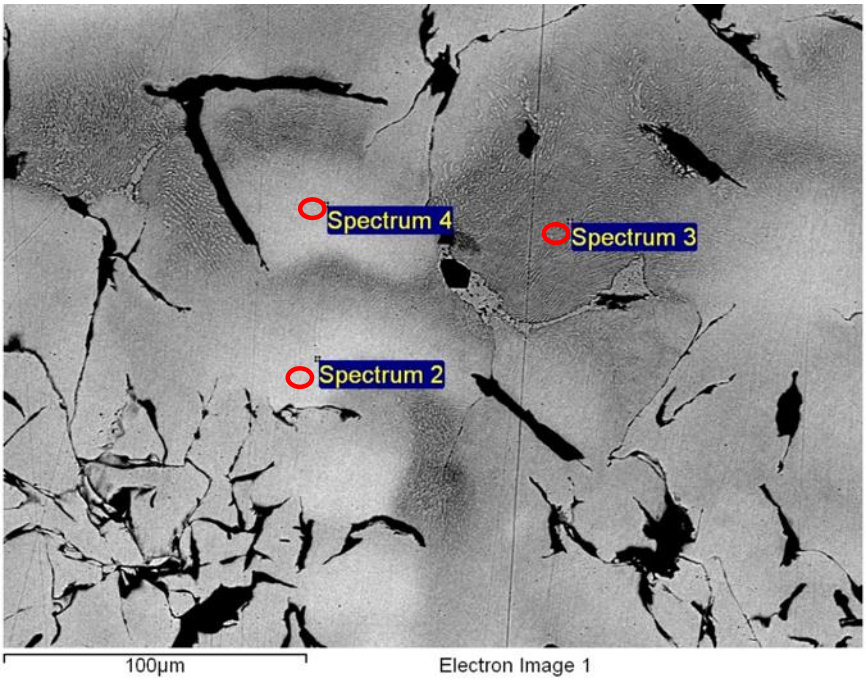

Element	Sum spectrum (wt%)	Spectrum 2 (wt%)	Spectrum 3 (wt%)	Spectrum 4 (wt%)
C K	8	-	6.9	3.5
Si K	2.3	2.8	2	2.6
Fe K	87.3	93	90.7	90.6
Re L	0.96	1.32	-	1.45
Pt L	1.42	3.68	-	1.87
Totals	100	100	100	100

Figure 4-31: EDX analysis for various points of the collector metal alloy.

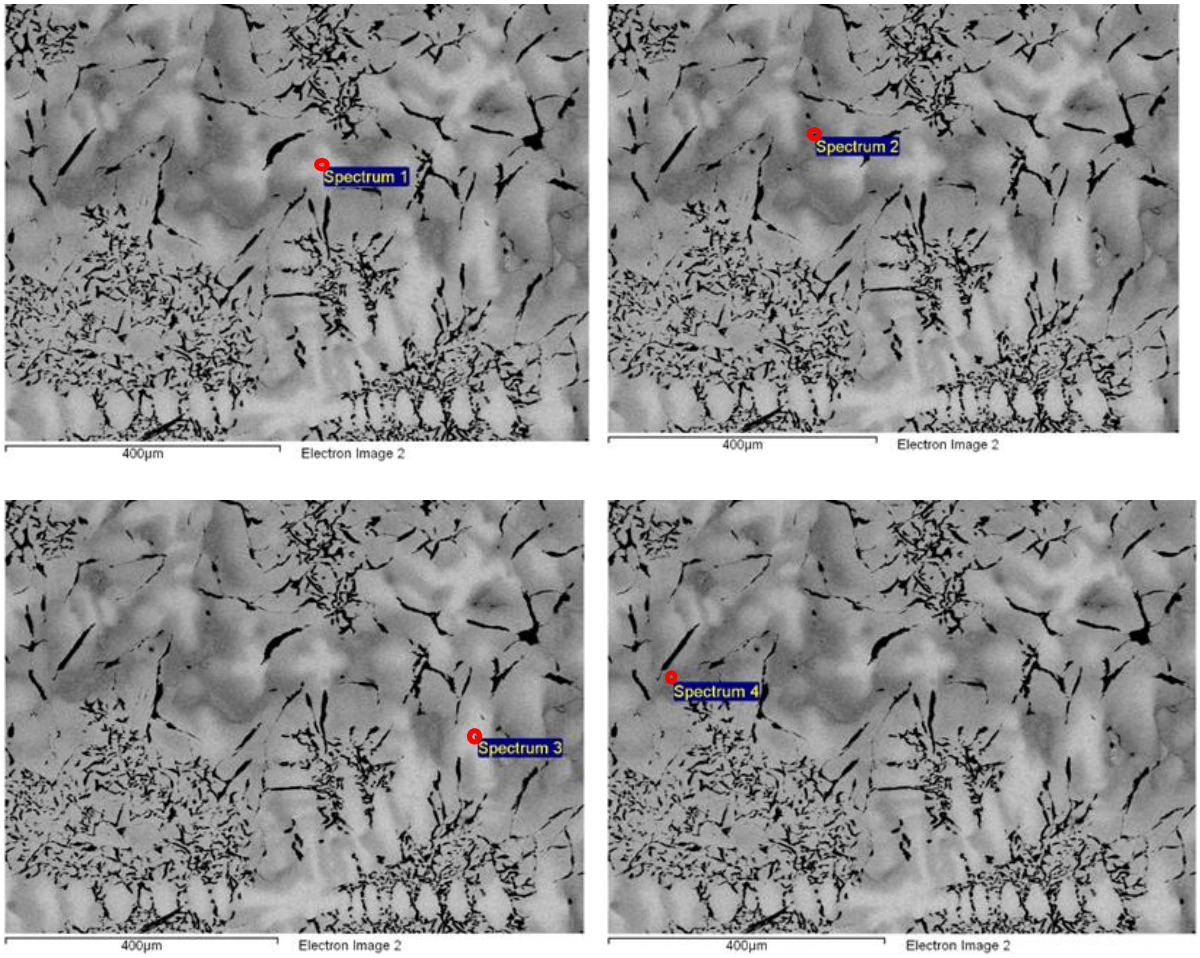

Element	Spectrum 1 (wt%)	Spectrum 2 (wt%)	Spectrum 3 (wt%)	Spectrum 4 (wt%)
C K	2.6	7.41	2.5	5.9
Si K	2.6	1.2	2.7	2.1
Fe K	89.6	87.5	89.4	91.3
Re L	1.26	-	1.4	-
Pt L	3.92	-	4.1	-
P	-	3.2	-	0.23
V	-	0.4	-	0.23
Cr	-	0.4	-	0.21
Totals	100	100	100	100

Figure 4-32: EDX analysis of the collector metal at alternative locations.

The dendritic nature of the bright phases in the alloy indicate that during cooling the alloy containing the platinum and rhenium begins to solidify first and then causes the lateral rejection of the lower melting point alloy phases to the grain boundaries which causes the formation on the inhomogeneous microstructure in the alloy.

The platinum and rhenium deficient phase of the alloy has a microstructure which is similar to that of pearlite (Figure 4-33). Perlite contains two phases, ferrite and cementite. Ferrite is α-Fe and cementite is Fe_3C and is usually characterised by alternating bands of cementite (darker phases) and ferrite (lighter phases). Fe_3C was predicted to form in the thermodynamic modelling and so this supports the evidence of the microstructure of the metal. The phase diagram (Figure 4-7) indicates that at the estimated carbon addition in the collector metal 5%, these phases would form and so gives further evidence for the formation of perlite in the alloy.

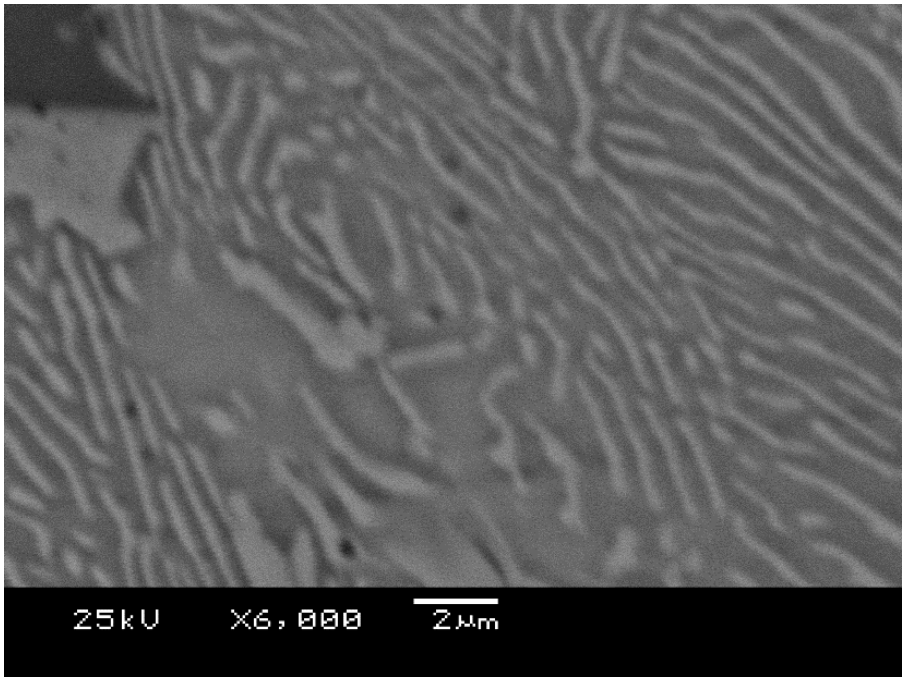

Figure 4-33: SEM image of pearlite-like structure of the Pt and Re deficient phase of the alloy.

Silicon's concentration in the collector metal can be up to 2 wt% and the distribution of this element throughout the alloy seems to be quite uniformly distributed. The other elements which can be present such as vanadium and aluminium are present only as inclusions in small and concentrated areas and so this indicates that they are not miscible with the iron alloy and so form singular inclusions in the alloy which can be seen in Figure 4-34.

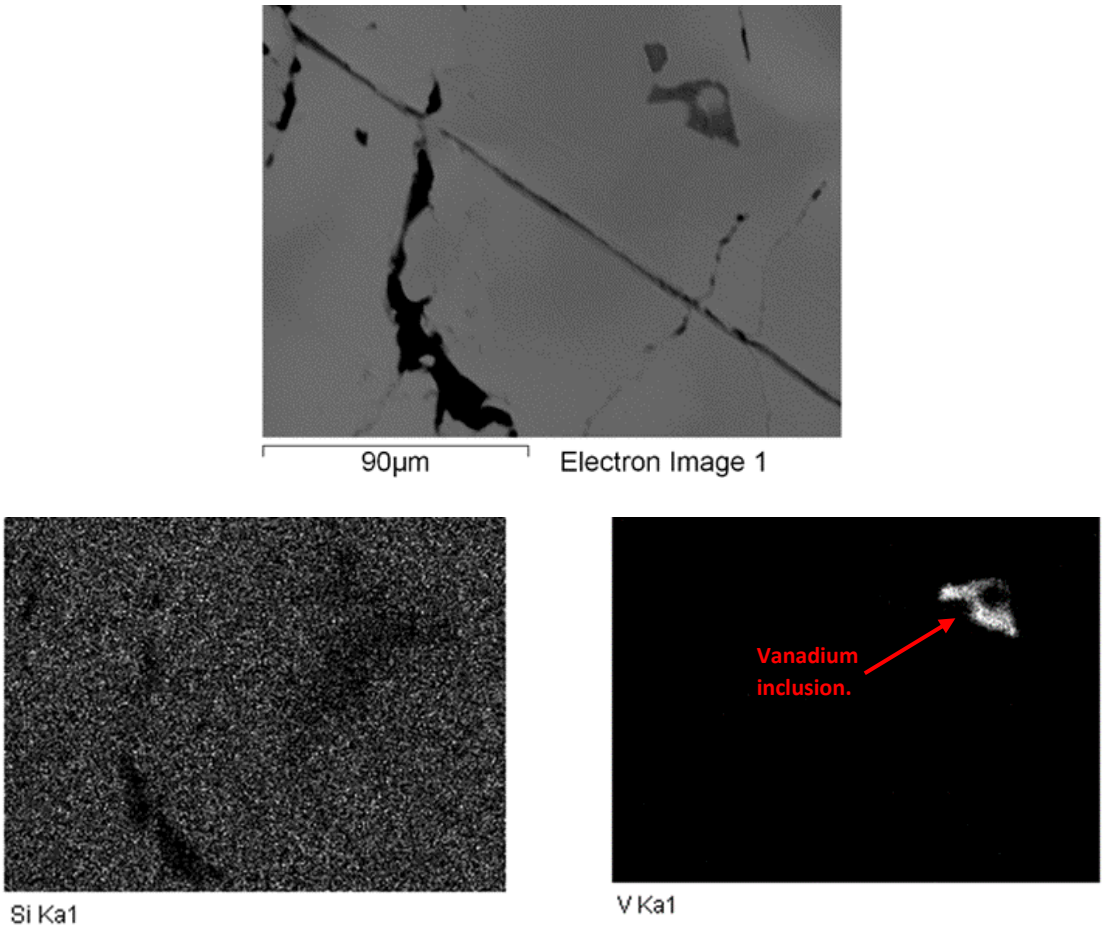

Figure 4-34: EDX analysis of minor components in the collector metal.

Slag Analysis.

Table 4-24: Trial 1 slag XRF analysis.

Component	OF1	OF2	MT
Al_2O_3	34	39	41
SiO_2	34	30	29
CaO	27	29	28
Fe_2O_3	3.0	0.7	1.0
Na_2O	0.6	1.3	1.0
Cl	0.1	0.0	0.2
TiO_2	0.1	0.2	0.2
Total	99.2	99.7	99.4

Table 4-25: Trial 2 slag XRF analysis.

Component	OF1	OF2	MT
Al_2O_3	39	37	42
SiO_2	30	30	28
CaO	28	28	29
Fe_2O_3	1.1	1	1.2
Na_2O	1.4	1.4	0
Cl	0.3	0.2	0
TiO_2	0.2	0	0.3
Total	99.1	98.2	99.5

Table 4-26: Trial 3 slag XRF analysis.

Component	OF1	OF2	MT
Al_2O_3	38	34	36
SiO_2	30	32	32
CaO	29	30	29
Fe_2O_3	1	2	1.6
Na_2O	1	1.8	0.91
Cl	0.25	0.29	0.2
TiO_2	0.13	0.18	0
Total	99.9	99.6	99.5

Table 4-27: Trial 4 slag XRF analysis.

Component	OF1	OF2	MT
Al_2O_3	40	38	39
SiO_2	26	27	27
CaO	31	32	32
Fe_2O_3	0.8	0.5	0.7
Na_2O	1	0.2	0.4
Cl	0.2	0.1	0.1
TiO_2	0.3	0.1	0.1
Total	99.3	97.9	99.3

Table 4-28: Trial 5 slag XRF analysis.

Component	OF1	OF2	MT
Al_2O_3	39	35	31
SiO_2	27	28	26
CaO	32	35	37
Fe_2O_3	1	1.4	2.8
Na_2O	0.5	0.2	0.5
Cl	0.1	0.1	0.1
TiO_2	0.1	0.1	0.1
Total	99.7	99.8	97.5

Table 4-24 to Table 4-28 show the XRF analysis of the slags collected from the trials. The tables show only the major components of the slags which are of quite simple compositions and predominately calcium, aluminium and silicon oxides. The slag has a residual iron oxide content which originates from iron oxide which was not fully reduced during the process. There does not seem to be any clear link to the iron oxide in the slag and the recovery rate of the target metals. The presence of trace metals in the slag is very low, the chlorine content is 0.1 wt% or less and there was almost no loss on drying or loss on ignition of the slag.

4.6.2. Particulate Analysis.

The particulate dusts were residues from the thermal oxidiser, quench column and the baghouse in the off-gas system. The residue collected from the baghouse accounted for most of the mass collected from the off-gas system and only a small amount of mass was collected from the other two units. The particulate dust is composed both of 'carry over', the fines from feed material which were sucked straight from the furnace and condensed components which were volatilised during the process. These volatile components include rhenium but also other metals such as zinc for example.

The XRF analysis of the particulates from the quench column, thermal oxidiser and the baghouse are shown in Table 4-29 to Table 4-31. Although CaO, SiO_2 and Al_2O_3 account for a high proportion of the composition there is also a high amount of condensed volatile compounds such as SO_3 and Cl.

Table 4-29: XRF analysis of the quench column residue.

Oxide (wt%)	Trial 1	Trial 3	Trial 4	Trial 5
CaO	15.2	21.4	19.7	27.4
SiO_2	14.8	17.8	15.9	15.6
Al_2O_3	6.5	12.7	7.7	16.4
SO_3	14.0	11.2	16.8	9.7
Fe_2O_3	5.7	10.3	4.9	5.6
CuO	6.4	3.2	5.4	2.8
Re	-	3.0	-	3.8
PbO	3.7	2.9	3.9	-
Cl	9.7	2.5	4.5	2.4
Na_2O	7.3	2.3	2.5	1.6
ZnO	-	1.9	3.1	1.3
K_2O	4.6	1.9	3.3	1.6
P_2O_5	0.9	0.7	1.2	0.8
SnO_2	1.1	0.6	1.0	0.8
Sb_2O_3	1.0	0.6	0.8	0.8
Pt	-	0.1	-	0.1
TiO_2	0.3	0.1	0.3	0.1
LOD	1.0	1.0	1.0	1.0
LOI	6.6	4.6	6.6	5.1

Table 4-30: XRF analysis of the thermal oxidiser residue.

Oxide (wt%)	Trial 1	Trial 2	Trial 3	Trial 4	Trial 5
CaO	19.2	31.8	28.3	26.7	29.7
SiO_2	7.8	20.1	24.0	24.5	24.1
Al_2O_3	10.8	17.0	19.6	21.1	20.2
Fe_2O_3	11.1	6.7	7.4	7.1	6.5
SO_3	9.2	4.7	4.6	4.4	4.3
Cl	12.5	4.7	2.3	2.5	2.4
Na_2O	4.6	2.0	1.6	1.2	1.0
Re	-	1.6	1.3	0.1	0.2
K_2O	5.2	1.5	1.3	1.0	1.0
ZnO	3.1	0.8	0.7	0.8	0.8
CuO	2.5	0.5	0.5	0.4	0.3
P_2O_5	1.3	0.2	0.3	-	-
PbO	0.9	0.2	0.2	0.1	0.1
Pt	-	0.2	0.1	0.2	0.2
CdO	-	-	0.1	0.2	0.2
LOD	0.8	0.7	0.4	0.4	0.6
LOI	7.9	6.3	6.5	8.8	7.7

Table 4-31: XRF analysis of the baghouse residue.

Oxides (wt%)	Trial 1	Trial 2	Trial 3	Trial 4	Trial 5
SiO_2	17.4	47.4	49.1	43.6	41.1
CaO	8.1	12.2	10.8	14.3	16.3
Al_2O_3	3.5	6.2	7.9	10.4	10.4
Fe_2O_3	8.6	9.2	8.6	9.7	8.1
SO_3	12.2	3.0	3.3	3.0	2.7
Cl	11.4	3.4	2.6	2.2	2.6
Na_2O	8.4	2.4	2.4	1.8	2.2
K_2O	6.0	3.1	2.7	2.6	2.1
ZnO	6.3	1.9	1.7	1.7	1.7
CuO	3.8	0.9	0.8	0.8	0.7
PbO	2.4	0.6	0.5	0.5	0.5
Re	-	-	0.02	0.2	0.4
CdO	-	-	0.2	0.2	0.3
P_2O_5	0.8	0.2	0.2	-	0.2
Br	2.0	0.2	0.2	0.2	0.2
TiO_2	-	-	-	-	0.1
LOD	0.6	0.7	0.7	0.7	0.8
LOI	5.5	7.0	7.3	7.0	8.8

XRD analysis of the particulate phases shows the residues contain condensed phases which have formed during the process either in the furnace or in the off-gas system itself. There is a distinct difference in the types of phases which are present in the residues from the separate off-gas units.

Complementary to XRF analysis the XRD analysis gives an indication of how the components are present in the residues. Chlorine is present in high quantities in the dust and it is shown by XRD data that it is present in halite (NaCl) at approximately 36° 2θ in the baghouse and in other mineral salts in the dusts. Interestingly, halite is present in the baghouse but not in the thermal oxidiser residue and this may be due to the temperature of the baghouse being lower than the thermal oxidiser meaning it is not until the baghouse where these phases condense.

The XRD patterns of the thermal oxidiser dust and the baghouse dust in Figure 4-35 show that the dusts are different and contain different condensed phases to each other.

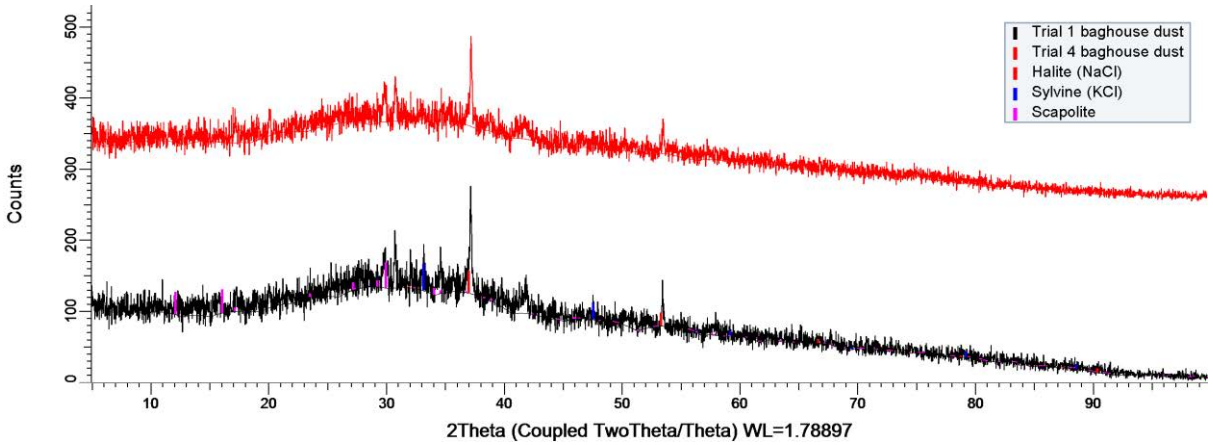

Figure 4-35: XRD patterns of the baghouse and thermal oxidiser residues.

The XRD patterns of the baghouse particulate shown in Figure 4-35 indicate that the material is composed of amorphous materials, shown by the noisy pattern and some crystalline phases indicated by the peaks which are present. The major peaks which are present in the residue are at 36° 2θ and 53° 2θ and these are characteristic peaks of sodium chloride (NaCl) or halite. This salt is produced from the removal of chlorine from the off-gas stream by the introduction of caustic soda (NaOH) in the quench column. The baghouse temperature is typically around 250°C which is a lower temperature than the upstream off-gas units (thermal oxidiser 900°C and quench column 450°C).

The thermal oxidiser residue and the quench column residue both, on average, contain more wt% of rhenium than the baghouse residue indicated by XRF analysis. The XRD patterns of the thermal oxidiser residue show the presence of rhenium containing phases. These phases are seen at the lower end of the pattern at around 13° 2θ and 21° 2θ. They have been formed when rhenium has reacted and formed compounds with other volatile elements in the process

such as bromine, potassium and some hydrocarbons. The phases which are indicated on the XRD patterns are $Br_9KRe_6S_5$ and $C_{12}N_6O_{12}Re_3$. Although these are rather complex compounds and may not be accurate due to the limitation of the peak fitting database, the data does indicate that rhenium will and does form compounds throughout the process. It is interesting to note that no rhenium oxides were found during the XRD analysis and this is interesting because it means that it is not only oxygen which may cause loss of rhenium recovery but also other volatile compounds such as bromine or chlorine. This may be problematic if the particulate residue is recycled into the process as it may introduce excess volatile elements such as the halogens which may react with rhenium. The formation of these rhenium compounds in the thermal oxidiser residue is consistent throughout the process as can be seen in Figure 4-36 and Figure 4-37.

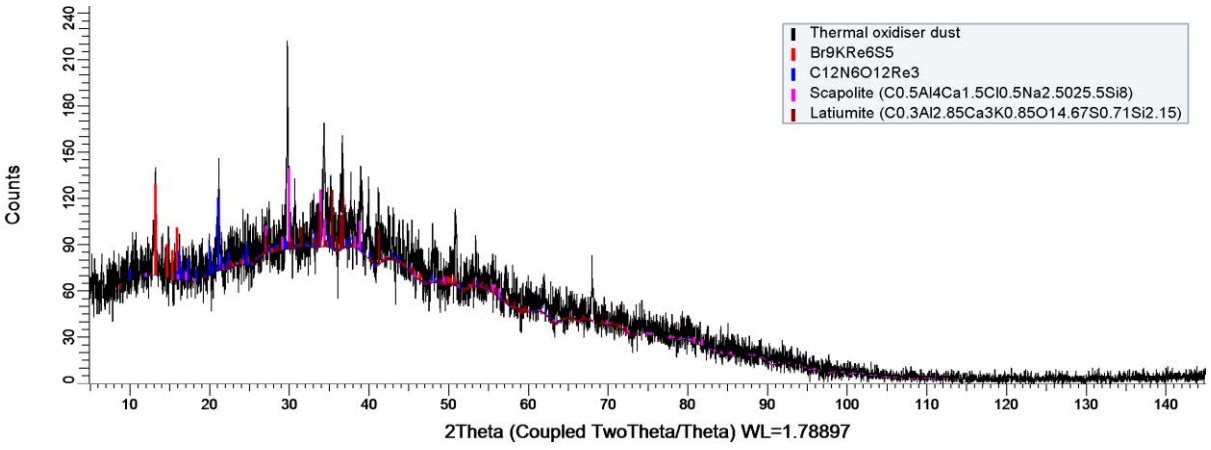

Figure 4-36: Rhenium compounds formed in the thermal oxidiser particulate.

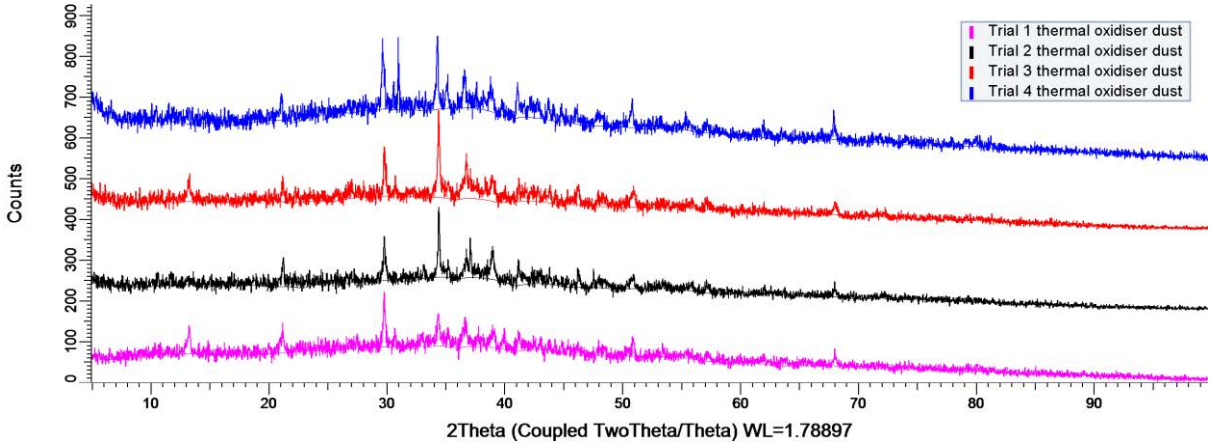

Figure 4-37: XRD patterns of the thermal oxidiser residues.

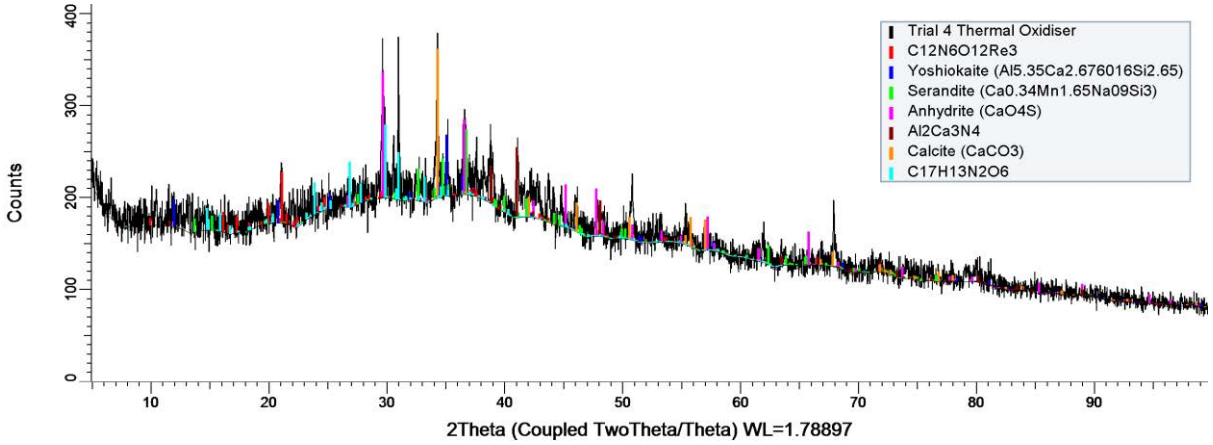

Figure 4-38: XRF pattern of thermal oxidiser residue produced during trial 4.

Like the baghouse dust, the thermal oxidiser residue is composed of amorphous materials and crystalline phases (Figure 4-38). Other than the rhenium containing compounds, the phases which are present in the material are calcium aluminosilicate minerals which may also contain sulphur, manganese and nitrogen. The amorphous nature of much of the components in the off gas dust shows that although some of the material is carry over of the input the high temperatures of the process causes phase changes in the material which is shown by the lack of SiO_2 and CaO peaks in the XRD analysis of the dusts.

The crystalline phases which are present in the residues are quite consistent with each other which shows that it is possible to predict which phases will be recoverable or produced at different stages of the off-gas system. The changing temperature profile of the off-gas system will mean that phases will drop out into the residue depending on their condensation point.

4.6.3. Iron Partitioning.

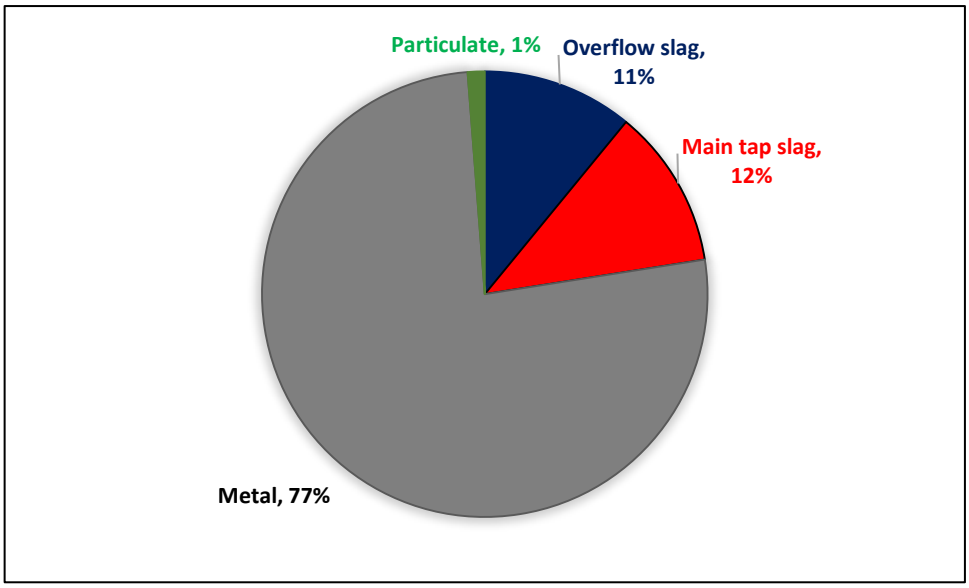

Figure 4-39: Iron partitioning over the five trials.

The iron partitioning over the five trials is shown in Figure 4-39. Not all the iron partitions to the alloy. The partitioning of the iron is dependent on it being reduced from magnetite and so unreduced iron is maintained in the slag. The analysis shows that 23% of the iron partitions to the slag phase. The model however predicted that 97% of the iron would partition to the metal phase and only 3% would be left in the slag.

The difference in the partitioning behaviour may be due to the difficulty in the process being able to reach true steady state conditions during the trial and not achieving a true equilibrium

inside the furnace. The soaking period before the tapping may not have been long enough to allow for the complete reaction of the material which had been fed into the furnace and so some of the magnetite may not have been reduced or was only partly reduced.

Despite the partitioning of the iron to the metal phase being only 77% the metal accountability was however good at almost 95%. It is possible that the composition of the iron in the slag may be slightly over estimated due to limitations in the analysis.

4.7. Commercial Plant Data.

A commercial plant designed for the recovery of platinum and rhenium was designed and built for EZOCM in Yekaterinburg, Russia. The plant was commissioned in late 2016 and has a designed throughput of between 130 to 150 kg catalyst/hr with an energy requirement of 3475 kWh/tonne of catalyst. This commercial plasma furnace does not operate with a graphite electrode, but with a water cooled plasma torch. This torch is manipulated by a robot which moves the torch around the furnace in a figure of eight motion which distributes the heat over the surface of the melt pool more efficiently. The process operates with a continuous overflow of slag for prolonged campaigns and the process halted periodically for metal removal from the furnace.

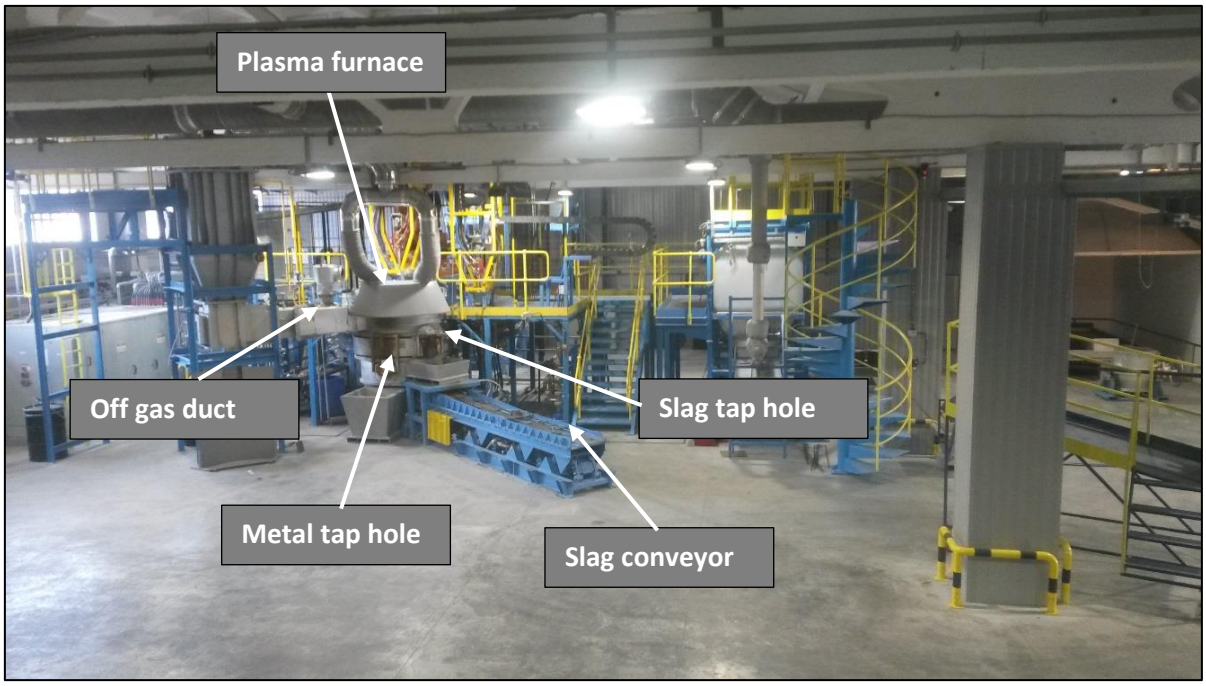

Figure 4-40: Photograph of the commercial Pt-Re recovery plant.

Data from the acceptance testing runs which were performed once the plant had been operating for around two months is shown in Table 4-32. The platinum and rhenium recovery rates are similar to those achieved in the trials being 97.3% for Pt and 96.7% for Re. It is believed that these recovery rates will increase with further modifications to the process formulation which would optimise the physicochemical properties of the slag such as the viscosity and liquidus temperature. The recovery rates should also increase with user experience and skill of the operators.

The commercial data indicated that the behaviour of platinum and rhenium in the process is similar and there are not the differences in the partitioning of the elements which were recorded in the trials. This may be due to the greater control of the process conditions inside a new plasma furnace and the rotation of the plasma torch inside the furnace may help to reduce the fuming of rhenium in the process.

Table 4-32: Pt and Re mass partitioning in the commercial plant.

Material	Pt (g)	Re (g)
Catalyst	10,516	10,772
Metal	9,385	8,624
Slag	286	355
Dust	57.3	58.7
Recovery efficiency (SBR)	97.3%	96.7%

4.8. Life Cycle Assessment.

From the data obtained during the trails, a life cycle assessment can be made of the process to determine its environmental impact. The energy data, the amount of raw materials use and the output streams analysis can be used for the assessment.

A life cycle assessment was performed using the Open LCA software which enables the calculation of the global warming potential, the eutrophication potential, the acidification potential and the marine ecotoxicity of the process.

A life cycle assessment is dependent on the definition of the system boundary and the functional unit. The LCA study done on this process is a 'gate to gate' process where the system boundary encompassed the plasma processing of the catalysts and the production of the metal bullion. The LCA does not calculate the environmental impact of the overall refining of either platinum or rhenium as this would require data from the methods of hydrometallurgical refining which without knowledge of the specific process used and the assessment would be inherently inaccurate.

However, this study can be used to understand the 'environmental bottlenecks' of the plasma process and the main causes of impact the environment.

The choice of the functional unit must be representative of the process and useful for the comparison which other processes, or used to complement other studies i.e. an expanded LCA of this work. The functional unit for this study was the recovery of 1 kg of platinum into a metal alloy. This was chosen because platinum is the most valuable metal in this process and so would be the main driver in the process economics.

4.8.1. Process Data.

Table 4-33 to Table 4-36 display the data used in the LCA study. The material mass inputs are required to include the environmental impact of their production and the outputs are required such as the gas volume and composition to determine emissions to the environment. Slag leaching data has been included in this study. The slag has numerous potential uses but in this case it is assumed that it would be sent to landfill, representing a worst case scenario. The leaching data is required to calculate the impact of elements leaching into ground water etc. The slag is a vitreous, non-hazardous material and so it does have very low leaching characteristics which reduce its environmental impact.

Table 4-33: Material inputs and outputs per kg of platinum recovered.

Material Input	Mass In (kg)	Material Output	Mass Out (kg)
Catalysts	283	Alloy	44
SiO_2	227	Slag	694
CaO	227	Flue Gas Residue	27
Fe_3O_4	40	Flue Gas	992 (Nm^3)
Coke	24		

Table 4-34: Energy requirements for the recovery of 1kg of platinum.

Electricity Requirements	MJ/kg platinum recovered
Plasma Power	2344
Auxiliary Power	437

Table 4-35: gaseous emissions from the process per kg of platinum recovered.

Gas Emissions	g/kg platinum recovered
Total Particulate Matter	8.8
Volatile Organic Compounds	3.4
NO_x	32.6
SO_x	17.6
CO	141.6
CO_2	16.4 (Nm^3/kg platinum recovered)
HCl	0.01
Pb	0.002

Table 4-36: Slag leaching per kg of platinum recovered.

Leachate	g/kg Pt recovered
As	0.062
Ba	0.347
Cd	0
Cr	0.021
Cu	0.014
Hg	0
Mo	0.014
Ni	0
Pb	0.007
Sb	0.007
Se	0.014
Zn	0.090
Cl	13.9
Fl	20.1
SO_4	69.4
Dissolved organic carbon	21.5

As the plasma process is highly dependent on electricity, the source of the electricity will be a major contributor to the environmental impact of the process. In this LCA three scenarios were employed with each scenario placing the plasma plant in a different country which has a different energy portfolio. In this study, the United Kingdom, France and Germany were chosen. The UK relies heavily on coal and oil and gas for their electricity generation, whereas in France nuclear power accounts for almost 81% of their generation and in Germany, although their coal generation is like the UK's, renewable energy electricity generation is almost twice that of the UK (Eurostat, 2014). Table 4-37 breaks down the energy portfolios of the three countries used in the scenarios (the data used was from 2014 by Eurostat).

Table 4-37: Energy portfolios of the UK, France and Germany (Eurostat, 2014).

Country	Coal	Oil	Natural Gas	Nuclear	Renewables
United Kingdom	36.3%	0.7%	26.8%	19.8%	14.8%
France	0%	0.6%	0.23%	80.9%	17%
Germany	37.4%	2.16%	7.4%	20.8%	27.9%

The environmental impacts of the plasma process can be seen in the summary Table 4-39. The process is very sensitive to the type of electricity generation and so the impact of plasma on the environment changes depending on which country the process operates in. In all the impact categories, the French scenario is the most environmentally friendly, but there is not a great difference between the impacts of the UK or German process. Despite the higher use of renewable energies, the German process for some categories has a greater impact than the UK process. This can be attributed to the high usage of bioenergy in Germany which, for the case of the eutrophication potential, results in ammonium leaching into ground water.

However, since 2014 there has been a significant reduction in the coal usage in the UK. The use of coal to produce electricity has fallen from 36% to 11% and there is a plan for the UK to close all coal fired power stations by 2025 (Department for Business, Energy and Industrial Strategy, 2017).

Table 4-38: Change in the UK's electricity generation from 2014 to 2016.

Year	Coal	Oil	Natural gas	Nuclear	Hydro	Wind and solar	Other
2014	36%	0.7%	27%	20%	1%	5%	11%
2016	11%	1%	41%	25%	1%	7%	15%

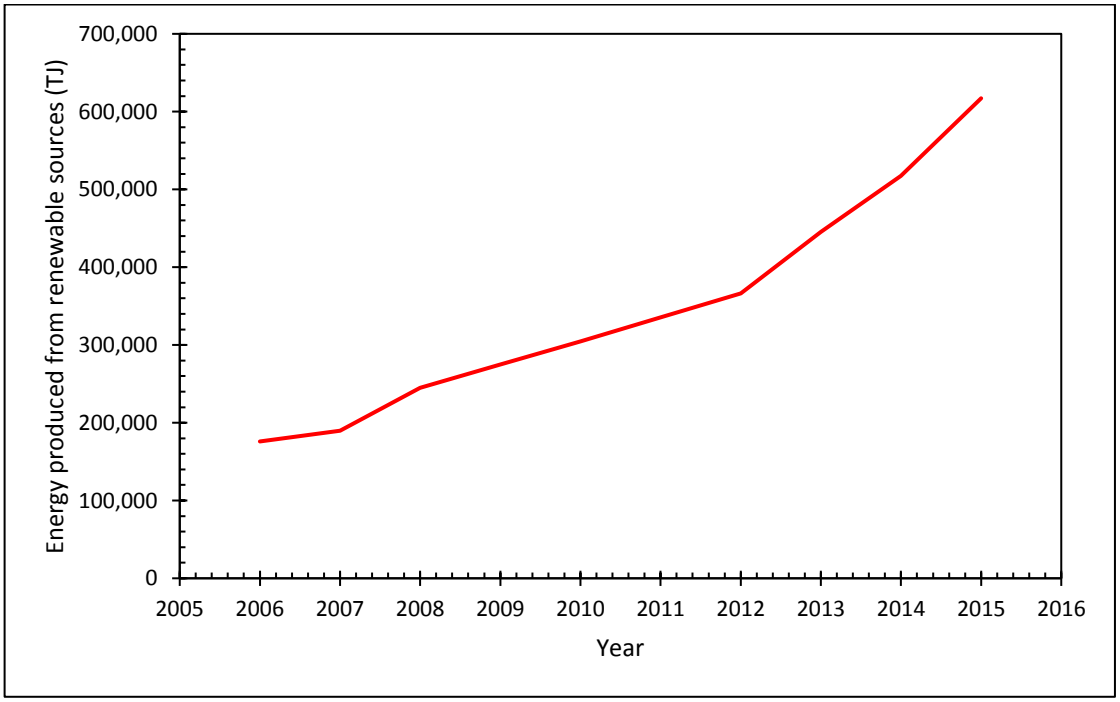

Figure 4-41: The change in the UK's energy production from renewable energy sources (Eurostat, 2017).

Table 4-38 shows the change in the UK's electricity generation from 2014 to 2016. It can be seen that there has been a significant reduction in the use of coal and although Figure 4-41 shows a steady increase in the use of renewable energy to generate electricity in the UK, there has also been a rise in natural gas and nuclear fuel use to generate electricity. Despite this, the drop in coal consumption in preference to other sources has a positive effect on the carbon footprint of the plasma process in the UK.

Table 4-39: Environmental impacts of the plasma process in the three chosen scenarios.

Impact Category	Unit	UK	FR	DE
Acidification potential	kg SO2 eq.	5.04E-01	2.4E-01	4.90E-01
Terrestrial ecotoxicity	kg 1,4-DCB eq.	6.21E-01	4.1E-01	6.31E-01
Marine aquatic ecotoxicity	kg 1,4-DCB eq.	9.43E+04	1.6E+04	9.66E+04
Photochemical oxidation	kg ethylene eq.	6.21E-02	4.6E-02	5.75E-02
Climate change GWP	kg CO2 eq.	5.93E+02	3.0E+02	5.48E+02
Eutrophication Potential	kg PO4 eq.	7.31E-02	3.9E-02	7.69E-02

A graphical representation of the impact categories and the three country scenarios are shown in Figure 4-42. It is interesting that electricity usage does not represent the overall majority of the environmental impact of the process in Figure 4-43 to Figure 4-45 and actually the use of lime as a fluxing agent contributes a significant amount to the environmental impact of the plasma process.

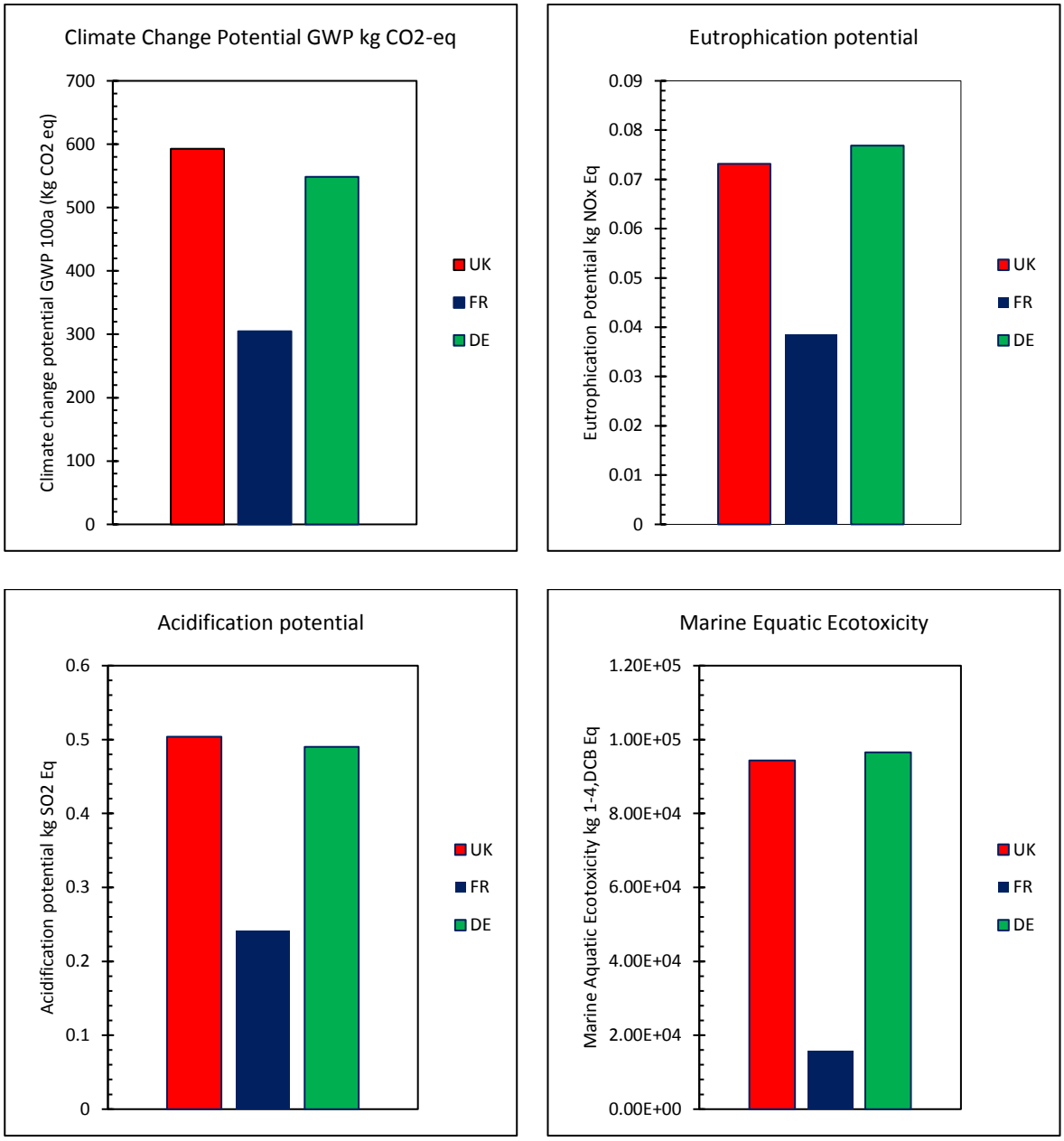

Figure 4-42: Graphical representation of the impact of the plasma process across three country scenarios.

In the UK, the use of lime accounts for 44% of the climate change potential impact category and 66% of the photochemical oxidation impact category which is secondary air pollution or summer smog. In France, due to the low environmental impact of nuclear energy generation, the use of lime accounts for the overwhelming majority of the impact of the plasma process.

The production of lime is very energy intensive and it involves the initial mining of the limestone from quarries followed by crushing then calcining where one of the major products is CO_2.

Lime is used as a fluxing agent in this process to help to lower the melting temperature of the melt and to improve the process operating conditions i.e. slag viscosity. The use of lime is favoured because the SiO_2-Al_2O_3-CaO slag system is well known and well defined, but it is possible to use alternative fluxing agents in the process.

Alternative fluxing agents could include waste glass (cullet) which is a recycled product and so would have a lower environmental impact associated with it.

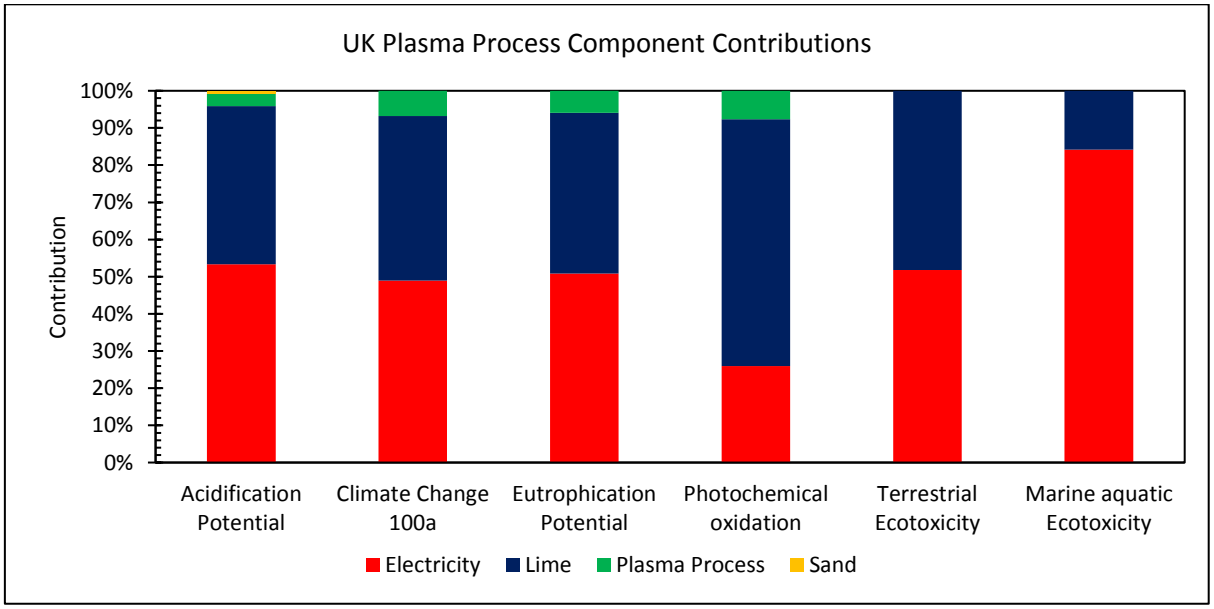

Figure 4-43: Factor contributions to the environmental impact of the plasma process in the UK.

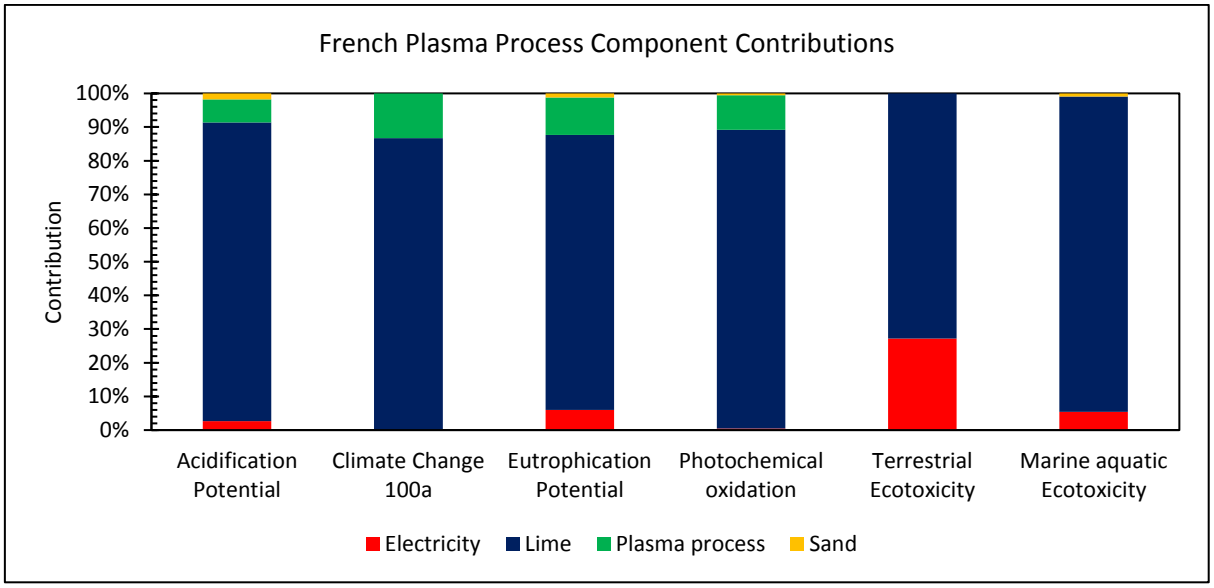

Figure 4-44: Factor contributions to the environmental impact of the plasma process in France.

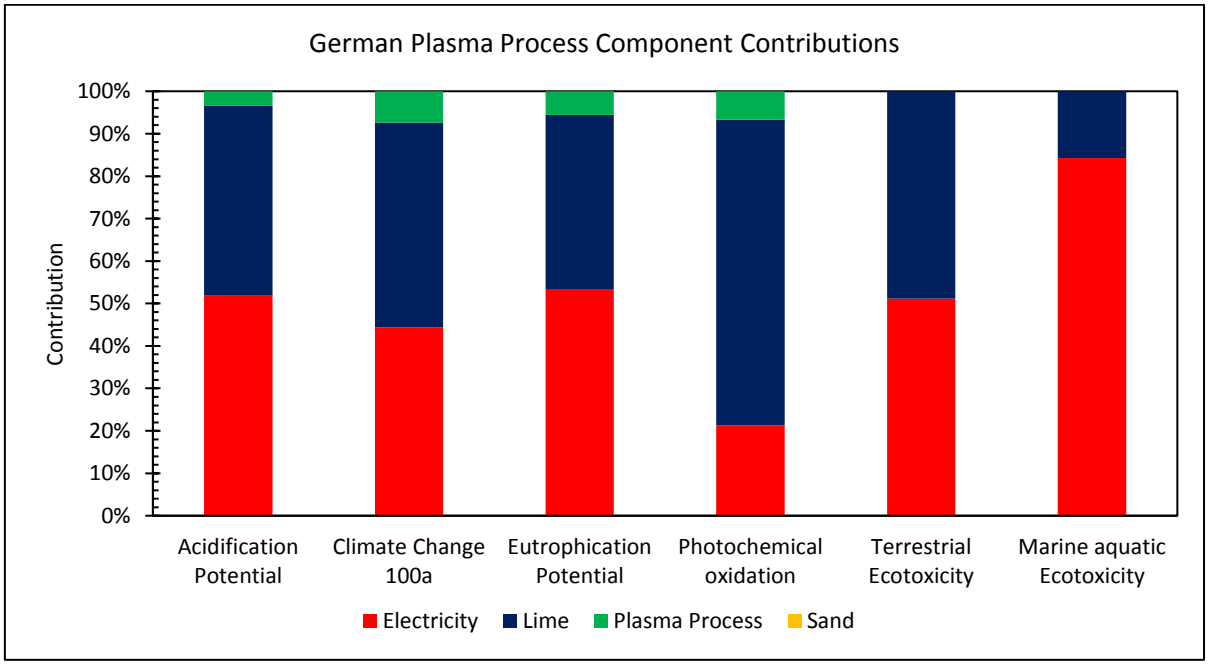

Figure 4-45: Factor contributions to the environmental impact of the plasma process in Germany.

Table 4-40: Breakdown of the impact of the UK based plasma process.

Life cycle impact categories	Unit	Hard coal	Natural gas	Bio	Nuclear	Wind	Lime	Plasma process (auxiliary)	Sand
Acidification Potential	kg SO2-eq	38%	11%	3%	-	-	42%	3%	1%
Climate Change Potential	kg CO2-eq	34%	14%	-	-	-	44%	7%	-
Eutrophication Potential	kg PO4-eq	32%	9%	9%	-	-	43%	6%	-
Photochemical oxidation	kg ethylene -eq	16%	10%	-	-	-	66%	8%	-
Terrestrial Ecotoxicity	kg 1,4-DCB-eq	40%	6%	-	4%	1%	4%	-	-
Marine aquatic Ecotoxicity	kg 1,4-DCB-eq	79%	5%	-	-	-	15%	-	-

The breakdown of the UK's environmental impact is shown in Table 4-40 and shows that the major contributors to its impact are the energy source and lime. Plasma technology can be a clean technology, but is reliant on the source of electricity, but choices can be made to use low impact raw materials too. The LCA study was based on the functional unit of 1 kg of platinum being recovered. The data which was used in the process was based on a 98% recovery of platinum. This recovery rate may vary which would mean the energy inputs and material usage per kg of platinum recovered may change.

The results of the LCA give an overall picture of the environmental impact of the plasma process. Using electricity to run a plasma arc can, if sourced in a certain way, be very environmentally friendly and the low direct CO_2 emissions from the process shows that the plasma process could be a technology that can operate in a sustainable economy. The interesting results from the study highlight that the choice of the raw materials do have a serious impact on the environmental impact and if it was desired to design a plasma process where the environmental impact was minimised, the choice of the fluxing agents would be very important.

4.9. Conclusions and Further Work.

Platinum and rhenium were both recovered from spent petrochemical reforming catalysts via a pyrometallurgical process. This is a novel method of recovering rhenium which had not previously been achieved in industry. The concept of rhenium recovery via a smelting route was shown to be theoretically possible via equilibrium modelling and then empirically proven at both pilot plant and commercial scale where recovery efficiencies of over 97% were achieved for both metals. This shows the great flexibility offered by a plasma based furnace which can control the chemistry of the furnace to suit the chemistry of the target metals in

the raw material. The successful application of this technique may mean that plasma may be successfully applied to recover other volatile or easily oxidised rare metals in future work. Elements such as rare earth oxides are notoriously difficult to smelt due to their oxides being retained in the slag phase and so it may be possible to recover them using plasma.

An environmental assessment of the plasma process shows that plasma technology can be a 'green' technology because of the use of electricity to power the process. However, the environmental impact is governed by the source of the electricity, which in many cases is out of the control of the user, but the choice of fluxing agents also has a large impact on its environmental impact. The use of lime has a high environmental impact associated with it and an avenue for further research would be to experiment with the use of alternative fluxing agents which have a lower environmental impact. The use of waste glass may be an option due to it being composed of sodium and calcium oxides which would be able to lower the melting temperature of the slag. The plasma process is often marketed as clean technology and this may be one way to enhance this credential. The impact of using different fluxes on process variables like energy use, slag viscosity, metal recovery rate and refractory wear would be an interesting topic of research.

The plasma process produces a precious metal rich alloy which is sent for final hydrometallurgical refining and although this has been a successful application of the technology, a full recovery process may be of interest for the business in the future. In-house refining of the bullion may give the technology a distinct market advantage and so research into how to do this may also be an interesting avenue of research in the future.

5. Slag Valorisation – A Review of the Current Literature.

5.1. Introduction.

Slag is a molten material produced in metallurgical furnaces and is formed from the unwanted oxides of the raw materials. Iron and steel slags are the most abundant with an annual worldwide production of around 400 and 350 million tonnes respectively (Motz et al. 2013). The extraction of iron from iron ore in the blast furnace produces around 0.25 to 0.3 tonnes of slag per tonne of crude pig iron and around 0.2 tonnes of slag per tonne of steel is produced in an electric arc (EAF) or basic oxygen furnace(BOF) (Piatak et al. 2015). Most of the published research on slags has focused on these two types due to their wide availability and industrial importance, but there are various other slags produced from processes such as platinum group metal (PGM) and copper smelting (Piatak et al. 2015, Gomez et al. 2008). A typical PGM recovery process developed by Tetronics would produce around 4000 tonnes per year of slag and an air pollution control residue (APCr) vitrification plant could produce up to 50,000 tonnes per year. Although this production is not quite at the scale seen from the blast furnace, it is still significant and increasing the value of this slag would have a meaningful impact on the economics of the plasma process.

Finding a use for industrial slags has been a challenge for researchers since the industrial revolution. A review of a paper presented by Dr. Frederick George Finch in 1862 at the British Association for the Advancement of Science in Cambridge, describes the utilisation of slag in France and Belgium: *"In this paper the author, after referring to the various attempts that have been made both in this country and abroad to utilize the slag from iron-smelting furnaces, described a method now adopted to effect this object at several ironworks in France and*

Belgium. The slag is there allowed to run direct from the furnace into pits about 8 or 9 feet in diameter at the top, with sides sloping inwards towards the centre, where they are about 3 feet deep. The mass is left for eight or nine days to cool, when a hard, compact crystalline stone is obtained, which is quarried and used for building purposes, but chiefly for paving stones. It is on this last application that its commercial value seems principally to depend. These paving stones are laid down in several provincial towns in France and Belgium, and also in some parts of Paris. They appear to wear exceedingly well, and are certainly superior to the grits and sandstones used for that purpose in those countries. This manufacture, besides the means of getting rid of what has hitherto been a useless and cumbersome material, is found at the above works to answer in a pecuniary point of view. The large area required for the pits would prevent its adoption in many iron works in this country."

The note emphasises what is still a modern problem for slag utilisation; that although many products can be produced with excellent properties, the feasibility of their production is variable and specific to slag type, location of producer and volume of production. From as early as the 17th century slag has been made into various construction materials; streets in Paris and Puerto Rico were paved with slag cobble stones and buildings were constructed with slag blocks. In the UK, examples of these buildings can be seen in Cornwall, Gloucestershire and Bristol where brass and copper smelting works were common. However, the difficulties in casting building blocks make them less competitive with common bricks used today. Nevertheless, it is still possible to utilise slags in applications where they have excellent properties and are competitive with and sometimes advantageous over traditional materials.

5.2. Slag Production.

The production of slag from a variety of sources leads to its use in various possible applications due to differences in the slag's properties. For example, steel slags from the now outdated Bessemer process were used effectively as fertilisers due to their high phosphorous content. However, the major current application for slags is in the construction industry as either an aggregate in road construction or as a cement replacement. The properties of the slag required for these applications are quite different; slags for aggregates need to be crystalline, hard and unreactive, whereas for a cement replacement the slag has to be glassy and reactive to be able to display latent hydraulic or pozzolanic behaviour. Controlling the slag's cooling from a molten to a solid state has an enormous effect on its properties as this dictates the slag's mineralogical and physical properties.

Slow cooling of the slag allows for crystallisation to occur forming a stable material similar to natural igneous rocks such as basalts which are also used as aggregates. These crystalline slags require high strength and low reactivity so that they do not react with other materials in the construction mix, which causes unwanted expansion and cracking of concrete. However, when the slag is a glass, it is able to react with alkaline solutions to form high a strength binding phase similar the one produced from cement hydration allowing slag to be used as an effective cement replacement.

The value of these materials differs considerably, a slag used as an aggregate would achieve a market value of around £6 per tonne whereas a ground granulated blast furnace (GGBFS) slag for cement replacement can achieve £60 to £80 per tonne. Therefore, it is not surprising that 80% of blast furnace slag is formed into the ground granulated type of slag whereas only 20% is air cooled for use as an aggregate (Euroslag, 2016).

Slags produced from steel processes and can be separated into three classifications; basic oxygen furnace (BOF) slag, electric arc furnace slag (EAF) and secondary metallurgical slag (SECS). A comparison between the composition of blast furnace slag and steel making slag can be seen in Table 5-1. Most steel slags are used as a road aggregate and so these slags are allowed to cool slowly in open pits or slag pots forming a crystalline product. They are not used as a cement replacement because of the restrictive regulations (BS EN 15167-1) regarding slags which are narrow enough to only include blast furnace slag.

Table 5-1: A comparison of the compositions of blast furnace and steel making slags.

Component (wt%)	Blast furnace slag (BFS)	Basic oxygen furnace slag (BOFS)	Electric arc Furnace slag (EAFS)
CaO	34-43	42-55	25-40
SiO_2	27-38	12-18	10-17
Al_2O_3	7-122	<3	4-7
MgO	7-12	3-8	4-15
MnO	0.15-0.76	<5	<6
Fe_2O_3	0.2-1.6	14-20	18-29

In Europe, there are high rates of utilisation of ferrous slags, 100% for BFS and 76% for steel slags (Euroslag, 2017) and Table 5-2 and Table 5-3 show their respective uses. Around the world utilisation rates are different and in China only 76% of blast furnace slag and 21% of steel slag is utilised (Li et al., 2014). The higher utilisation rate of blast furnace slag is partly due to the more defined regulations in place which accept the material as a by-product and not a waste which requires processing (Isawa, 2014). Therefore, some steel slags due to their composition and physical nature are treated as waste and cannot be used in applications without further treatment (Euroslag, 2017).

Table 5-2: Uses of blast furnace slag (Euroslag, 2017).

Use	Proportion of use
Cement production	66%
Road construction	23%
Interim storage	10%
Other	1%

Table 5-3: Uses of steel slag (Euroslag, 2017).

Use	Proportion of use
Road construction	48%
Cement production	6%
Hydraulic engineering	3%
Fertiliser	3%
Internal use for metallurgical processing	10%
Interim storage	11%
Other	6%
Final disposal	13%

5.3. Slag Cooling.

To produce a vitreous slag, the molten slag must be supercooled past its crystallisation temperature and this can be done using high cooling rates. As the supercooled slag approaches the glass transition temperature T_g, the viscosity of the slag increases significantly and this causes a massive reduction in the mobility of the structural species in the liquid causing it to essentially freeze in place creating a randomly ordered solid structure – a glass. The low mobility of the structural components of the molten slag as it approaches the glass transition temperature means that the atoms cannot organise themselves into ordered structures and so crystallisation cannot occur. Crystallisation can only occur when the viscosity of the system is low enough for the atoms to organise themselves to form nuclei and begin crystal growth. This occurs when the molten slag is at a high temperature, but in many slag systems this also requires sufficient holding time at these temperatures. Figure 5-1 shows the

different volumetric changes which are associated with a material under different cooling regimes. The glass transition temperature can be seen to be lower than the crystallisation temperature and if the material is still a liquid as it approaches the T_g, it will form a glass.

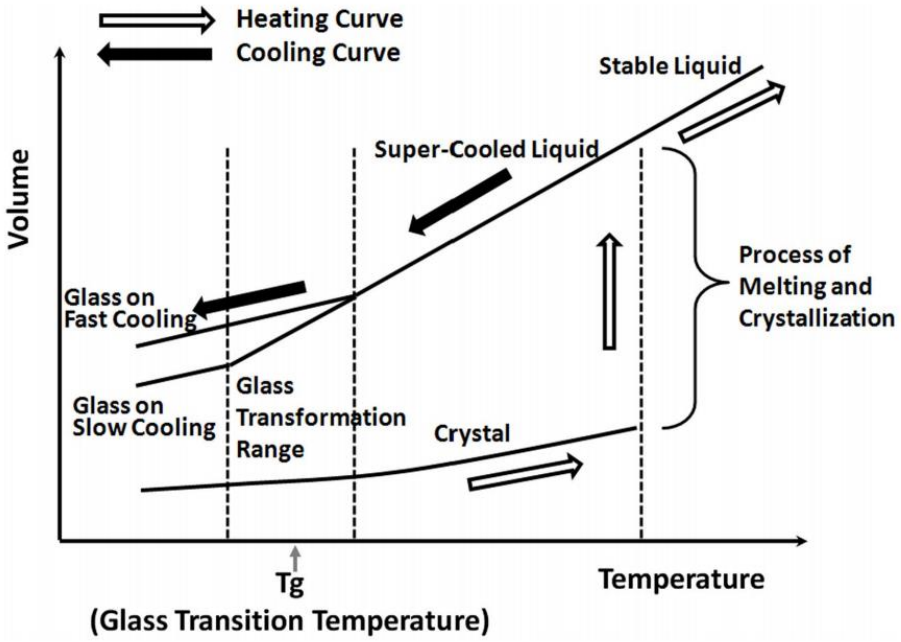

Figure 5-1: A typical curve showing the volume changes associated with heating and cooling in systems susceptible to glass formation (Fulchiron et al. 2015).

A rule of thumb states that the T_g is about two-thirds of the melting temperature of a material (Turkdogan, 1982), but the T_g is not a property which has a consistent value and is effected by the material's thermal history and cooling rate. However, for the estimation of the T_g, two-thirds of the melting temperature is a good start. Examples of glass transition temperature of glasses from the literature are given in Table 5-4.

Table 5-4: Examples of the glass transition temperature Tg and melting temperature T_m of various glass compositions (Turkdogan, 1982).

Composition	T_g (K)	T_m (K)
SiO_2	1381	1996
Na_2SiO_7	790	1073
$CaMgSi_2O_6$	1026	1665
$NaAlSi_3O_8$	1088	1391
$KAlSi_3O_8$	1178	1806
$CaAl_2Si_2O_8$	1086	1826

The fast cooling of the slag requires high temperature gradients and is often achieved by quenching the molten slag in large volumes of water. One method of water quenching is to feed the slag into jets of water causing the slag to solidify and cool quickly forming glassy granules. Water quenching of slag causes the resulting material to have a high residual water content which can be between 10 and 15% which requires the slag to be dried which is a high energy and cost expenditure of the process.

Recently there have been initiatives into developing dry granulation processes which produce glassy slags without the need for water. The advantages of dry granulation systems are that there would be a reduced energy requirement for drying the slag, a lower health and safety risk from steam generation and also a greater opportunity to recover heat from the slag. Motz et al. (2013) reported that the associated heat energy of blast furnace slag was between 1-2 GJ per tonne of slag and for a flow of BFS at 60 t/h this equated to 20 MW_{th}. Therefore, there is a potential to recover a significant amount of energy during slag cooling and two dry granulation methods have been developed by Paul Wurth and Hatch. The process developed

by Paul Wurth uses cold steel spheres that are dropped into molten slag and as these spheres have a high thermal conductivity, they quickly cool the slag forming a glass and a solidified mass. The pot is then emptied and dropped, fracturing the solidified mass and the steel spheres recovered using magnets. The heat of the spheres can be removed by cold air.

The second method, developed by Hatch, is to granulate the slag using a rotating cup. The slag falls onto a rotating cup which causes the slag to form droplets and be thrown towards a water cooled vessel wall. The slag solidifies and cools as it travels to the wall where after it drops into a fluidised bed and is cooled by cold air. Both these methods are reported to generate good quality slag for use as a cement replacement and avoid dangerous steam generation, but the efficiency of heat recovery is questionable. Due to its relative simplicity, the majority of glassy slag is still prepared by water quenching.

Controlling the water addition to slag during cooling can introduce porosity into the final slag which produces foamed or expanded slags. These slags can be used as lightweight aggregates due to their low density and their semi-crystalline nature. The high surface area to volume ratio of foamed slags may lead to further application of them in water filtration.

5.4. The Use of Slag as Cast Materials and Glass Ceramics.

When slag crystallises, it can form a very hard material making it suitable for construction applications. There have been many attempts to create slag blocks for construction by casting them into a mould and many historical examples can still be seen today. To create a cast block from the slag requires careful and controlled cooling of the material to ensure that the correct crystalline phases are produced. Generally, this requires large slag processing equipment including a holding furnace and cooling tunnel (Pioro and Pioro, 2004). A typical slag casting process involves the pouring of the slag from the main furnace into a gas-heated ladle where

additives are added to the slag. The additives are required because of the need to avoid phases such as dicalciumsilicate (Ca_2SiO_4) forming. Dicalciumsilicate can cause crystalline slags to completely disintegrate upon solidification because it can go through a phase change from β-Ca_2SiO_4 to γ-Ca_2SiO_4 at 400-550°C which is accompanied by a volume increase. This volumetric change causes the slag to break apart and can form a powdery dust. To avoid this phase formation, SiO_2 is added to the slag, this is not done in the furnace due to the requirements for a low viscosity basic (high CaO content) slag during the furnace operation. The treated slag is then passed to another furnace, similar to a glass furnace from where it is poured into moulds and slowly cooled in a tunnel. This process can be very complex and requires precise cooling regimes which are very dependent on the chemistry of the slag and mineral additives, such as basalts can be added to control the chemistry.

Similar to these cast slag shapes are glass ceramics produced from slag. Glass ceramics are produced by controlled thermal treatment of glass to produce a crystalline structure which is usually surrounded by a glassy matrix. Glass ceramics can be made from some silicate glass compositions including slags. The production of a glass ceramic is also a complex and precise process and requires detailed knowledge of the crystallisation kinetics of the material. The crystallisation of the glass is a two stage process which requires the formation of nuclei after which the growth of crystals occurs. Both these stages take place at high temperatures, although the exact temperatures are specific to the composition of the material. The slag is usually ground to a fine material and placed into a mould and compacted under high pressure. It is then heated to the nucleation temperature (T_N) at which it is held for a period of time to allow for a large number of nuclei to form. Then the temperature is increased to the crystal growth temperature (T_G) and held to allow crystallisation to occur after which the

temperature is slowly reduced. The nucleation and crystal growth rates are temperature dependent and are at a maximum at T_N and T_G as shown in Figure 5-2. However, it is possible that for specific compositions, there is a significant overlap between the T_N and T_G curves so that there only need be a one stage process where at a certain temperature both nucleation and crystallisation occurs, T_{NG}, which is shown in Figure 5-3. It was shown that when this overlapping of peaks occurs, it is possible to approach this temperature from the cooling of a molten glass rather than heating it up which results in a significant saving of energy (Rawlings et al., 2006).

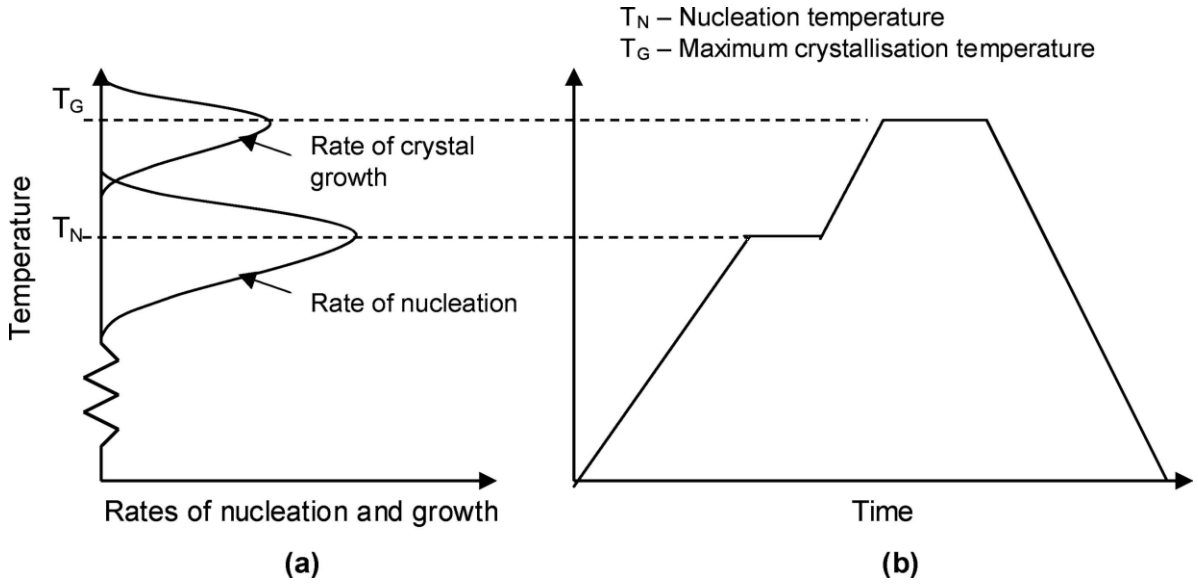

Figure 5-2: A diagram showing the nucleation and growth rates of a glass during the production of a glass ceramic (Rawlings et al., 2006).

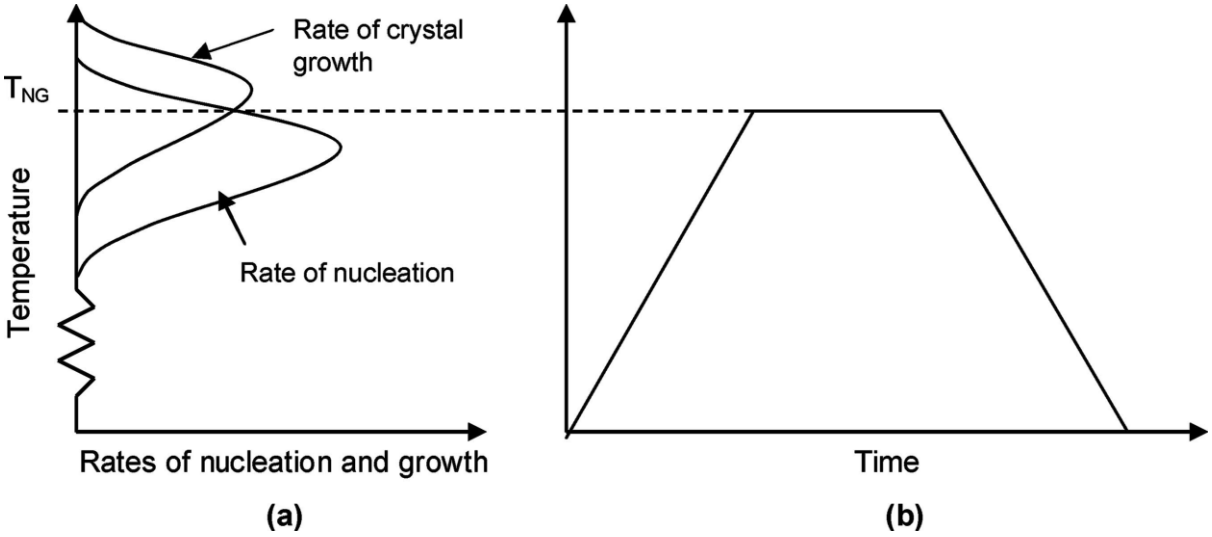

Figure 5-3: A diagram showing the overlap between the nucleation and crystal growth curves of a glass for the production of a glass ceramic requiring only a one stage process (Rawlings et al, 2006).

Slags which have been produced from the vitrification of air pollution control residue via thermal plasma technology have been successfully made into glass ceramics with very good properties. The glass ceramics were produced by powder pressing finely ground slag in a mould at between 25 – 30 MPa and sintering it at 950 to 1100°C (Roether et al, 2009; Chang et al. 2007). The resulting glass ceramics had a Vicker's hardness, Young's modulus, and bending strength of 6 GPa, 93 MPa and 81 Mpa respectively which are superior properties than granite (5.1-6.9 GPa, 43-61 MPa and 12-15 MPa) and other commercial glass ceramics (2.3 GPa, 66.9 MPa and 90 MPa) (Roether et al. 2009).

TiO_2 and Fe_2O_3 can act as nucleating agents in the process having positive effects on the material's properties by lowering the internal porosity and increasing the strength (Cheng et al. 2007). The introduction of TiO_2 at levels of 5 wt% showed a significant increase of the compressive strength of the material from 30-40 MPa to 45-98 MPa. Acting as a nucleation

agent the TiO_2 acts as seeds for the nuclei to develop producing a greater number of nuclei and so a greater number of points for crystal growth creating a dense microstructure which increases the strength of the material.

As well as glass ceramics, porous blocks have been made via a similar sintering route from slag derived from the vitrification of APCr. The ground slag was mixed with a sintering accelerator and then sintered at 1200°C producing a porous, water permeable block for the construction of pathways (Nishigaki, 1999). However, this process was extremely energy intensive as the sintering process lasted for 80 hours in a tunnel furnace. The energy intensive nature of these types of casting and ceramic making processes are a great drawback and although these final products can demand high market prices (£200 - £400/tonne), the high capital cost and complex production route makes their production unattractive. The precise nature of the process also means that it is not flexible to compositional variations making them difficult to control on a commercial basis.

5.5. The Use of Slags as Man-Made Mineral Fibres.

Thermal insulation is used worldwide to improve the energy efficiency of homes and since asbestos was discovered to be highly carcinogenic, alternative materials were developed and used to replace it (Wagner, 1972). Man-made mineral fibres (MMMF) are the alternatives to asbestos which are used to provide thermal and acoustic insulation in buildings (Moore et al. 2002). MMMF can be made of glass wool, refractory ceramics, natural minerals and slag. Slag wool has been used successfully as a MMMF and in Europe accounts for 50% of the market (Zhao et al. 2014). The MMMF market is a multi-billion dollar industry and the value of MMMFs are around £2000 - £4500 per/tonne making them a potentially very lucrative product for slag.

Slag wool is typically made of fibres with an average diameter of 6 µm and has a thermal conductivity of 0.035 W/m.K. Slag wool products contain around 70% slag and the remaining 30% is formed of natural minerals such as basalt, limestone and dolomite (Zhang et al. 2016).

The production route for slag wool consists of the slag being melted in a furnace and then poured into a ladle which feeds to the material into a superheating furnace. The slag is superheated to reduce the viscosity of the melt so that when it is passed into a centrifuge which spins out the fibres, the slag is fluid enough to be workable. After the centrifuge, the fibres are bound together using a binder. Traditionally the binder is a synthetic tar such as phenolic resin. This binder allows the material to be compacted and shaped for sale (Chudakov et al. 1972). Phenolic resins can give off toxic gases when they are used and so it is possible to use less harmful binders such as polyvinyl alcohol (PVA). The binder additions are usually between 2-10 wt% of the slag fibres, depending on the exact binder used (Zhang et al. 2016).

Unfortunately, man-made mineral fibres (MMMF) are not without dangers. Like asbestos, there is a concern that these MMMFs may also be carcinogenic (Steenland and Stayner, 1997). The toxicity and carcinogenicity of these materials is dependent on their formulation and processing routes and strict legislation is in place governing their (Maxim et al, 2002; HSE, 2008; WATCH, 2008). The safety of MMMFs is dependent on their microstructure, size and composition and these properties need to be controlled to ensure that the MMMF is not dangerous.

The fibres are dangerous if they can be inhaled but not removed from the body i.e. they have a high bio-persistence because this can cause cancer or fibrosis of the lungs (Brown et al. 2005; Oberdörster, 2000). The bio-persistence is related to the length and diameter of the fibre and

the toxicity of the fibres can be broadly summarised by the 'three Ds'; dose, dimension and durability (Brown and Harrison, 2012).

In the UK the exposure limit for MMMF is 2 fibres/ml air, but the dose of the fibres is not the exposure to the fibres but their retention in the lungs (Luoto et al. 1997). The retention is the amount of fibres deposited minus the amount of fibres cleared. If there is a high clearance of the fibres the dose is low, similarly if the fibres cannot be removed from the body, then the dose is high and it is the dimensions of the fibres which governs the dose.

Fibres which have a diameter less than 3 µm can enter the lungs via inhalation, the fibres which have a diameter greater than this cannot be inhaled and so are considered non-toxic. The aerodynamic diameter (Equation 5-1) describes the equivalent diameter of a sphere of the same density which has the same terminal settling velocity in air as the fibre (Maxim et al. 2006).

$$\mathrm{d_a} = \mathrm{f}_n \rho^{\frac{1}{2}} \mathrm{d}^{\frac{5}{6}} \mathrm{l}^{\frac{1}{6}} \qquad \text{Equation 5-1}$$

Where d_a is the aerodynamic diameter (m), f_n is a shape factor given as 1.3 m^2/kg for a sphere, ρ is the density of the fibre (kg/m^3), d is the fibre diameter (m) and l is the fibre length (m). The aerodynamic diameter can be substituted into Stoke's law to calculate the terminal settling velocity of the equivalent sphere shown in Equation 5-2.

$$V_\infty = \frac{d_a^2 g(\rho_p - \rho_a)}{18\mu}$$ Equation 5-2

Where V_∞ is the terminal setlling velocity of the fibre (m/s), g is the acceleration due to gravity (m/s^2), ρ_p is the density of the particle (kg/m^3), ρ_a is the density of air (kg/m^3) and μ is the dynamic viscosity of air (Pa.s).

If this settling velocity is very small the particle is likely to be remain airborne and so can be inhaled by a human (or an animal).

Phagocytosis is the main removal mechanism of the fibres during which the fibres are engulfed by phagocyte cells (in this case, these are alveolar macrophages) and then are digested by enzymes and toxic peroxides (Kim et al. 2000). Other mechanisms of removal are via the lymphatic system and also by dissolution by the biological medium to be removed via the bloodstream.

The mechanism which is employed depends on the material's properties and dimensions. Short fibres can be removed by all three mechanisms however longer fibres cannot be fully engulfed by the alveolar macrophages and so remain in the body. The key mechanism for removal of long fibres from the body is via dissolution (Luoto et al. 1995).

The chemical composition of the fibres strongly determines the ability of the body to dissolve the fibres. The chemical composition can be assessed using the Z index or the K_i index (the German carcinogenicity index). They asses the bio-persistence and carcinogenicity of the fibres from their composition and are centred on the ease in which the fibres are dissolved. The Z index (Equation 5-3) is the sum of the mass percentages of alkali and alkaline earth oxides

in the composition and is used to classify mineral wools from refractory ceramics (Moore et al. 2002).

$$Z = \sum(Na_2O + K_2O + CaO + MgO + BaO) \quad \text{Equation 5-3}$$

If Z is greater than 18 (18 wt%) then the material is classified as a mineral wool and is considered less hazardous than the materials which have a Z index under 18. Materials which have a Z index less than 18 are required to be labelled as carcinogens unless it can be proven that the material does not pose a risk. The German K_i index (Equation 5-4) is similar but takes into account the effect of the concentration of alumina in the fibres as alumina decreases the dissolution rate of the fibres at neutral pH as opposed to the components in the first set of brackets which increase the rate of dissolution:

$$K_i = \sum(Na_2O + K_2O + CaO + MgO + B_2O_3 + BaO) - 2(Al_2O_3) \quad \text{Equation 5-4}$$

Compositions with a Ki index ≥40 are deemed to have low bio-persistence whereas those with an index less than 40 require further testing (Moore et al. 2002). Inside phagocyte cells there is an aggressive acidic medium of around pH 4 which aides dissolution, whereas outside the cells there is a pH of around 7.4 and so if the fibre is too big the be engulfed by a phagocyte cell it must have a composition which can be dissolved at a neutral pH.

Long fibres can be broken into smaller ones if broken transversely which allows them to be removed via phagocytosis. The fibres should be able to be broken under the stresses which are applied to the fibres by the body and vitreous fibres are generally more brittle than crystalline ones making them more likely to break transversely. Crystalline materials are more

likely to break longitudinally creating fibres of the same length, but of a shorter diameter (Brown and Harrison, 2012). This increases the toxicity of the fibres as they can be inhaled more easily and as they are of the same length they may have a higher bio-persistence.

Crystalline materials are also more likely to cause fibrosis than the amorphous fibres due to the sharper edges of the crystals which cause irritation of the lungs (Moore et al. 2002). To create the vitreous fibres, the slag is cooled very quickly at the exit of the centrifuge. The slag's composition can be altered to have a higher SiO_2 content which helps the slag form a glass on cooling and so sand or other additives can be added to control the composition whilst the slag is molten (Kuo et al. 2008).

The use of slags in slag wool is a potentially lucrative option for the material, but the production of the material would require large capital investment and high quality control. The market is dominated by companies such as Rockwool and so breaking into this market may be difficult unless the slag was supplied directly to one of the major players. This may mean that the price obtained for the slag would be very low and may only serve as an option to get rid of it.

5.6. The Use of Slags as Aggregates.

The major uses of slags are as an aggregate or as a cement replacement. These routes require less capital investment than the above methods. Slags which are to be used as an aggregate are allowed to just be poured into slag pits where they crystallise. Steel slag is widely used as an aggregate for construction applications and one of the most successful applications of slag as an aggregate is for road construction. The slag is mixed with asphalt where the slag aggregate acts as a structural skeleton and the asphalt is the binder. The properties of the slag are generally comparable to or superior to those of natural aggregates, which can be seen in

Table 5-5 (Motz and Geiseler, 2001). These properties of the slag has meant that it can be used on road surfaces because of its high strength, friction and abrasion resistance and it has been used to create anti-skid road surfaces. The steel slags which are used for this application are crystalline slags and the main crystalline components of BOA and EAF slag are dicalciumsilicate (Ca_2SiO_4), dicalciumferrite ($Ca_2Fe_2O_5$) and wustite (FeO). Although dicalciumsilicate can be unstable, in steel slags it is stabilized by the presence of P_2O_5. However, the most important aspect of the slag's chemical composition for this application is the free CaO and free MgO content. These phases are detrimental to the properties of the slag during its use as an aggregate because they react easily with water and produce hydroxides. This reaction causes a volumetric change in the slag which results a reduction of its strength and disintegrating. The free lime and magnesia content has to be below 4 wt% individually, but their presence in the slag can be significantly higher than this up to around 10%. There are methods which are employed to reduce their presence and the first is to simply leave the slag in the slag pit and allow it to be exposed to rain water where the free lime will be reduced naturally. This method is time consuming and so another method is to hold the molten slag in a ladle add silica (SiO_2) to increase the Ca/Si and Mg/Si ratio. Increasing this ratio will cause the Ca and Mg species in the slag to be chemically bound and not precipitate upon cooling.

Table 5-5: A comparison between the technical properties of basic oxygen furnace (BOF) slag and electric arc furnace slag (EAF) aggregates with natural aggregates (Motz and Geiseler, 2001).

Characteristics	BOF -slag	EAF - slag	Granite	Flint gravel
Bulk density (g/cm3)	3.3	3.5	2.5	2.6
Shape - thin and elongated pieces (%)	< 10	< 10	< 10	< 10
Impact value (%/wt)	22	18	12	21
Crushing value (%/wt)	15	13	17	21
10% Fines (KN)	320	350	260	250
Polishing (PSV)	58	61	48	45
Water absorption (%/wt)	1	0.7	<0.5	<0.5
Resistance to freeze-thaw (%/wt)	<0.5	<0.5	<0.5	<1
Binder adhesion (%)	>90	>90	>90	>85

The use of slag as an aggregate has been widely successful and this is partly due to its low value and high availability. Slags as an aggregate will only achieve around £6/tonne which does not create a valuable revenue stream for the producer. The use of the slag as a cement replacement is a much more valuable opportunity and when slag is used as an aggregate it is due to the material not being able to comply with the regulations which surround the use of slag as a cement replacement (Euroslag, 2012). These regulations are restrictive and not necessarily a reflection on the properties of the material making the market somewhat unfair.

5.7. The Reuse of Slag as a Cement Replacement.

After water, cement is the world's most used material and around 4.1 billion tonnes of cement was produced in 2016 (Statista, 2017). Cement is used because it is cheap, easy to use and when it reacts with water it produces a very strong material. However, for every tonne of cement produced around 750 kg of CO_2 is emitted. On a per-tonne basis, the CO_2 emissions associated with cement are less than the emissions for metals like steel; between 1000-2000 kg of CO_2 are emitted per tonne of steel (Lisienko, 2016), but the sheer quantity of cement's annual production means that the industry produces around 2 Gt of CO_2 which equates to 5 to 7% of the world's anthropogenic CO_2 emissions (Barcelo et al. 2014). Therefore, with a global drive to reduce CO_2 emissions, reducing cement consumption would have a significant impact on the carbon footprints of construction projects.

The product of the reaction between cement and water is calcium-silicate-hydrate (CSH) gel which acts as a binding phase and is largely responsible for the strength of concrete. The equation for this reaction is shown in Equation 5-5.

$$3CaO_3SiO_5 + 7H_2O \rightarrow 3CaO \cdot 2SiO_2 \cdot 4H_2O + 3Ca(OH_2) \qquad \text{Equation 5-5}$$

The use of blast furnace slag as a cement replacement has been well established for many years due to its latent hydraulic properties and its ability to be used as a pozzolanic material. The latent hydraulic property of slag means that it can react with water to produce CSH, but the reaction between slag and water does not proceed sufficiently to produce enough CSH to effectively replace cement. This is due to the deposition of the CSH gel on the surface of unreactive slag particles which stops the reaction. However, when slag reacts with an alkaline solution the reaction proceeds to a much greater extent and is able to produce enough CSH

to act as a cement substitute, due to the faster reaction rate and dissolution of the slag particle in the alkaline environment (Walker and Pavía, 2011). During cement hydration, calcium hydroxide ($CaOH_2$) is produced as a by-product and this provides the alkaline conditions required for the slag – alkali reaction to proceed. This is known as the pozzolanic reaction and it is named after the Roman city Pozzuoli which was a source of the volcanic ash the Roman's used to make their concrete. The volcanic ash was mixed with lime and water and this reaction is the basis for many alternative cements used today.

The use of cement-pozzolan blends is very common in commercial applications not only due to the lower CO_2 footprint of these materials, but also due to their higher strength and greater corrosion resistance than ordinary Portland cement based concretes. This is because the pozzolanic reaction occurs after cement hydration and the CSH phase produced by the slag is a secondary phase that reinforces the primary CSH produced by cement. This secondary phase reduces the porosity of the material which increases the material's strength and reduces the ingress of aggressive chemicals that can cause deterioration in concrete. The strength development of cement-slag blends is slower than that of ordinary hydrated cement, but the final strength of the cement-slag blends has been widely reported to be greater (Kourti et al. 2013).

Typically, slag replaces cement by around 40% but it is becoming more common to find higher cement substitutions; the foundations of the Shard in London were built using 70% ground granulated blast furnace slag, using Hanson's Regen blend, which saw the building win awards for its environmentally sustainable design. However, when the slag substitution increases over

40-50% the strength development of the concrete is considerably slower and the mixture requires accelerators to increase the reaction rate of the slag (Taylor et al. 2010).

It is possible to completely replace cement using slags and create low carbon construction materials known as alkali-activated slag binders. The reaction between a finely ground and glassy slag and an alkaline activating solution such as an alkali-hydroxide produces a binding phase which is analogous to CSH. However, the major binding phase is not the CSH structure produced from cement hydration, but a calcium-aluminium-silicate-hydrate CASH phase, or a C(N)ASH gel when sodium ions are present from the activating solution. The difference between these two phases is that the CSH structure is formed of short silicate chains and resembles a poorly crystalline tobermorite whereas the CASH gel is formed of longer alumino-silicate chains having a sheet like structure and can form poorly crystalline zeolite structures (Taylor, 1986; Li et al, 2010; Fernández-Jiménez and Puertas, 2003).

Alkali-activated slag binders have been of interest since the early part of the 20th century. In the 1950s, Glukovski developed slag based concretes which were used to build various pieces of infrastructure, especially in Ukraine (Pacheco-Torgal et al. 2008). However, since then there has not been much commercial success for these materials partly due to the overall lack of long term durability data and also very little regulations surrounding them which discourages potential users. Despite this, the interest in these materials is growing in both academia and in industry and this is helped by the drive to develop environmentally sustainable construction materials (Deventer et al. 2011).

Many aluminosilicate materials can undergo ‘alkali-activation’ and produce alkali-activated binders via the mechanism shown in Figure 5-4. Theoretically any aluminosilicate source which

can dissolve in an alkaline environment can produce an alkali-activated binder, but the term 'alkali-activated binder' is a generic term for these types of materials and there are various sub-groups for them, one of which is the alkali-activated slags and another is the geopolymers. Geopolymers were developed in the 1970s by Davidovtis and are made using calcined clays such as metakaolin and class F-fly ash. Geopolymers and alkali-activated slags are similar and often confused, but the differentiation between a geopolymer and an alkali-activated slag is caused by the products of their alkali-activation. The product of the geopolymer reaction is a sodium-alumino-silicate-hydrate (NASH) gel where the alumino-silicate chains display a fully polymerised 3 dimensional structure which can be determined using nuclear magnetic resonance (NMR) spectroscopy or Fourier transform infrared (FTIR) spectroscopy. The CASH gel produced by the alkali-activation of slag does not display 3 dimensional polymerisation, but is formed of less interconnected aluminosilicate chains forming a sheet like structure (Provis et al. 2015). A simplified schematic of the differences can be seen in Figure 5-5. The cause of the difference between these two materials is the calcium content in the slag. The aluminosilicate chains are composed of silicon and aluminium tetrahedra which are interconnected by T-O-T bonds. Calcium ions reduce the number of these T-O-T bonds which does not allow for a fully polymerised structure to form. The raw materials for geopolymers contain very little or no calcium and so this effect is not seen.

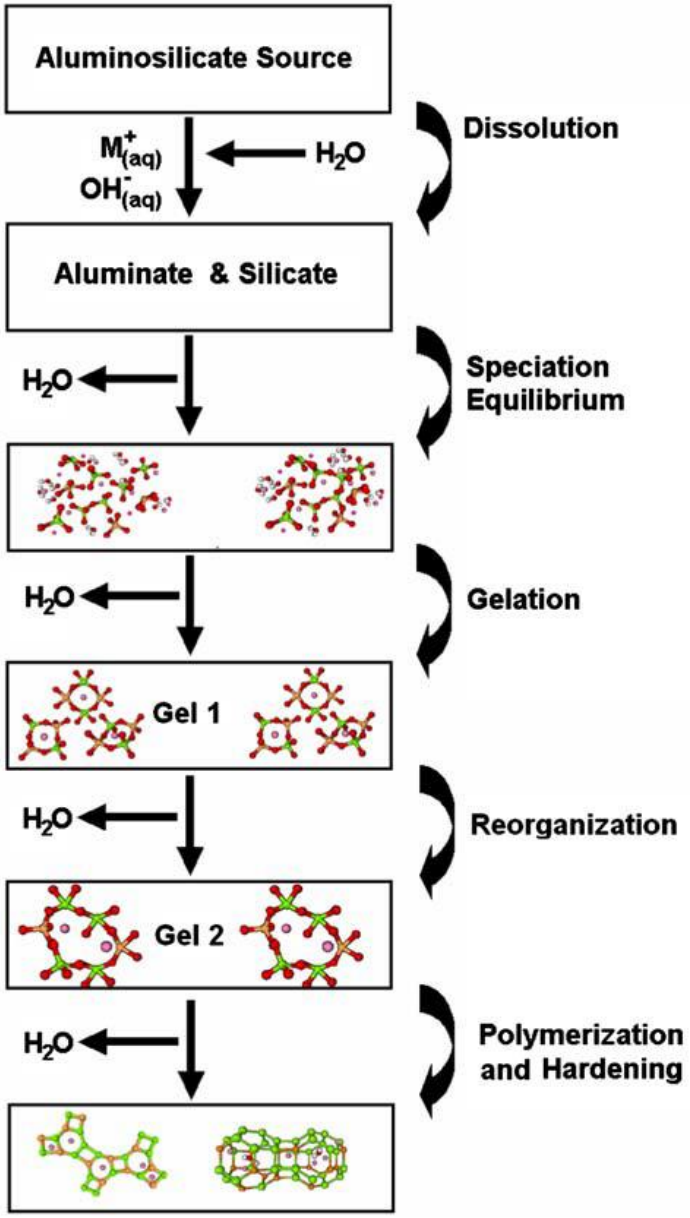

Figure 5-4: A conceptual model for alkali-activation of aluminosilicates (Duxson et al. 2007).

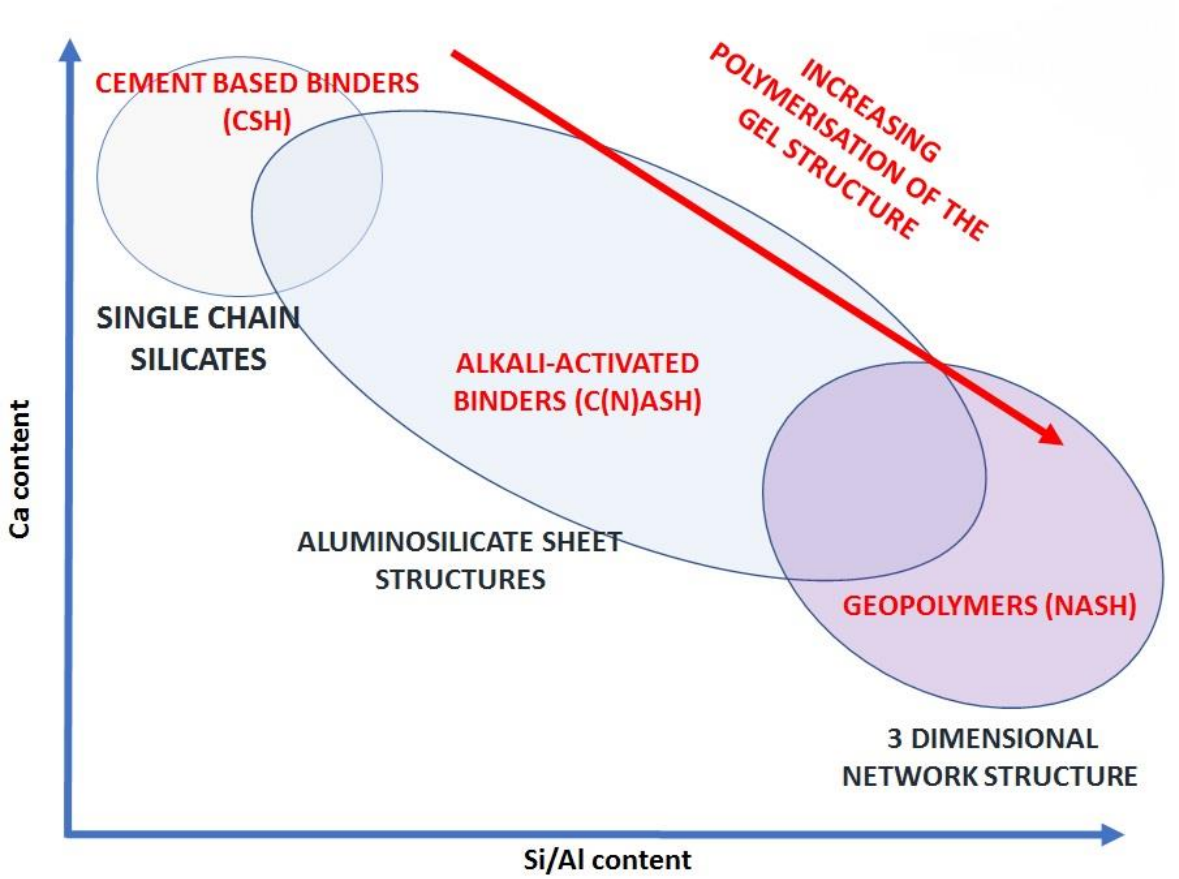

Figure 5-5: A simplified schematic of the structures of alkali activated binding phases (Keeley, 2017).

The mechanism for alkali-activation of slag is similar to the conceptual model shown in Figure 5-4, the first step involves the dissolution of the slag in an alkaline environment. The dissolution releases Si, Al and Ca species into the solution which coagulate and condense to form the gel phase. The gel phase undergoes some reorganisation before it hardens and develops high mechanical strengths. The alkaline environment is usually provided by an alkali-hydroxide such as sodium hydroxide or an alkali-silicate solution. The requirement of the alkaline solution is to provide OH^- ions which attack the slag and cause it to dissolve. Slag will only dissolve at a very high or very low pH, but only the solid product from the alkaline

activation is stable. As well as the requirement for a high pH, the slag must also be metastable. Most crystalline slags are too stable to undergo sufficient dissolution to produce the binding phase and so glassy slags are required for the reaction. A finer particle size of the slag is also beneficial to aid the dissolution step by increasing the surface area available (Provis et al. 2014).

There has been a large amount of research on potential precursors for alkali-activated binder production and the raw materials generally fall into the two categories; natural clays (calcined or otherwise) and industrial by-products. The main requirement for a precursor is that it can react in an alkaline environment which will cause the liberation of aluminium and silicon species into solution. Although there is a wide variety of raw materials they all have three common properties; they have a high silicon and aluminium content, they contain major amorphous or metastable phases and have a fine particle size. The amorphous or metastable phases may be natural or introduced by process routes such as calcination, but these facilitate the dissolution of the material in alkaline conditions as opposed to more stable crystalline phases.

Research on alkali-activated slags has, for the most part, focused on ground granulated blast furnace slags (GGBFS) (Haha et al. 2011; Burciaga-Diaz and Escalante-Garcia, 2013). However, there are various other slags which are produced and may also be suitable for alkali-activation. Slags derived from the vitrification of APCr via the thermal plasma process have been shown to produce strong akali-activated slag binders with compressive strengths greater than alkali-activated blast furnace slags and metakaolin based geopolymers (Kourti et al. 2011).

There have been numerous studies which have focused on the effect of compositional variations on the properties of alkali-activated binders and in particular, geopolymers (Duxson et al, 2005). The properties of the binding gel phase have been shown to be effected by the Si/Al ratio, the alkali cation content and the calcium content. Most of the work has focused on metakaolin and fly ash based geopolymers, but the properties of the gel phase produced from the alkali-activation of slag is similar (Fernández-Jiménez et al, 1999). An increasing Si/Al ratio in the binder leads to geopolymers with greater mechanical strengths, but also increased stability in the geopolymer structure which reduces the tendency of the system to form crystalline structures (Duxson et al. 2007; He et al. 2016). The increase in the strength of the material has been attributed to a lower substitution of Al in the chains for Si and also a densification of the binding phase resulting in a reduction in the open porosity of the material. However, despite the benefits of a high Si/Al ratio, the presence of aluminium is important due to its role in promoting the hardening of the gel phase (Duxson and Provis, 2008). Alkali metals present in the activating solution firstly facilitate the liberation of silicon and aluminium species from the precursor and then to alleviate the charge imbalance caused by the substitution of Al^{3+} for Si^{4+} in the gel framework.

The Si/Al ratio can be increased and controlled by adding silicon species to the formulation by using alkali-silicate solutions instead of alkali-hydroxide solutions (Haha et al. 2011). The presence of calcium in the binding phase has not been studied as extensively as the Si/Al ratio, partly due to the importance of this ratio in geopolymers and the low calcium content of the common geopolymer precursors, metakaolin and class F fly ash. However, the significant presence of calcium in slags make it an important contributor to the properties of the material. When a small amount of calcium ions are present in the system, there is little affect as they

substitute in for the Na^+ or K^+ ions as charge balancers (García-Lodeiro and Fernández-Jiménez, 2010). However, when the calcium concentration increases further, the calcium plays an important structural role, shortening the aluminosilicate chain lengths developing the CASH structures described above. However, as well as the CASH structures, calcium-silicate-hydrate (CSH) phases have been reported to co-exist alongside them (Yip et al., 2005; Ben Haha et al. 2011). These CSH phases are similar to those formed from cement hydration and are thought to increase the strength of the binding phase by acting as nucleation sites for the formation of the CASH gel.

The multicomponent nature of the slag means that the resulting binding phase is complex and is of a heterogeneous nature. Thermodynamic modelling used to predict the phases formed from the alkali-activation of slags show that although the C(N)ASH gel is the major product, the formation of secondary phases are dependent on composition; for example the formation of zeolite phases are predicted to increase as the silicon content increases (Myers et al. 2015).

Many investigations into the effect of compositional variation of the binding phase focus on the strength of the material and few studies are concerned with its durability and the lack of durability data has significantly hampered the uptake of these materials in the market. The leaching of heavy metals from alkali-activated slags and geopolymers based on industrial waste has been shown to be low, but these heavy metals are present in very low concentrations and their leaching is more important for applications such as encapsulation of industrial wastes (Deja, 2002; Zhang, 2017). Efflorescence is a phenomenon which occurs in many construction materials, but there have been few studies on efflorescence in these types

of binders and there is a requirement for more data to understand how to reduce its occurrence.

Efflorescence in alkali-activated slag is caused by mobile Na^+ and OH^- ions present in the pore solution which migrate from the binding matrix, react with CO_2 from the atmosphere and form precipitates on the surface of the material. A proposed mechanism for efflorescence in alkali-activated slags is shown in Equation 5-6 and Equation 5-7. Where CO_2 first forms a carbonate when it reacts with free OH^- in the pore solution then then reacts with the free sodium ions to form carbonates (Zhang et al. 2014).

$$CO_{2(g)} + 2OH^-_{(aq)} \rightarrow CO_3^{2-}{}_{(aq)} + H_2O_{(aq)} \qquad \text{Equation 5-6}$$

$$2Na^+_{(aq)} + CO_3^{2+}{}_{(aq)} + 7H_2O_{(aq)} \rightarrow Na_2CO_3 \cdot 7H_20_{(aq)} \qquad \text{Equation 5-7}$$

Therefore, the mobility of the Na^+ ions in the pore solution must be reduced to reduce efflorescence and an excess alkali content, open pore structure and weak alkali binding are the three main causes of efflorescence (Allahverdi et al. 2015). In fly-ash based geopolymers, small additions of slag had a positive impact on reducing efflorescence by reducing the pore sizes of the binding phase (Zhang et al. 2014), but leaching of alkalis was found to increase at higher slag loadings over 40% (Yao et al. 2016).

The binding of Na^+ in the binding matrix occurs by the ion acting as a charge balancer for the substitution of Si^{4+} by Al^{3+}. Therefore, efflorescence can be reduced by designing the Na/Al ratio to be ≤ 1 which should reduce the presence of excess Na^+ (Yao et al. 2016; Allahverdi et al. 2015; Najafi Kani et al. 2011). However, this is difficult to achieve since the reactivity of slag is usually less than 100% and it can vary depending on its composition and structure (Keeley

et al. 2017). In cement chemistry Na^+ ions have been theorised to bind to silanol sites ($Si\text{-}OH^-$) sites in CSH structures. The alkali binding reduces when the Ca/Si ratio increases because this causes a reduction in the number of silanol sites available due to the bridging action of Ca^{2+} (Hong and Glassser, 2002; Shehata and Tomas, 2006). Even when the Na^+ are bound within the matrix the ions have been found to be interchangeable with larger cations and so may end up mobile in the pore solution despite efforts to reduce this (Dědeček et al. (2008). The compositional variation of the formulation clearly plays an important role in the causes of efflorescence of alkali-activated slag and so more investigation is required to control it.

Understanding the compositional variation of slags on their performance as alkali-activated materials is of interest for Tetronics because the various applications of Plasma technology produce various different slags with different compositions. The composition of the slag is dependent on the composition of the waste material and the fluxing agents which are added to it to reduce the melting temperature. The slag composition can then be further altered to optimise its viscosity and thermal conductivity as well as reduce excessive refractory wear. Therefore, the composition of a slag is generally unique to a specific process and this can even be seen by the variations of blast furnace slags around the world.

Table 5-6 shows the differences between the compositions of slags derived from PGM recovery from chemical and automotive catalysts and the vitrification of APCr. The high Al_2O_3 content from the chemical catalyst slag is derived from these catalysts being Al_2O_3 supports and so a high lime addition is required to lower the melting point. The difference in the catalytic support of a chemical catalyst and an automotive catalyst can be seen by the high MgO content in the automotive catalyst which comes from the cordierite and the CeO_2

content which comes from the washcoat. The air pollution control residue (APCr) slag composition is quite different than that of the others mainly due to the high CaO content which is present because of lime to remove the acidic components from the gas.

Table 5-6: Variations in the slag composition from different plasma processes.

	Raw material		
Oxide (wt%)	**Chemical Catalyst**	**Automotive Catalyst**	**APCr**
Al_2O_3	37.2	34.1	17
SiO_2	30.5	33.6	34.1
CaO	28.6	13.8	40.8
Fe_2O_3	1.6	2.2	2.1
Na_2O	1.1	0.1	0.4
TiO_2	0.2	0.5	1.7
ZrO_2	0.1	1.5	0
K_2O	0.1	0.4	0
MnO	0.1	0	0.1
MgO	0	9.3	2.3
CeO_2	0	4.6	0
P_2O_5	0	0.2	1.5

APCr is the solid residue produced during the emission gas cleaning during the incineration process. The off-gas or emission gas from an incinerator contains various hazardous chemicals such as lead, zinc and chlorine which need to be removed from the gas before its release to the environment (Rani et al. 2008). These chemicals are removed from the gas via various treatment processes and they end up in as fine solid material known as APCr. This APCr is classified as a hazardous waste, having a European Waste Catalogue (EWC) code of 19 01 07*[4], and must be sent to hazardous landfill. In the UK, the amount of waste which is incinerated has increased year on year from just under 5 million tonnes in 2006 to 10 million tonnes in 2016(DEFRA, 2017). 2-5 wt% of waste incinerated becomes APCr and an estimated 300,000

[4] An asterisk (*) next to a EWC code means that the material is a hazardous waste.

tonnes of APCr is produced each year. As the amount of waste incinerated is expected to increase, so too is the amount of APCr.

A number of technologies have been developed to treat this material, for example carbonation of the residue to make solid carbonate blocks. This process involves the reaction between CO_2 and the lime in the APCr which produces a solid that can be used in breeze block applications. The process is known as the accelerated carbonation reaction and requires the addition of water to the APCr to promote the reaction. The mechanism involves the dissolution of CO_2 gas and Ca^{2+} from the solid into water where the reaction takes place to form a carbonate shown in Equation 5-8 to Equation 5-10 (Li et al. 2007).

$$H_2O + CO_2 \rightarrow H_2CO_3 \qquad \text{Equation 5-8}$$

$$H_2CO_3 \rightarrow H^+ + HCO_3^- \rightarrow 2H^+ + CO_3^{2-} \qquad \text{Equation 5-9}$$

$$Ca^{2+} + CO_3^{2-} \rightarrow CaCO_3 \qquad \text{Equation 5-10}$$

However, this method does not deal with the heavy metal components which could potentially leach into the environment. Vitrification of the material on the other hand transforms the APCr into a non-hazardous glass. Plasma technology can be used for this application and the advantage of using plasma is that it can volatilise the heavy metals and other volatile components such as chlorine and remove them from the bulk material. The resulting bulk material is a non-hazardous glass which has very low leaching characteristics shown in Table 5-7.

However, the glass as it is has little value and although it could be used as an aggregate it would only achieve around £6/tonne. The low value of the slag makes the economic benefits of the process lie on the avoidance of the gate fee costs of hazardous landfill. This makes the process only marginally economic, but increasing the value of the slag, even modestly to £50/tonne would have an enormous impact on the process economics. For a plasma vitrification plant producing around 20,000 to 30,000 tonnes per year of slag, such a value of the slag would generate around £1.2m revenue per annum which would cut the processing costs of APCr via this technology by 30% making it much more attractive for potential clients.

Table 5-7: Leaching results for vitrified APCr via thermal plasma. The leaching tests were performed to EN 12457-3 at liquid/solid ratio 2 with a particle size less than 4 mm.

Element	**leaching results (mg/kg)**		
	Sample A	**Sample B**	**Limits of inert landfill**
As	0.003	0.0046	0.5
Ba	0.012	0.009	20
Cd	0.0005	0.0005	0.04
Cr	0.0082	0.0168	0.5
Cu	0.0146	0.017	2
Hg	0.0005	0.00056	0.01
Mo	0.0036	0.001	0.5
Ni	0.005	0.001	0.4
Pb	0.0036	0.001	0.5
Sb	0.044	0.034	0.06
Se	0.001	0.001	0.1
Zn	0.002	0.001	4
F	0.22	0.2	10
Cl	10	4	800
SO4	10	10	1000
Total dissolved solids	506	90	4000
Dissolved organic carbon	13.8	90	4000
Phenol index	0.2	0.2	1

The composition of the APCr is dependent on the composition of the waste which is being incinerated. The differences in habits and customs around the world means that composition of waste is different and consequently so is the composition of APCr. A survey by the author of the composition of APCr in the literature and from commercial data from various sources around the world has shown that the material's composition is extremely variable. The composition generally has a similar Si/Al, but the bulk composition changes due to the lime addition. The emissions cleaning processes in incineration plants would vary and employ different technologies. Wet scrubbing is widely employed to remove pollutants such as chlorine and ammonia from gas streams. These wet scrubbing technologies often use chemical scrubbing agents to increase the removal efficiency of the pollutant. The chemical agent is usually either lime or sodium hydroxide and the composition of the APCr will reflect the chemicals used in the abatement system.

The compositional variation of the major and minor components in the APCr is shown in Figure 5-7 and Figure 5-8 respectively. The figures show the wide deviation of the SiO_2 and CaO. Similarly to Figure 5-6, the CaO composition can vary significantly and this can have a major impact on the fluxing requirements for the process. The compositional variation of the majority of the components is much less variable. The concentration of chlorine in the material is also very variable and its concentration can be very high at over 20%. This means that there would be a significant amount of volatile components produced during the process including Na, K species which are present at around 5%.

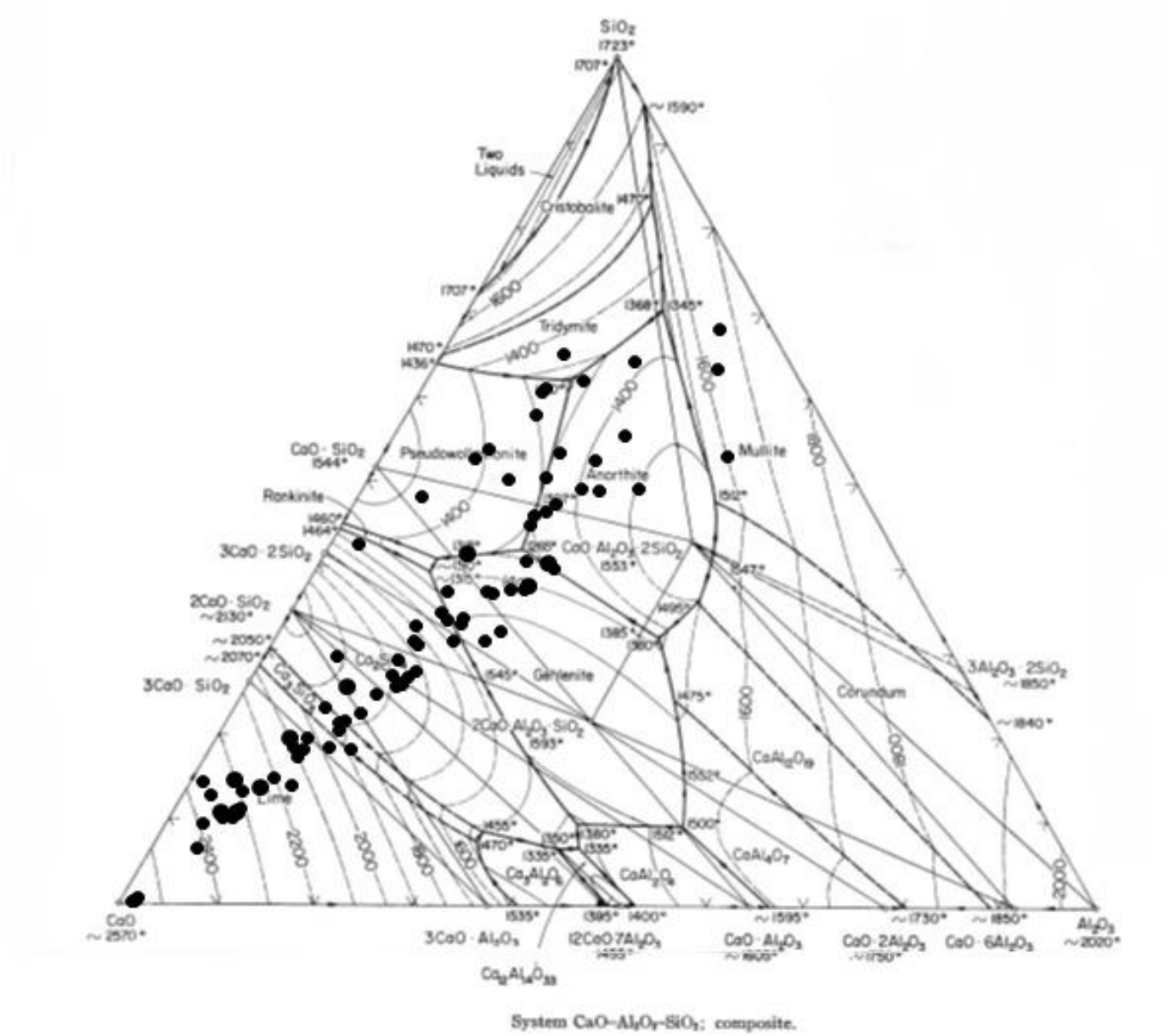

System CaO–Al_2O_3–SiO_2; composite.

Figure 5-6: Normalised CaO-SiO_2-Al_2O_3 compositions of APCr produced from industrial data and literature by the author.

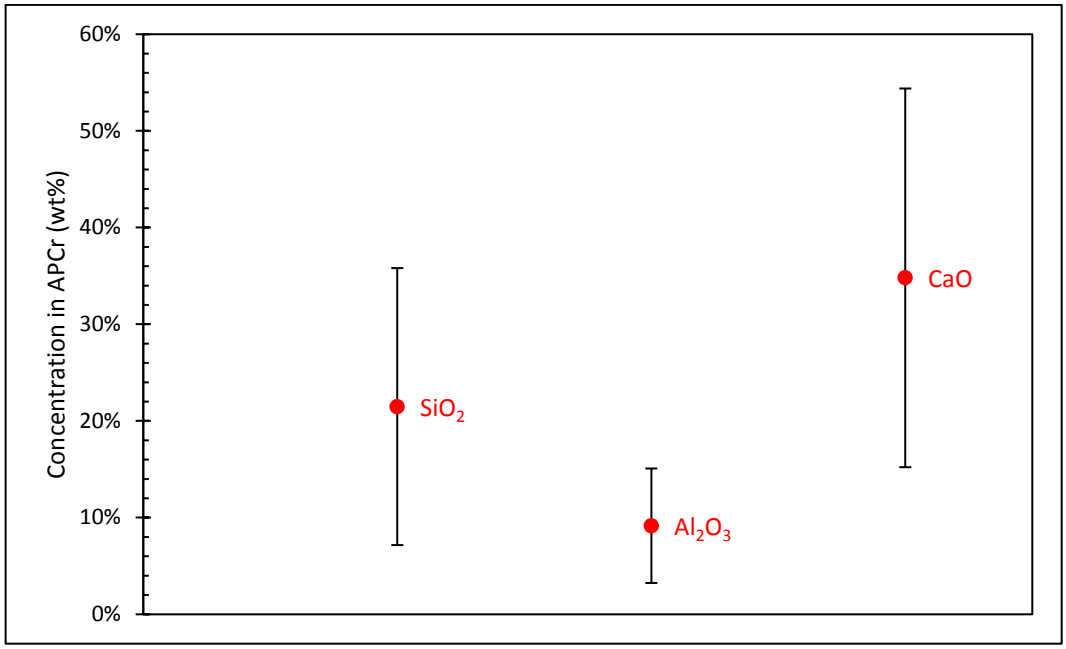

Figure 5-7: Average composition of the major components in the APCr. The error bars represent the standard deviation. Data from survey taken by the author.

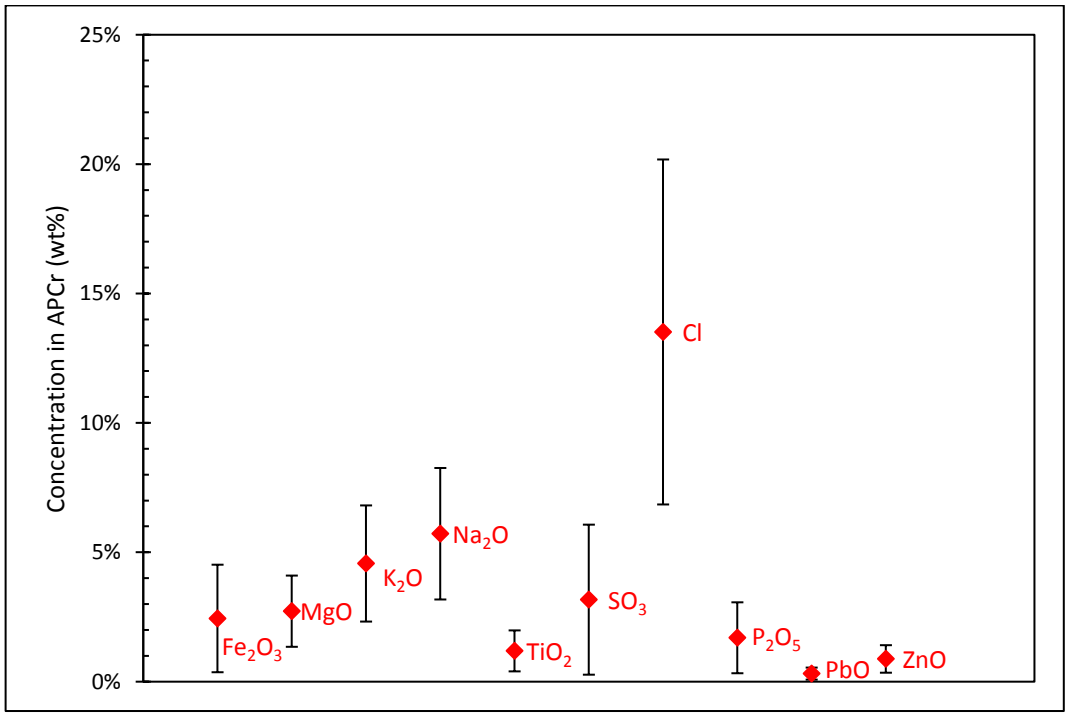

Figure 5-8: Average concentration of minor components in APCr. The error bars represent the standard deviation. Data from survey taken by the author.

Components such as Na, K, S and Cl species are volatile and so the variation of their concentration is less important to the resulting slag because the majority of these components will volatilise and partition to the off-gas system during the vitrification process. Therefore, it is the variation of the concentration of the major species which will partition to the slag phase which is of most importance to the properties of the resulting slag.

Based on a survey by the author of vitrification trials by Tetronics and other reported data the partitioning of the components of APCr during the process could be produced and a predicted slag composition can be predicted from the empirical partitioning data shown in Table 5-8 and Table 5-9. For some components the accountability is not good due to the limitations of the analytical procedures used and that some of these materials may have partitioned to various other solid residues during the process for example the thermal oxidiser dust which was not included due to the lack of data.

Table 5-8: Partitioning of components to the slag phase and baghouse dust (off-gas particulate) during the plasma vitrification of air pollution control residue (APCr).

Component partitioning	Slag	Baghouse	Accountability
Na2O	4%	19%	23%
MgO	76%	2%	78%
Al2O3	99%	1%	100%
SiO2	99%	1%	100%
P2O5	51%	6%	57%
K2O	0%	18%	18%
CaO	98%	2%	100%
TiO2	81%	0%	81%
Mn3O4	66%	14%	79%
Fe2O3	86%	13%	99%
BaO	65%	8%	72%
ZnO	0%	22%	22%
PbO	0%	17%	17%
CuO	3%	41%	44%
SnO2	0%	27%	27%
TC	0%	36%	36%
S	33%	7%	40%
Cl	13%	13%	26%

Table 5-9: Predicted slag composition produced from empirical partitioning data during the vitrification of air pollution control residue (APCr).

Component	wt %
SiO2	29.1%
Al2O3	12.4%
CaO	46.7%
Fe2O3	2.7%
MgO	2.7%
K2O	0.0%
Na2O	0.3%
TiO2	1.3%
SO3	1.4%
Cl	2.3%
P2O5	1.1%
PbO	0.0%
ZnO	0.0%

It is therefore of interest to understand if the changing composition of slag has an effect on the ability of the material to be used as a cement replacement. If there was a significant difference in the performance of the various slag compositions, it may mean that there could be limitations on which slags could be used as a cement replacement or slag compositions may have to be redesigned with this performance in mind.

5.8. Conclusions.

There are a number of opportunities to reuse slag and generate a significant revenue for the material. The properties of slag derived products are, on the whole, very good and often superior to traditional products on the market and glass ceramic tiles or slag wools can demand very high prices. However, to produce products which such a high value, significant capital investment would have to be made to build a process to make them. Such an investment would have to be decided on the basis of the scale of the slag production and probability of breaking into the market. It is important to remember that markets such as the slag wool market have very dominant players making it hard to release a competitive product. The use of slag as an aggregate may be the easiest application for the material to be used for further applications, but the low value of these materials make it an unattractive route. On the other hand, the use of slag as a cement replacement is more attractive due to the higher value of the material than as aggregate (£50/tonne as opposed to £6/tonne), and simpler preparation requirements compared to glass ceramics or other cast products. The use of slag as a cement replacement needs only a fast cooling rate followed by grinding which requires less unit operations and may require less energy than the casting routes. The energy requirement for grinding may be significant and must be accounted for in the commercialisation of the material. The small footprint of the plasma process is an advantage

of the technology allowing it to be easily retrofitted onto existing sites and so not increasing the footprint too much would be beneficial. The downside of the use of slag as a cement replacement is the dominance of the industry by blast furnace slag. This material is the most widely used slag and is highly regulated making it potentially difficult for competing material to enter to market. However, GGBFS can be sold at prices between £60-80/tonne and so offering a cheaper alternative may a good gateway to the market. This would be helped by proving that the composition of the material is not a vital performance criteria for the slag and this is a main focus of this chapter. There is a trend in the industry to accept low carbon construction materials and so this may be met in a rise in the demand for slag. The steel industry in the UK and in parts of Europe is not performing well and with the closure of some steel plants and blast furnaces within the UK there may be a reduced supply of GGBFS which could potentially be met by an alternative slag.

6. Increasing the Value of Plasma Derived Slag.

6.1. Slag as a pozzolan.

The pozzolanic reaction is the reaction between slag and calcium hydroxide ($Ca(OH)_2$) produced during cement hydration forming additional calcium silicate hydrate (CSH). The pozzolanic activity of the slag will determine the extent of the reaction with $Ca(OH)_2$ and determine the strength of the concrete. The pozzolanic activity of slag can be assessed using a direct Frattini test or an indirect strength activity index (SAI) test. The Frattini test determines the consumption of $Ca(OH)_2$ by slag via a titration and the SAI compares the strength of a concrete cube with a certain level of cement substitution to one made just with ordinary Portland cement (OPC). The SAI is calculated via Equation 6-1 where S_p is the strength of the concrete block with the pozzolan (MPa) and S_O is the strength of the concrete block using only OPC. As a control, the OPC block would have a SAI of 1.

$$\frac{S_P}{S_O} \qquad \text{Equation 6-1}$$

Typically, the SAI of a cement-pozzolan blend after 28 days is less than 1, because the pozzolanic reaction is slow as cement must first react with water and produce $Ca(OH)_2$. The British Standard (BS EN 196-5:2011) states that the acceptable SAI for a 20% substitution of OPC by a pozzolan is at least 0.8 after 28 days as this means the pozzolan is contributing to the strength of the material.

In this study, 50 x 50 mm concrete cubes were made using cement specification I (CEM I) produced by Rugby Cement, aggregate, ground slag and water. The mix, shown in Table 6-1, was prepared following BS EN 196-5:2011 and Donatello et al. (2010). The slag used was

derived from the process outlined in chapter 4. The ingredients were mechanically mixed for 5 minutes to ensure all the particles were covered with water then placed into steel cube moulds before being vibrated to compact the ingredients. The cubes were left for 24 hours to set before being removed from the moulds and allowed to cure for 7 and 28 days wrapped in plastic before their compression strength was determined using a Denison compression testing machine with a compressive rate of 2 kN/s.

The results in Figure 6-1 show that the slag displays pozzolanic activity and contributes to the strength of the concrete. At 28 days, the SAI of the slag-cement blend is 0.81 which is a positive indicator of the consumption of calcium hydroxide by the slag. The SAI for all the different slag substitutions at 28 days is greater than at 7 days which shows that the pozzolanic reaction is slow and the effects cannot be seen immediately. However, it can be seen in Figure 6-2 that the strength development of slag-pozzolan blends continues to increase and after 90 days the SAI of the cement-slag blend is greater than 1.

Table 6-1: Test mixtures prepared to test the pozzolanic activity of slag.

% cement substitution	OPC (g)	Aggregate (g)	Slag (g)	Water (ml)
0	450	1350	0	225
20	360	1350	90	225
40	270	1350	180	225
50	225	1350	225	225
60	180	1350	270	225
80	90	1350	360	225

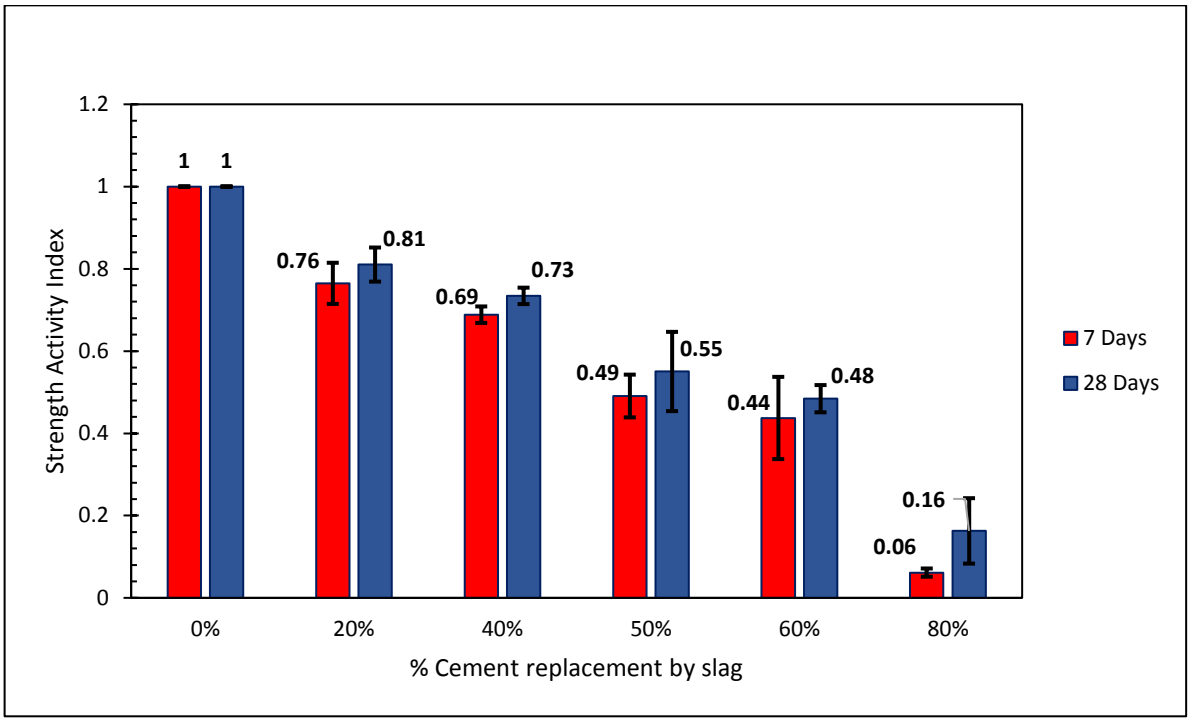

Figure 6-1: The strength activity index of concrete blocks made by the substitution of cement using different amount of plasma derived slag (average of 6 tests).

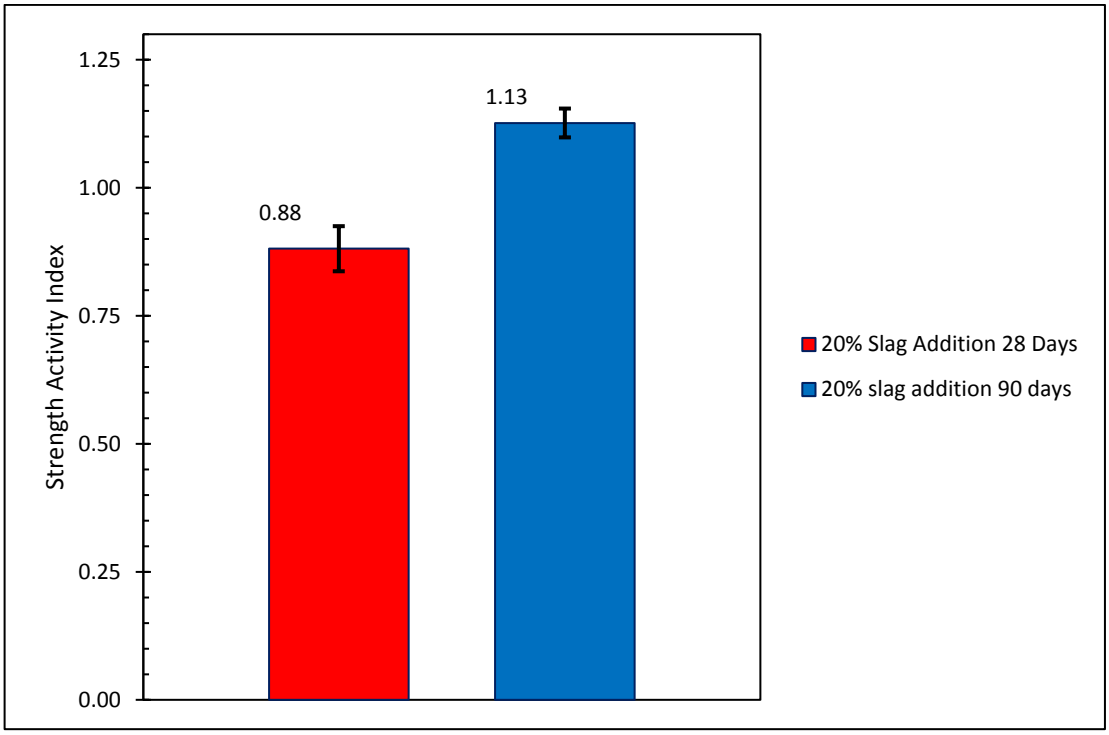

Figure 6-2: The strength activity index of a slag-cement blend after 28 days and 90 days.

The SAI of the slag is dependent on the level of cement substituted and the SAI decreases as the slag addition increases because the amount of $Ca(OH)_2$ produced is reduced limiting the reaction.

However, the reactivity of the slag can be improved by reducing the particle size of the slag. As the particle size of the slag decreases, its reactivity increases causing an increase in the SAI. This is shown in Figure 6-3 where the SAI of the slags with a d90 of 63 µm or less show an SAI at or above 0.8. The SAI of these slags are comparable to commercially available pozzolan-cement blends shown by the CEM II bar which was a commercially available fly ash-cement blend which have a typical fly ash addition of around 20-30%. As the particle size of the slag

becomes coarser, the SAI drops and these particles of slag are not reactive enough to effectively contribute to the strength of the material.

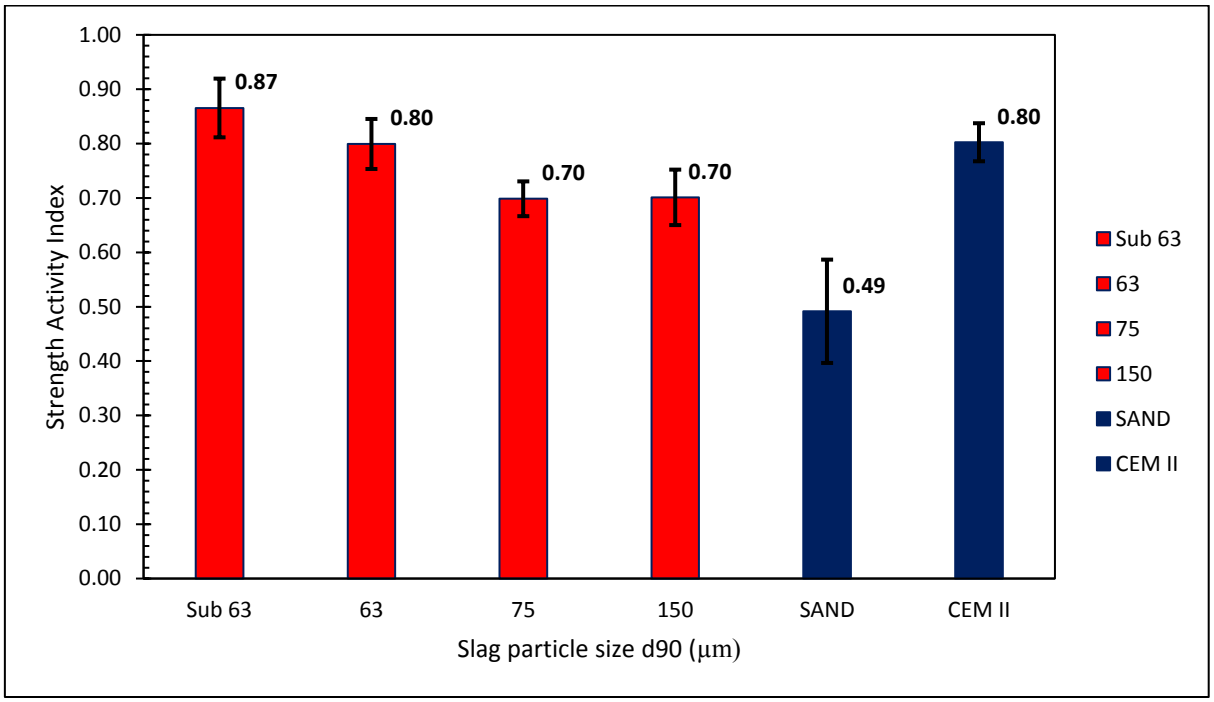

Figure 6-3: A graph showing the effect of particle size on the strength activity index (SAI) of a cement-slag blend with 20% slag substitution after 28 days.

Therefore, the physical properties of the slag are important for the reactivity of the material, but the composition of the material also appears to play an important role. Table 6-2 shows the compositions of various plasma derived slags and Figure 6-4 shows the differences in the SAI of these different compositions. The slags which were tested were all fully vitreous and ground to a particle size with a d90 less than 65 µm.

Although all the slags show pozzolanic activity and have an SAI of over 0.8 at 20% substitution, there is an apparent difference in their pozzolanic activity.

Table 6-2: Compositions of various plasma derived slags.

	Raw material			
Oxide (wt%)	**Chemical catalyst slag**	**Automotive catalyst slag**	**APCr**	**Lead cleaning slag**
Al_2O_3	37.2	34.1	17	10.5
SiO_2	30.5	33.6	34.1	42
CaO	28.6	13.8	40.8	18.4
Fe_2O_3	1.6	2.2	2.1	8.1
Na_2O	1.1	0.1	0.4	1.6
TiO_2	0.2	0.5	1.7	0.5
ZrO_2	0.1	1.5	0	0.1
K_2O	0.1	0.4	0	0.9
MnO	0.1	0	0.1	4.7
MgO	0	9.3	2.3	10
CeO_2	0	4.6	0	0
P_2O_5	0	0.2	1.5	0

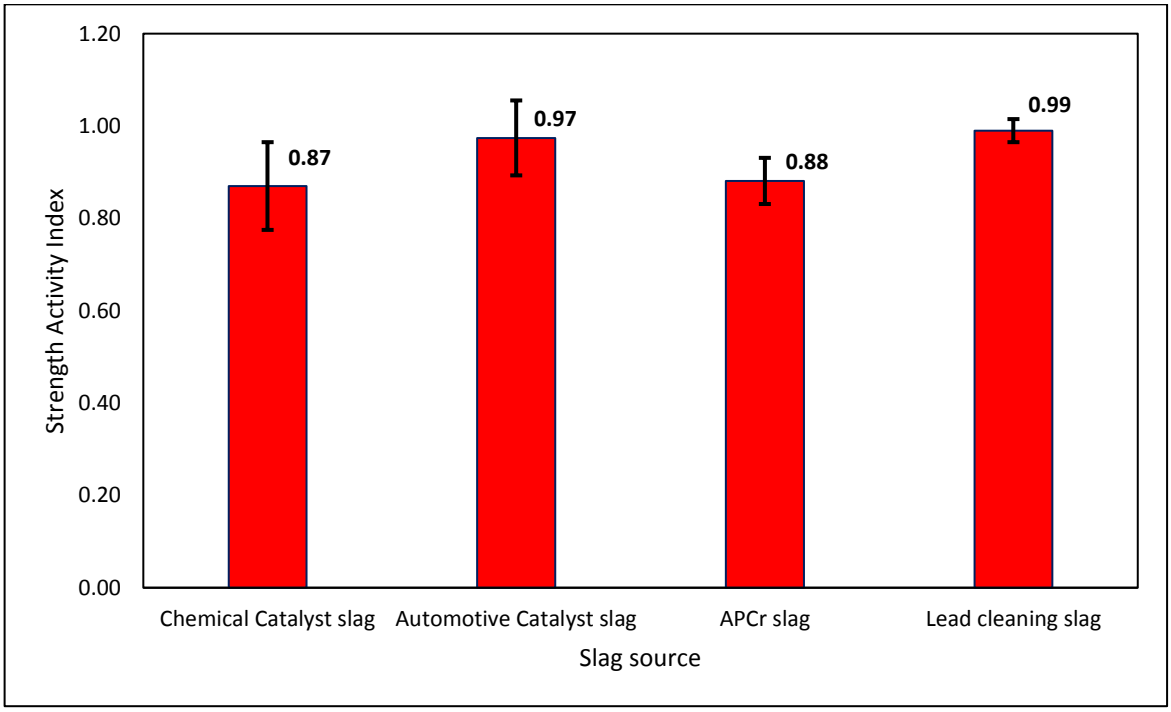

Figure 6-4: A graph showing the strength activity index of various plasma derived slags with a particle size less than 63 μm.

The composition of the slag seems to have a role in determining its pozzolanic activity, but the data above is not sufficient to give an indication as to why that is.

To assess the effect of compositional variation on the pozzolanic performance of the slag several slag compositions were made by modifiying the composition of a plasma derived slag with CaO, SiO_2, Al_2O_3 and TiO_2 powders. The powders were mixed with the slag and then remelted in a graphite crucible inside a muffle furnace at 1600°C for 1 hour to ensure the material was fully molten before being removed and quenched in air to form a glass. The slag was analysised using XRD to ensure that the material was vitreous and its composition was obtained using XRF and presented in Table 6-3.

The pozzolanic activity of the samples was tested using the Frattini test using the method outlined in 196-5:2011. In the Frattini test, 20 g of cement is mixed with 100 ml of water and left for 8 days in a sealed container at 40°C after which the calcium ion concentration in the solution is determined via a titration. Samples containing 4 g slag and 20 g cement were prepared in the same way and after 8 days the calcium concentration in the solution was obtained and compared to the concentration of the cement only blend. If there was a decrease in the calcium ion concentration then it is assumed that this has been consumed by the slag. The extent of the consumption of calcium hydroxide could then be related to the pozzolanic activity of the slag.

The hydroxyl ion concentration was also determined via a titration because the solubility of calcium is dependent on the pH of the solution. The hydroxyl ion concentration was determined by titrating the solution against 0.1 mol/l hydrochloric (HCl) acid and using

methyl-oragne indicator. The end point was when there was a colour change of the solution from yellow to orange. The hydroxyl concentration was calculated using Equation 6-2.

$$[OH]^{-} = \frac{1000 \times 0.1 \times V_h \times f_h}{50} \quad \text{Equation 6-2}$$

Where V_h is the volume of HCl solution used for the titration (ml) and f_h is the calibration factor for HCl determined using BS EN 196-5:2011. The factor was determined for each batch of HCl produced and was between 0.9 and 1.4.

This titrated solution was then used to determine the concentration of calcium ions. The solution's pH was adjusted to 12.5 using sodium hydroxide and then titrated using 0.03 mol/l EDTA solution with the end point determined using Patton and Reeder's regent which shows a colour change from purple to clear blue. The calcium concentration was determined using Equation 6-3.

$$[CaO] = \frac{1000 \times 0.03 \times V_E \times f_E}{50} \quad \text{Equation 6-3}$$

Where V_E is the volume of EDTA solution used for the titration (ml) and f_E was the calibration factor for EDTA which was also determined using BS EN 196-5:2011 and was determined for each batch of EDTA made and ranged from 0.6 to 0.8.

Table 6-3: The compositions of the slag samples tested for their pozzolanic activity.

	Oxide (wt%)								
Sample	**SiO_2**	**Al_2O_3**	**CaO**	**MgO**	**Na_2O**	**TiO_2**	**Fe_2O_3**	**Mn_3O_4**	**P_2O_5**
1	42.4	9.5	40.5	1.4	0.2	1.1	1.2	0.1	0.4
2	42.9	10.4	37.2	1.3	0.3	5.3	0.3	0.1	0.1
3	41.5	10.8	36	2	0.5	8.5	0.3	0.1	0.1
4	38.4	9	33.3	1.1	0.2	16.5	0.4	0.1	0.1
5	42.6	11.1	36.7	5.5	0.3	1.1	0.3	0.1	0.1
6	39.5	10.2	34.9	11.2	0.3	1	1.1	0.1	0.4
7	37.5	8.8	33.8	15.9	0.2	1	0.8	0.1	0.3
8	33.9	17.5	36.7	1.4	5.2	1.1	2.6	0.1	0.4
9	28.9	13.9	44.2	1.2	10	0.8	0.9	0.1	0.3
10	36.4	19.3	30.8	1.4	3.3	5.7	1.4	0.1	0.2
11	36.5	18.5	29.2	1.3	2.7	9.6	0.6	0.1	0.1
12	37.8	21.5	33.3	1.6	0.5	1.4	1.8	0.1	0.8
13	34.6	21.7	36.6	1.5	0.3	1.2	1.7	0.1	0.8
14	32.3	27.5	32.5	1.4	1.2	1.1	1.9	0.2	0.7
15	37.8	15.3	34	1.6	4	1.3	4	0.1	1.4
16	40.4	16.4	35.7	2.1	0.7	1.4	2.3	0.1	1
17	40.7	16.6	32.5	1.7	3.2	1.4	1.8	0.1	0.7
18	37.4	15.5	33.5	1.6	1.7	5.7	2	0.1	0.8
19	35.1	14.2	30.5	1.4	0.5	17.2	0.6	0.1	0.2
20	37.4	16.9	27.5	1.4	11.3	1.2	3.2	0.1	0.7
21	37.5	19.7	28.6	1.5	8.1	1.3	2.8	0.1	0.9

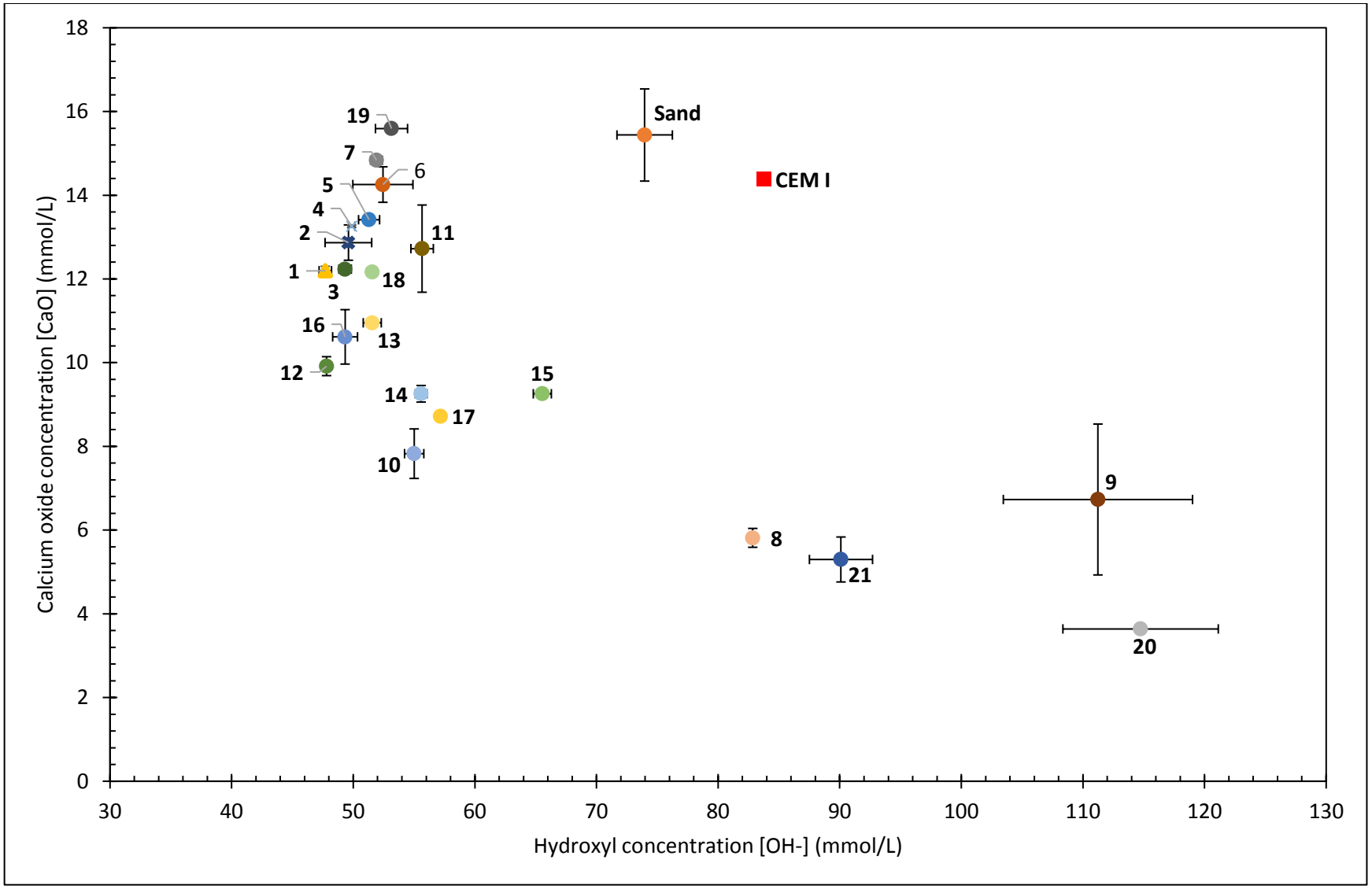

Figure 6-5: Frattini test results for various slag compositions with particle size d90 of less than 63 µm.

The results of the Frattini test are shown in Figure 6-5 and they show that the slag compositions in Table 6-3 all show calcium consumption to some degree. The control experiments which were CEM I (the cement only sample) and sand show no consumption of calcium whilst the other samples show that there has been a reduction to some degree.

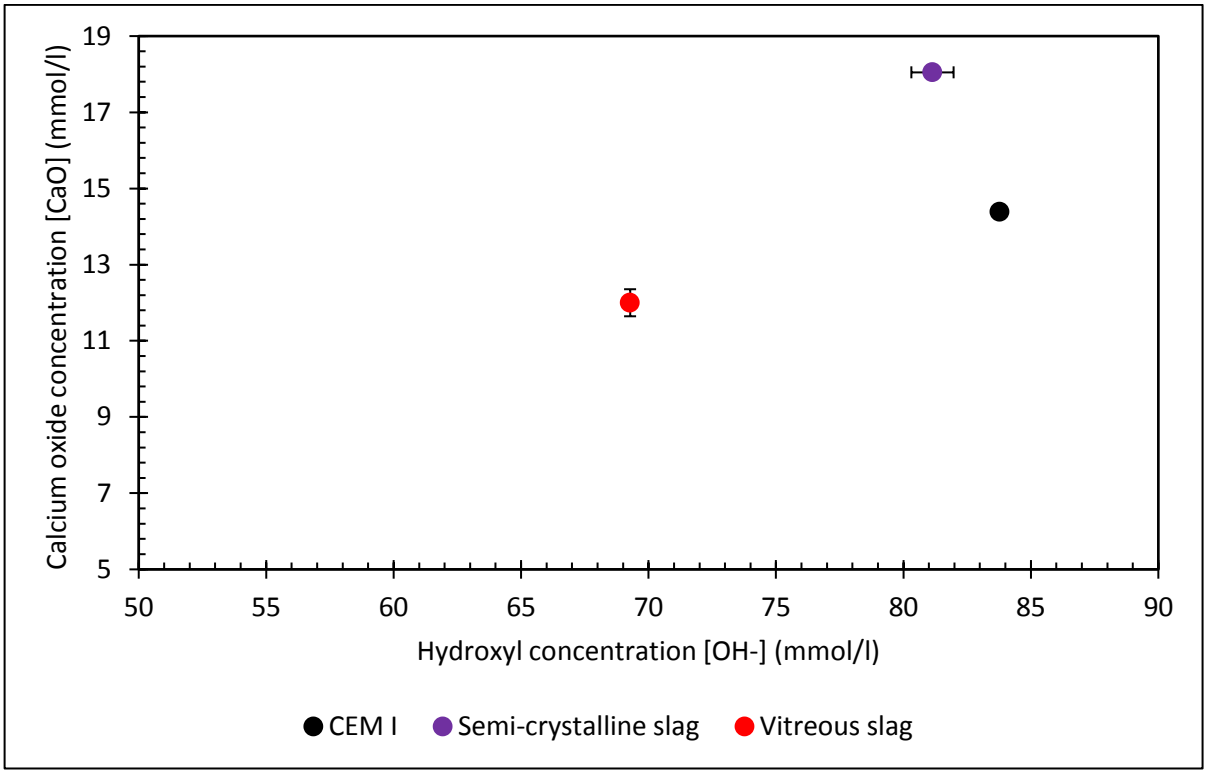

Figure 6-6: A comparison of the results of the Frattini test between a semi-crystalline slag and a vitreous slag with the same particle size (d90 less than 63 μm).

Figure 6-6 compares the results of the Frattini test between a vitreous slag and a semi-crystalline slag. The semi-crystalline slag shows no calcium consumption whereas the vitreous slag does. This means that as the slag crystallises it becomes less reactive and semi-crystalline slags are not able to be used as a cement replacement. Figure 6-7 and Figure 6-8 show the XRD patterns of the semi-crystalline and vitreous slag respectively. The pattern of the semi-crystalline slag shows that the material has anorthite ($CaAl_2Si_2O_8$) and mellilite

($(Ca,Na)_2(Al,Mg,Fe^{2+})(Si,Al)_2O_7$) as major phases and gehlenite (Ca_2Al) as a minor phase. The vitreous slag is characterised by a broad halo in the XRD pattern showing no sharp peaks characteristic of crystalline phases.

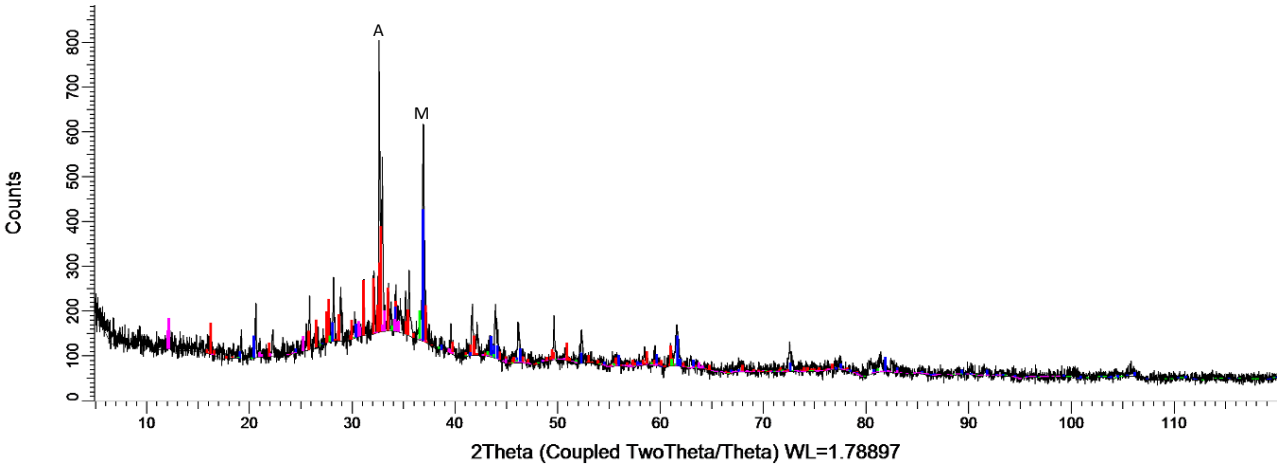

Figure 6-7: XRD pattern of a semi-crystalline slag.

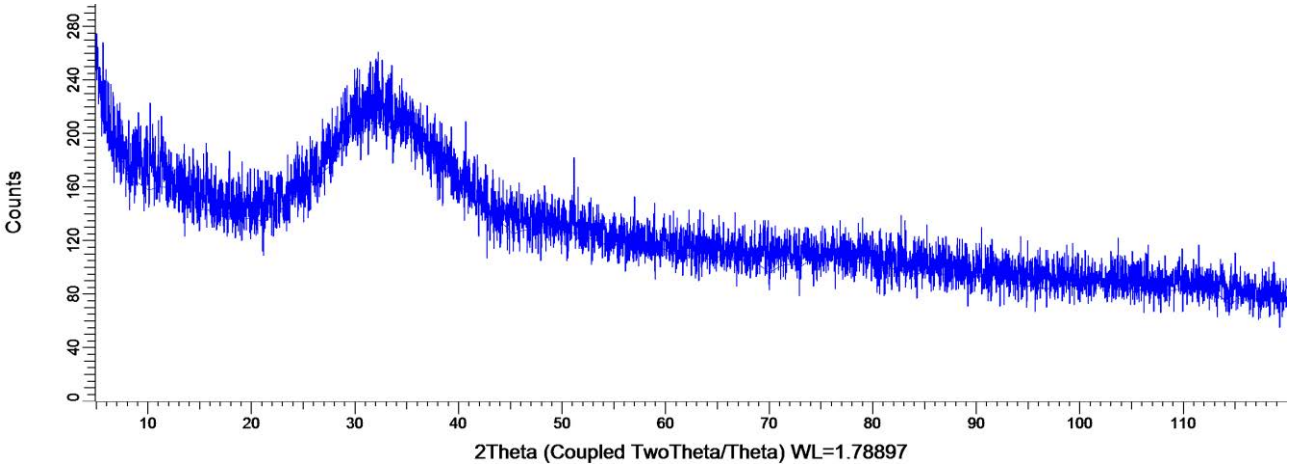

Figure 6-8: XRD pattern of a vitreous slag.

Similarly to the SAI tests, a finer particle size has a positive impact on the pozzolanic activty. Figure 6-9 compares the results of the Frattini test with two slag samples with a coarse particle size with a d90 of 73 µm and a fine particle size of with a d90 of 63 µm. As the particle size reduces, the calcium consumption increases for both slag types.

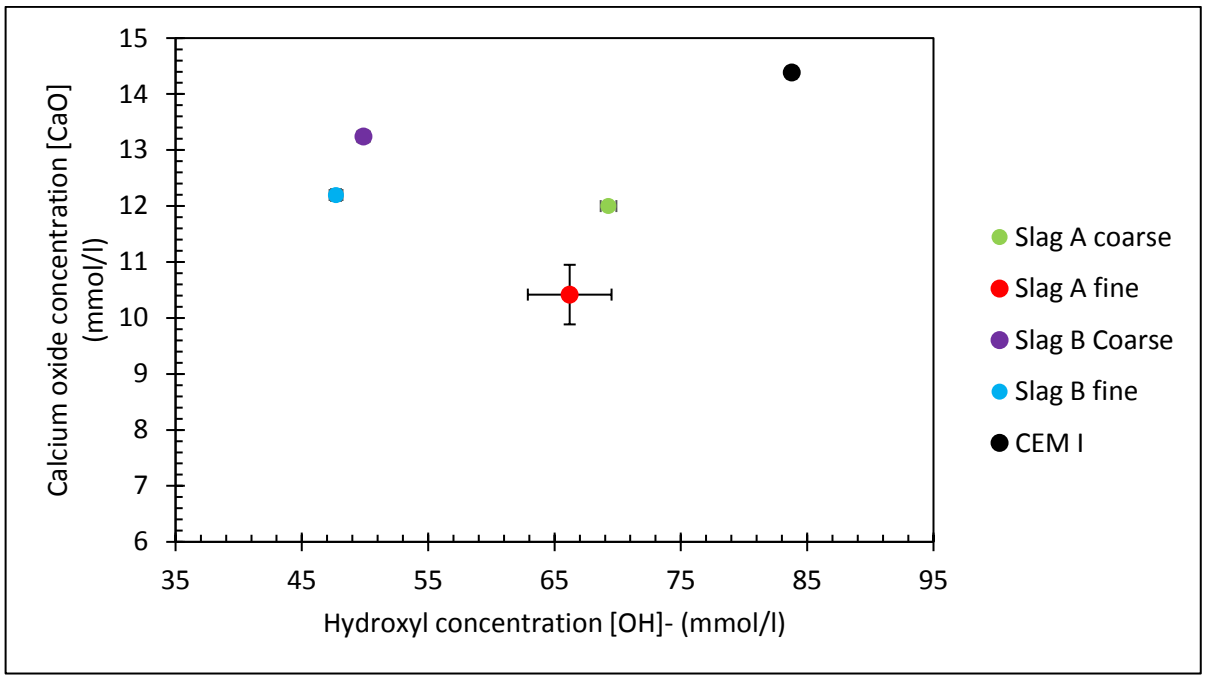

Figure 6-9: The effect of particle size on calcium consumption of slag from the Frattini test (fine slag d90 63 µm and coarse slag d90 73 µm).

Although the Frattini test is useful in determining whether or not the slag is pozzolanic, it is difficult to compare the pozzolanic activity of different slag compositions. The complex multi-component nature of the slag means that the behaviour of the slag in the solution can differ. When the slag is the solution it will leach components that have an impact on the pH of the solution and may cause an increase in the calcium concentration due to it being leached from the slag. This can cause inaccuracies of the results and so the Frattini test may not be suitable to compare slag compositions. Other components leach from the slag, for example sodium.

As the sodium leaches from the slag the hydroxyl concentration of the surrounding solution increases due to Na^+ interacting with wither water causing an increase in the pH, shown in Figure 6-10. This has an impact on the test results as calcium's solubility in water decreases with an increasing pH. However, in Figure 6-5 those slags which have the highest Na_2O content (compositions 8, 9, 20 and 21) show the highest calcium consumption. This may mean that the slag may become more reactive as the pH of the solution increases.

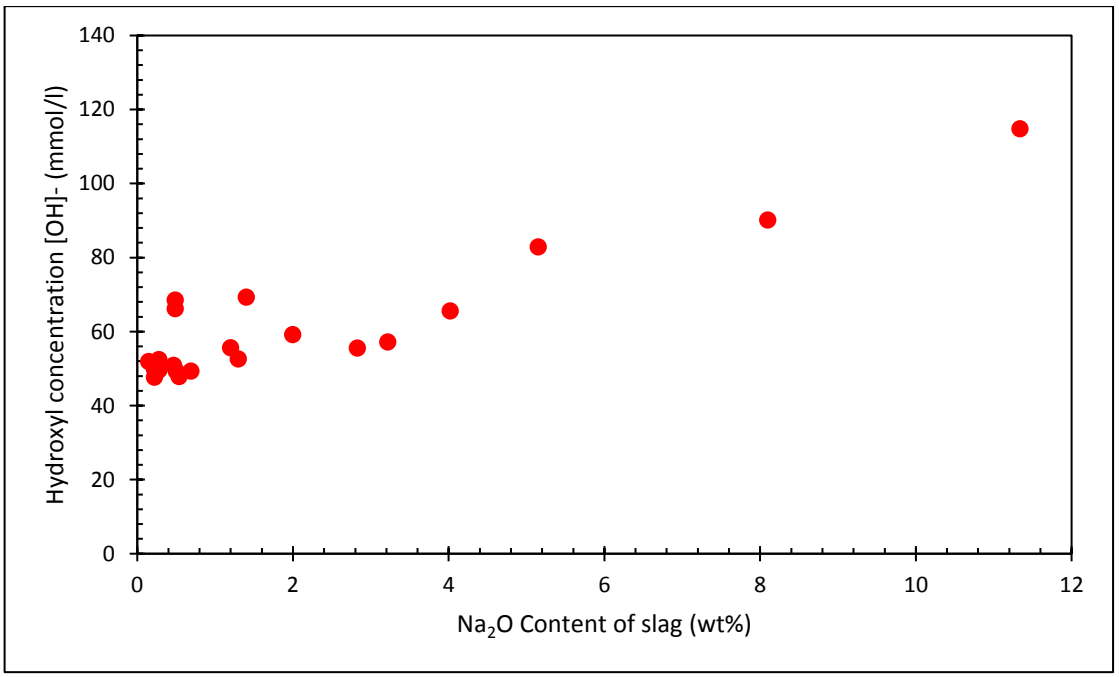

Figure 6-10: The effect of the Na2O content of a slag on the hydroxyl concentration in the Frattini test solution.

The complexity of the mixtures of pozzolanic-cement blends show that it is difficult to obtain satisfactory data to be able to fully compare the pozzolanic activity of different slag compositions. Mixing the slag with cement adds difficulty in quantifying the contribution of the slag to the strength of the material other than only being able to confirm its pozzolanic activity.

However, the reaction between $Ca(OH)_2$ and slag is not too dissimilar to the reaction between a slag and another alkaline solution. During the formation of an alkali-activated slag binder, the slag reacts with the alkaline solution and there are no other components within the system which can complicate the results. Therefore, to investigate the ability of using the slag as a cement replacement, investigating alkali-activated binders gives a clearer picture of the reactivity of the slag and enables for a better comparison between samples.

6.2. Alkali-Activated Slag (AAS) Binders.

6.2.1. Binder characterisation.

AAS binders are produced by mixing a ground slag with an alkaline solution such as sodium hydroxide at a specified solid/liquid ratio. The two components are mixed to allow for all the slag particles to be in contact with the activating solution and then placed into a mould and left for 24 hours. The material is then demoulded and cured in a sealed plastic container and a controlled environment for between 7 and 28 days.

A photograph of some alkaline activated slag (AAS) blocks can be seen in Figure 6-11 and it shows that these blocks are light coloured and would not appear unappealing if they were used as construction materials. The figure also shows a statue which was made from AAS. This shows the ease of which the material can be placed into a mould to produce intricate shapes.

Figure 6-11: A photograph of alkaline activated slag blocks.

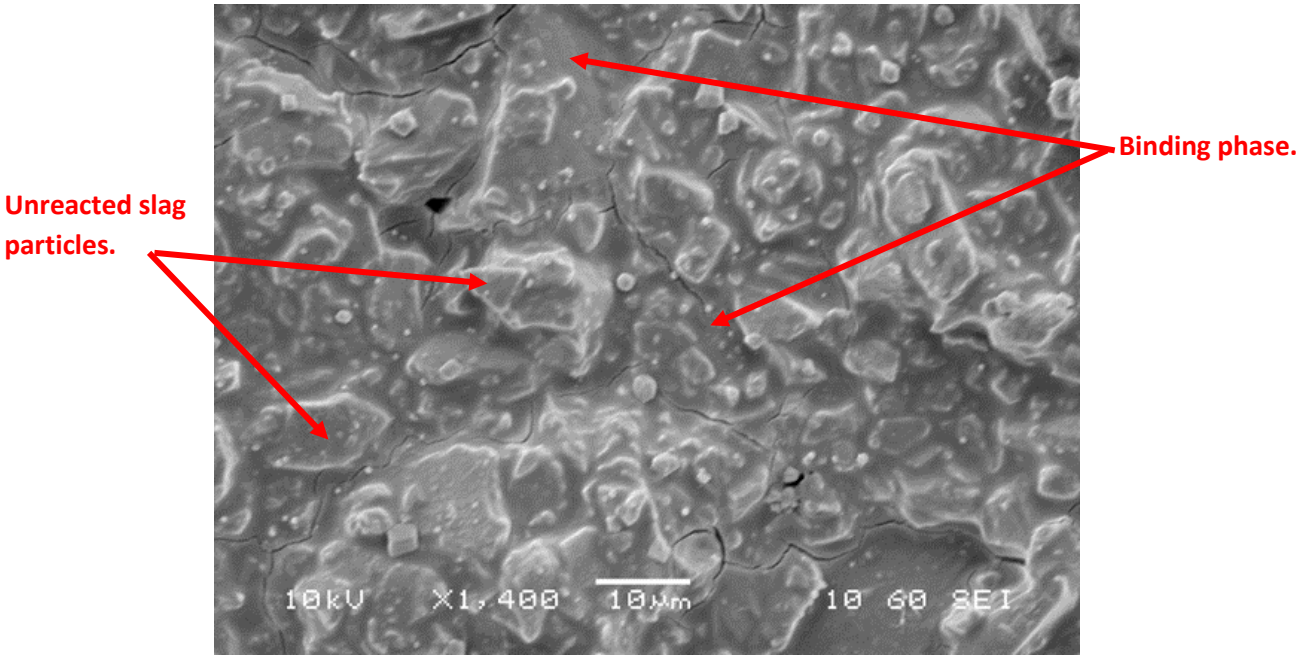

Figure 6-12: A scanning electron microscope image showing the microstructure of the alkali-activated slag.

Figure 6-12 shows the material's microstructure as a smooth binding phase surrounding the unreacted slag particles. The binding phase is composed of calcium, sodium, aluminium and silicon and SEM-EDX analysis in Figure 6-13 show the binding phase surrounding an unreacted slag particle. The unreacted slag particle contains no sodium meaning when the binding phase

is formed, the sodium from the activating solution, NaOH, combines with the Ca, Al and Si species dissolved from the slag.

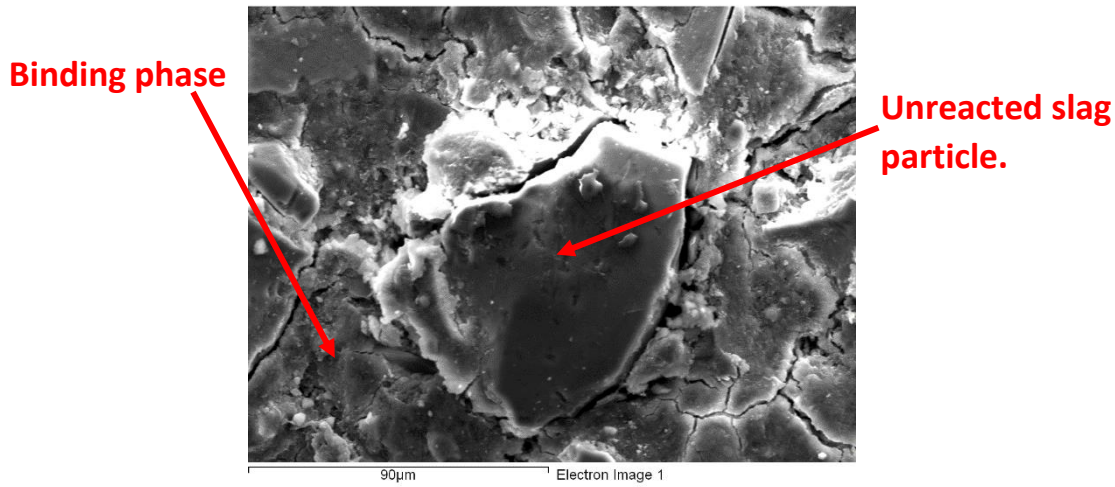

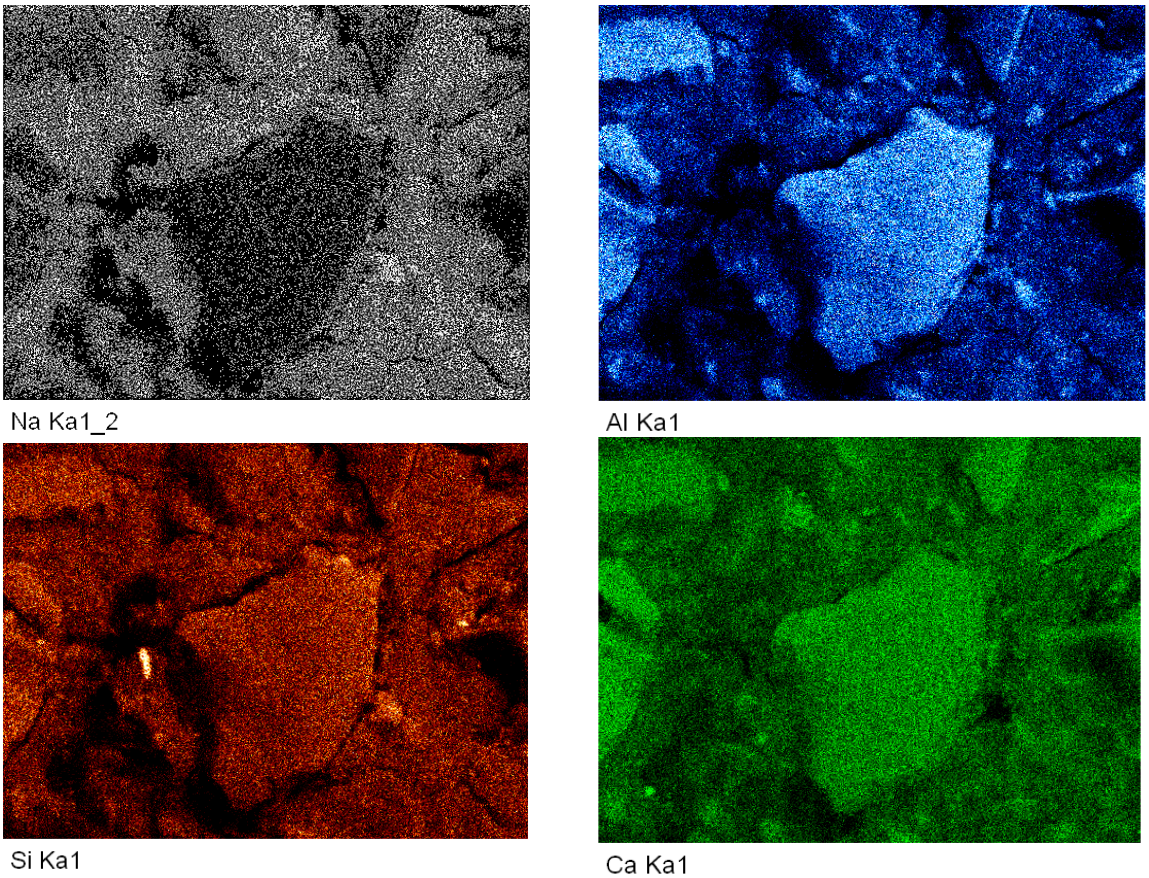

Figure 6-13: SEM-EDX images showing the composition of the binding phase of the alkali-activated slag binder. The elements shown clockwise from the top left; sodium, aluminium, silicon and calcium.

This binding phase is a calcium-sodium-alumino-silicate hydrate (C(N)ASH) gel and using FTIR spectroscopy, an idea of the binding structure its obtained. In Figure 6-14 the FTIR spectra is shown for the unreacted slag and the AAS binder. Both show a peak between 900 and 1100 cm^{-1} characteristic of aluminosilicates, but there is a shift to higher wavenumbers of the spectra when the slag undergoes alkali-activation. The centre of the unreacted slag peak is at 902 cm^{-1} whereas for the AAS binder the centre of the peak is as 953 cm^{-1}. The shift to a higher wavenumbers shows a greater ordering and polymerisation of the aluminosilicate chains which make up the binding phase. With the peak being in this region the structure of the binding gel is probably an aluminosilicate sheet structure rather than a fully polymerised three dimensional structure shown by geopolymers, whose FTIR spectra show peaks centred at wavenumbers between 1100 and 1000 cm^{-1}.

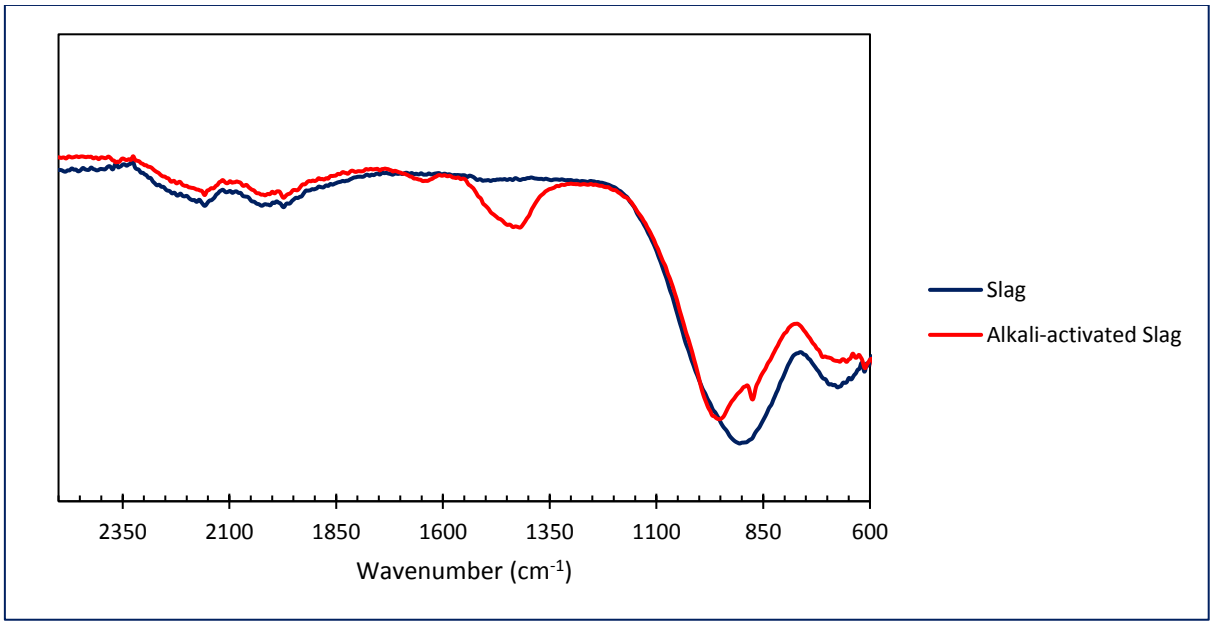

Figure 6-14: Fourier transform infrared (FTIR) spectra of an unreacted slag and an alkali-activated slag binder.

When the binding phase is formed it is X-ray amorphous, but the material slowly gains some degree of crystallinity over time shown in Figure 6-15 where after 6 months, crystalline peaks have emerged. These peaks are characteristic of zeolite phases, but due to the material still being mostly amorphous accurately identifying them is difficult.

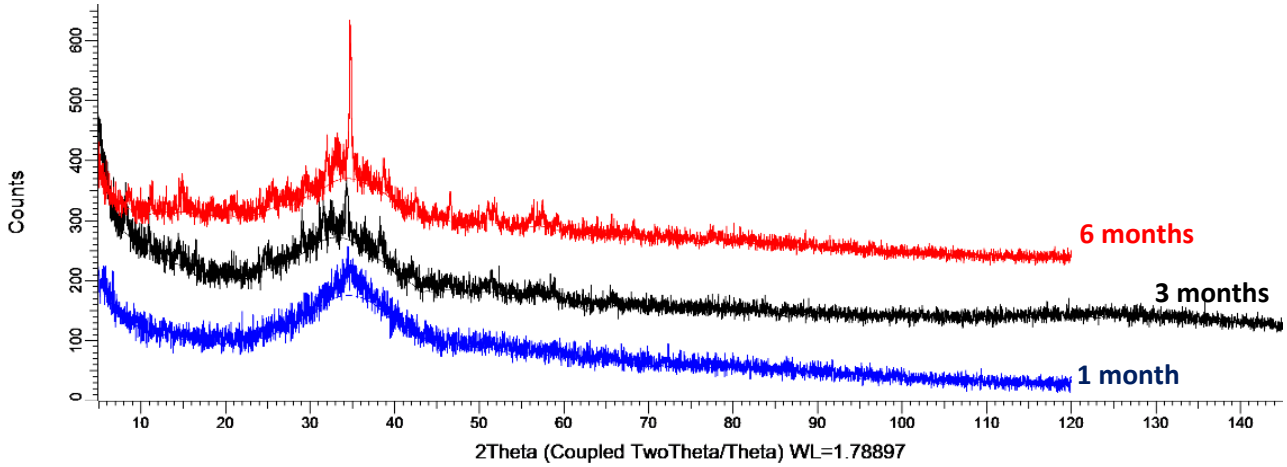

Figure 6-15: XRD patterns of alkali-activated slag binders over a period of 6 months showing a gradual formation of crystalline phases.

The crystallisation of the material occurs very slowly and may be due to the loss of water over time. It may also be caused by natural efflorescence which occurs because of the reaction between mobile components in the binding phase and CO_2 from the atmosphere. Nevertheless, the crystallisation of the binding phase seems to be promoted by unreacted slag particles acting as nucleation sites, as crystals can be seen to be growing on unreacted slag particles in the SEM images in Figure 6-16. Although no detrimental effects are observed due to crystallisation, i.e. no significant decrease in the material's strength, crystallisation may make predictions of the long term durability of the material difficult. It may be possible to reduce crystallisation by enhancing the reactivity of the slag which would reduce the number

of unreacted slag particles. This may be done by reducing the slag's particle size, changing the activating solution or altering the slag's chemistry.

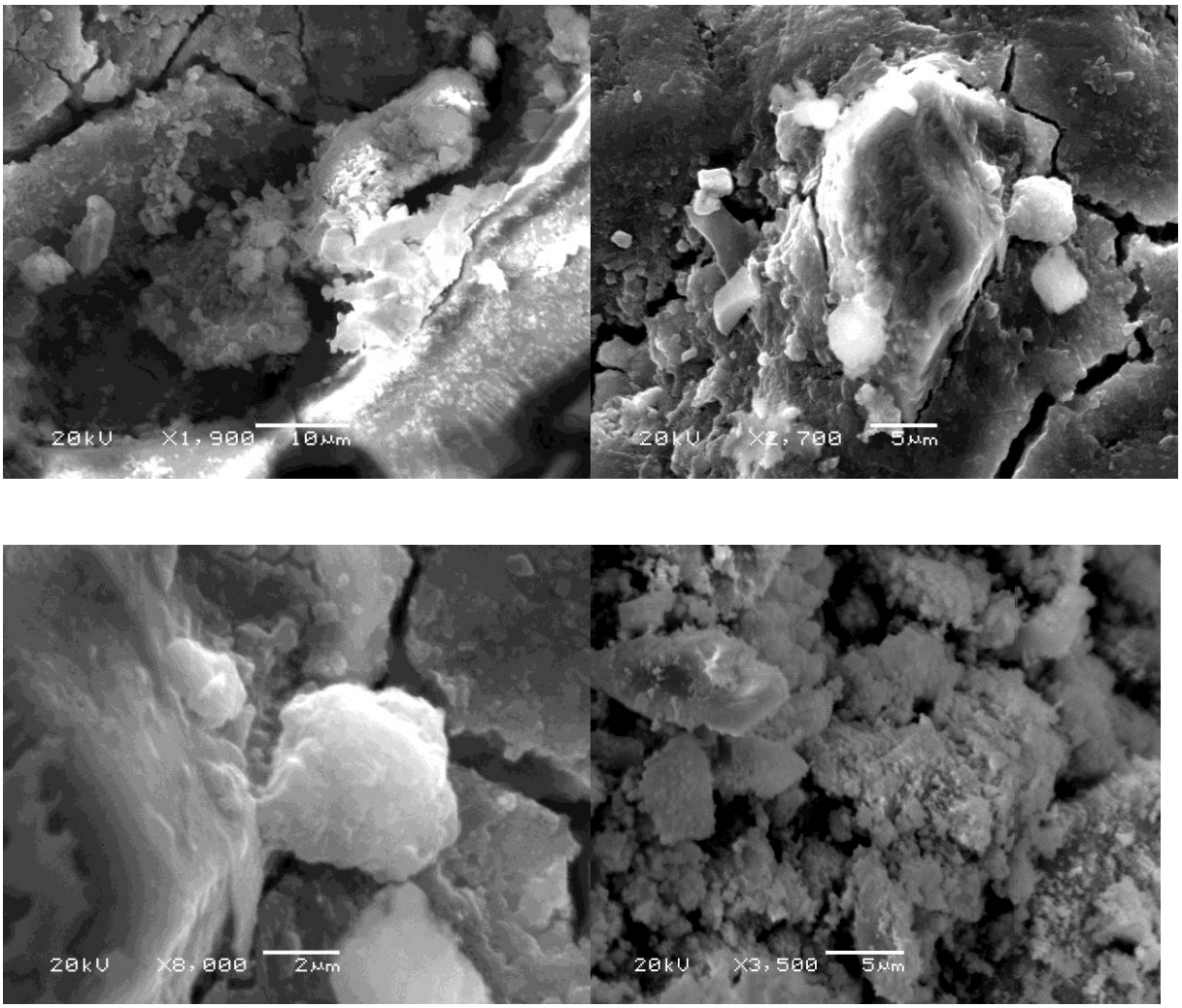

Figure 6-16: SEM images showing crystal growth on unreacted slag particles in the alkali-activated slag binder.

When the slag reacts with an alkaline solution it begins to dissolve and release species into the surroundings. Figure 6-17 shows the change in the electrical conductivity of a 200 ml, 0.25 M NaOH solution containing 10 g of slag. After around 10 minutes, the electrical conductivity begins to rise after the slag starts to react and leach components. The conductivity increases

for around 100 minutes before it levels off. Figure 6-18 shows that when the slag is put into water, there is only a very small increase in the electrical conductivity and so it is the alkaline environment which promotes the dissolution of the slag. During the production of the AAS binders, a stronger NaOH solution is used and so the reaction would be faster. Data for a stronger solution could not be obtained due to the high electrical conductivity of a NaOH solution over 1 M which was above the upper reading limit of the conductivity probe.

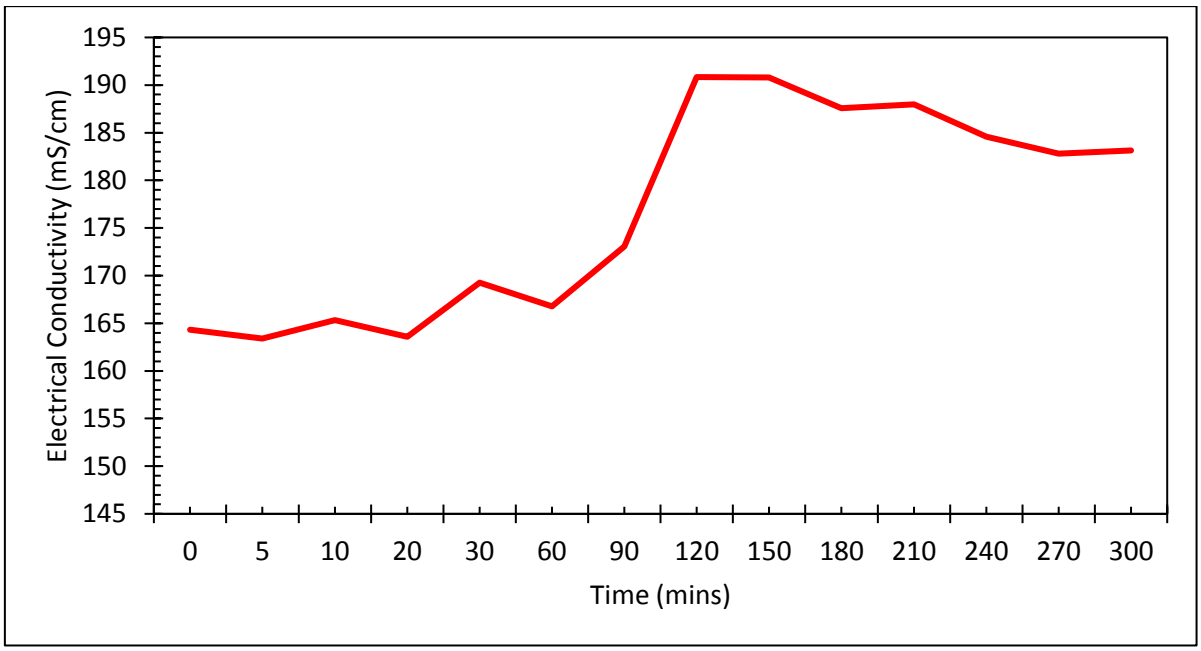

Figure 6-17: The increase in the electrical conductivity over time of a 200 ml, 0.25 M NaOH solution containing 10 g slag.

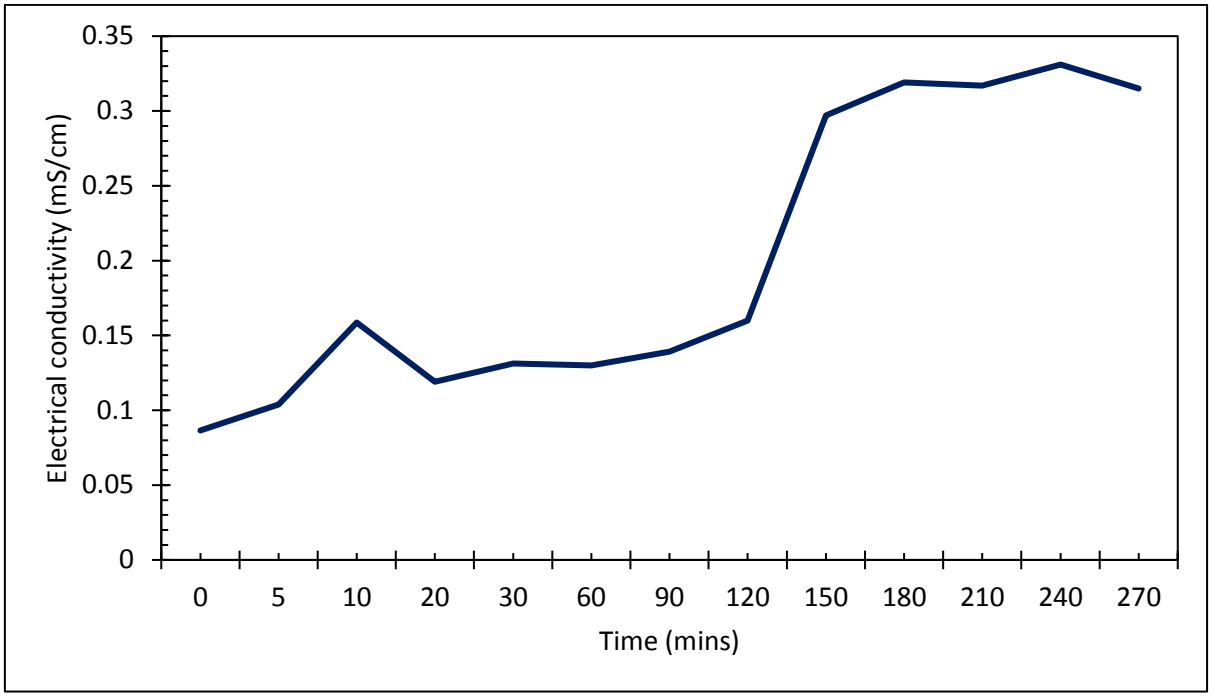

Figure 6-18: The increase of electrical conductivity over time of 200 ml distilled water containing 10 g slag.

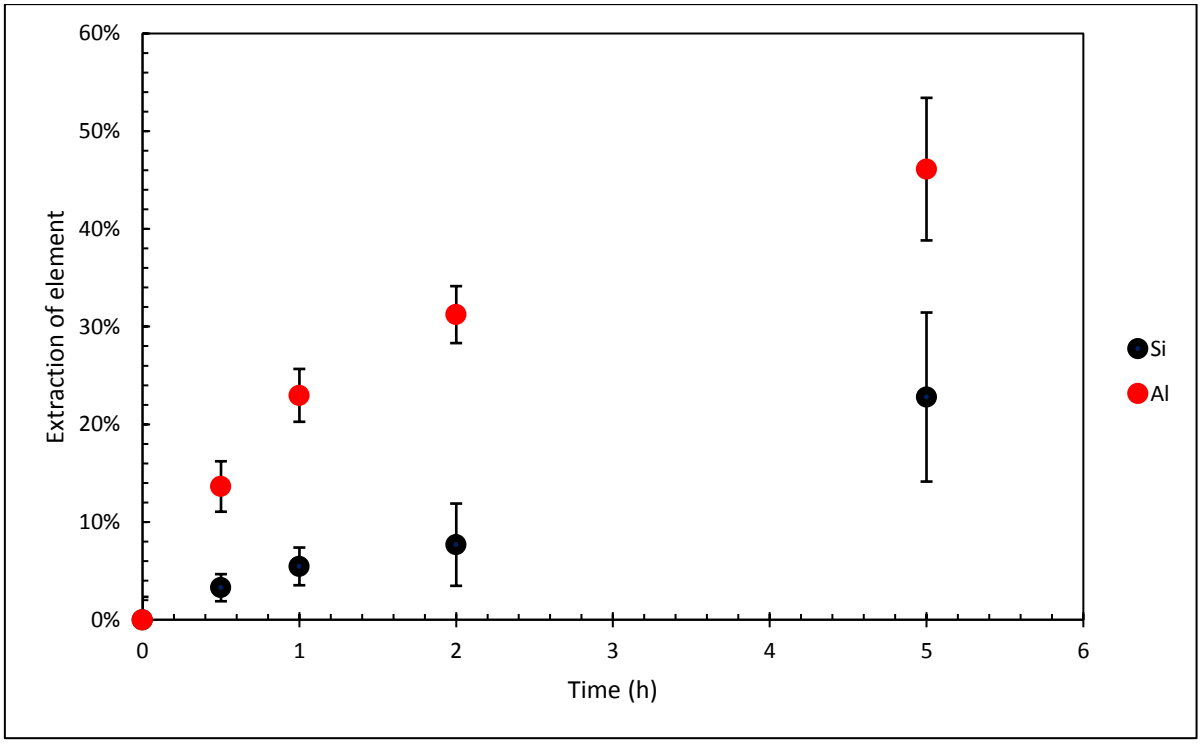

Figure 6-19: The release of Si and Al in a 6 M NaOH solution as a % of total from the slag over time.

The alkali-activated binding phase produced is composed of alumino-silicate chains formed from the aluminium and silicon species dissolved from the slag. Figure 6-19 shows the dissolution of silicon and aluminium from the slag. The data was obtained by putting 10 g of slag with a 6 M NaOH solution in a stirred vessel at room temperature. Samples of the solution were taken at various time intervals and ICP-OES was used to determine the Si and Al concentration and calculate the % extraction of the elements.

The data in Figure 6-19 shows that the release of Al from the slag is faster than the release of Si from the solution. This is because of the stability of the Si-O bond is greater than the Al-O bond and so the breaking of Al-O bonds requires less energy and Al species are more easily released into the solution (Zhang and Lüttge, 2007; Oelkers, 2001).

The significance of this is that the Si/Al ratio of the binding phase effects the strength of the material. As the Si/Al ratio increases, the strength of the binding phase increases which is shown in Figure 6-20. Therefore, the greater ease of dissolution of Al from the slag may have a detrimental effect on the final strength of the material especially if the slag does not react fully.

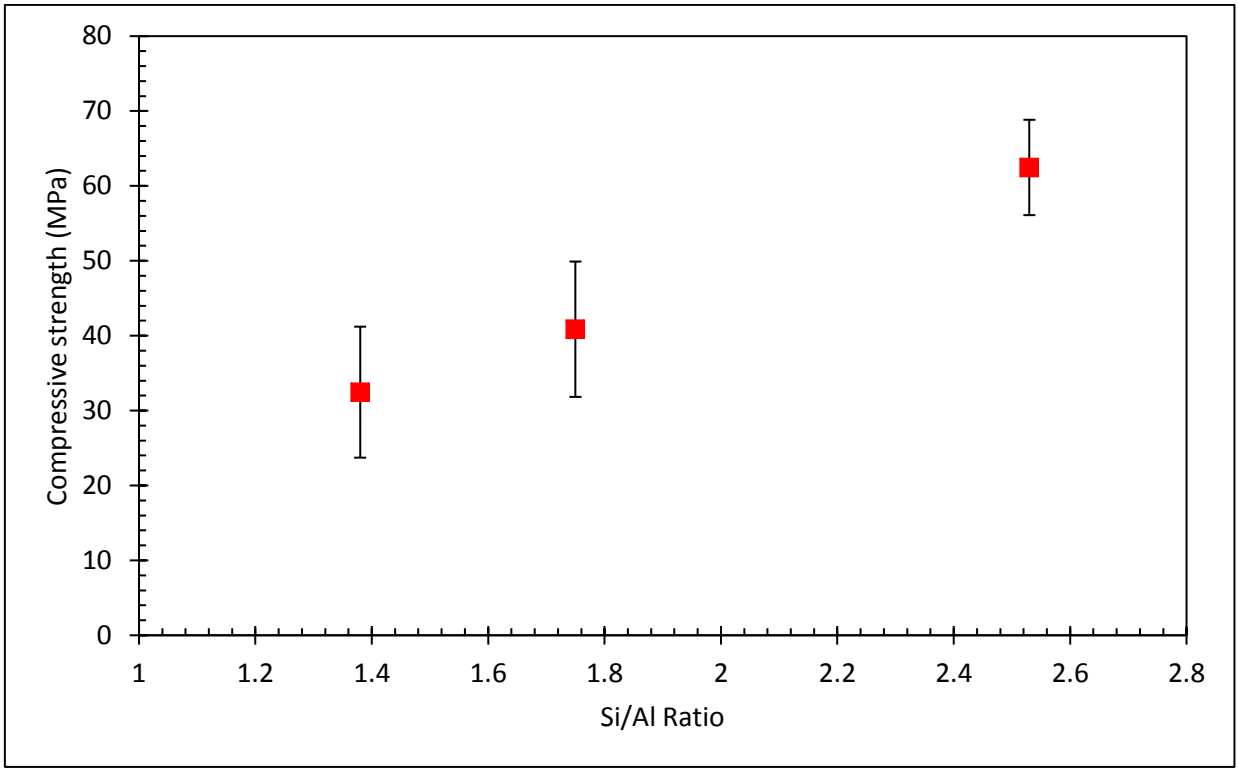

Figure 6-20: The effect of the Si/Al ratio on the strength of alkali-activated binders.

The dissolution of the slag and the formation of the binding phase can be enhanced by the alkaline-activator and the particle size of the slag. As the particle size of the slag becomes finer, the strength of the alkali-activated binder increases, shown in Figure 6-21. A finer particle size means that there is a greater surface area available for dissolution and so this increases the formation of the binding phase. The dissolution of the slag is also enhanced by the strength of the alkali-activating solution. As the activating solution's strength increases, the strength of the binder increases which is shown in Figure 6-22.

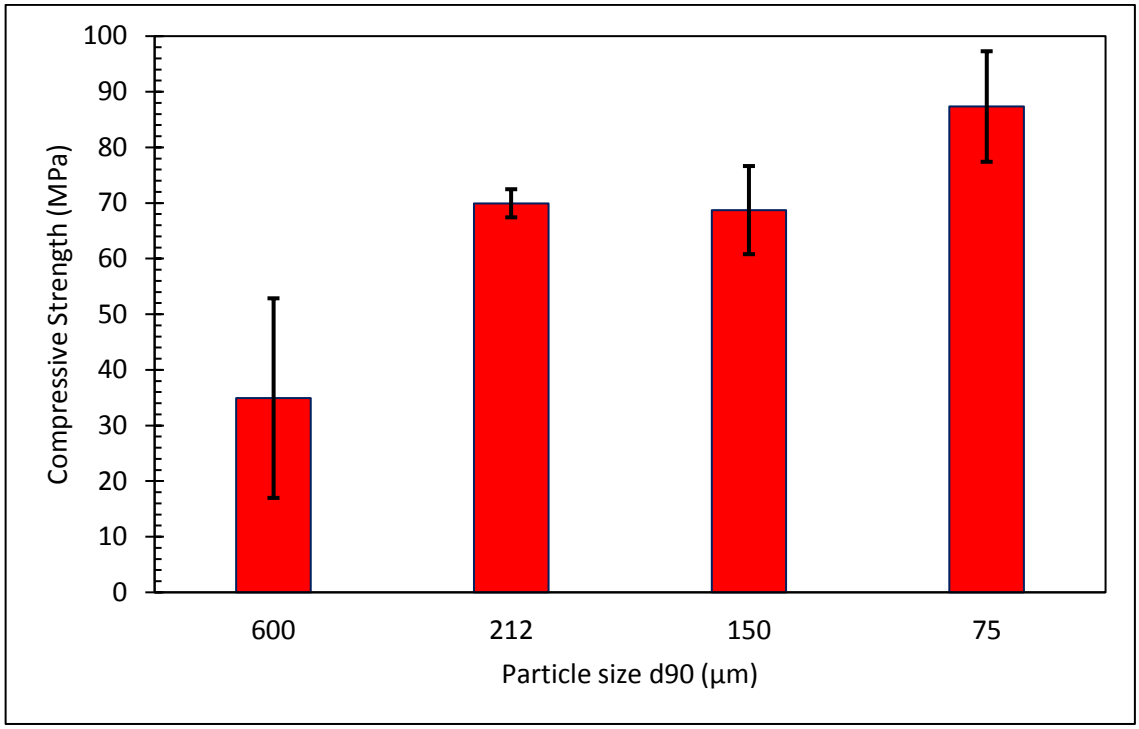

Figure 6-21: A graph showing the effect of the particle size of the slag on the strength of the alkali-activated binder.

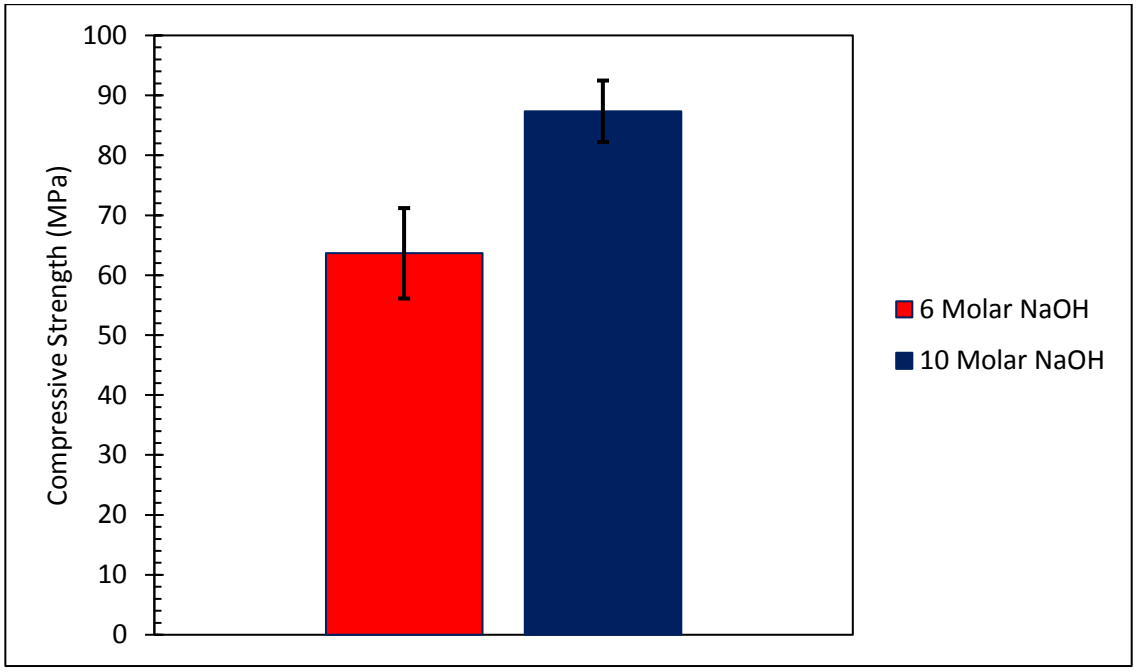

Figure 6-22: A graph showing the effect of the concentration of NaOH on the strength of the alkali-activated binder.

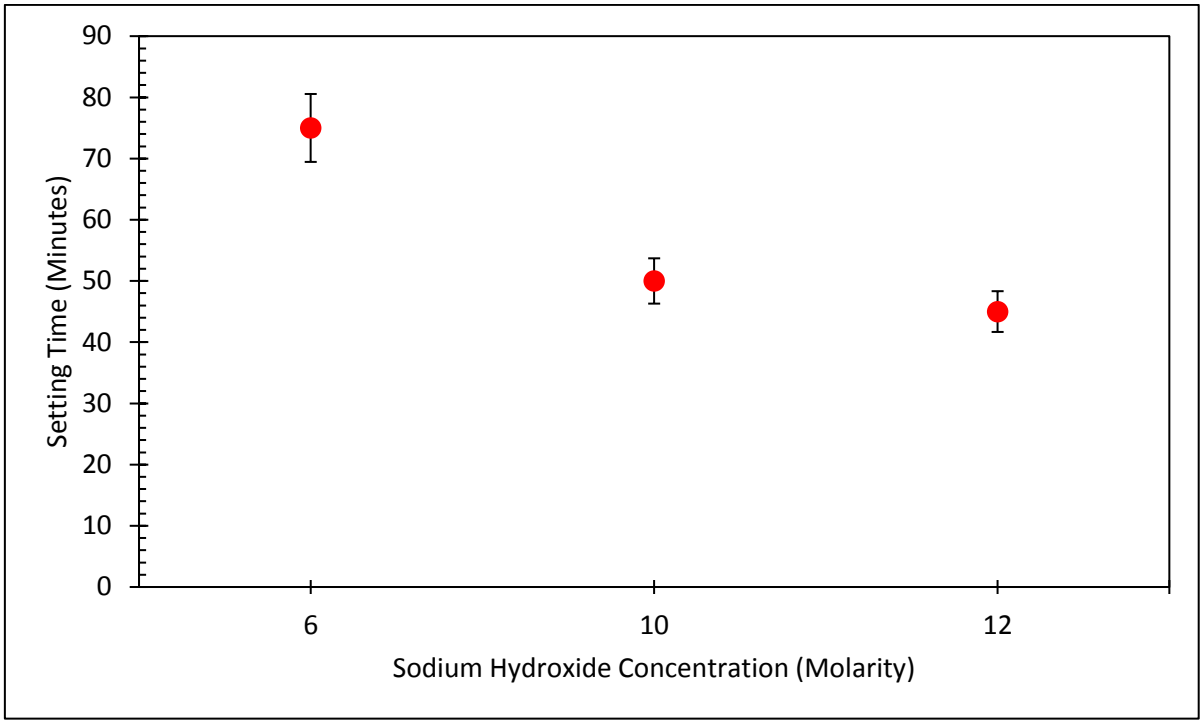

Figure 6-23: The effect of concentration of NaOH on the setting time of the alkali-activated binders.

An increased NaOH concentration has an impact on the setting time of the slag shown in Figure 6-23. The setting time decreases as the concentration of the NaOH increases. The setting time was determined via a penetration test using the Vicat method. This is where a 1 mm needle is used to penetrate the material's surface and it is judged to have set when the needle no longer visibly penetrates the material. The faster setting times of the binders produced using the higher concentrations of NaOH may be linked to the reaction rate of the alkali-activation. The setting times for all these materials is much faster than cement whose typical setting times are around 300 minutes, but this depends on the cement classification. The fast settling times of AAS may be useful in finding niche applications for them for example, quick setting of runways or roads in military applications. The addition of unreactive particles

or aggregates to the AAS mixes can increase the setting time, shown in Figure 6-24 and so there is an element of control which can be manipulation of properties is possible.

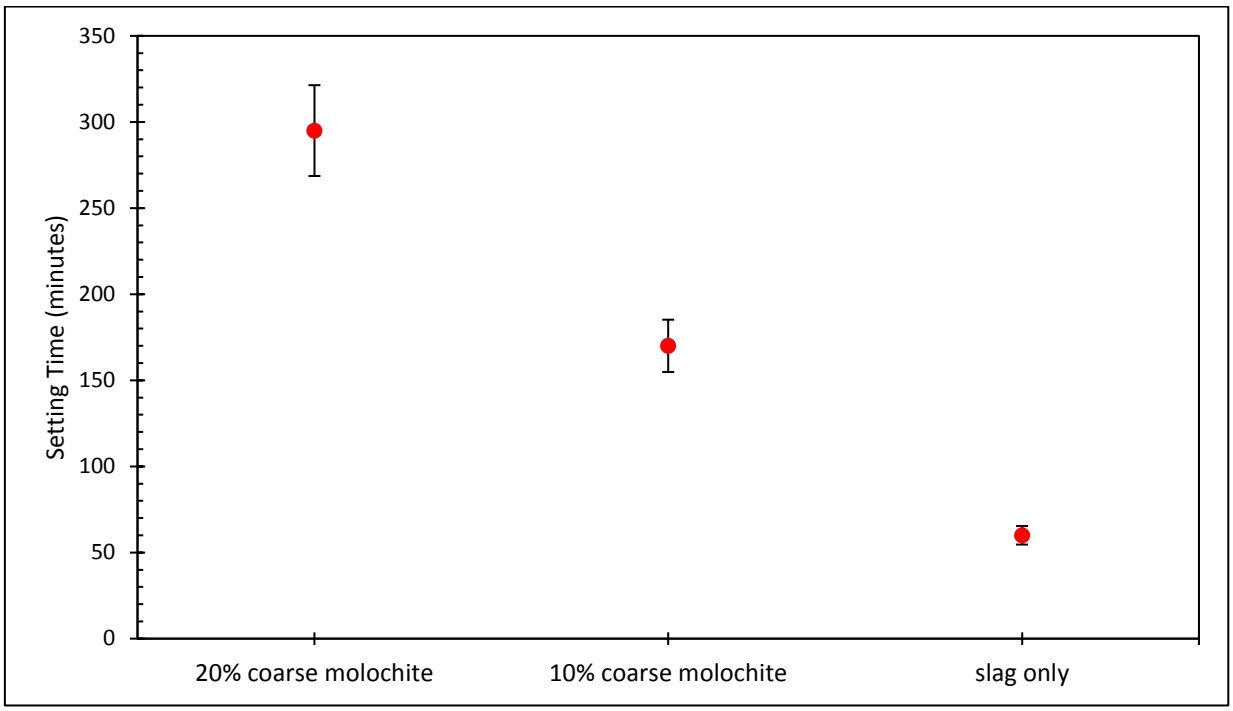

Figure 6-24: The effect of the addition of unreactive coarse molochite (>500 µm) slag on the setting time of the alkali-activated slag binders.

The slag compositions produced to investigate the effect of compositional variation on the pozzolanic activity of the slag were used to investigate differences in their alkali-activation. Each slag sample was milled to a particle size less than 65 µm using a TEMA planetary disc mill. Small alkali-activated slag cylinders with a diameter of 13 mm and a height of 13 mm were made by mixing 3 g of ground slag with 6 M NaOH at a solid/liquid ratio of 3.75, placed in a mould and compacted using a die press. The cylinders were removed from the mould and cured at 40°C in sealed plastic containers before their compression strength was determined using a Zwick Z030 universal testing machine with a 50 kN load and a loading rate of 2 N/s. A

total of six samples per composition were tested to determine their average compression strength.

The L/S ratio was determined via experimentation. Due to the small size of the cylinders, internal flaws of the material would have a greater impact on the material's strength than larger specimens. Weibull statistics were used to investigate the variability of the strength of the binders to gain confidence in the results. The Weibull modulus gives an indication on the variability of a material property and a low Weibull modulus indicates a high variability of the property. Weibull statistics can also be used to determine a characteristic strength of the material, although this has no physical significance, it can be used to predict the probability of survival of the material under given stress. The probability of survival can be calculated using Equation 6-4:

$$\mathrm{P_{sj}}(V_0) = 1 - (\frac{\mathrm{j} - 0.5}{\mathrm{N}}) \qquad \text{Equation 6-4}$$

Where, $P_{sj}(V_0)$ is the probability of survival at a given sample volume, j is the rank (the strongest sample was rank 1, the next strongest rank 2 etc.) and N is the number of samples.

The probability of survival of a sample under a given stress can be related to the material's characteristic strength and Weibull modulus by Equation 6-5:

$$\mathrm{P_s V_0} = \mathrm{e}^{\left(\left(-\frac{\sigma}{\sigma_0}\right)^{\mathrm{m}}\right)} \qquad \text{Equation 6-5}$$

Where σ is the given stress (MPa), σ_0 characteristic strength (MPa) and m is the Weibull modulus.

The solid/liquid ratio was changed to determine its effect on the strength of the material. Figure 6-25 and Figure 6-26 show the results of using Weibull statistical methods to assess the variability of the material's strength. Table 6-4 shows the characteristic strength and the Weibull moduli of the material determined from the graphs. The characteristic strength of the material is determined by the intercept of the straight lines in Figure 6-26 and as the solid/liquid ratio decreases, the characteristic strength of the material increases. However, even though the characteristic strength and the probability of survival of the material at higher stresses increases as the solid/liquid ratio decreases, the variability of the material's strength increases. This is shown by the decrease in the Weibull modulus which is determined by the gradients of the lines in Figure 6-26. The Weibull modulus for a typical ceramic is between 12 and 20 and so the Weibull moduli for these samples are low and so makes predictions about the material's strength difficult.

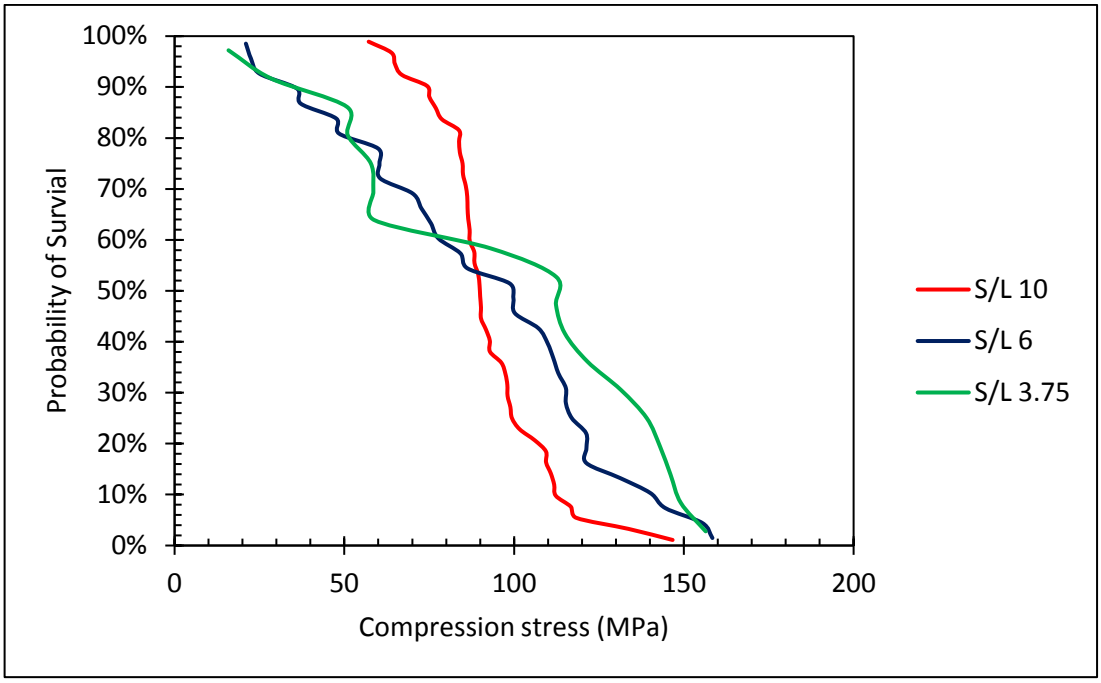

Figure 6-25: A graph showing the probability of survival at a given stress of an alkali-activated slag cylinder produced with different solid/liquid ratios.

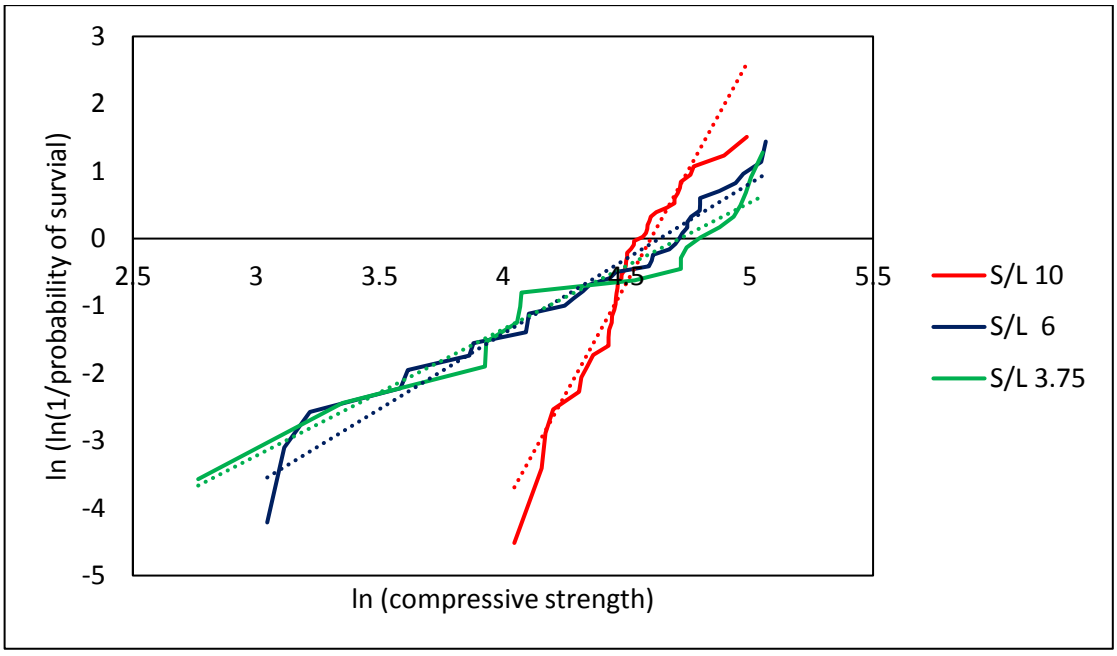

Figure 6-26: Weibull statistics plot of the natural logarithm of the probability of survival vs the natural logarithm of the compression stress for alkali-activated slag cylinders used to determine the characteristic strength (x-intercept) and the Weibull modulus (line gradient).

Table 6-4: The characteristic strength and the Weibull modulus of alkali-activated slag binders with different solid/liquid ratios.

Solid/liquid ratio	Characteristic strength (MPa)	Weibull modulus
10	99	6.7
6	103	2.2
3.75	112	1.9

SEM images of the alkali-activated slag binders in Figure 6-27 show that as the solid/liquid ratio decreases, there is an apparent increase in the amount of binding phase produced. This means that the binding phase is denser due to a greater extent of reaction of the slag making the material stronger. The increase in variability of the material as the solid/liquid ratio decreases is interesting and this may be caused by the greater ease at which a crack can propagate through the material and reach a critical crack length. The increased amount of unreacted slag particles and open pores in the material at higher solid/liquid ratios may be detrimental for crack growth and act to arrest crack growth making it more difficult for a critical crack length to be obtained.

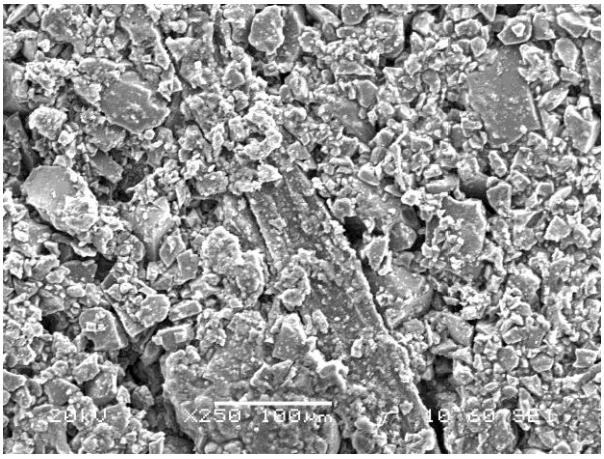

Solid/liquid ratio 10

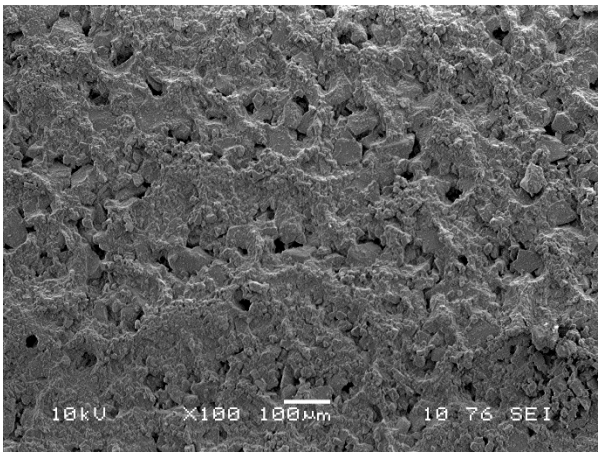

Solid/liquid ratio 6

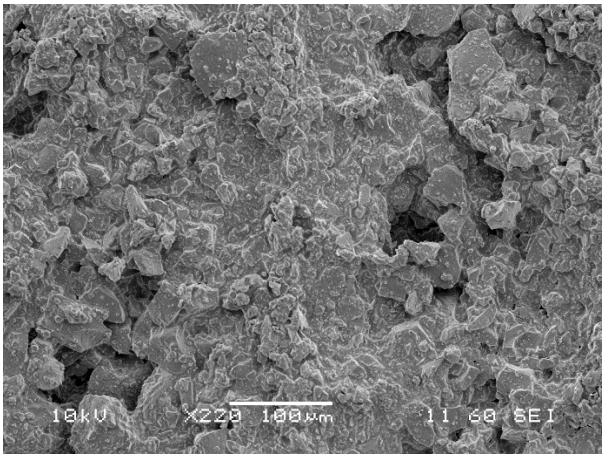

Solid/liquid ratio 3.75

Figure 6-27: SEM images showing the effect of changing the solid/liquid ratio on the appearance of the binding phase of the alkali-activated slag binders.

It is possible to reduce the variability of the material by altering the production method. When in the mould, compacting the material with higher pressures leads to an increase of the Weibull modulus. For a solid/liquid ratio of 3.75, increasing the compaction to 69 MPa resulted in a Weibull modulus of 12.8 which is more like a commercial ceramic. This gives greater confidence and predictability of the strength of the material. The increase in the compaction also results in an increase in the characteristic strength which is shown in Figure 6-29, which changes from 71 MPa to 82 MPa as the compaction pressure is increased from 41 to 69 MPa Note that the slag composition used for Figure 6-28 and Figure 6-29 is different from the slag used for Figure 6-25 and Figure 6-26 because of material availability restrictions, which resulted in lower characteristic strengths.

Increasing the compaction probably reduces the variability because of more efficient packing of the particles inside the mix. This can be seen in Figure 6-30 and Figure 6-31 showing the results of porosity measurements of AAS binders performed using mercury intrusion porosimetry. The results show that there is a slight reduction in the % porosity of the binder as the compaction increases. The average % porosity for samples sampled with 69 MPa was 15% compared with almost 17% when compacted with just 14 MPa. This is accompanied by a reduction in the mean pore diameter. However, a much greater decrease in the porosity is achieved when the activating solution is changed to sodium silicate solution. When the samples are compacted with 69 MPa but made using sodium silicate solution instead of NaOH the porosity % reduces from 15% to 8% and the mean pore diameter reduces from 0.067 μm to 0.0515 μm.

Even though the maximum strength of the binders increase as the solid/liquid ratio decreases, the material reaches its maximum strength after 7 days curing regardless of the solid/liquid ratio (Figure 6-32). The curing temperature does not seem to have an effect on the material's maximum strength (Figure 6-33), but the strength development of the material cured at 25°C is slower than when they were held at 40 or 60°C. At 25°C the material did not reach its maximum strength until 21 days and so increasing the temperature increases the reaction kinetics and it also allows for the curing time between production and testing to be reduced.

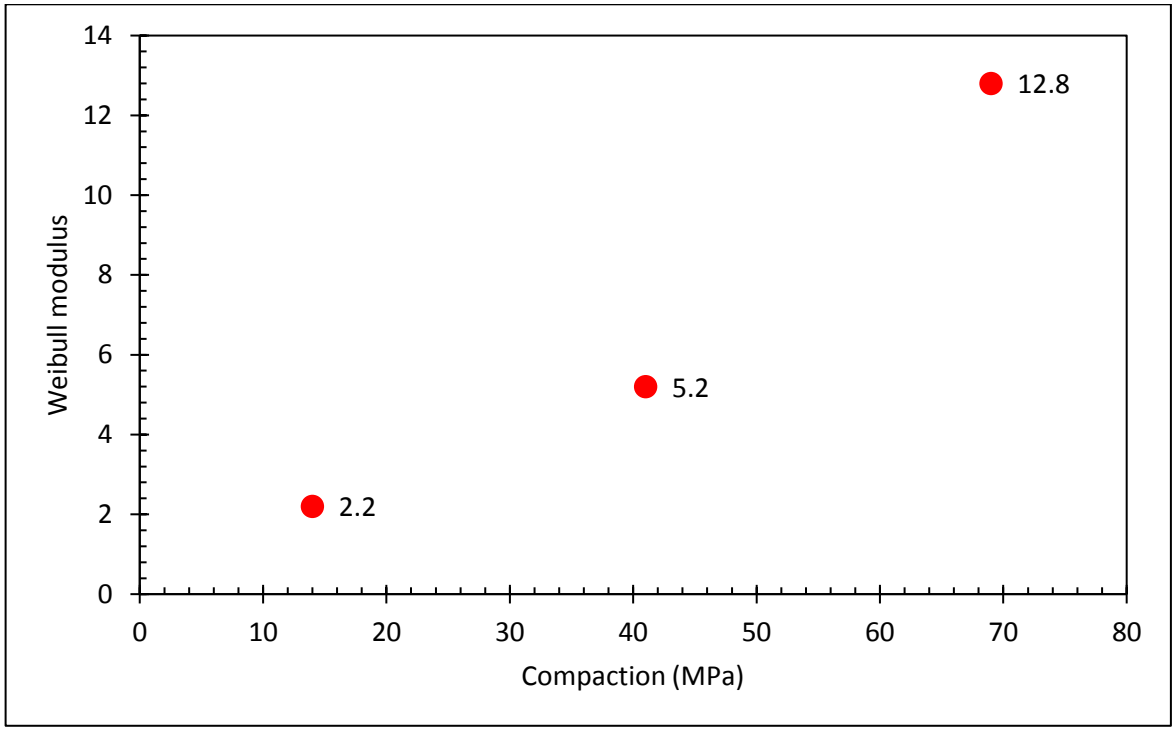

Figure 6-28: The effect of the compaction pressure on the alkali-activation mix during its production on the Weibull modulus.

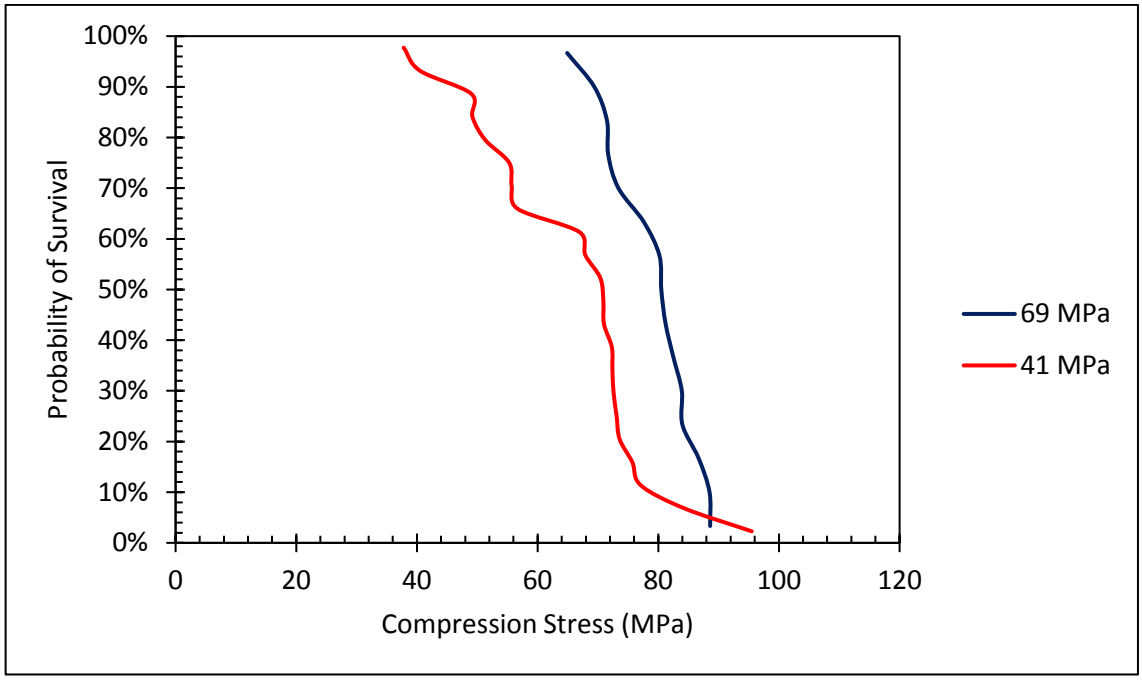

Figure 6-29: The effect of the compaction pressure on the probability of survival of the alkali-activated slag binders at a given strength.

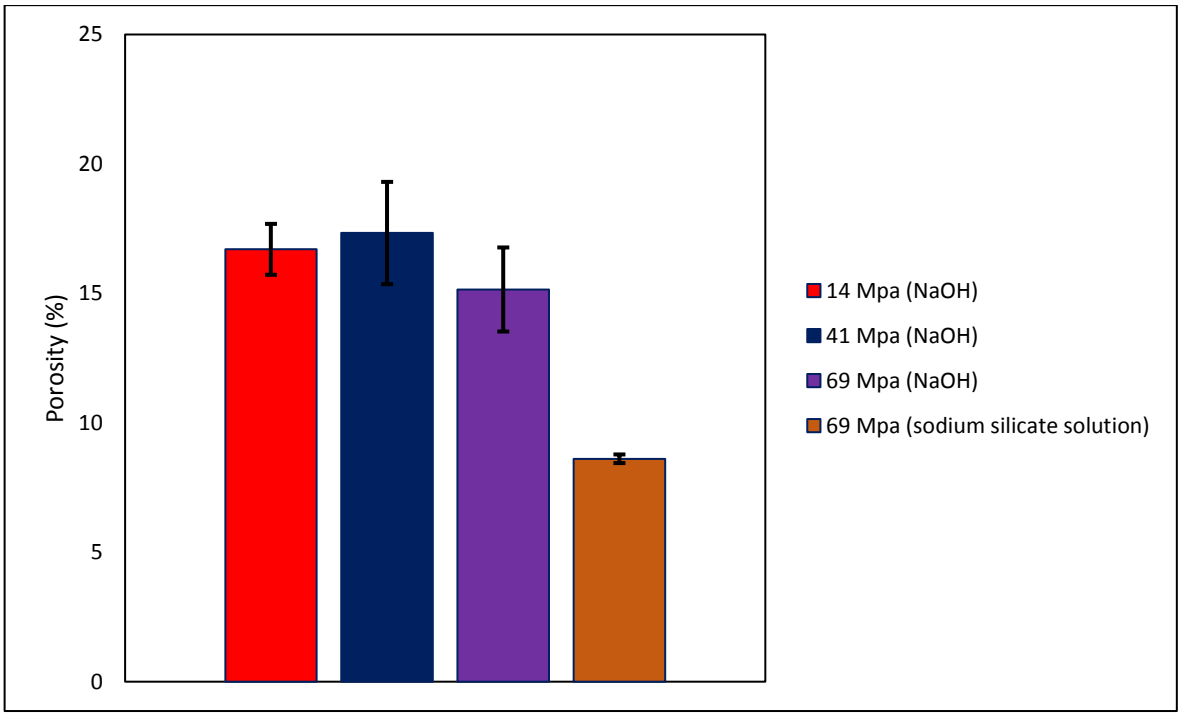

Figure 6-30: The effect of compaction and activating solution on the % porosity of alkali-activted slag samples. The samples were made using NaOH and sodium silicate solution as the activating solution.

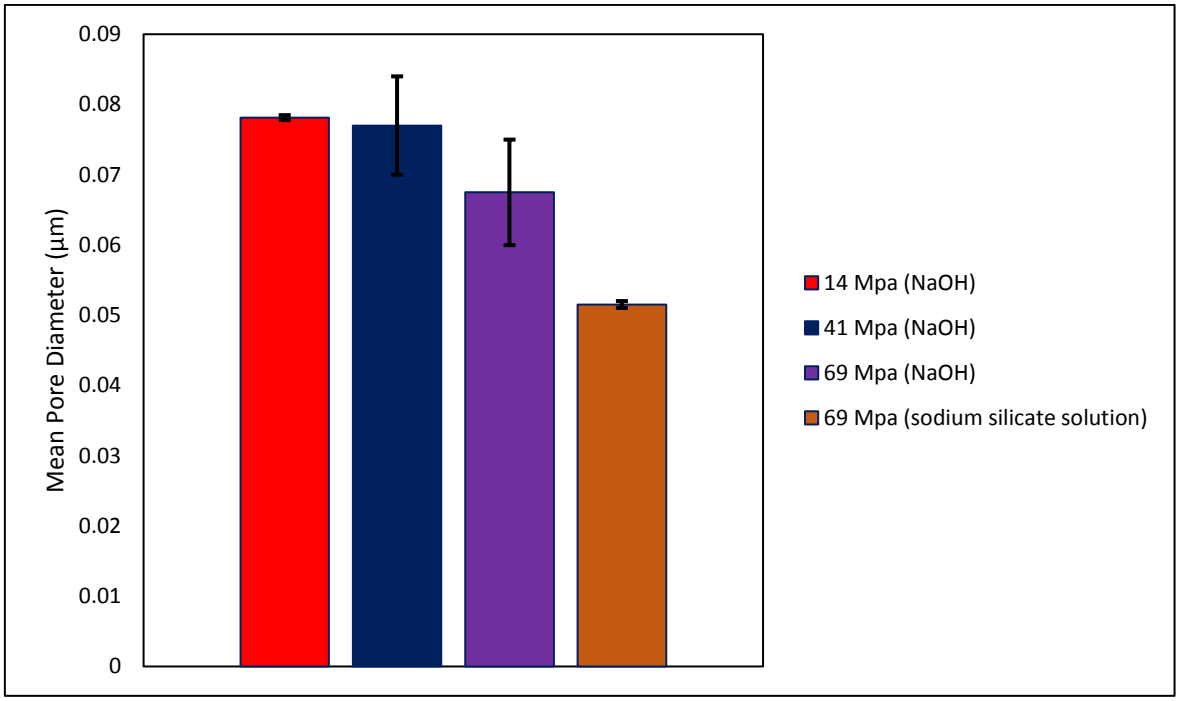

Figure 6-31: The effect of compaction and activating solution on the mean pore diameter of alkali-activated slag samples. The samples were made using NaOH and sodium silicate solution as the activating solution.

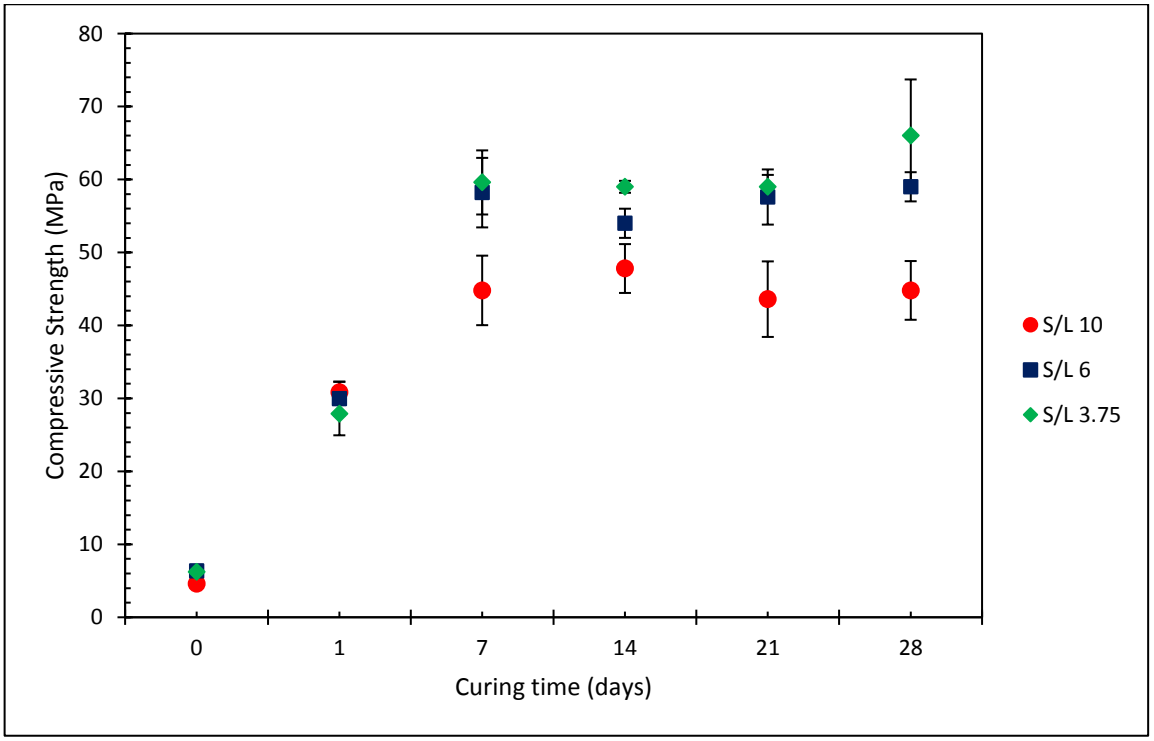

Figure 6-32: A graph showing the strength development of alkali-activated slag samples with different solid/liquid ratios (the samples were held at a curing temperature of 40°C).

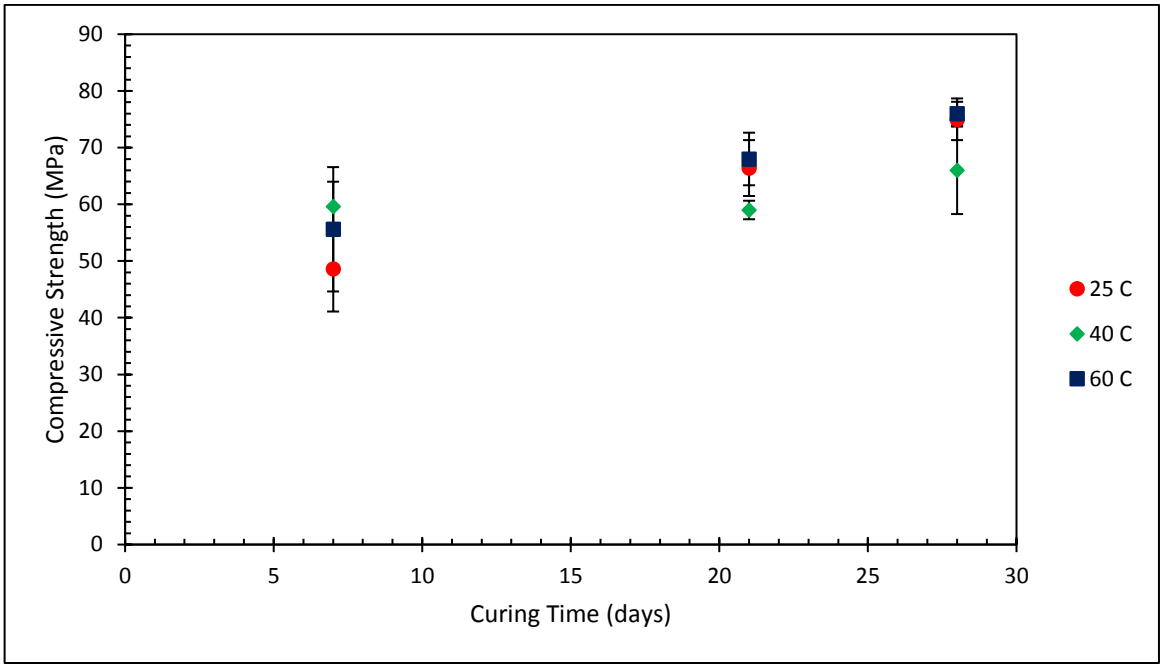

Figure 6-33: A graph showing the strength development of alkali-activated slags with a solid/liquid ratio of 3.75 at different curing temperatures.

6.3. The Effect of Slag Composition.

An amorphous slag is formed of randomly orientated chain network of interconnected silicate tetrahedra (SiO_4). The other components present in the slag interact with these chains by either promoting bonding between silica tetrahedra or by disrupting them. Those components which promote the bonding are known as 'network formers' and those which disrupt the bonding are known as 'network modifiers'.

The silicon tetrahedra are connected by Si-O-Si bonds where these oxygens are known as bridging oxygens. Network modifiers reduce the number of bridging oxygens in the slag's structure and increase the number of non-bridging oxygens (NBO). As the number of NBO in the slag increases, the chains become broken and slag's structure is less polymerised. Network formers reduce the number of NBO and so increase the polymerisation of the slag

network structure. Table 6-5 shows common network formers (acidic oxides) and modifiers (basic oxides) in slags and silicate glasses. Al_2O_3 and Fe_2O_3 are amphoteric oxides which can act as either acidic or basic oxides in a slag, although iron Fe^{2+} is thought of as a network modifier.

Table 6-5: Common network formers and modifiers in silicate glasses.

Network Modifiers (Basic oxides)	Network Formers (Acidic oxides)	Amphoteric Oxides
Na_2O	SiO_2	Al_2O_3
CaO	TiO_2	Fe_2O_3
MgO	P_2O_5	
FeO		

The molar ratio between the basic oxides and acidic oxides present in slag is called the basicity. A higher basicity indicates a greater degree of depolymerisation of the slag due to the greater number of NBOs present. In the field of geopolymers, researchers have used Equation 6-6 to describe the 'depolymerisation' (DP) of ground granulated blast furnace slags (GGBFS) (Duxson and Provis, 2008; Li et al, 2010):

$$\mathrm{DP} = \frac{\mathrm{n(CaO)} - 2\mathrm{n(MgO)} - \mathrm{n(Al_2O_3)} - \mathrm{n(SO_3)}}{\mathrm{n(SiO_2)} - 2\mathrm{n(MgO)} - 0.5\mathrm{n(Al_2O_3)}} \qquad \text{Equation 6-6}$$

Although a good correlation between a slag's reactivity during geopolymerisation and the calculated DP has been reported, this equation is specific to GGBFS and is not suitable to be used for slags with a wider composition containing components such as TiO_2, Fe_2O_3 and Na_2O.

The 'optical basicity' of a slag in another equation which has been used to develop models for slag viscosity, density and sulphide capacity as the polymerisation of the slag effects these

properties (Duffy and Ingram, 1976; Hu et al. 2012; Zhang and Chou; 2010; Duffy et al. 1978). The equation has been derived empirically and the term 'optical' refers to the use of ultra-violet (UV) spectroscopy used to experimentally determine the basicity of the glass components. The advantage of this method is that it considers all the components of the slag during the calculation.

The optical basicity of a multi-component slag can be calculated by Equation 6-7:

$$\Lambda = \frac{\sum x_i n_i \Lambda_i}{\sum x_i n_i} \qquad \text{Equation 6-7}$$

Where x_i is the molar fraction of component i, n is the number of oxygens in the component i.e. n = 2 for SiO_2, 3 for Al_2O_3 etc. and Λ_i is the optical basicity of component i.

The optical basicity for a component Λ_i can be calculated for using Pauling's electronegativity value χ_i for the metal in the component from the empirical Equation 6-8:

$$\Lambda_i = \frac{1}{1.36(\chi_i - 0.26)} \qquad \text{Equation 6-8}$$

Table 6-6 shows the optical basicity of eight slag compositions. The optical basicity ranges from 0.614 (S3) to 0.652 (S5). As the presence of network formers in the slag increases, the optical basicity decreases which is shown by samples S1 to S3 where the TiO_2 content increases from 1.2 to 16.6 wt% and the optical basicity reduces from 0.630 0.614.

Table 6-6: The optical basicity of eight slag compositions.

Oxide (wt%)	S1	S2	S3	S4	S5	S6	S7	S8
SiO_2	43.7	43.8	38.6	32.7	34.3	37.3	40.3	42.9
Al_2O_3	9.8	10.6	9.1	27.8	17.7	19.5	16.3	9.9
CaO	41.7	38.0	33.5	32.8	37.1	28.4	35.6	42.2
TiO_2	1.2	5.4	16.6	1.2	1.1	1.3	1.4	1.9
Na_2O	0.2	0.3	0.2	1.2	5.2	8.1	0.7	0.5
MgO	1.5	1.3	1.1	1.4	1.4	1.5	2.1	1.6
Fe_2O_3	1.2	0.3	0.4	2.0	2.6	2.8	2.3	0.4
P_2O_5	0.5	0.1	0.1	0.7	0.4	0.8	0.9	0.0
Total	99.8	99.8	99.6	99.8	99.8	99.7	99.7	99.4
Optical Basicity	0.630	0.620	0.614	0.629	0.652	0.629	0.620	0.634

XRD analysis in Figure 6-34 of these slags show them all to be glassy, which is ideal for alkali-activation. However, when the different slag compositions are examined using Raman spectroscopy a greater idea of their structure can be determined. Figure 6-35 shows the Raman spectra for samples S1 to S3 and Figure 6-36 show the spectra for samples S4 to S8. It is clear that even though all the samples are amorphous, they contain different silicate structures. Although quantitative analysis of the volume fraction of the different silicate structures present is not easy due to their different Raman scattering coefficients of the silicon tetrahedral species, these results still show that there are clear differences in the slag structures due to confirmation of the presence of these species. A summary of Raman data for the slag samples is shown in Table 6-7.

In Figure 6-35, as the TiO_2 content increases there is a shift to lower Raman frequencies. The shift to lower wavenumbers is due to the increased Ti-O-Ti bonds in the material and increased Si-O-Si bonds which indicate a greater degree of polymerisation of the network structure. This

is consistent with the theory that TiO_2 is a network former where the addition of TiO_2 causes a decrease in the NBO content because it competes with silicate tetrahedra to form complexes with network modifiers.

Figure 6-36 show that the samples S4 to S8 display different degrees of polymerisation. S5 and S7 show the presence of Q^0_{Si} species in the glass due to shoulder peaks at 850 cm^{-1} whereas the other samples have peaks centred at higher Raman frequencies. All the samples show some degree of depolymerisation with all peaks suggesting the presence of at least one non-bridging oxygen in the silicate structure.

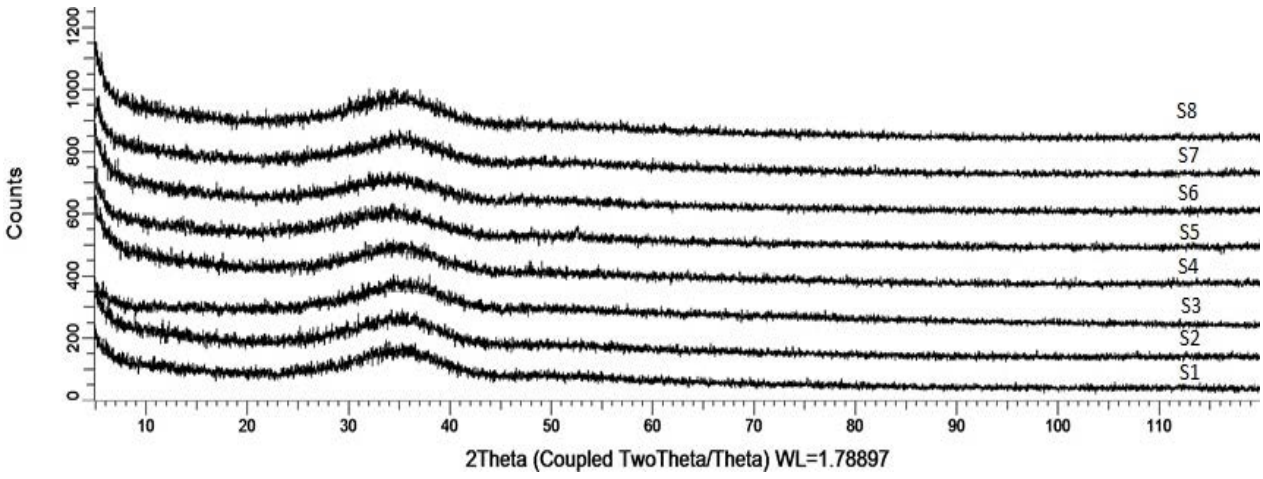

Figure 6-34: X-ray diffraction spectra of several different slag compositions.

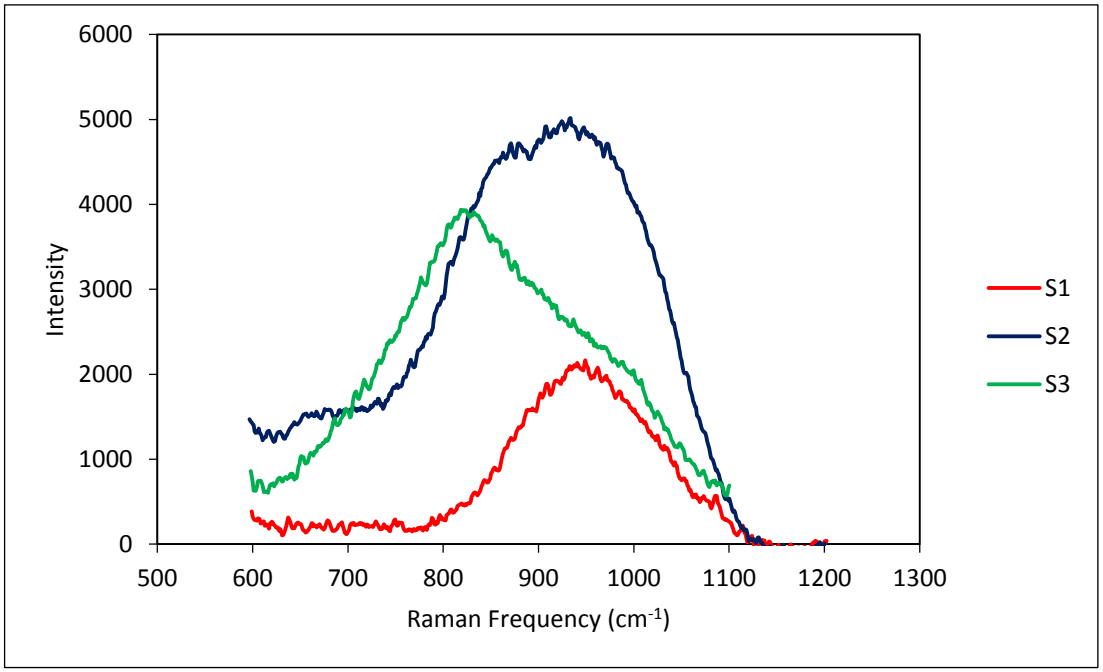

Figure 6-35: Raman spectra of slag samples with increasing TiO_2 content.

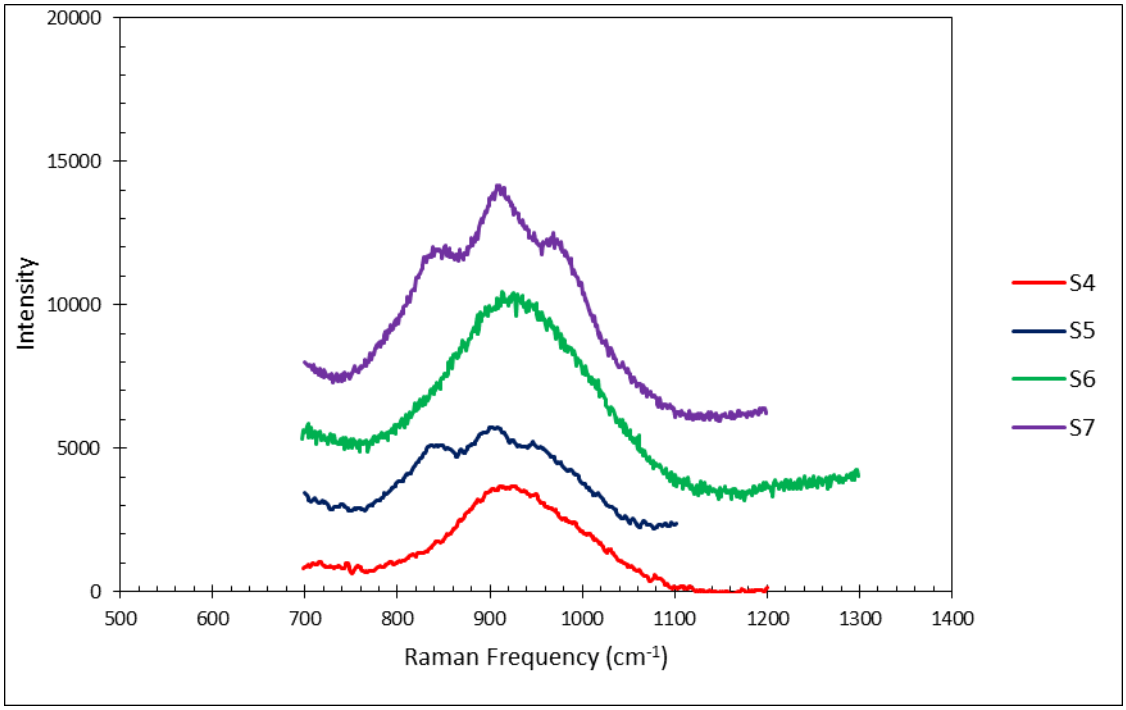

Figure 6-36: Raman spectra of the various slags with different compositions.

Table 6-7: A table of the deconvoluted peaks determined from the Raman spectra of slag samples.

Sample	Deconvoluted peaks (cm^{-1})	Attribution	Reference[5,6,7]
S1	920, 1000	Q^1_{Si} , Q^2_{Si}	1
S2	802, 907	Ti-O-Si or Ti-O-Ti, Q^1_{Si}	1, 2
S3	714, 819, 945	Si-O-Si symmetric bonding ,Ti-O-Si or Ti-O-Ti, Q^2_{Si}	1,2,3
S4	935	Q^2_{Si}	1
S5	850, 900, 960	Q^0_{Si} , Q^1_{Si} , Q^2_{Si}	1
S6	920, 939, 1000	Q^1_{Si} , Q^2_{Si} , Q^3_{Si}	1
S7	850, 914, 960, 1000	Q^0_{Si} , Q^1_{Si} , Q^2_{Si} , Q^3_{Si}	1
S8	920, 1000	Q^1_{Si} , Q^3_{Si}	1

SiO_2, Al_2O_3 and CaO are the main components of the slag and aluminium and calcium can interfere with the network to reduce the polymerisation of the silicon tetrahedra. Aluminium substitutes with silicon tetrahedra to form -Si-O-Al-O-Si bonds acting as a network modifier, but the introduction of aluminium into the network structure decreases its stability due to the Al-O bond being weaker than the Si-O bond which allows for a greater solubility in an alkaline solution. The calcium also acts as a network modifier by forming -Si-O-Ca bonds which, as these bonds increase, the tetrahedral network is reduced and so the depolymerisation of the silicate network increases.

[5] Mysen et al. (1980)
[6] Zheng et al. (2013)
[7] Wang et al. (2011)

In general, the optical basicity of the slag shows a good correlation with the presence of depolymerised structural units seen using Raman spectroscopy. However, sample S7 shows the presence of Q^0_{Si} species despite having a low optical basicity and so this indicates that the structure of the slag is dependant not wholly dependent on the composition, but also on other factors such as the thermal history (quench rate).

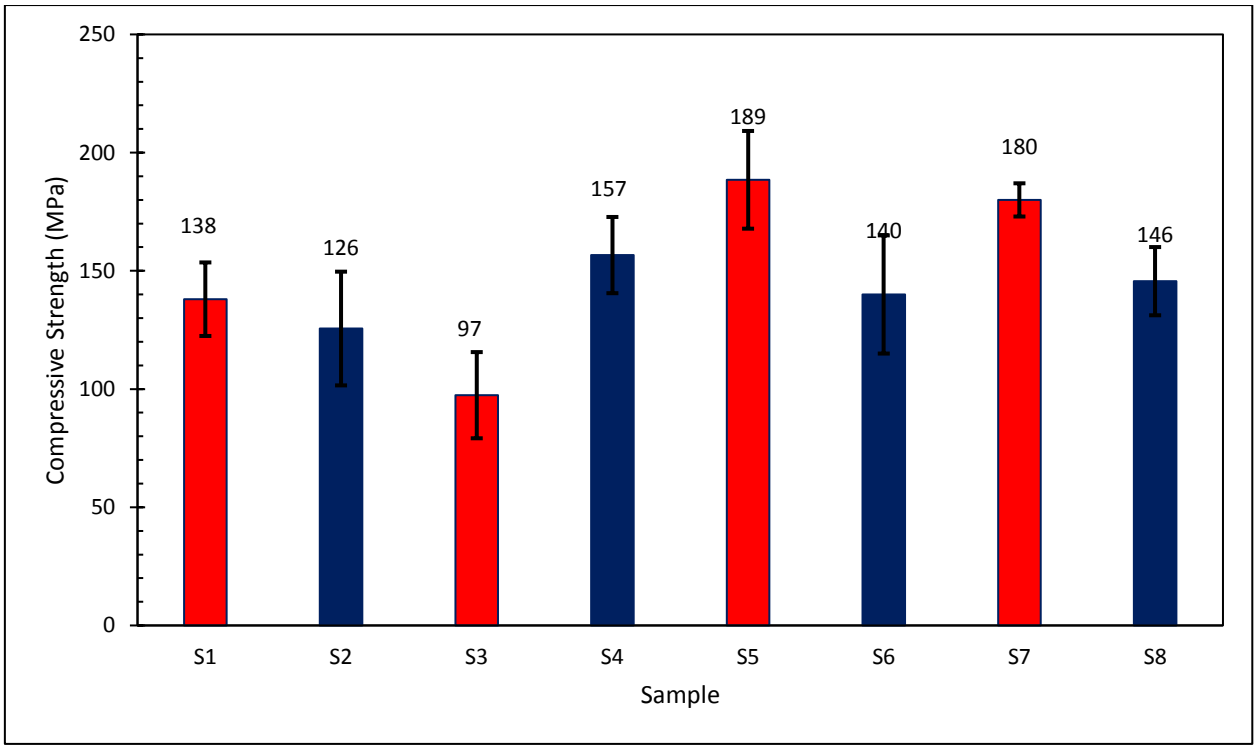

Figure 6-37: Compressive strengths of samples S1 to S8.

The compressive strengths of samples S1 to S8 are shown in Figure 6-37 and the samples which have the highest compressive strengths are S5 and S7. The Raman spectroscopy data indicated that these samples show the presence of SiO_4^{4-} (Q^0_{Si}) structures which indicate a high degree of polymerisation in the slag. The samples which display a lower compressive strength for example, S6 and S8, show the presence of Q^3_{Si} structures that indicate a greater

degree of slag polymerisation. The results indicate that as the polymerisation of the slag's structure decreases, the resulting alkali-activated binders are stronger. Figure 6-38 shows the results of the selective dissolution tests which were performed to determine the % of unreacted slag in the binder. The tests followed the method outlined by Luke and Glasser (1987) which involves the dissolution of the binding phase leaving only unreacted slag particles. A solution of 1:1 ratio 0.05 M ethylene diamine tetra-acetic acid in 0.1 M Na_2CO_3 was prepared and 9.5 ml was added to 0.95 ml of 1:1 triethanolamine:H_2O solution which was then mixed with 9.5 ml of distilled water. 25 mg of alkali-activated slag binders was added to this solution in a vial which was then put into an ultrasonic bath for 30 mins to aid dissolution. The solution was then vacuum filtered and the solid residue washed with distilled water and acetone before being dried to a constant weight and the mass weighed. The undissolved residue was then related to the initial mass used in the experiment to determine the % slag reacted.

The graph shows that as the % of slag reacted increases, the strength of the alkali-activated binder increases and the samples which showed the greatest reactivity are the slags which have a less polymerised structure. Therefore, the less polymerised the slag's structure, the greater its reactivity which results in the alkali-activated binders being stronger.

Figure 6-39 show the strengths of alkali-activated slag binders which have been produced with various slag compositions. It can be seen that those slags which contain the structures which have more NBOs then the alkali-activated slag should be stronger.

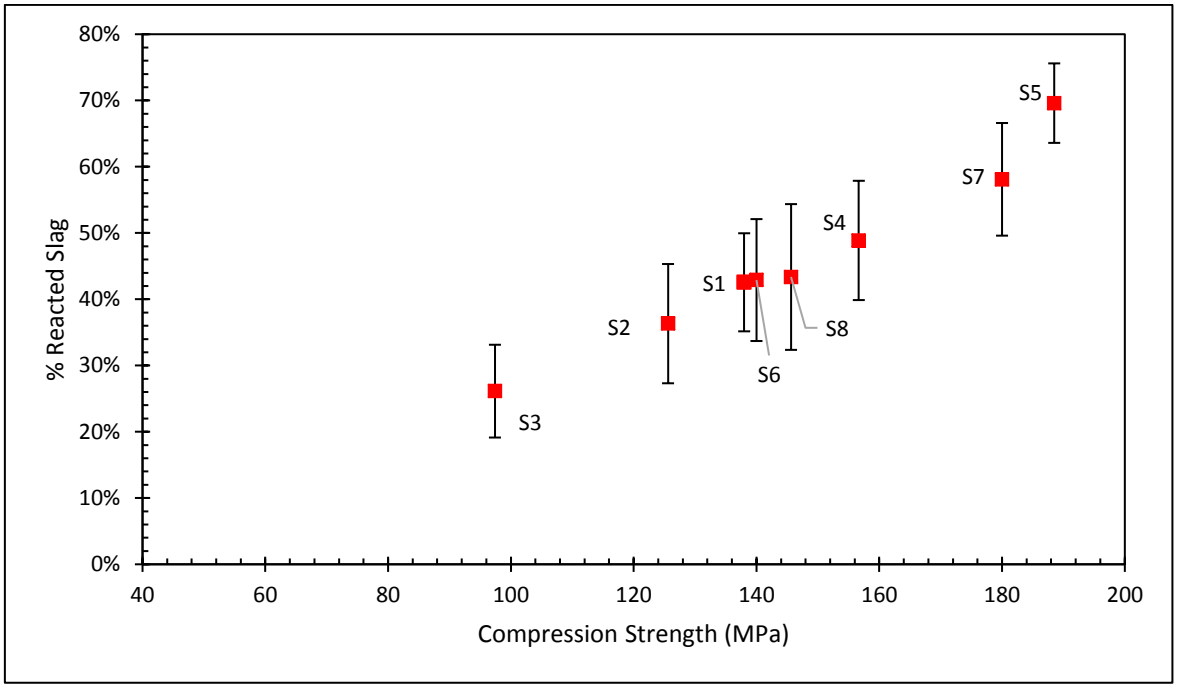

Figure 6-38: Results of selective dissolution experiments to determine the % slag reacted for samples S1 to S8 and their relation to the compressive strength of the alkali-activated binders.

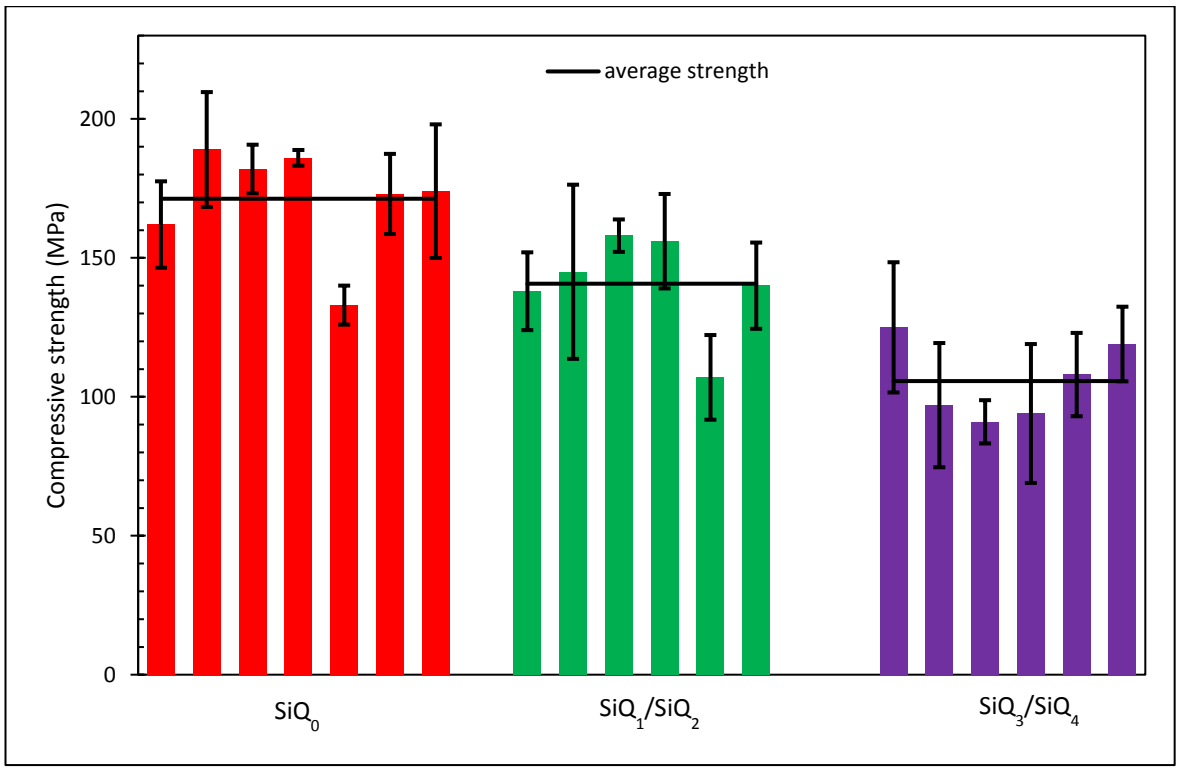

Figure 6-39: The compressive strength of slags showing the presence of certain silicate structural units determined by Raman spectroscopy.

The optical basicity shows a good correllation with the data obtained from the Raman spectroscopy. Figure 6-40 shows that as the optical basicity is increased, it is more likely that the resulting slag would have a lesser degree of polymerisation. An optical basicity of greater than 0.615 seems to produce slags which are more depolymerised and more reactive which is also shown in Figure 6-41. This would help with the design of slag compositions to try and enhance the reactivity of the slag during alkali-activation which would result in stronger binders.

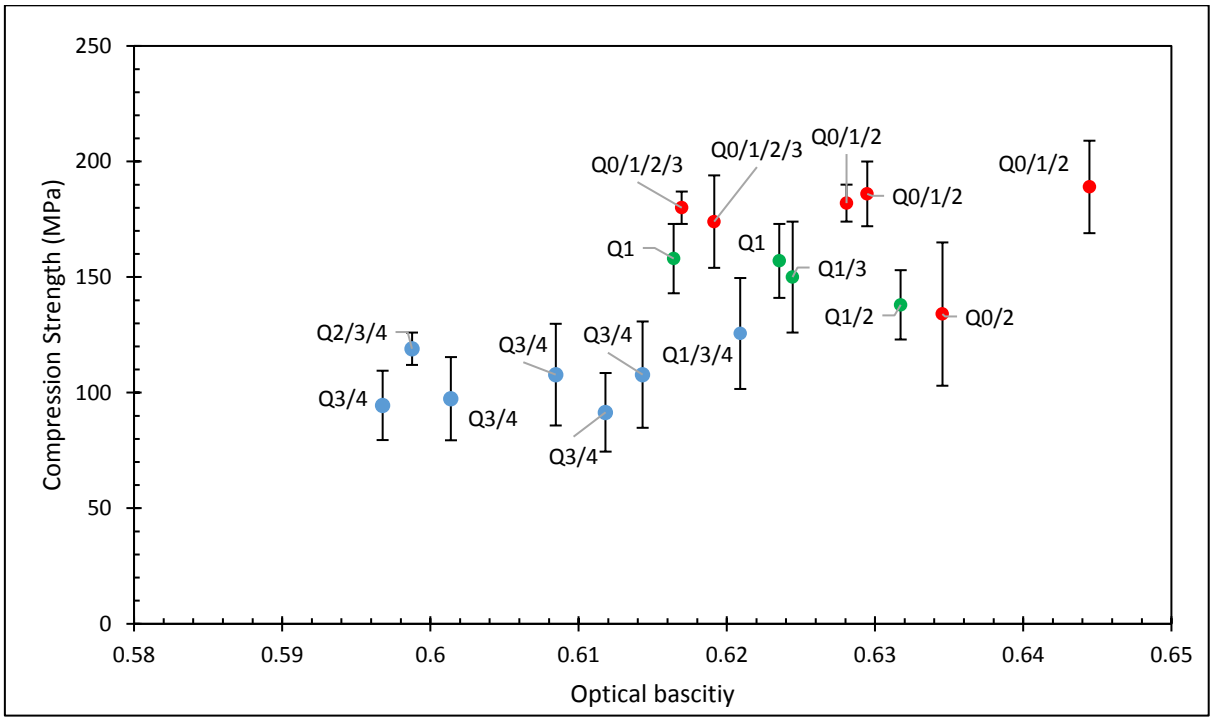

Figure 6-40: The relationship between the compressive strength of an alkali-activated slag binder and the optical basicity of the original slag.

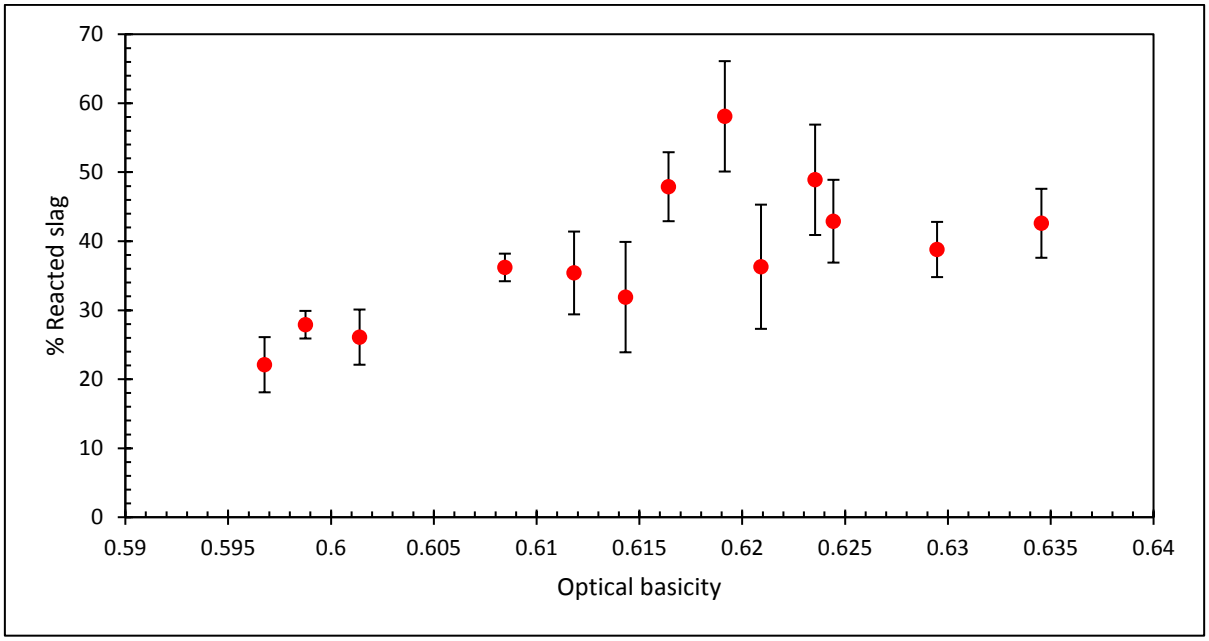

Figure 6-41: The relationship between the optical basicity of a slag and the % reaction of the slag during alkali-activation.

Increasing the depolymerisation of the structure can be achieved by increasing the concentration of network modifiers with the slag system. However, this may create a reactive slag, but if the silicon content is reduced too much the strength of the binding phase will also be reduced due to the effect of a reduced Si/Al ratio. This problem can be overcome by using sodium silicate solution as the activator. The silicon species in this solution are able to reinforce the silicon which are released from the slag as it dissolves and increase the Si/Al ratio in the binding phase. By using this activating solution it is possible to overcome the effect of compositional variation and still create strong binders.

6.4. Slag Durability.

6.4.1. Efflorescence.

To investigate the effect of the compositional variation on the appearance of efflorescence on an alkali-activated slag binder, five slag mixes were made which varied the Si concentration and the calcium concentration. The silicon concentration was modified by dissolving amorphous silica in 6 M NaOH. The calcium addition was changed by adding powdered $CaCO_3$ to the mix. The formulation mixes are shown in Table 6-8.

Table 6-8: Formulation mix per sample for the experiment.

Mix	Slag (g)	H_2O (ml)	NaOH (g)	SiO_2 (g)	$CaCO_3$ (g)
A	3	0.8	0.192	0	0
B	3	0.8	0.192	0.08	0
C	3	0.8	0.192	0.16	0
D	3	0.8	0.192	0.32	0
E	3	0.8	0.192	0	0.3

Both FTIR analysis and EDX analysis were used to characterise the binders and they both show that the binding phase of the material is of a heterogeneous nature. The broad spectra shown in the FTIR analysis between 850-1150 cm^{-1} is caused by an accumulation of contributions from different silicate and aluminosilicate structures that are present in the binding phase. Shorter chained structural units contribute to the presence of peaks at lower wavenumbers and more complex, more polymerised structural units produce peaks at higher wavenumbers. The EDX analysis which was performed on various sites on the paste, show varied Si/Al and Ca/Si ratios which indicate a heterogeneous binding phase.

The addition of silicon to the material causes an increase in the silicon content in the binding phase which corresponded to an increase in the Si/Al ratio and a decrease in the Ca/Si ratio. This is supported by an apparent shift to higher wavenumbers of the FTIR peaks around the 850-1150 cm^{-1} region showed in Figure 6-42. A peak at around 870 cm^{-1} can be seen in samples A, B and E which have low Si/Al ratios and high Ca/Si ratios, but disappears in samples C and D. Although some authors have attributed this peak to $CaCO_3$, but the absence of peaks at 710 and 1419 cm^{-1} indicate that this is more likely to be caused by short chain silicate structural units, possibly CSH. As additional SiO_2 is added to the formulation, in samples C and D the peak disappears and there is an apparent shift of the spectra to higher wavenumbers. This indicates that when the Ca/Si ratio in the formulation is increased, the formation of short chain CSH structures is promoted, whilst when it is reduced there is a preference of the system to form more polymerised CASH structures.

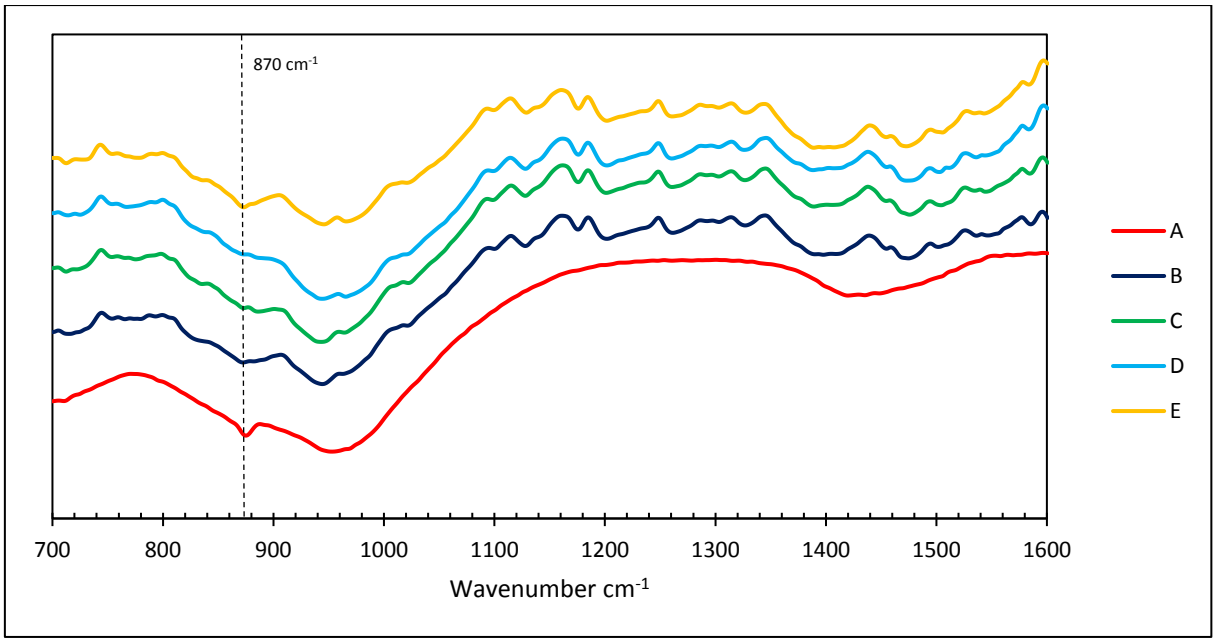

Figure 6-42: FTIR Spectra of the various AAS binders.

This is supported by the EDX data, shown in Figure 6-43, which shows a decreasing Ca/Si ratio in the binding phase of the AAS paste as the silicon content of the formulation increases and this is accompanied by an increase in the Si/Al ratio. This confirms that when both SiO_2 and $CaCO_3$ is added to the formulation Si and Ca are taken up by the binding phase, altering its composition and the increase in the Si/Al ratio from samples A to D and the sharp increase in the Ca/Si ratio in sample E shows how the composition of the binding phase can be manipulated. The wide variation of the ratios can be seen in the figure by the error bars which represent the maximum and minimum ratios found over the 20 to 30 sites analysed on each sample, meaning that each binding phase displays heterogeneity as confirmed by the broad FTIR peaks. However, the range of the Ca/Si in the binding phase reduces as the silicon content increases. This is particularly evident when comparing sample A and D where the maximum Ca/Si ratio was around 1.75 in sample D, whereas in sample A it was around 1 and so this explains the shift to higher wavenumbers of the FTIR spectra as the silicon content increases. Therefore, this indicates that as the silicon content increases, the formation of distinct CSH phases in the binding phase is reduced and the formation of longer chained structural units is preferred.

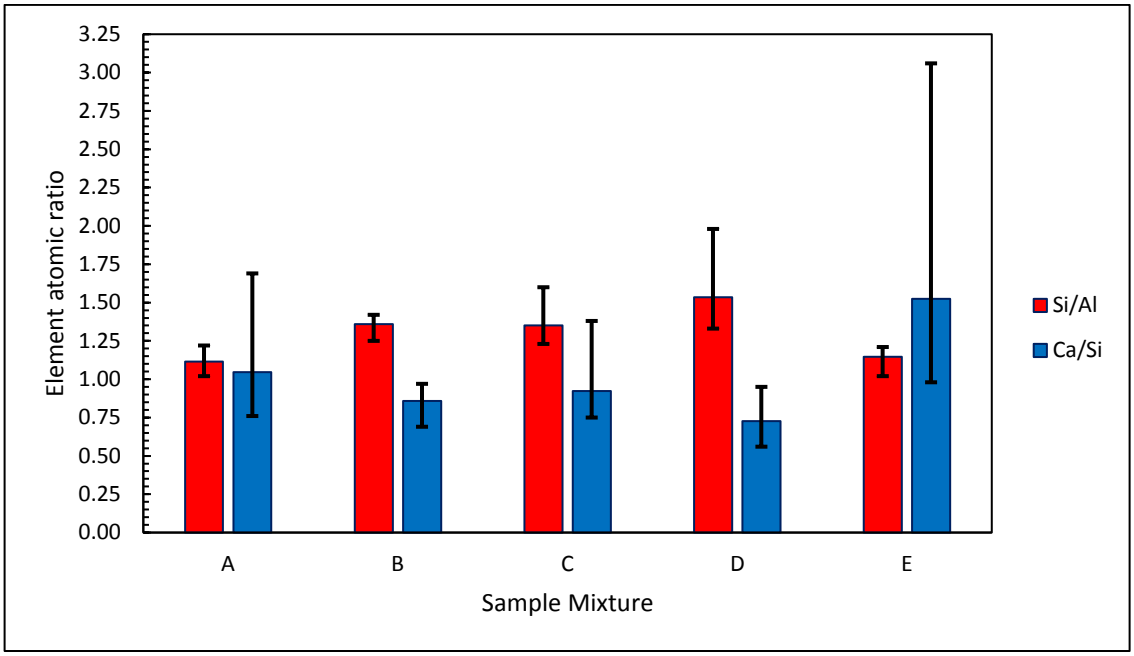

Figure 6-43: EDX analysis of the Si/Al and Ca/Si ratios of the binding phase. The error bars represent the maximum and minimum ratios of the binding phases. The bars represent the average value.

The addition of both SiO_2 and $CaCO_3$ to the formulation has a positive effect on the compressive strength of the AAS binders. An increase in the Si/Al ratio increases the compressive strength of the material and although a slight decrease in strength was observed as the Si/Al ratio increased from 1.57 to 1.71 from sample C to D, the strength was still significantly higher than the AAS binder produced just using NaOH (sample A). The addition of $CaCO_3$ caused an increase in the compressive strength and this may be due to the early formation of CSH phases which would act as nucleation sites aiding further gel phase formation. The addition of SiO_2 seems to have a greater impact on the compressive strength and this may mean that longer chain silicate units are stronger than shorter ones and also a lower substitution of Si by Al tetrahedron has a positive impact, but also the effect of reducing

the open porosity of the binding phase which would reduce internal stresses in the material, reducing crack formation (Duxson and Provis, 2008).

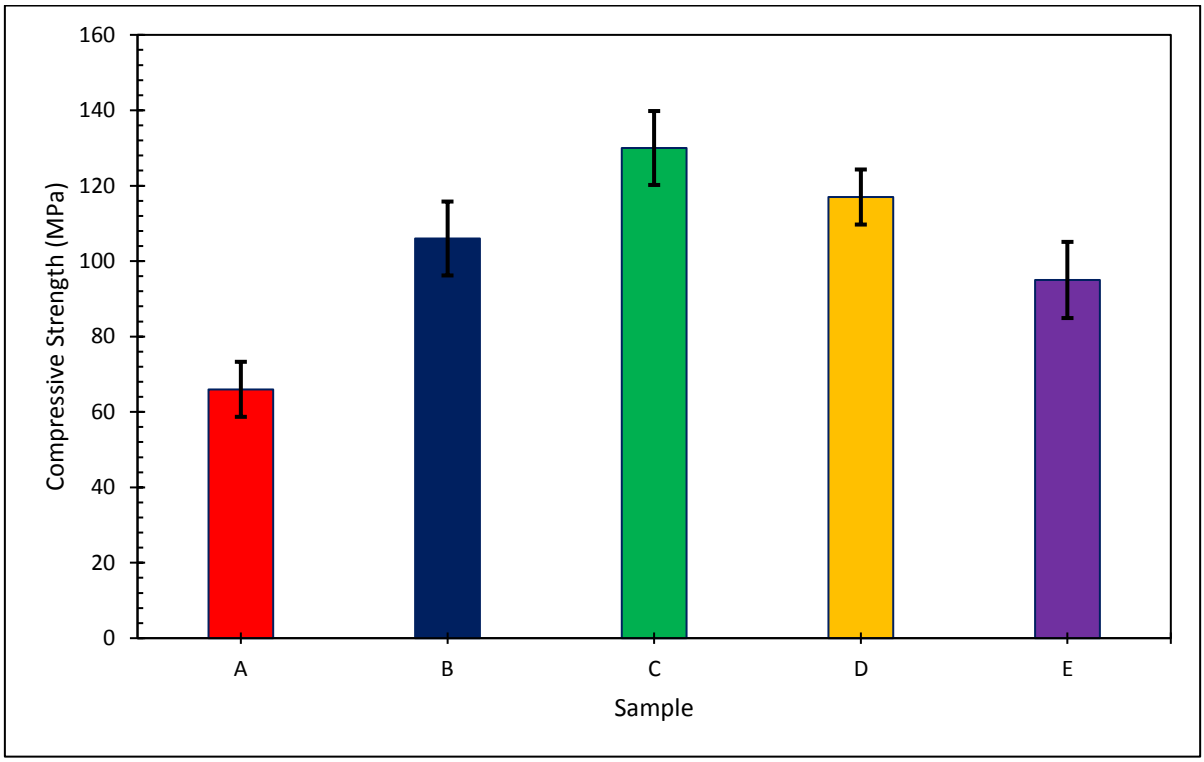

Figure 6-44: Compressive strengths of the various binding phases. The error bars represent the standard deviation of the results.

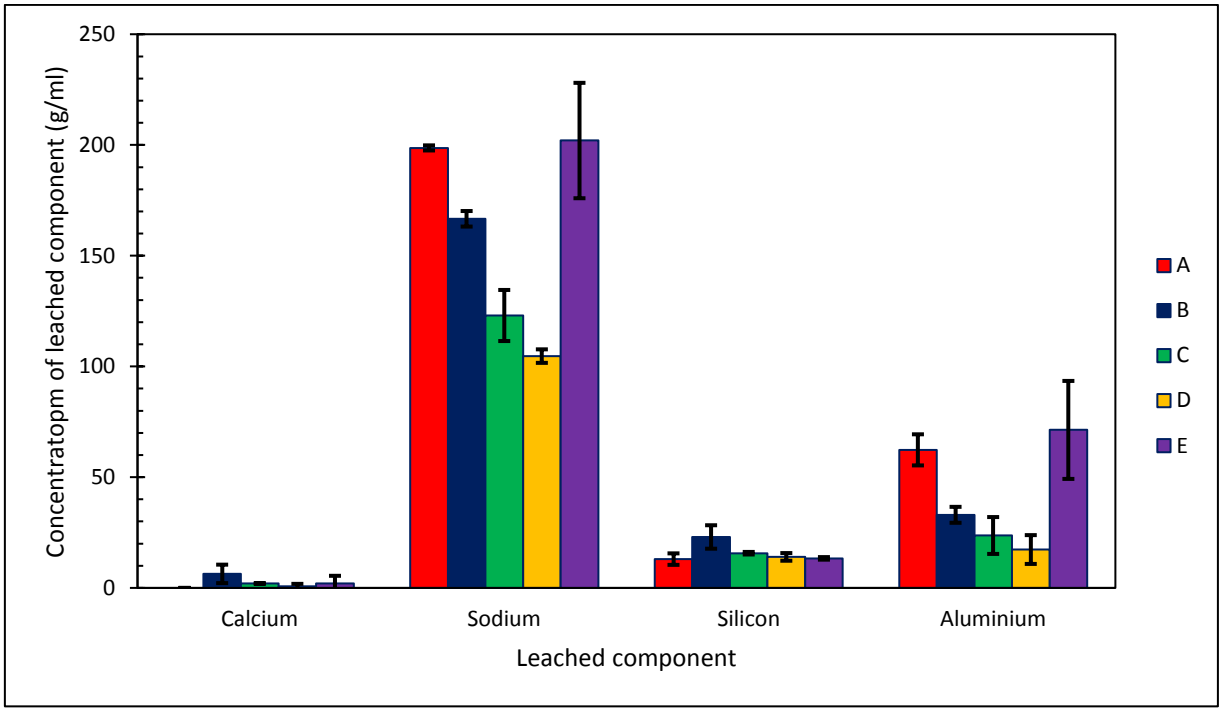

Figure 6-45: Leaching analysis of the binding phases. The error bars represent the standard deviation of the analysis.

The results of the leaching tests in Figure 6-45 show that sodium and aluminium were the most mobile elements from the binding phase. There was very little leaching of silicon and calcium and the leaching of these components was similar across all samples. This suggests that calcium and silicon are strongly held in the structures of the binding phase. The leaching of aluminium from the material was significantly lower than that of sodium indicating Al is mostly bound in the material and there is only a small fraction which is present in the pore solution and mobile. Aluminium substitutes for silicon in the network chain, but the leaching of aluminium was increased when the calcium content of the binding phase increases. Therefore, the preference of the formation of shorter chain CSH structures at higher Ca/Si ratios may reduce the incorporation of Al into these silicate chains and as the CSH content in

the binding phase increases, there is an increase in free and mobile Al species in the pore solution.

Similarly, the mobility of Na ions in the material decreases as the silicon content of the material increases. This can be seen by the leaching of Na from sample D was 52% less than from sample A in Figure 6-45. An increase in the silicon content of the material also reduces the Al mobility and so it can be proposed that there is an increased incorporation of Al species into the silicate chains. This increase in the Al substitution of Si would mean that there is an increase in the requirement for Na^+ ions to balance the negative charge and therefore be held by the gel structure. An increase in the silicon content reduces the Ca/Si ratio and this has a number of effects on the binding of Na in the material. Firstly, the average aluminosilicate chain length increases and this would increase the number of silanol sites available for the binding of Na in the structure. Secondly, increasing the silicon content of the binding phase may promote the formation of zeolites or NASH gels which would more strongly bind the sodium cations to the structure, reducing the amount of excess sodium in the pore solution. Thirdly, studies have shown the decrease in the open porosity of the microstructure of the binding phase as the Si/Al ratio increases. This would reduce the mobility of excess ions in the pore solution and so reduce the leaching capacity of the material.

Efflorescence is caused by mobility of excess Na^+ ions in the material and controlling the microstructure could have a significant effect on reducing efflorescence over the material's lifetime. It is possible to gain more control over the phases which are formed from alkali-activation by introducing additives to the initial formulation. The addition of silicon has been previously shown to increase the mechanical strength of the material, but it has been shown

in this work to reduce the mobility of Na^+ ions. There are difficulties in accurately designing a formulation for the alkali-activation of slag for reduced Na^+ mobility based on the Na/Al ratio due to the varied reactivity of slag and also some Al not being taken up into solution. However, it may be possible to alleviate these issues by increasing the silicon addition to produce the effects stated above.

6.4.2. Behaviour at High Temperatures.

When the alkali-activated binders are heated over a temperature range the material experiences a loss of mass. The mass loss between 0 and 1000°C is shown in Figure 6-46 and it shows that there is a small mass of just over 5% at 90°C. The mass loss is then significantly increased at 200°C and after there is little mass loss up to 1000°C. The mass loss below 200°C is associated with free water and the mass loss between 200 and 300°C is associated with chemically bound water.

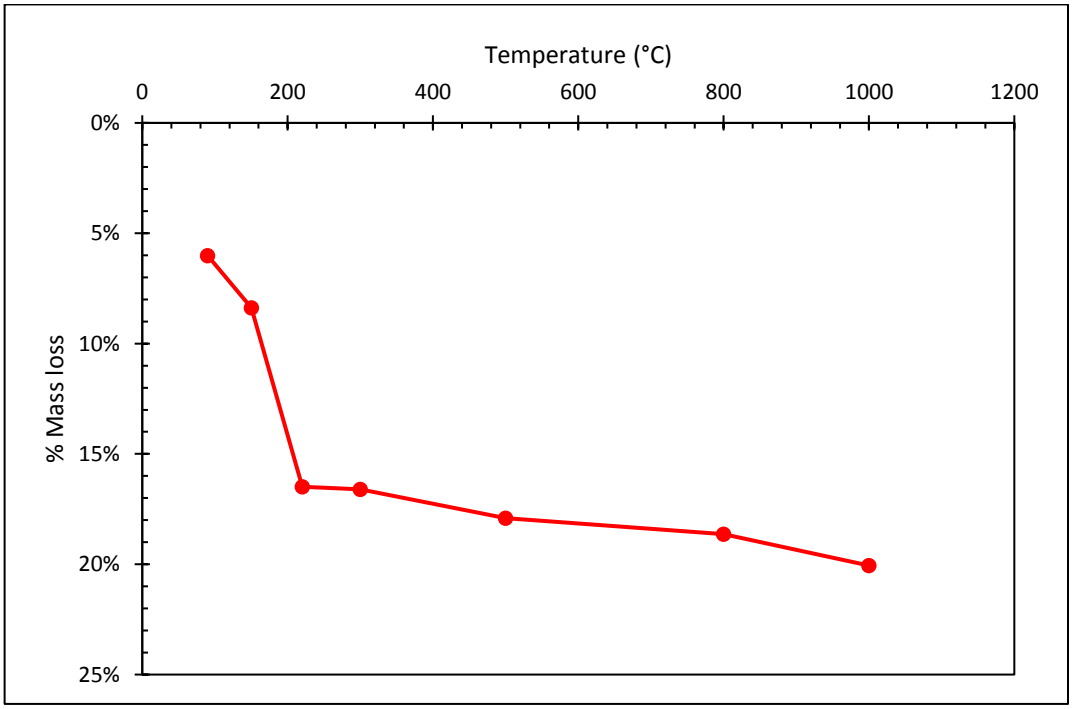

Figure 6-46: The mass loss of an alkali-activated binder between 0 and 1000°C.

When the binders are exposed to higher temperatures, the material begins to crystallise. Alkali-activated slag binders were exposed to various temperatures for two hours in a muffle furnace and Figure 6-47 shows the effect of this exposure on the binding phase. At lower temperatures up to 300°C the binder experiences no crystallisation during the exposure time. From temperatures at and above 500°C the material beings to crystallise and at 1000°C the material is fully crystallised. The phases which appear are melilite ($CaNaAlSi_2O7$) and lisetite ($Na_2CaAl_4SiO_{16}$) and these phases are the crystalline versions of the hydrated binding phase.

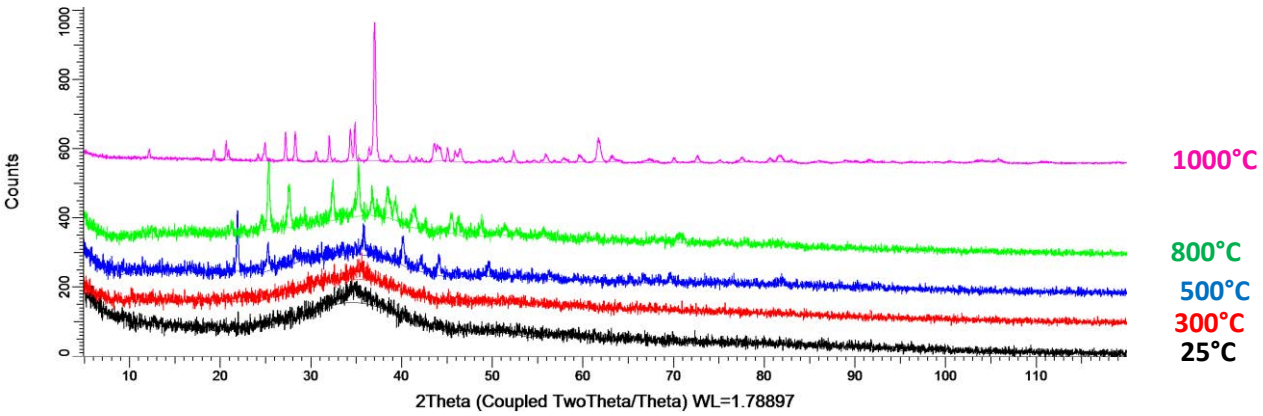

Figure 6-47: XRD spectra showing the crystallisation after the alkali-activated slag binder was held for 2 hours in a muffle furnace at temperatures between 300 and 1000°C.

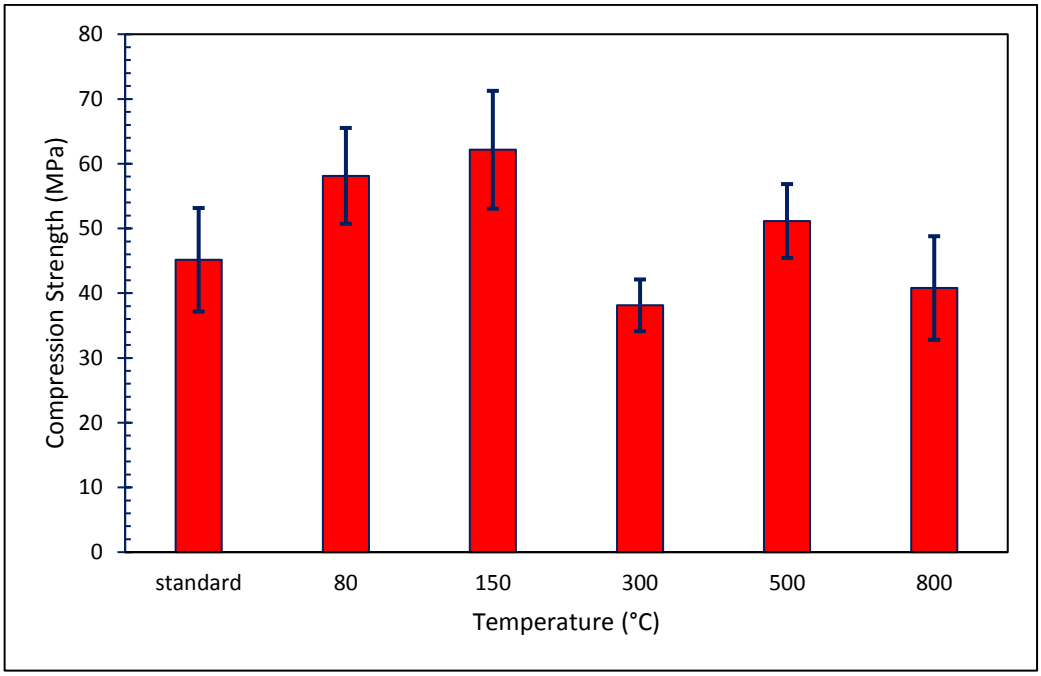

Figure 6-48: Compressive strengths of alkali-activated slag samples exposed to various temperatures for 2 hours.

The impacts of the crystallisation does not have an effect on the strength of the material. The strength of the material increases after the material is exposed to temperatures up to 150°C (Figure 6-48). This strengthening occurs below the temperature at which chemically bound water is released from the binding phase and so the chemistry of the binder is unchanged and may just undergo some sort of densification. There is a drop in the strength of the material at 300°C which is the temperature at which the chemically bound water is released and so the binding phase is being broken without any crystallisation.

This data shows that the material will not become significantly weaker when it is exposed to high temperatures. However, the crystallisation of the material at these temperatures would mean that because the material has changed it may not be suitable for continued use. For example, if the material was exposed to a fire, it may be able to keep its structural integrity

but as it has undergone such a significant change of its microstructure its long term performance would be unknown.

6.5. Conclusions and Further Work.

The work presented in this chapter has shown that slags derived from the plasma process are suitable to be used as a cement replacement. It has shown that the composition of the slag does have an effect on the material's reactivity which is linked to the slag's structure and dissolution behaviour. However, there are various methods to alleviate and issues regarding the chemical variation of the slag on the properties of the resulting binders for example using sodium silicate solution to introduce additional silicate species in to the mix or the altering production methods to reduce internal flaws in the material.

One of the major issues regarding the use of these slags as a cement replacement are the regulations which currently cover slags. BS EN 197-1:2011 is the regulation which defines the allowed composition of slag for use as a cement replacement and is very specific to blast furnace slag. However, there are routes for which plasma derived slags can become CE marked for use as a cement replacement and these are outlined in Appendix B. There are also no regulations in the UK which cover alkali-activated binders and so this currently discourages users from using them. However, the large amount of research currently being undertaken on AAS seems to suggest that they will become more popular in the future especially when considering the current trend for highly substituted slag-cement blends. In the UK a document was released in 2016; PAS 8820:2016 which is seen as a predecessor to a British Standard. It is a first attempt to develop standards for alkali-activated cementitious materials and essentially follows the same testing criteria for normal concrete. The document was co-funded by Hanson UK which shows the intent from the cement industry to produce low carbon

cements. Slags are included in this document but are still subjected to the same composition limits as current cement standards. It is important to note that under current cement regulation up to 95% of cement can be substituted and so it is most likely that for the foreseeable future greater amounts +90% cement substituted blends will be seen rather than AAS binders. This would have advantages in helping to gain confidence in the material by end users who would probably feel more comfortable with cement.

An issue with plasma derived slag from APCr is the presence of chlorine in the final slag. The chlorine content of the slag can be up to 5 wt% which is well above the upper limit of 0.1 wt% for steel reinforced concrete. Ensuring that the chlorine content is lower than 0.1 wt% would be required so the slag could achieve a high value. During the vitrification of APCr, most of the chlorine is volatilised and partitions to the off-gas, but there is a residual amount which ends up in the slag. The chlorine content in the slag could be reduced by optimising the furnace operating conditions and possibly the chemistry of the slag causing a greater amount of the chlorine to move into the off-gas. Another method would be to have a post-furnace treatment of the slag. Thermogravimetric analysis of the slag in Figure 6-49 show that at temperatures around 1200°C the slag experiences a mass loss which is similar to the volatile component content in the slag. Therefore this means that if the slag was held at a temperature between 1200 and 1400°C in a vacuum holding furnace, the volatile components should be released from the slag and when it is removed the slag should be clean of chlorine making it suitable for cement replacement applications.

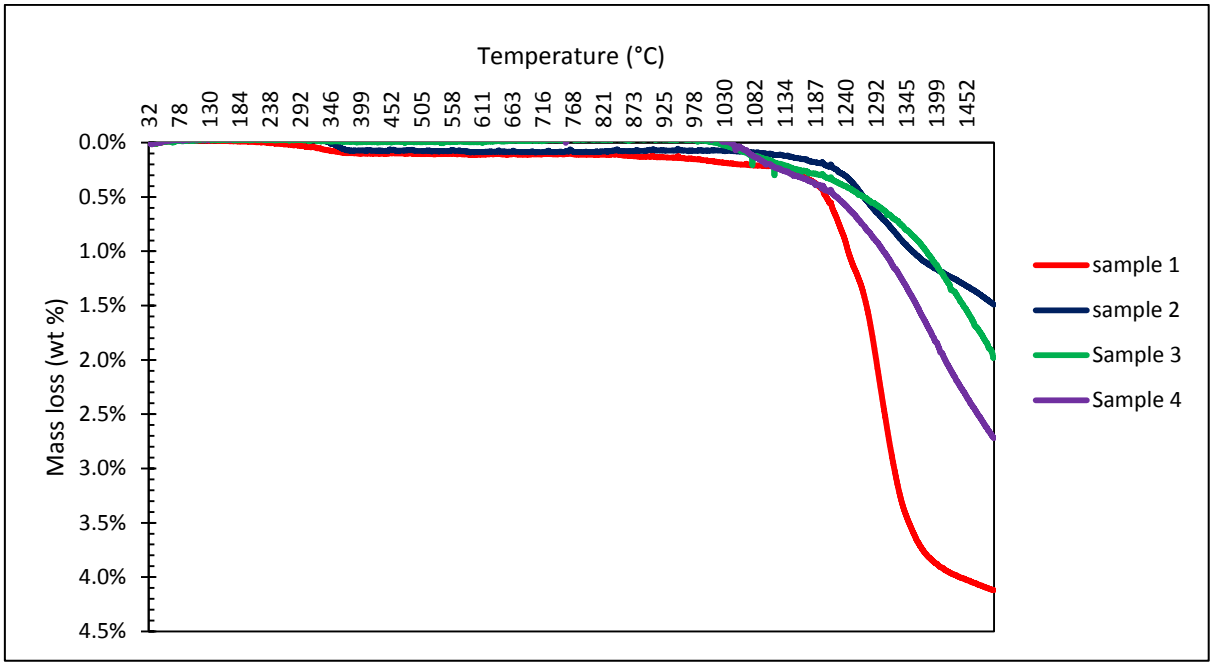

Figure 6-49: Thermogravimetric analysis of slag derived from air pollution control residue.

The use of aggressive chemicals in the production of AAS binders is a considerable disadvantage which may limit their applications to pre-fabricated production methods or carefully controlled field pours which may be expensive. Developing less aggressive activation solutions would be beneficial. Mixing the slag with cement would enable the activating solution to just be water which would promote the pozzolanic reaction, but at high slag loading in the mix this may not produce very strong materials without the addition of other additives.

The slag can be mixed with solid alkaline materials where a just add water mix can be achieved. In Figure 6-50 the strength of an alkali-activated binder made by mixing slag with solid sodium carbonate (Na_2CO3) and just adding water to allow the reaction to proceed. The solid Na_2CO_3 will react to produce an alkaline solution which would allow the alkali-activation of the slag to occur. The results show that this does produce a material with some compressive strength,

but this is not as strong as the binder produced from the reaction between a slag and NaOH. However, it does show it is possible to achieve a mix where just adding water is necessary and so by experimenting with other alkaline materials such as lime it may be possible to increase the strength of these mixes. The high strength of the alkali-activated binders produced from the reaction between the slag and NaOH is good but it may not be necessary and so a strength somewhere in the middle might be ideal for most normal applications.

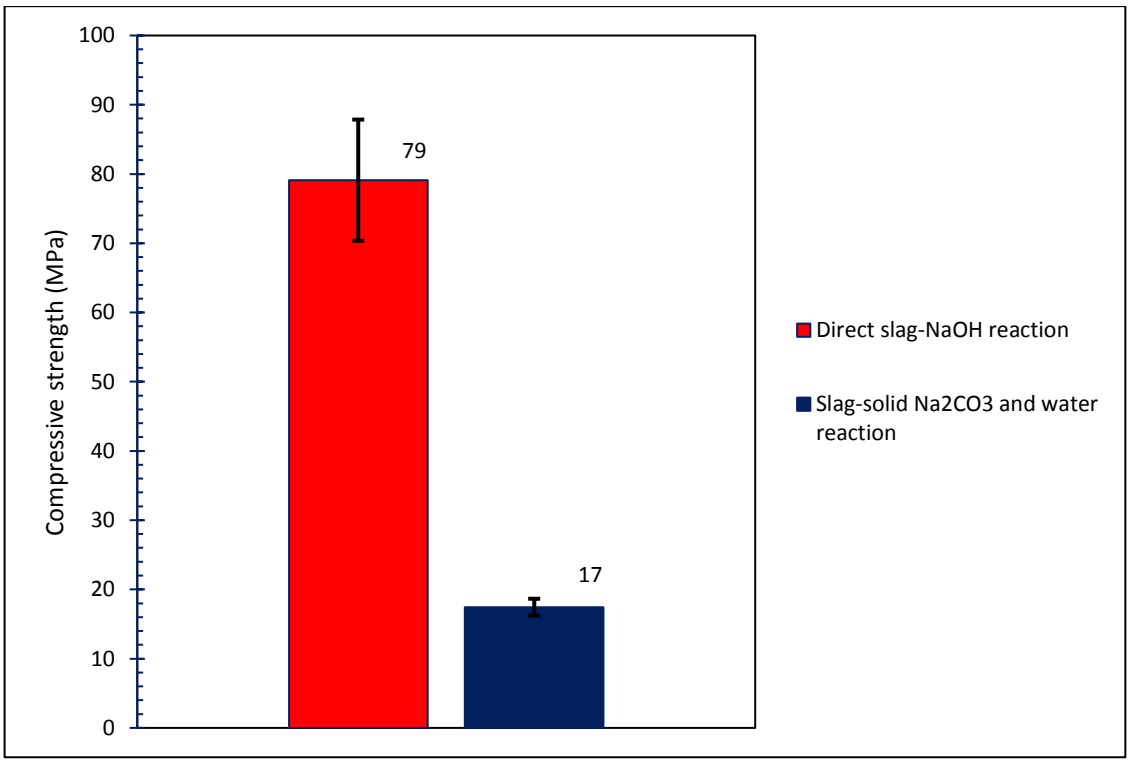

Figure 6-50: A comparison between the compressive strengths of an alkali-activated binder made from a direct reaction between a slag and NaOH and an indirect reaction between a slag, solid Na_2CO_3 and water.

The use of plasma derived slag as a cement replacement would be an ideal opportunity to increase the value of the slag to around £50 per tonne which would significantly enhance the process economics of the plasma process. The use of this slag as a cement replacement would

have great environmental benefits by reforming a waste to a construction product with low CO_2 credentials and so also presents a good marketing opportunity.

7. Environmental Applications of Plasma - Industrial Gaseous Emissions Abatement.

7.1. Introduction.

Emissions from industrial processes can contain chemicals that have a negative impact on human health and the planet by contributing to climate change. A drive to reduce the negative environmental impact of industrial processes has been driven by the public, governments and industry, which has seen the introduction of more stringent regulations regarding emissions to the air and surrounding environment. There is an incentive to find new technological solutions to reduce pollution, especially carbon emissions, and with more electricity being generated from renewable energy sources, using plasma could be an interesting and effective application of the technology.

Currently, non-thermal plasma is favoured for the treatment of gaseous emissions. Complex and hazardous emissions such as volatile organic compounds (VOCs), chlorofluorocarbons (CFCs) and hydrofluorocarbons (HFCs), can be treated by plasma to form less hazardous compounds, such as CO_2. The treatment of these chemicals is particularly important for the semiconductor industry and when using non-thermal plasma, the process relies on the production of high temperature electrons which collide with the organic compounds to produce free radicals and ions. This causes the formation of highly reactive species which ultimately lead to their dissociation (Bahri & Haghighat, 2013). However, this technology is has not been used to treat CO_2.

7.1.1. Treatment of Carbon Dioxide with Thermal Plasma.

CO_2 is a stable molecule and using it as a raw material to form reaction products is, in many cases, thermodynamically unfavourable. Reacting CO_2 with minerals such as lime can form carbonates which has been a method of carbon sequestration adopted to make products like aerated blocks. However, it is possible to reform CO_2 into other chemicals which have higher value applications for example, as a synthetic gas (syngas) which can be used for power generation by burning it or for the production of hydrocarbons.

At high temperatures, CO_2 can dissociate into CO and O_2 and this dissociation takes place between 3500 – and 6000 K shown in the thermodynamic model in Figure 7-1 and shown by Davies (1964, 1965). Huczko and Szymański (1983) used a plasma system to dissociate CO_2 by injecting it into an Ar plasma jet which facilitated the dissociation. The main products of this reaction were CO and O_2 and there was no solid carbon formed. However, CO and O_2 quickly reformed CO_2 which meant that there was a low overall CO_2 conversion was between 20 and 30%. This meant that very high quenching rates were required avoid the reformation of CO_2 in the process which would probably result in a very dilute gas stream and a low value product.

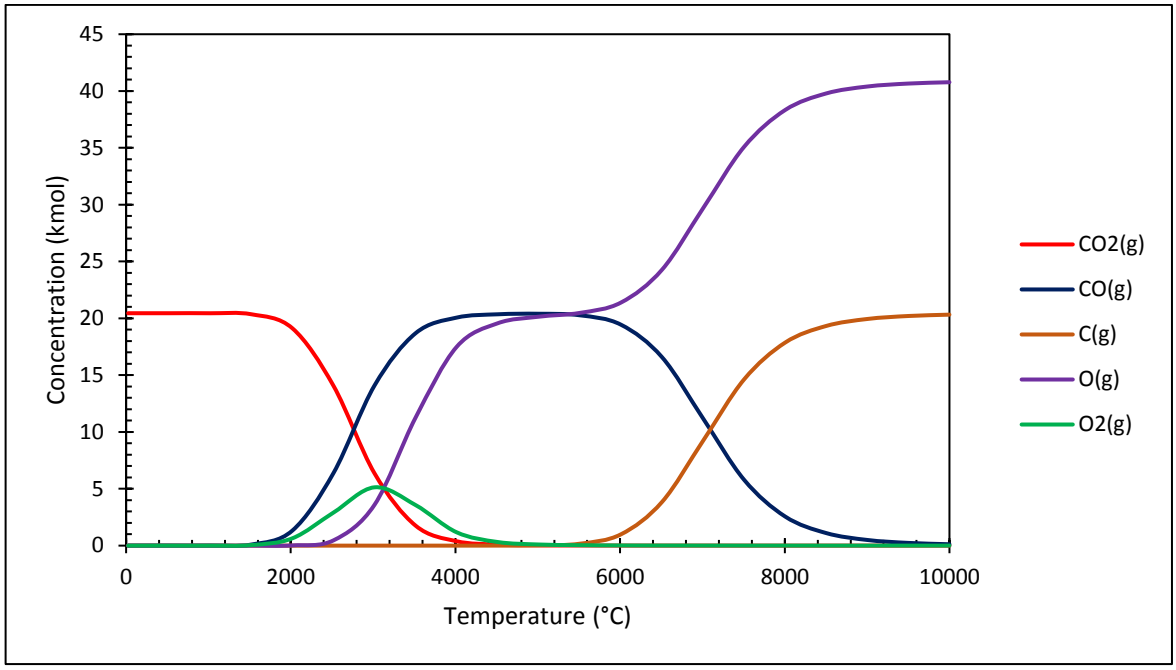

Figure 7-1: HSC model showing the dissociation of carbon dioxide.

Another high temperature reformation process is the reformation of methane with carbon dioxide. It is possible to react methane with CO_2 to form a synthetic gas. The reaction itself is endothermic and requires high temperatures for it to proceed. The change in Gibbs energy of reaction becomes negative, and therefore spontaneous, after 640°C (Figure 7-2) and the high temperatures produced by plasma make it an ideal technology to achieve these temperatures.

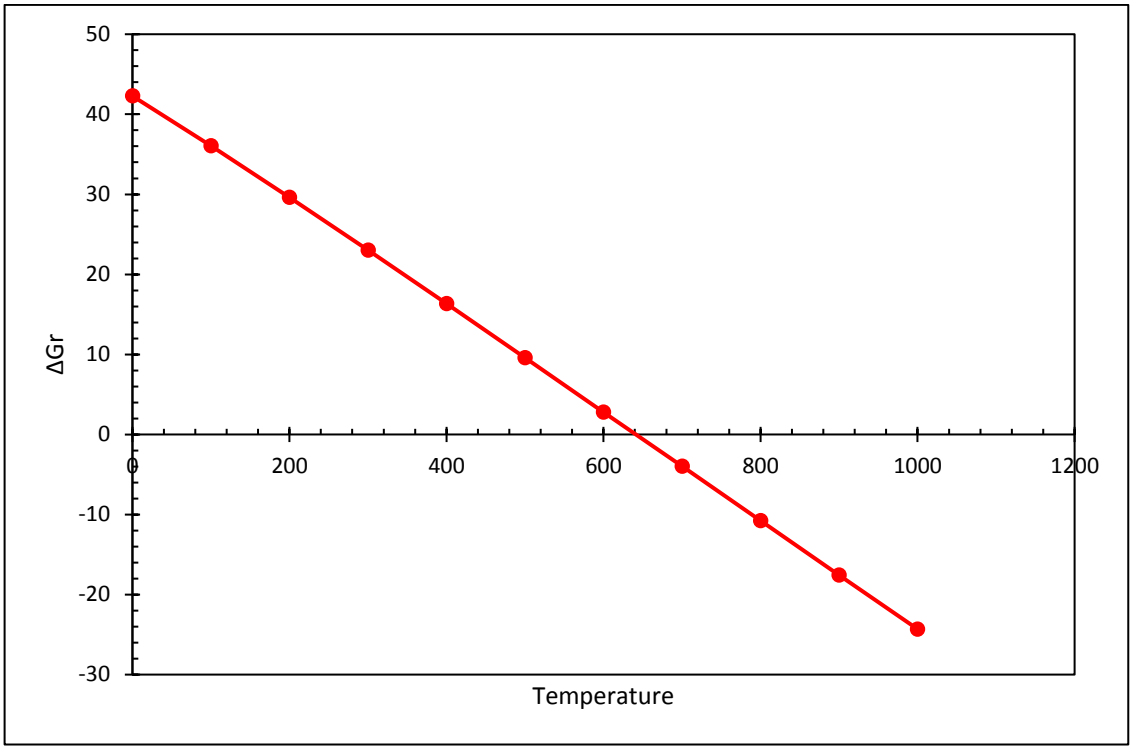

Figure 7-2: The change of Gibbs free energy for the reaction between methane and carbon dioxide to form carbon monoxide and hydrogen (calculated using HSC).

Non-thermal plasma was used by Yao et al. (2001) to attempt to achieve this reaction. The gas mixture was injected into a reactor pass a twin electrode which generated a non-thermal plasma. They reported a conversion of CH_4 and CO_2 of 66% and 58% respectively. The main products of the process were CO and H_2, but by-products were also formed such as C_2H_2 and C_2H_4. The results also indicated the requirement for rapid quenching of the products to stabilise them.

However, Sun et al. (2012) used direct current thermal plasma to reform CH_4 and CO_2. The results using thermal plasma were superior to those derived from the non-thermal plasma tests, probably due to the higher temperatures achieved and therefore a greater thermodynamic driving force for reaction. The results achieved showed a 90% CH_4 conversion

and 88.3% CO_2 conversion, but these were increased to 100% when the flow rate of the gases were reduced from 0.96 m^3/h to 0.12 m^3/h. There were small volumes of C_2H_2 formed, but the overall results were positive showing the feasibility of using plasma as a tool for gas reformation.

7.2. CO_2 and the Carbon Tax.

Due to the emission regulations and government incentives, reducing CO_2 emissions remains a target for industry. The UK's carbon budget is designed by 2050 to reduce the UK's greenhouse gas (GHG) emissions by 80% compared to the 1990 emissions baseline. The carbon budget is a restriction on the total amount of GHG emissions allowed in the UK over 5 year periods. This is designed to keep track of and gradually reduce the emissions. The current 5 year period is 2013-2017 and the cap is 2782 $MtCO_2$ equivalent which will be reduced to 2544 $MtCO_2e$ during the 2018-2022 period and then 1,950 $MtCO_2$ for the period 2023-2027.

The EU ETS, like the carbon budget, is designed to help the EU reach an emissions reduction target of 20% by 2020. Around 11,000 installations in the EU are involved that operate in energy intensive industries such as power generation, refining, manufacturing and aviation (a recent addition). Each company is given emission allowances which serve as a 'cap' and these allowances are gradually reduced over time. One allowance equates to the right to emit one tonne of CO_2. If a company is to exceed their allowance then they can purchase allowances from other companies which have a surplus in an auction style system. The idea is to give carbon emissions a high price so to encourage investment in low carbon technologies which would ultimately reduce emissions. Figure 7-3 shows the price trend of the carbon emissions allowances in the EU ETS. The price of the allowances are dependent on the supply and demand of the market and although the price has dropped significantly between 2011 and

2014, partly due to companies holding stocks of the allowances, a reduction of the emissions cap should eventually give the allowances a higher price and become more valuable.

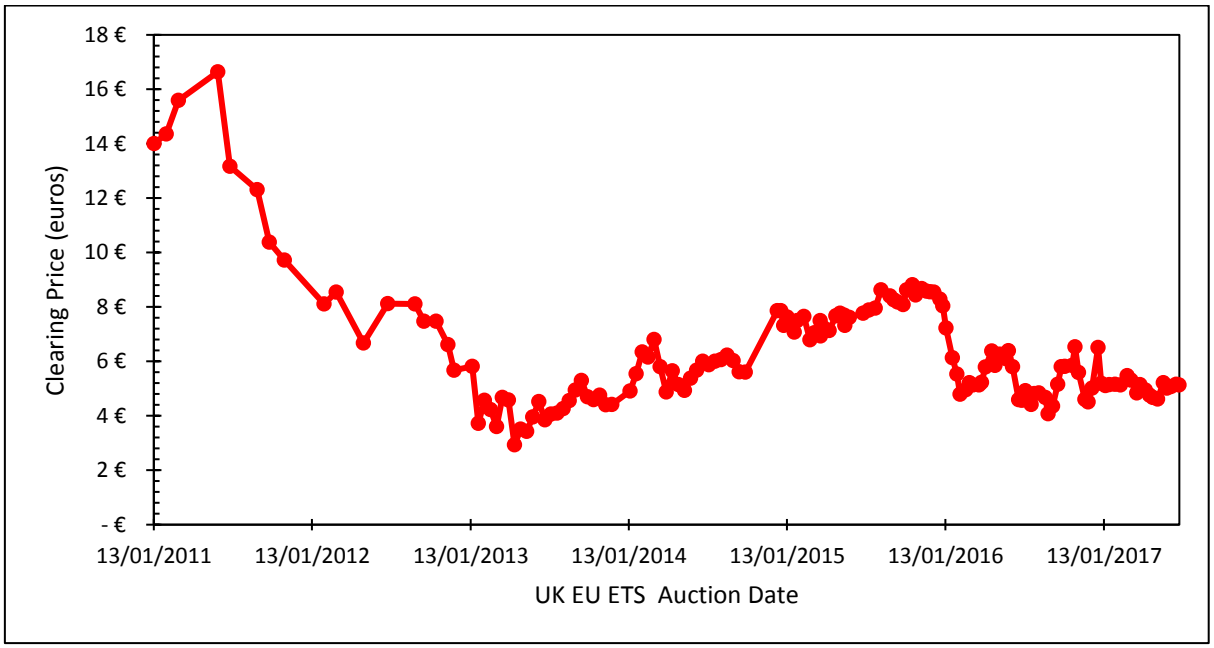

Figure 7-3: Auction clearing price of carbon emissions allowances in the EU ETS. Note the transition from phase II to III was 21st November 2012 (sources United Kingdom Debt management office, 2012 and The Intercontinental Exchange ICE, 2017).

7.3. Reformation of Blast Furnace Top Gas.

The steel industry has come under pressure to reduce its carbon emissions; for every tonne of steel produced around 2.4 tonnes of CO_2 are emitted. Currently the carbon tax is around €5/tonne CO_2, but a rise in the cost of CO_2 to around €15-17/tonne CO_2 would have a serious impact on the profitability of steel making. However, due to the development of European renewable energy source infrastructure and changes in market circumstances, electrical energy prices have fallen in value to a point where it has become competitive as an alternative heat source to natural gas.

The cost of electricity has reduced in Germany to €35/MWh although it can get as low as €25/MWh, in France the energy costs are €38/MWh, in Belgium €41/MWh and in the Netherlands €50/MWh. Therefore, with the cost of electricity being competitive with that of natural gas (€41/MWh) it is possible that plasma technology could have a wide range of applications throughout a steel manufacturer's organisation.

1.1. The Reformation of Blast Furnace Gas.

Blast furnace top gas (BFG) is the gaseous emissions from the smelting of iron ore. The gas has a relatively simple composition being composed mainly of CO_2, CO, H_2, N_2 and O_2 with a very small dust fraction (0.01 g/Nm^3). The CO and H_2 content gives the gas a calorific value and the typical lower heating value (LHV) is around 0.93 kWh/Nm^3, but this can vary over a year and even during a day and depends largely on the raw materials added to the furnace. The variability of composition of the BFG and the daily variation of its LHV can be seen in Table 7-1 and Figure 7-4, the data was provided by ArcelorMittal. Although the H_2O content (moisture) is not recorded in the table, it varies between 3 and 10 vol%.

The calorific value of the BFG is limited by the high concentration of CO_2. The reformation of CO_2 to CO would increase the calorific value of the BFG enabling it to be used as a high quality synthetic gas for other applications in the steel making process, for example in reheating steel blooms. The current practice to reheat steel blooms is by burning natural gas and so substituting this with a reformed BFG would result in significant cost savings from natural gas use and carbon emissions.

An investigation into the feasibility of using thermal plasma to produce a 10 MW_t output synthetic gas from BFG for the reheating of steel blooms was performed. The sensitivity of compositional variations of the BFG and the resulting effect on the energy requirements and

profitability of the process was assessed. The study was made via equilibrium modelling using HSC which led to a preliminary furnace design and operational cost estimate. Gas compositions for the modelling work were determined on the basis of the data supplied by ArcelorMittal and varied to cover the upper and lower LHV expected of the BFG and taking into account the moisture content of the gas which can reach 10%, but is usually between 3 to 6%. Six compositions were modelled with moisture levels at 3%, 6% and 10% of the dry gas. For each of these the CO, CO_2 and H_2 content were adjusted, whilst maintaining their relative proportions, to reach the target LHVs through dilution with nitrogen gas.

The target LHVs of the streams were 825, 800 and 750 kcal/Nm^3 (0.96, 0.93 and 0.87 kWh/Nm^3 respectively) based on the data provided. The compositions are shown in Table 7-2.

Table 7-1: Blast furnace gas compositions across numerous months in 2014 (Data supplied by ArcelorMittal). The moisture content can vary between 3 to 10%.

Component (vol%)	**January**	**February**	**March**	**April**	**May**	**June**	**July**
CO_2	22.23	22.56	22.56	23.30	22.96	22.92	22.57
CO	23.56	23.39	23.39	22.84	23.36	23.63	23.39
H_2	4.42	4.47	4.47	4.35	4.48	4.44	4.34
N_2	49.07	48.79	48.79	48.73	48.44	48.27	48.92
O_2	0.73	0.78	0.78	0.78	0.76	0.75	0.79
LHV Kcal/Nm^3	821.42	816.23	816.23	797.23	815.94	823.07	813.84
LHV kWh/Nm^3	0.96	0.95	0.95	0.92	0.95	0.96	0.95

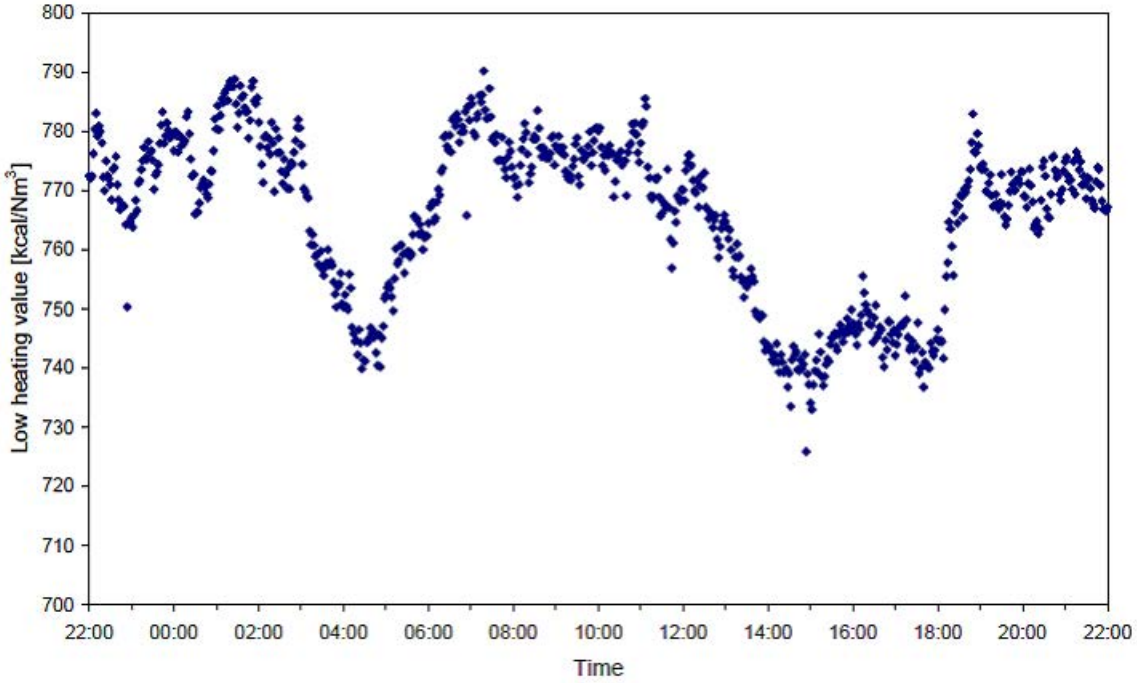

Figure 7-4: Variation of the lower heating value of blast furnace gas in one day (data supplied by ArcelorMittal).

Table 7-2: Blast furnace gas compositions modelled in this work.

	3% moisture		
Gas Species	**Composition 1 (Vol%)**	**Composition 2 (Vol%)**	**Composition 3 (Vol%)**
CO_2	22.44	21.58	22.08
CO	23.72	22.81	21.52
H_2	4.3	4.65	4.33
N_2	45.79	47.31	48.26
O_2	0.72	0.75	0.78
H_2O	3.02	2.9	3.03
Total	100	100	100
LHV (kcal/Nm^3)	826	807	759
LHV (kWh/Nm^3)	0.96	0.94	0.88
CO/CO2 volume ratio	1.06	1.06	0.97

6 and 10% moisture			
Gas Species	**Composition 4 6% moisture (Vol%)**	**Composition 5 6% moisture (Vol%)**	**Composition 6 10% moisture (Vol%)**
CO_2	23.04	21.70	21.91
CO	23.68	21.15	22.52
H_2	4.31	4.34	4.63
N_2	42.34	46.17	40.57
O_2	0.68	0.73	0.64
H_2O	5.95	5.91	9.74
Total	100	100	100
LHV (kcal/Nm3)	825	750	797
LHV (kWh/Nm^3)	0.96	0.87	0.93
CO/CO2 volume ratio	1.03	0.97	1.03

7.3.1. Natural gas composition.

The proposed process would be to react natural gas with carbon dioxide to form hydrogen and carbon monoxide as shown in Equation 7-1. The reaction is endothermic and the energy for the reaction would be supplied by the plasma.

$$CO_{2(g)} + CH_{4(g)} \rightarrow 2H_{2(g)} + 2CO_{(g)} \qquad \Delta H = +258 \text{ kJ} \quad \text{Equation 7-1}$$

The composition of natural gas used in the process is shown in Table 7-3. The composition of natural gas was provided by ArcelorMittal and its LHV was calculated using HSC. The economic benefits of the process were determined by comparing the operational costs of the plasma based reformation system with the current technology which burns natural gas to heat the

blooms. Therefore, the natural gas process was the baseline for which the comparison was made.

Table 7-3: Composition of natural gas used in the process.

Component	Mol%
Methane	91.05
Ethane	6.07
Propane	1.81
iso-Butane	0.27
n-Butane	0.30
iso-pentane	0.01
n-pentane	0.002
Nitrogen	0.50
LHV (kWh/Nm^3)	10.77

7.3.2. Modelling Conditions.

The models were constructed to calculate the composition at equilibrium at 1000°C and at ambient pressure and a further study was done to examine the process at 3.5 barg, which is the operational pressure of the blast furnace. The total gas energy was calculated as a combination of the sensible heat and the chemical energy of the output steam (i.e. the energy released upon the combustion of the stream based on its LHV).

The efficiency of the furnace was assumed to be 85% which was based on the efficiency of a standard refractory lined combustion chamber and the heat losses of the furnace were kept constant at 435 kW.

7.4. Modelling Results.

7.4.1. Model summary.

The models show that a high conversion of over 99% of CO_2 could be achieved and a simple gas composition of CO, H_2 and N_2 would be produced as shown in Figure 7-5 and Table 7-4. Nitrogen is present in a significant amount, but this is generally inert throughout the process although there may be a small fraction of nitrogen which will form ammonia (NH_3).

The results show a significant upgrade of the energy content of the gas and the LHV of the output gas is raised from around 0.9 kWh/Nm^3 to around 2.5 kWh/Nm^3. To achieve a 10 MW_t output of the gas around 80% of the energy is supplied by the chemical energy of the BFG and 20% is supplied by its latent heat. The plasma energy provides the energy for the endothermic reaction, heat the gases up to 1000°C and overcomes the heat losses of the system. The calculated plasma energy required to achieve a 10 MW_t output was around 3.2 MW. A summary of the energy balance and the gas flow rates is shown in Table 7-5 and Table 7-6.

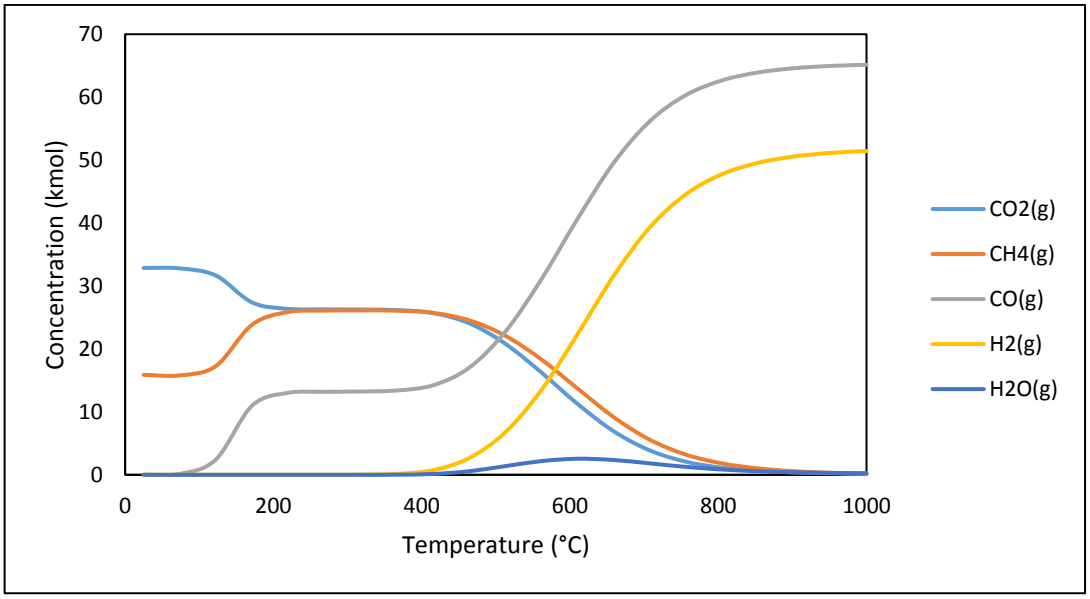

Figure 7-5: Equilibrium model showing the reformation of blast furnace gas at 1000°C.

Table 7-4: The output gas composition from the initial BFG composition 1.

Output species	Mol%
CO(g)	40%
H_2(g)	32%
N_2(g)	28%
CO_2(g)	0.047%
CH_4(g)	0.228%
HCN(g)	0.015%
NH_3(g)	0.001%
Total	100%

Table 7-5: Summary of the results of the modelling of the reformation of the blast furnace gas (BFG).

Composition	Moisture (vol%)	BFG flow rate (Nm^3/hr)	Natural gas flow rate (Nm^3/hr)	BFG/NG molar ratio	CO_2/CH_4 molar ratio	CO_2 conversion (%)	Output gas flow rate (Nm^3/hr)	HCN (vol%)
1	3.02	2017	487	4.14	1.02	99.3	3594	0.008
2	2.9	2075	487	4.26	1.01	99.48	3648	0.011
3	3.03	2045	496	4.15	1	99.62	3653	0.015
4	5.95	1845	504	3.66	0.93	99.35	3474	0.009
5	5.91	1940	509	3.81	0.91	99.4	3584	0.010
6	9.74	1735	522	3.33	0.8	99.56	3416	0.013

Table 7-6: Continuation of the summary of the modelling of the reformation of the blast furnace gas (BFG).

Composition	BFG LHV (kWh/Nm^3)	BFG chemical energy (MW)	Natural gas LHV (kWh/Nm^3)	Chemical energy LHV (MW)	Plasma power (MW)	Gross energy requirement (kWh/Nm^3)	Sensible heat of output gas (MW)	Chemical energy of output gas (MW)	Total energy of output gas (MW)
1	0.961	1.94	10.78	5.25	3.25	1.61	1.35	8.65	10
2	0.939	1.95	10.78	5.25	3.26	1.57	1.37	8.65	10.2
3	0.883	1.81	10.79	5.35	3.28	1.6	1.37	8.66	10.03
4	0.959	1.77	10.77	5.43	3.25	1.76	1.3	8.71	10.01
5	0.872	1.69	10.77	5.48	3.29	1.69	1.35	8.68	10.03
6	0.927	1.61	10.79	5.63	3.24	1.87	1.28	8.76	10.4

7.4.2. Effect of Moisture Content on the CO_2 conversion.

As the moisture content in the blast furnace gas increases there is a reduction in the overall CO_2 conversion, if the natural gas addition is kept constant. This is due to competing reactions between the species in the gaseous stream, especially the reaction between CO and H_2O which causes the reformation of CO_2 (Equation 7-2).

$$CO_{(g)} + H_2O_{(g)} \rightleftharpoons CO_{2(g)} + H_{2(g)} \qquad \text{Equation 7-2}$$

To improve the CO_2 conversion at a higher moisture, an increased natural gas flow is required in the process. Figure 7-6 shows the increase in natural gas required to achieve a CO_2 conversion of over 99% and a 10 MW_t power output scale.

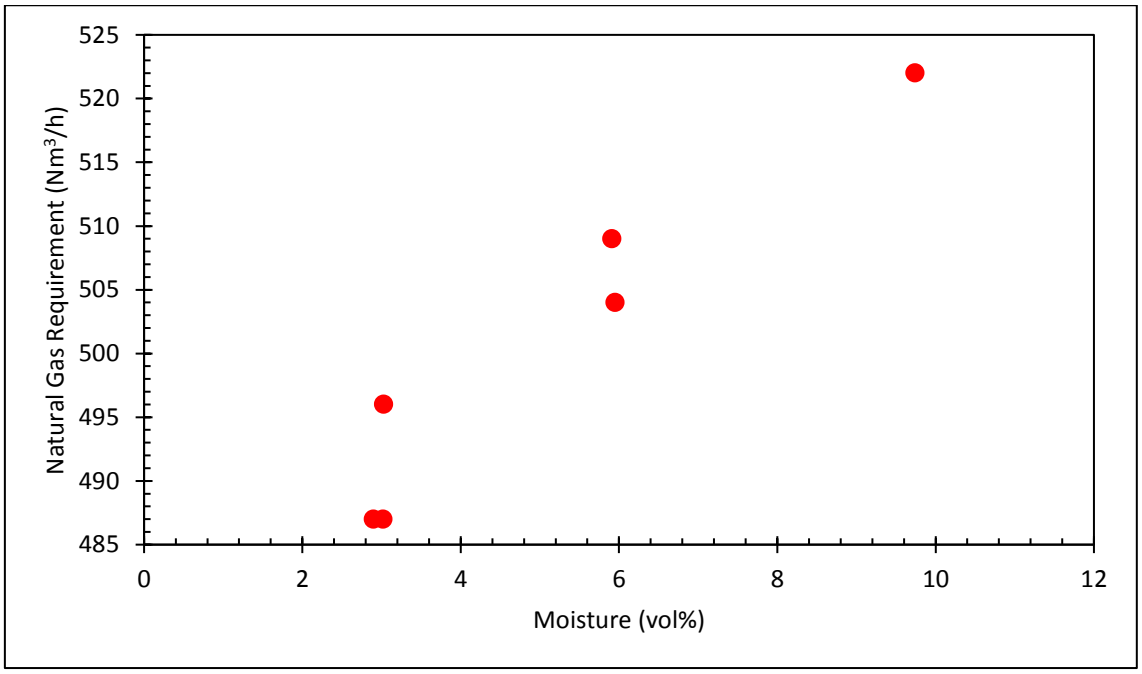

Figure 7-6: The effect of increasing moisture content on the natural gas requirement to reform BFG.

The natural gas requirement can be expressed as the blast furnace gas to natural gas ratio (BFG/NG) to allow for scaling of the flows in the process. Figure 7-7 shows that as the BFG/NG

ratio decreases a higher CO_2 conversion is achieved. Similarly to Figure 7-6 the natural gas requirement is increased as the moisture content of the BFG increases, therefore a lowering of the required BFG/NG ratio is seen to achieve a specific CO_2 conversion, which is also seen in Figure 7-8.

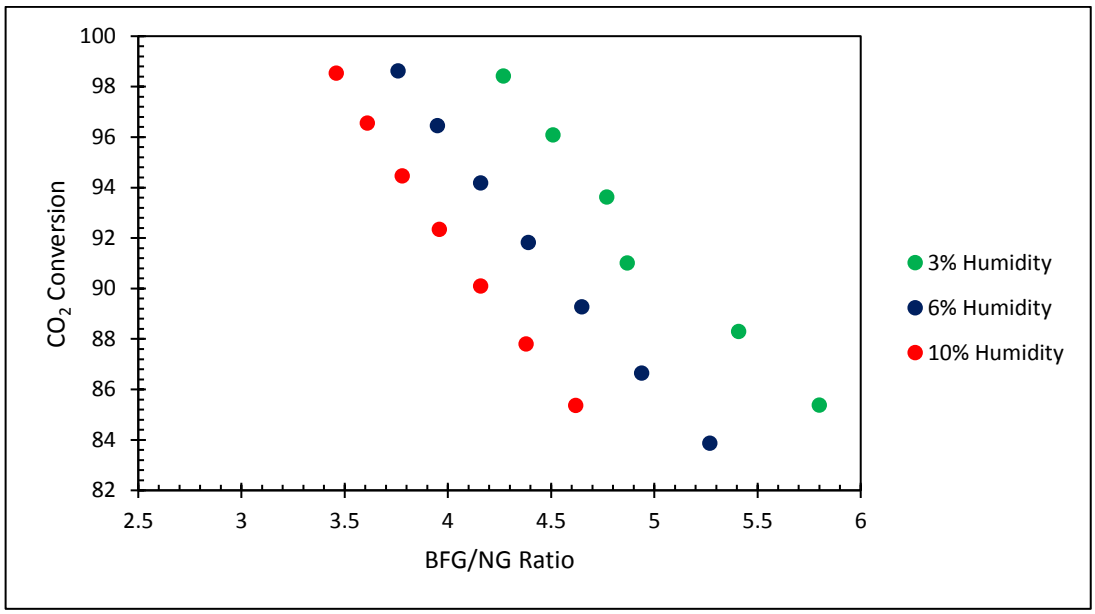

Figure 7-7: The effect of the BFG/NG ratio on the CO_2 conversion.

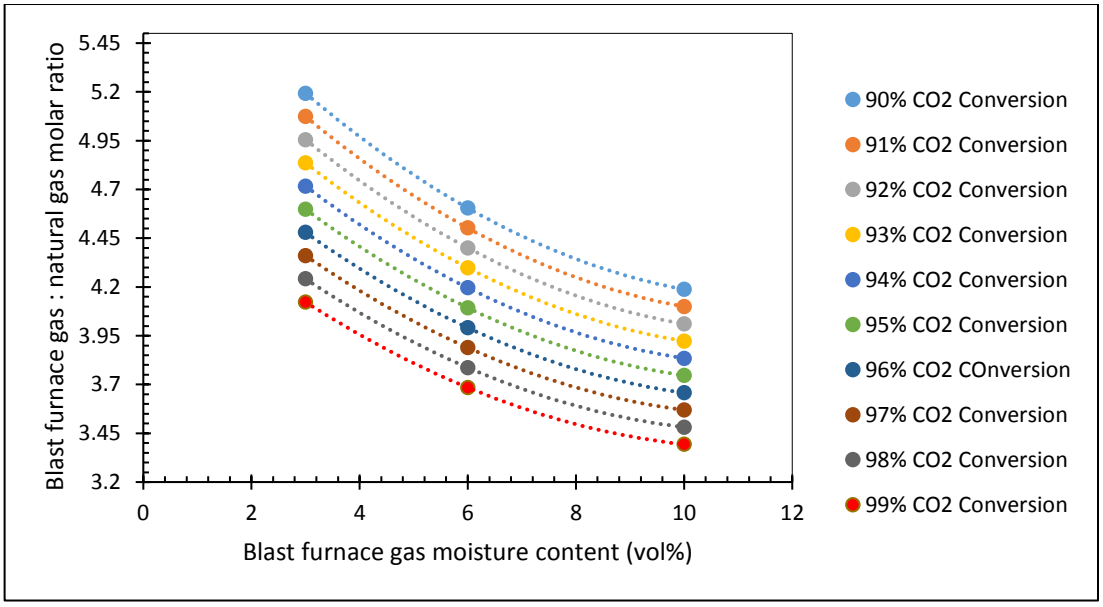

Figure 7-8: The BFG/NG ratio vs moisture content for a given CO_2 conversion.

The BFG/NG ratio required to achieve a desired CO_2 conversion (up to 99%) can be calculated from the desired CO_2 conversion and the moisture content of the BFG via the relationship shown in Equation 7-3:

$$\frac{\mathrm{BFG}}{\mathrm{NG}} = (-0.0003\mathrm{K_C} + 0.0401)\mathrm{w}^2 + (0.0082\mathrm{K_c} - 1.0477)\mathrm{w} - 0.1407\,\mathrm{K_c} + 18.677$$

Equation 7-3

$$\text{Where: } \mathrm{K_C} = \mathrm{CO_2}\text{ conversion: } \frac{\mathrm{mol\ CO_2\ final}}{\mathrm{mol\ CO_2\ inital}} \times 100; \mathrm{w} = \text{moisture content (vol\%)}$$

This equation, although based on theoretical calculations, shows that it may be possible to develop a control philosophy to maintain the desired output (CO_2 conversion) whilst monitoring the composition of the blast furnace gas and adapt the process conditions and flows as required. Showing that relationships can be developed between the process variables and with empirical data from trial work more realistic equations for control could be developed to account for kinetic factors in the reactions.

The gross energy requirement per Nm^3 of blast furnace gas increases as the moisture content of the BFG increases (Figure 7-9) because of the increased natural gas requirement when the moisture is higher and a resulting reduction in the BFG flow. An increase in plasma power is required, because of the lower heating value (LHV) of the BFG.

Although there is an increase in plasma power requirement for the BFG stream with low LHV, there is not a large range between the highest and lowest plasma power requirements (3.29 MW for composition 5 and 3.24 MW for composition 6) demonstrating that the electrical power input would not have to swing significantly to match the BFG input and so the process could be controlled and flexible to match the input gas.

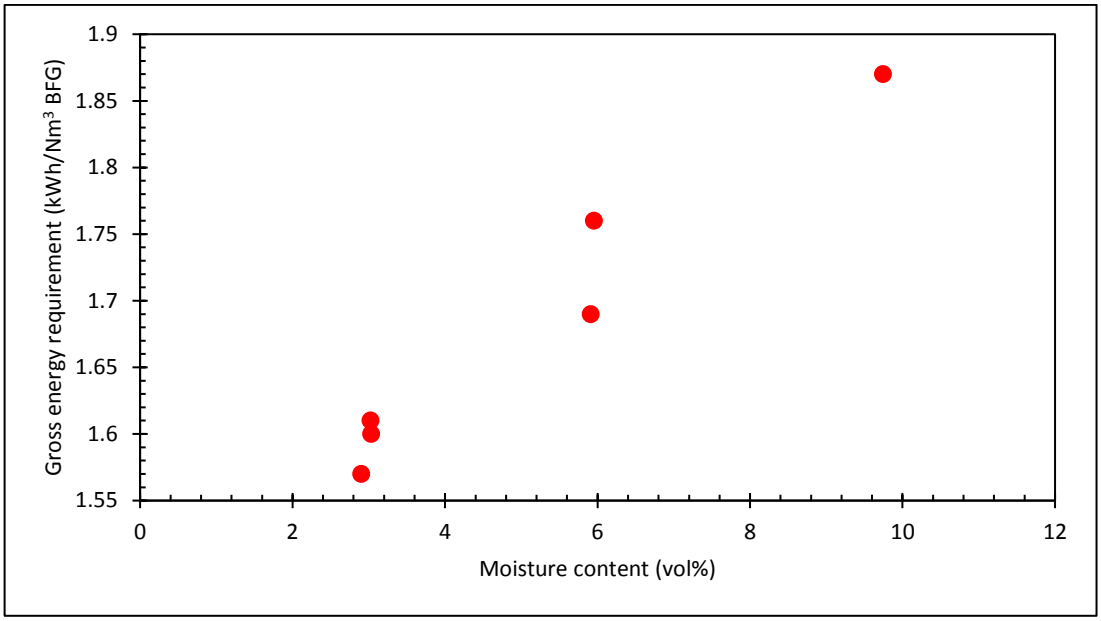

Figure 7-9: The effect of the moisture content on the gross energy requirement of the BFG.

7.4.3. Carbon Conversion.

Table 7-7: CO_2 conversion calculated from the modelling.

	Ambient Pressure Operation					
Composition	**1**	**2**	**3**	**4**	**5**	**6**
CO_2 Conversion	99.3%	99.5%	99.6%	99.4%	99.4%	99.6%
kg CO_2 Removed at 10 MW_t scale.	883	875	883	829	822	741
Kg CO_2 Removed/MWh	88.3	87.5	88.3	82.9	82.2	74.1

Table 7-7 shows the amount of CO_2 removed during this process at the scale modelled. There is a high percentage removal of CO_2 from the original blast furnace gas and this equates to a large mass of CO_2 removed during the process as it is transformed into CO. The amount of CO_2 removed per MW_t output of the outlet stream varies between 74 and 88 kg, providing a significant reduction in CO_2 emissions.

7.4.4. Hydrogen cyanide production.

Hydrogen cyanide (HCN) is a by-product from the gaseous reactions and its production is a potential hazard, although this depends on the final use of the output gas. Its formation was shown to be stimulated by the presence of excess methane in the process. A possible mechanism of formation of HCN is the reaction between ammonia (NH_3) and CH_4 in the process to form HCN via Equation 7-4 or by reacting with the plasma gas, nitrogen.

$$\mathrm{CH_{4(g)} + NH_{3(g)} \rightarrow HCN_{(g)} + H_{2(g)}} \qquad \text{Equation 7-4}$$

Figure 7-10 shows the HCN production increases exponentially as the natural gas addition is increased in the process. The natural gas addition is required to achieve a high CO_2 conversion but, there is a plateau in the CO_2 conversion at around 21 kmol natural gas addition and increasing the gas addition has a minimal effect on the conversion of CO_2. It is at this plateau of the CO_2 conversion graph where the dramatic increase in the HCN production begins as it is here where there will be excess CH_4 in the system.

Therefore, a compromise between the total CO_2 conversion and the HCN production may have to be accepted for safety reasons; regardless of the HCN production, it may not be economical to try and achieve a 100% CO_2 conversion with the large increase in natural gas requirement. Table 7-5 and Table 7-6 shows the results of the models where a maximum amount HCN content in the output stream of 150 ppm by volume was fixed as the upper limit.

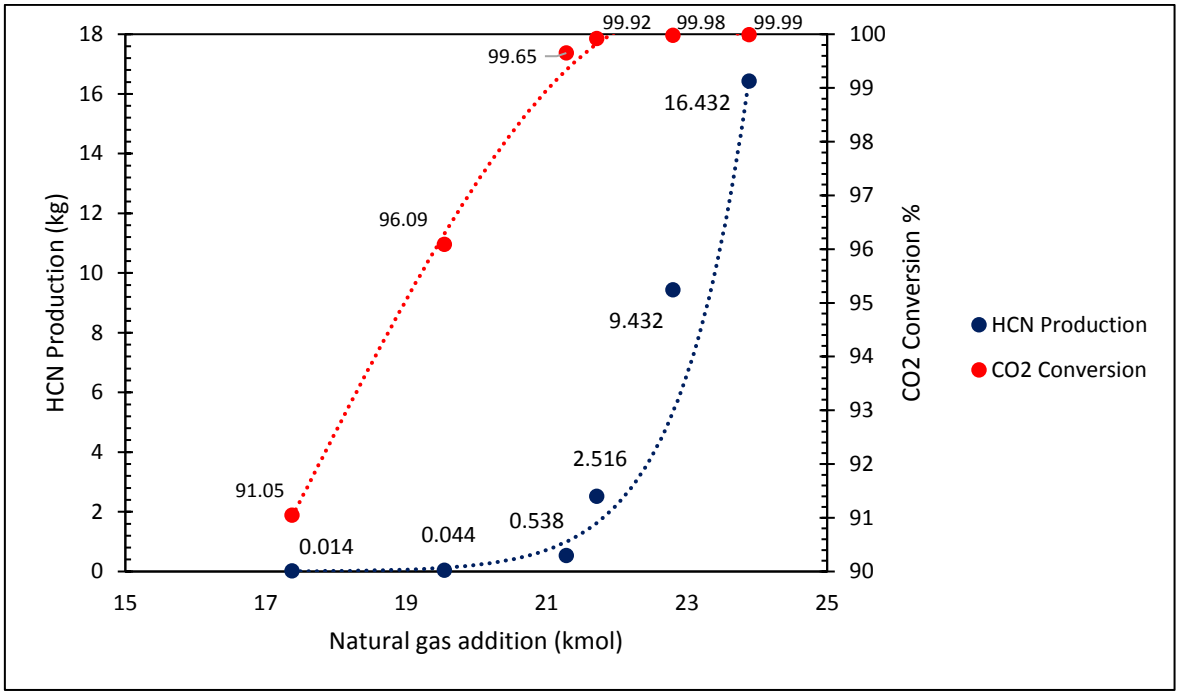

Figure 7-10: The production of hydrogen cyanide vs the natural gas addition.

7.4.5. Minor component formation.

NO_x and SO_x compounds are not predicted to form in the thermodynamic models. This is due to the very low concentration of sulphur in the input steam (which is present as part of the dust composition) and so if any SO_x compounds were to form they would be in a tiny concentration. There is also a low oxygen concentration in the input streams meaning that reactions between nitrogen and oxygen and sulphur and oxygen to form their oxides is unlikely to occur. The solid metals and oxides in the dust fraction remained virtually unchanged through the process, but as the solids fraction is very small compared to the bulk flow their appearance in the output stream is not significant. Alkaline metals (K, Na) are predicted to form hydroxide compounds (KOH and NaOH), but not in significant concentrations.

In summary, all the dust components generally are unchanged although some other compounds may be formed however the concentration of all these species are in the order of 0.01g/Nm^3 and so at the modelled scale the dust mass is around 20g (at 2000 Nm^3 of BFG) and are therefore not regarded as a significant part of the output stream.

7.4.6. Baseline Consumption Comparison.

The current process used for the heating of steel blooms is to burn natural gas. A limiting factor for this process is the efficiency of the burner used. The efficiency of the natural gas burners used to compare these processes was 60% (this figure was supplied by ArcelorMittal) and so to achieve a 10 MW_t output the natural gas consumption was calculated to be 16.7 MW. In the plasma reformation of BFG, the natural gas requirements to achieve a 10 MW_t output ranges between 5.3 and 5.6 MW depending on the composition of the BFG. This therefore equates to a natural gas saving of 11.4 MW.

The electrical energy which is required to power the plasma in this process ranges from 3.6 to 4.1 MW and the total power consumption of the plasma process which includes the blast furnace gas chemical energy ranges from 10.8 to 11.2 MW. This equates to a total power saving of 5.9 to 6.2 MW, a clear saving of natural gas usage.

7.4.7. Higher Pressure Modelling.

The pressure of the blast furnace gas as it comes out of the furnace is 3.5 barg and so the operation of a plasma reactor in this application should be at this pressure. Therefore, the equilibrium compositions were also modelled at 3.5 barg to determine the theoretical behaviour of the species in the gaseous inputs at these higher pressures. The compositions which were modelled at 3.5 barg were 1, 2, 5 and 6.

The modelling results found that there was a slight decrease in the CO_2 conversion at higher pressures for the same flow rates of BFG and NG compared with the compositions modelled at ambient pressures, this is represented in the graph in Figure 7-11 and Table 7-8. The output gas stream contains a slightly higher CO_2 concentration at 3.5 bar than at 1 bar. A summary of the results is shown in Table 7-9 and Table 7-10.

Therefore, the addition of natural gas has to be adjusted for these conditions, but similarly to the ambient pressure operation there is an increase in the HCN production as the natural gas addition is increased. To achieve an output gas with a HCN upper limit concentration of 150 ppm the results of the modelling are shown in Table 7-9 and Table 7-10. At these higher pressure conditions, the CO_2 conversion is 98.3% as opposed to the 99.4% achieved at ambient pressure, but this is still high.

There are no significant changes to the plasma energy requirements between the processes at ambient pressure and at 3.5 barg and so the gross energy requirement per Nm^3 of blast furnace gas does not change with the conditions. There is a slight change in the overall plasma power input due to the different BFG/NG ratios required for the process which therefore slightly alters the flowrates of the input streams.

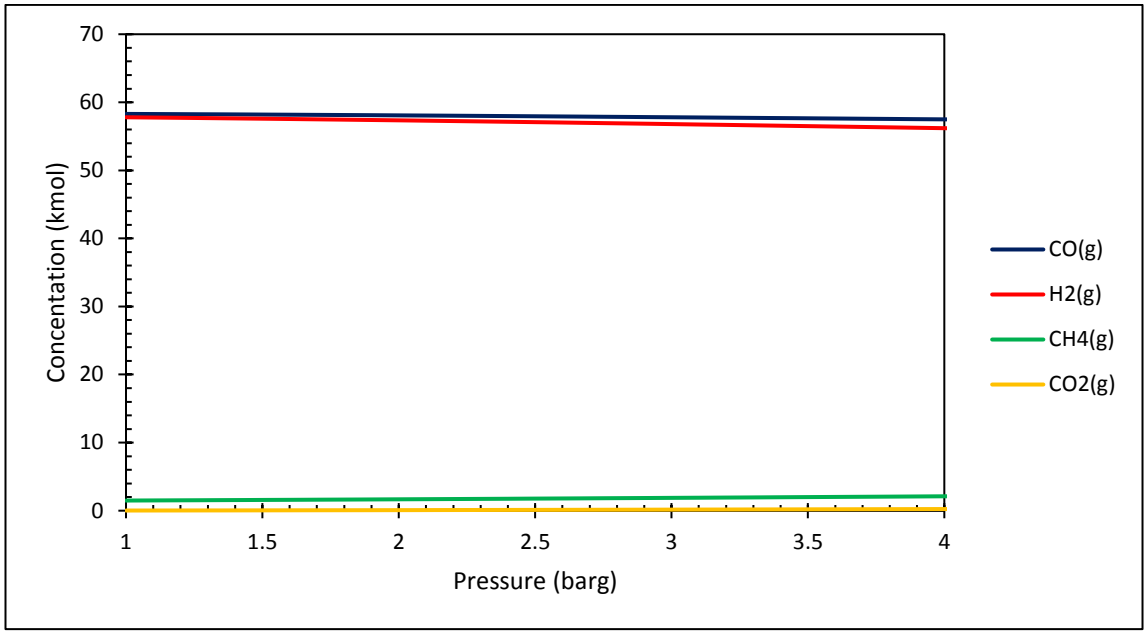

Figure 7-11: The effect of increasing the pressure on the output composition.

In Figure 7-11 above it can be seen that there is a slight decrease in the equilibrium concentration of CO and H_2 as the operating pressure is increased along the x-axis. The CO_2 concentration increases with an increase of pressure, resulting in a marginal reduction in the CO_2 conversion. Table 7-9 and Table 7-10 shows the results of the modelling calculations for operation at 3.5 barg. The energy density at of the output gas at 3.5 bar is 10.61 MJ/Nm^3 which is higher than the energy density at ambient pressure, 2.34 MJ/Nm^3. The difference lies in the decreased volume of the output gas due to the higher pressure operation and the compressible nature of the working fluid. The volume of the output gas at 3.5 barg is 3393 Nm^3 (based on the flow rates required for 10 MW_t output) whereas the volume of the output gas produced at ambient pressure would be 15361 Nm^3.

Table 7-8: Comparison between the output composition at ambient pressure and 3.5 barg.

Component	kMol (1 bar)	kMol (3.5 bar)
CO(g)	64.43	63.43
H_2(g)	51.34	49.47
N_2(g)	42.01	42.02
CH_4(g)	0.89	1.63
H_2O(g)	0.045	0.45
CO_2(g)	0.032	0.33
HCN(g)	0.055	0.023
NH_3(g)	0.002	0.009

Usually, a plasma chamber is operated at ambient pressure and the design of a plasma furnace to operate at increased pressures is novel and challenging. The gas feed system, plasma chamber and plasma device can all be designed to operate at 3.5 barg. Working pressure could be controlled through a combination of plasma power control and input gas feed rate controls. Electrode sealing will need to be carefully considered, but previous Tetronics designs have included a fully sealed electrode which would allow the system to be sealed to higher pressures. The plasma gas would need to be delivered at a higher pressure than the chamber. The outlet of the system would be tailored to the end application, this could be at pressure for a blast furnace and so the design of a pressurised plasma vessel is feasible.

Table 7-9: Results of the modelling of the plasma reformation process at 3.5 barg.

Composition	Moisture (vol%)	BFG flow rate (Nm^3/hr)	Natural gas flow rate (Nm^3/hr)	BFG/NG molar ratio	CO_2/CH_4 molar ratio	Output gas flow rate (Nm^3/hr)	HCN (vol%)
1	3.02	1980	498	3.98	0.98	3527	0.015
2	2.9	2045	495	4.13	0.98	3586	0.015
5	5.91	1895	519	3.65	0.87	3500	0.015
6	9.74	1690	533	3.17	0.76	3327	0.015

Table 7-10: Continued results of the modelling of the plasma reformation process at 3.5 barg.

Composition	BFG LHV (kWh/Nm^3)	BFG chemical energy (MW)	Natural gas LHV (kWh/Nm^3)	NG Chemical energy (MW)	Plasma power (MW)	Gross energy requirement (kWh/Nm^3)	Sensible heat of output gas (MW)	Chemical energy of output gas (MW)	Total energy of outpour gas (MW)
1	0.961	1.9	10.76	5.36	3.18	1.61	1.34	8.67	10.01
2	0.939	1.92	10.79	5.34	3.19	1.56	1.36	8.65	10.01
5	0.872	1.65	10.79	5.6	3.21	1.69	1.33	8.69	10.02
6	0.927	1.57	10.77	5.74	3.15	1.87	1.27	8.76	10.03

7.5. Concept Furnace Design.

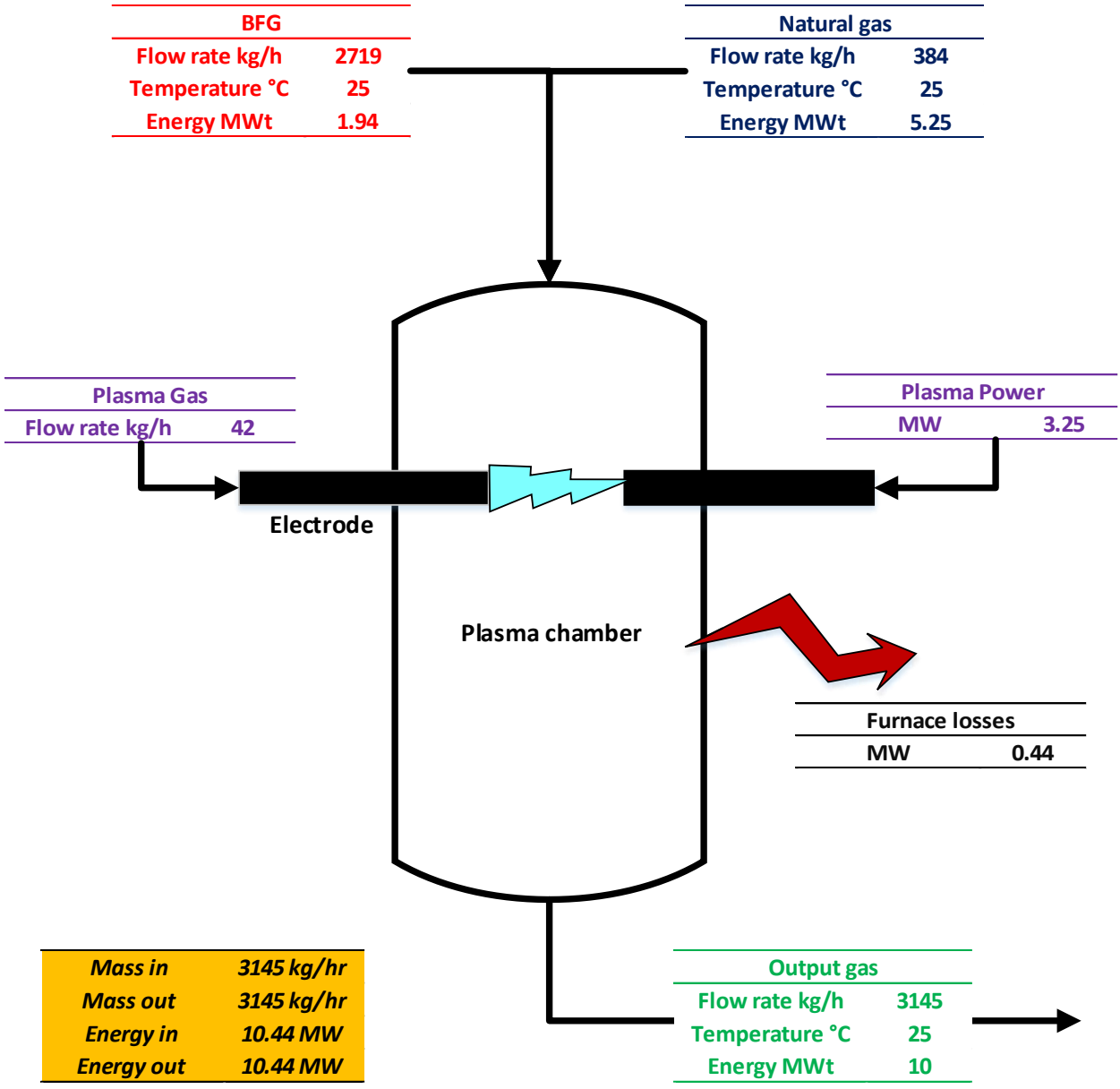

Figure 7-12: Process diagram showing the process concept with a heat and mass balance.

The concept of the process is shown in Figure 7-12 which also shows a mass and energy balance for the process. The concept of the design is to use a custom built plasma chamber for the reformation of blast furnace gas. The plasma chamber would be a refractory lined steel vessel designed to have an input flow of the reactant species (natural gas and blast furnace gas) and an output flow of the reformed gas.

7.5.1. Furnace Design and Dimensions.

The reaction between the natural gas and the blast furnace gas is to take place at 1000°C inside the chamber where a plasma arc will provide the energy to facilitate the reaction. The furnace design in this section is only for operation at ambient pressure to compare the process to the natural gas baseline.

The plasma would be delivered using a twin torch graphite electrode arrangement where the arc would be transferred between the two electrodes where one will act as the anode and the other the cathode.

The reacting gases will move through the chamber and through or near to the arc maximising the time spent at high temperature inside the furnace where the kinetics of the reaction would be favourable. The residence time of the reacting gas is designed to be 2 seconds which is believed to be enough time for the equilibrium compositions to form. Therefore, the furnace dimensions are calculated from the flow rate of the gas and the required residence time. The furnace dimensions are shown in Table 7-11.

Table 7-11: Concept furnace design dimensions.

Furnace Dimension Estimation		
Furnace aspect ratio		4
Maximum output gas flow	Actual m^3/h	17034
Residence time	s	2
Gas space volume	m^3	9.5
Furnace internal diameter	m	1.4
Furnace internal height	m	5.8
Furnace internal area	m^2	1.6

7.5.2. Refractory Requirements.

The furnace walls and roof would be refractory lined so that the furnace temperature can be maintained to reduce the gross plasma power requirements. The models shown above used an estimated plasma efficiency of 85%, based on standard combustion chamber design, and the heat losses assumed to be 0.44 MW. This value was based on a heat transfer study and is realistic when compared to combustion chamber designs. The refractory requirements initially developed in this study were approached conservatively and would likely cause the plasma chamber to be more efficient than 85% however this estimate was still used in the modelling.

The thickness of the refractory in this application would be approximately 0.189 m and the estimated refractory volume is 6.16 m^3 to maintain a hot face of 1000°C and a cold face (i.e. outside surface) of 200°C.

7.5.3. Arc Characteristics and Plasma Power Supply Rating.

The plasma will be generated using two hollow graphite electrodes and formed by passing a current between them. Nitrogen will be passed through the electrodes and this will stabilise the arc allowing for close control of its characteristics. The typical arc length between the electrodes envisioned in this process would be 150 mm. The length of the arc may however

be manipulated to control the operating voltage (and consequently power) in the system, but the typical operating voltage in this design is 200 V, which is similar to the existing plasma systems designed by Tetronics which range from 200 to 250 V.

The operating current of the electrode pair will change depending on the composition of the blast furnace gas the power required for its reformation. The operating current ranges from 16208 A (composition 6) to 18673 A (composition 3). The typical operating current for the majority of the compositions is between 16208 A and 16500 A. The maximum rating of the electrode system is designed to be 20% higher than the operating current.

The graphite electrodes are hollow tubes through which the plasma gas can pass through and the minimum required diameter of these tubes is 355 mm. Advantages of this type of electrode is the low maintenance and low cost compared to other plasma devices such as plasma torches which require bespoke spare and engineering maintenance. The graphite electrodes will erode over time and will need to be replaced, but the erosion rate is dependent on the operating conditions i.e. the power requirements, current and chemical conditions. The erosion of the electrodes in this application is estimated to be between 6.5 and 7.5 kg/h based on the power requirements of the process. This means that changing the electrodes will be required once every 55 hours if the electrodes used are 1 m and this is typical of a plasma system with graphite electrodes.

7.6. Operational Expenditure (OPEX) Summary.

The major operational costs for the plasma based process are derived from the use of electricity and the natural gas. The OPEX calculations for composition 1 are shown in Table 7-12.

The electricity requirement and natural gas requirements are dependent on the composition of the BFG and this is reflected in the operational costs for both electricity and natural gas, but the actual costs do not change significantly between compositions and ranges from €605,000/year (€16.25/MWh reformed gas) to €612,000/year (€16.42/MWh reformed gas) and so are quite consistent.

The natural gas addition requirements increase as the moisture content of the BFG increases to achieve a high CO_2 conversion (see section 3.2) and so this is matched by the increased costs for natural gas in the process. The natural gas costs increase from €796,000/year (€21.37/MWh reformed gas) at 3% moisture in composition 1 to €853,000/year (€22.82/MWh reformed gas) at 10% moisture in composition 6.

Auxiliary electrical requirements are typically assumed to be 10% of the plasma power and so are also consistent over the range of compositions and are in the range of €60,500/year.

Other OPEX costs are the consumables in the process, the graphite electrodes and the refractory replacement linings of the furnace. The graphite electrode erosion requires regular changing of the electrodes which costs €2.50 per kg and so equates to €121,824/year whilst the refractory lining costs would be €71,601/year.

The furnace would be designed to operate in standby mode where it would not be treating the BFG however it would be able to quickly be used and moved up to operating temperature

for the reformation process to be started. This would enable the quick transfer between the natural gas burning process and the plasma process as required. In this standby mode, the plasma process will be consuming electricity however on a low power requirement which would equate to €91,000 per year.

7.6.1. Cost Comparison to Baseline Process.

The use of blast furnace gas in the plasma process to achieve a 10 MW_t output reduces the requirement for natural gas which would be used in the baseline natural gas burning process. This causes a significant cost saving for the process being run using the plasma chamber which can be seen in Table 7-12. The overall cost saving per year is just over €1m a year.

Table 7-12: Energy defined OPEX calculation for composition 1.

Items	Cost/year	Cost/MWh reformed gas	Cost/year	Cost/MWh reformed gas	Unit of inputs	Cost of unit	No Units per MWh reformed gas	Reformed gas annual output
	(£)	(£)	(€)	(€)				(MWh/y)
Electrical power (plasma)	£447,690.75	£12.03	€604,988	€16.25	kWh	€0.050	325	37230
Electrical power (auxiliary)	£44,769.08	£1.20	€60,499	€1.63	kWh	€0.050	32.5	
Natural gas	£588,678.90	£15.81	€795,512	€21.37	kWh	€0.041	525	
Inert gas (nitrogen)	£5,454.94	£0.15	€7,372	€0.20	Nm3	€0.060	3.3	
Graphite electrodes	£90,149.87	£2.42	€121,824	€3.27	kg	€2.517	1.3	
Full refractory linings	£52,984.64	£1.42	€71,601	€1.92	No.	€71,601	0.00003	
Total	£1,229,728	£33.03	€1,661,795	€44.64				

Energy defined benefit calculation	£/year	£/ MWh reformed gas	€/year	€/ MWh reformed gas	Unit of inputs	Price of unit	No Units per MWh reformed gas
	(£)	(£)	(€)	(€)			
Baseline natural gas consumption	£ 1,868,821.90	£ 50.20	€2,525,435.00	€67.83	MWh	40.70	1.67
Natural gas consumption for BFG reformation	£ 588,678.90	£ 15.81	€795,512.03	€21.37	MWh	40.70	0.53
Electricity consumption for BFG reformation	£ 492,459.83	£ 13.23	€665,486.25	€17.88	MWh	50.00	0.36
Energy defined benefit	**£787,683.18**	**£21.16**	**€1,064,436.73**	**€28.59**			

7.7. Conclusions and Further Work.

This chapter has described a feasibility study into the use of thermal plasma to reform industrial waste gases. The reformation of blast furnace top gas to produce a synthetic gas offers an opportunity to reduce the carbon emissions of the steel making process by substituting natural gas with a recycled one. This process would not only reduce the carbon emissions of the process, but would have significant cost savings of around €1 million per year. However, the cost of a plasma unit would have to be considered, but the savings calculated with in the OPEX, the return on investment should not be prolonged.

The theoretical model would have to be validated with experimental tests and the OPEX recalculated. However, in line with previous research it seems that it is possible to achieve the near 100% conversion of CO_2 and CH_4 which were described in the model. It would also be interesting to perform a life cycle assessment (LCA) on the technology to more accurately determine the carbon savings of the process.

There are various other waste gas streams which are produced during the steel making process. Coke oven gas (COG) is another which has the potential to be reformed. Another feasibility study has been conducted on the reformation of the coke oven gas to produce a gas which is suitable to be used as a reductant in the blast furnace. The composition of COG is show in Table 7-13 and it can be seen to be rich in methane. This gas is already burnt to produce energy, but it is possible to crack methane with water, air or oxygen to produce CO and H_2, both of which are powerful reductants which can be directly injected into the blast furnace.

Table 7-13: The composition of coke oven gas.

Component	Volume%
Methane (CH_4)	22
Hydrogen (H_2)	54
Nitrogen (N_2)	9.50
Carbon monoxide (CO)	8.9
Carbon dioxide (CO_2)	3

The reaction between oxygen and methane is exothermic, but the use of plasma would be as a clean heat source to control the reaction and reaction products to produce a high quality output stream. The results of a thermodynamic model of a 10,000 Nm^3/h COG flow rate are show in in Table 7-14 and it is clear that there is a very low energy input requirement from the plasma due to the exothermic reaction. The role of the plasma would be to heat the gases to the reaction temperature (900°C) and control the chemistry of the unit.

Table 7-14: Thermodynamic model results for the cracking of methane in coke oven gas using oxygen.

Operation	Value
Plasma power input (theoretical)	3800 kWh
Gross plasma power input	4471 kWh
Theoretical energy requirement (TER)	0.34 kW/Normal m^3
Gross energy requirement (GER)	0.4 kW/Normal m^3
Coke oven gas flow rate	10000 Normal m^3
Oxygen flow rate	1130 Normal m^3
Methane conversion	98.3%
Temperature of output stream	900°C
Volume of input gas	2473 Actual m^3
Volume of output gas	12623 Actual m^3

Therefore, the use of plasma in gas phase reactions not only has a theoretical basis, there are clear business opportunities for the technology which could be developed. The worldwide

incentives to reduce carbon emissions are requiring many large companies to develop new technologies and it may well be that plasma could find an application in this field.

8. Thesis Conclusions and Further Work.

The work presented in this thesis has addressed issues across the plasma process which all aim to enhance the sustainability of resource management whether it be increasing the efficiency of rare metal recovery or avoiding waste going to landfill.

The separation of SiC and cordierite prior to the furnace enables a more consistent feed composition to be achieved. The negative effects of SiC have been an industry wide problem and in a market where the competition for the raw material is high, being able to handle low grade mixed scrap presents a significant advantage. The magnetic and electrostatic separation process presented in this thesis produces a high grade cordierite, of over 98% from a mixed raw material containing 28% SiC. This shows the efficiency of the process and produces an almost pure cordierite fraction which can be processed easily within the plasma furnace. The process is a very different approach to the common practice of treating the SiC within the furnace and the resulting negative consequences of the changes in the viscosity of the melt pool and the dilution of the collector metal. The next stage of this work would be to build and commission a pilot scale process to develop the optimum operating conditions over a range of SiC concentrations. Research and development must be done to optimise the crushing of the catalysts to ensure that there is not a large fine fraction produced which cannot be processed efficiently in the electrostatic unit. However, implementing this process would have many benefits for current and potential plasma users.

The recovery of rhenium from the spent reforming catalysts shows the flexibility of the operation of a plasma furnace in being able to closely control the chemistry recover less noble

metals via a pyrometallurgical route. The benefits of a pyrometallurgical process over a hydrometallurgical one for these catalysts is the ability to process almost 100% of the Pt-Re chemical catalysts by being flexible to compositional or mineralogical variations of the raw material. The initial modelling work performed to determine the operation conditions required was validated at pilot and commercial scales resulting in the recovery of over 97% of both platinum and rhenium and so the project proved to be successful. Further work may be to investigate the slag composition and the effect this has on the viscosity of the melt. This would have great practical benefits as most slag viscosity data is obtained from literature. Developing an empirical model which is based on the range of slag compositions which Tetronics experience would help to develop and improve the efficiency of plasma processes especially in the development of new plants and projects.

Investigating the slag composition would have an immediate effect on the potential uses of the slag after it has been removed from the furnace. The work presented in this thesis regarding the reuse of slag has shown that there are numerous potential applications for slags, but the application depends on many factors. Generally, the higher the value of a slag product requires a higher capital investment. The use of slag as a cement replacement was highlighted as one of the most favourable use because the slag requires only fast cooling to produce a glass and then for it to be ground to a fine particle size and these pozzolanic slags can obtain a market value of around £50/tonne, which would significantly enhance the business model of the plasma process. The price of the product must take into account all the costs of its production including the cost of grinding. The grinding of the material may require large amounts of energy and the energy requirement to crush the slag to less than 63 μm needs to be determined. Nevertheless, this cost is an estimate based on the commercial value of GGBS

and other pozzolanic materials and so seems realistic. The slags produced from the plasma process show good pozzolanic activity showing it could be used as a cement replacement and also can be used to produce low carbon construction materials via an alkali-slag reaction producing an alkali-activated binder. These materials have similar properties to ordinary Portland cement based binders, but their low carbon footprint has seen interest in them increase over the last ten years in both academia and industry. The difficulty for these materials is moving them towards the market which has significant regulatory hurdles. The use of slags as cement replacement in the current market is limited to blast furnace slags due to narrow composition ranges allowed under regulations. However, it is possible for slags from the plasma process to obtain CE marking by undergoing an assessment process outlined in Appendix B. Alkali-activated binders and geopolymers are a more distant application for slags due to the large amount of research required for safe and more practical activating solutions to be developed. However, due the carbon impact of cement it will be likely to see greater substitutions of cement by slags or other pozzolanic materials. The current regulations can allow for cement substitutions of up to 95% and so the development of these highly substituted cements using water and perhaps mild alkaline solutions may well become more common. Further work for the plasma derived slags are to ensure the consistency of the slag coming from the plasma processes and the reduction of any residual chlorine in the slag making it suitable for construction applications.

The advantage of plasma being generated via electricity means that when the sources of electricity are renewable, plasma can be used effectively for environmental applications. Plasma can be used as a heat source to power endothermic chemical reactions such as the conversion of CO_2 to a synthetic gas. The feasibility of this reaction was shown in Chapter 7

where the CO_2 blast furnace top gas was converted to a synthetic gas which could be used for reheating applications within a steel plant. The conversion of this waste gas means that there would be savings from CO_2 emissions and also cost savings from the reformed gas replacing natural gas. The economic savings of this process at a 10 MW_t scale amounts to just over €1 m per year, but the capital investment of this process would be significant and would be a stumbling block for potential clients. The economics of this process would be even more favourable if the CO_2 tax was increased. Also the requirement of such a process to be run at a high pressure is something which would present a significant technical challenge to achieve and would require much of the current plasma system to be redesigned. However, the process does show that plasma technology can be used to drive and control chemical reactions. This may have applications in the conversion of renewable electricity which cannot be stored into chemical energy via a reaction.

Thermal plasma technology can be implemented for a variety of applications which help to enhance the management of resources required for modern applications. The formation of a circular economy is an idea which can seem idealistic, but there are examples of the circular economy in action today especially in the platinum group metal industry. Here, plasma technology plays an important role, but it can be seen that it is the integration of various technologies, collection methods and market supply chains which truly makes it work. Sustainable resource management is a great challenge facing the world, especially as the demand for goods is increasing, but with clever applications of technologies such as plasma, achieving it is possible.

9. References.

Alessandro Mottura, M.W. Finnis, R.C. Reed, On the possibility of rhenium clustering in nickel-based superalloys, Acta Materialia, Volume 60, Issues 6–7, April 2012, Pages 2866-2872, ISSN 1359-6454,

Allahverdi, A., Najafri Kani, E., Shaverdi, B., (2015). Carbonation versus Efflorescence in Alkali-Activated Blast-Furnace Slag in Relation with Chemical Composition of Activator. International Journal of Civil Engineering. 15:565-573.

Angelidis, T.N., Rosopoulou, D., Tzizios, V., (1999). Selective Rhenium Recovery from Spent Reforming Catalysts. Industrial and Engineering Chemistry Research Vol 38 pp. 1830-1836. ACS Publications.

Arendorf, J. (2013). What Makes a Material Critical for Europe? European Raw Materials Information and Brokerage Event Presentation, 13th November 2013. Oakdene Hollins.

Bahri, M. Haghighat, F. (2104) Plasma-Based Indoor Air Cleaning Technologies: The State of the Art Review. Clean - Solid Air and Water. 42, pp 1-14. Wiley.

Barcelo, L., Kline, J. Walenta, G. Gartner, E. (2014). Cement and Carbon Emissions. Materials and Structures. 47:1055-1065.

BBC News (2014). How Uninhabited Islands Soured China – Japan Ties. http://www.bbc.co.uk/news/world-asia-pacific-11341139 Date of Access 21st December 2016.

BBC News (2016). DR Congo Country Profile http://www.bbc.co.uk/news/world-africa-13283212 Date of Access 21st December 2016.

Belov, S.F., Igumnov, M.S.M Kozlova, V.A., and Rysev, A.P. The Possibility of Rhenium and Platinum Separation from Aluminium-Platinum-Rhenium Catalysts. Proc. XIII Chernuaev Conference on Chemistry, Analysis and Technology of Platinum Group Metals, Sverldlovsk, 1986. Vol. 3. p.112.

Benson, M. Bennet, C.R. Harry, J.E. Patel, M.K. Cross, M. (2000). The Recovery Mechanism of Platinum Group Metals from Spent Catalytic Converters in Spent Automotive Exhaust Systems. Resources, Conservation and Recycling. 31 pp 1-7. Elsevier.

Benson, M. Bennet, C.R. Patel, M.K. Harry, J.E. Cross, M. (2000). Collector-metal Behaviour in the Recovery of Platinum Group Metals from Catalytic Converters. Minerals Processing and Extractive Metallurgy. 109, pp 1-6. Elsevier.

Bernal, S.A., Mejía de Gutierrez, R., Provis, J.L., Rose, V. (2010). Effect of Silicate Modulus and Metakaolin Incorporation on the Carbonation of Alkali Silicate-Activated Slags. Cement and Concrete Research. 40:898-907. Elsevier.

Borbat, V .F., Korneeva, I.N., Adeeva, L.N., and Belyi, A.S., (1998). Simultaneous Extraction of Platinum and Rhenium from Dead Platinum–Rhenium Catalysts, Izv. Vyssh. Uchebn.Zaved., Khim. Khim. Tekhnol., , vol. 42, no. 2, pp. 46–49.

British Standards Institute (2006). BS EN 15167-1, Ground granulated blast furnace slag for use in concrete, mortar and grout – Part 1: Definitions, specifications and conformity criteria. BSI Standards Limited 2006.

Brown, R., Bellmann, B., Muhle, H., Davis, J.M.G., Maxim, D.L. (2005). Survey of the Biological Effects of Refractory Ceramic Fibres: Overload and its Possible Consequences. The Annals of Occupational Hygiene. 49(4):295-307.

Brown, R.C. and Harrison, P. (2012). Alkaline Earth Silicate Wools – A New Generation of High Temperature Insulation. Regulatory Toxicology and Pharmacology. 64(2):296-309.

BS EN 196-5:2011. Methods of Testing Cement Part 5: Pozzolanicity Test for Pozzolanic Cement. British Standards Publication.

Buchwald, A., Hohmann, M., Posern, K., Brendler, E. (2009). The Suitability of Thermally Activated Illite/Smecite Clay as Raw Material for Geopolymer Binders. Applied Clay Science. 46:300-304. Elsevier.

Bukin, V .I., Igumnov, M.S., Safonov, V .V ., and Safonov, Vl.V . (2002), Pererabotka proizvodstvennykh otkhodov i vtorichnykh syr'evykh resursov, soderzhashchikh redkie, blagorodnye i tsvetnye metally (Processing of Industrial Waste and Secondary Raw Materials Containing the Rare–Earth, Precious and Non–Ferrous metals), Moscow: Delovaya stolitsa. Burciaga-Diaz, O. Escalante-Garcia, J. (2013) Structure, mechanisms of reaction and strength of an alkali-activated blast furnace slag. Journal of the American Ceramic Society, 96: 3939-3948.

Chatterjee,K.K. Uses of Metals and Metallic Minerals2007, New Age International, Daryaganj, Delhi, IND

Chen, L. Structure Characterization of Platinum/Alumina, Rhenium/Alumina, and Platinum-Rhenium/Alumina Catalysts. Journal of Catalysis 145, (1994).

Cheng, T.W., Huang, M.Z., Tzeng, C.C., Cheng, K.B., Ueng, T.H. (2007). Production of Coloured Glass-Ceramics from Incinerator Ash Using Thermal Plasma Technology. Chemosphere 68(10):1937-1945. Elsevier.

Chudakov, F.Y., Romanenko, A.G., Merkulova, G.A. (1972). Production of Slag Wool Products from Liquid Blast Furnace Slag. Urals Scientific Research Institute for Ferrous Metals and the Azovstal Steelworks. Translated from Metallurg 7:19-21.

Crundwell, F. Moats, M. Ramachandran, V. Robinson, T. Davenport, W.D. (2011). Extractive Metallurgy of Nickel, Cobalt and Platinum Group Metals. Extraction of Platinum Group Metals from Russian Ores. Oxford,pp 429 – 435. Elsevier.

Davies, W.O. (1964). Carbon Dioxide Dissociation at 3500 ° to 6000 °K. The Journal of Chemical Physics. 41, PP 1846-1852. AIP Publishing.

Davies, W.O. (1965). Carbon Dioxide Dissociation at 6000 ° to 11,000 °K. The Journal of Chemical Physics. 43 pp 2809 – 2818. AIP Publishing.

Dědeček, J., Tvarůžková, Z., Sobalík, Z., (2008). Metal Ions as Probes for Characterisation of Geopolymer Materials. Journal of the American Ceramic Society. 91(9):3052-3057.

Deja, J. (2002). Immobilization of Cr^{6+}, Cd^{2+}, Zn^{2+} and Pb^{2+} in Alkali-Activated Slag Binders. Cement and Concrete Research. 32:1971-1979.

Department for Business, Energy and Industrial Strategy (2017). Electricity Statistics, Historical Electricity Data: 1920 to 2016. Available at https://www.gov.uk/government/statistical-data-sets/historical-electricity-data-1920-to-2011

Department for Energy and Climate Change (2013) EU ETS Carbon Markets.

Department for Energy and Climate Change (2014). Annual Statement of Emissions for 2012. Available at www.gov.uk/government/publications

Department for Transport. (2017). Vehicle Licensing Statistics: Annual 2016. Available online from https://www.gov.uk/government/statistics/vehicle-licensing-statistics-2016. Date of Access 30/6/2017.

Department of Business, Energy and Industrial Strategy (2017). Annual Statement of Emissions for 2017. Available at https://www.gov.uk/government/publications/annual-statement-of-emissions-for-2015

Department of Environment, Energy Food & Rural Affairs (2017). Digest of Waste and Resource Statistics, 2017 Edition. Available at https://www.gov.uk/government/statistics/digest-of-waste-and-resource-statistics-2017-edition

Desiree E Polyak, USGS 2011 Minerals Yearbook Rhenium.

Deventer, J. Provis, J. Duxson, P. (2011) Technical and commercial progress in the adoption of geopolymer cement. Minerals Engineering, 29: 89-104.

Diaz, E.I., Allouche, E.N. (2010). Recycling of Fly Ash into Geopolymer Concrete: Creation of a Database. Green Technologies Conference, Grapevine, Texas, USA 15-16 April 2010. IEEE.

Diaz, E.I., Allouche, E.N., Eklund, S. (2010). Factors Affecting the Suitability of Fly Ash as Source Material for Geopolymers. Fuel. 89(5):992-996. Elsevier.

Donatelli, S., Tyrer, M., Cheeseman, C.R. (2010). Comparison of Test Methods to Assess Pozzolanic Activity. Cement and Concrete Composites. 32(2):121-127.

Dotterl, M., Wachsmuth, U., Waldmann, L. Flachberger, H. Mirkowska, M., Brands, L., Beier, P.M., Stahl, I. (2016). Electrostatic Separation. Ullmann's Encyclopedia of Industrial Chemistry. Wiley-VCH.

Drobot, Kupriyanova, Krenev, et al. (2009) Rhenium and platinum recovery from platinum and rhenium catalysts used. Theoretical Foundations of Chemical Engineering

Duffy, J.A. and Ingram, M.D. (1976), An interpretation of glass chemistry in terms of the optical basicity concept. Journal of Non-Crystalline Solids, 21:373-410.

Duffy, J.A., Ingram, M.D. and Sommerville, I.D. (1978), Acid-base properties of molten oxides and metallurgical slags. Journal of the Chemical Society, Faraday Transactions 1: Physical Chemistry in Condensed Phases, 74: 1410–1419.

Duxson, P. Fernandez-Jimenez, A. Provis, J.L. Lukey, G.C. Palomo, A. van Deventer, J.S.J. (2007) Geopolymer technology: the current state of the art. Journal of Materials Science, 42:2917-2933.

Duxson, P. Provis, J.L. (2008) Designing precursors for geopolymer cements. Journal of the American Ceramic Society, 12:3864-3869.

Duxson, P. Provis, J.L., Lukey, G.C., Mallicoat, S.W., Kriven, W.M., van Deventer, J.S.J., (2005). Understanding the Relationship between Geopolymer Composition, Microstructure and Mechanical Properties. Colloids and Surfaces A: Physiochem. Eng. Aspects 269:47-58.

Ertel, W. Dingwell, D.B. Sylvester, P.J. (2008). Siderophile elements in silicate metls – A review of the mechanically assisted equilibration technique and the nanonugget issue. Chemical Geology 248 pp. 119-139. Science Direct.

Escalante, J.I. Gomez, L.Y. Johal, K.K. Mendoza, G. Mancha, H. Mendez, J. (2001) Reactivity of blast-furnace slag in Portland cement blends hydrated under different conditions. Cement and Concrete Research, 31:1403-1409.

European Commission (2010). Report of the Ad-hoc Working Group on Defining Critical Raw Materials. Available online at http://www.euromines.org/files/what-we-do/sustainable-development-issues/2010-report-critical-raw-materials-eu.pdf

European Commission (2014). Report on Critical Raw Materials for the EU. Report on the ad hoc Working Group on Defining Critical Raw Materials. DG ENTR. Brussels.

Euroslag, 2012. Position Paper on the Status of Ferrous Slag Complying with the Waste Framework Directive (Articles 5/6) and the REACH Regulation. http://www.euroslag.com/fileadmin/_media/images/Status_of_slag/Position_Paper_April_2012.pdf

Euroslag, 2016. Statistical Data 2008 http://www.euroslag.com/fileadmin/_media/images/statistics/Statistics_2008_download.pdf

Euroslag, 2017. Statistical Data 2010 http://www.euroslag.com/fileadmin/_media/images/statistics/Statistics_2010_download.pdf

Eurostat (2014) Eurostat Energy Data Tables [online] Available at http://ec.europa.eu/eurostat/web/energy/data/main-tables [accessed 15th April 2015]

Fernández-Jiménez, A. and Puertas, F., (2003). Structure of Calcium Silicate Hydrate in Alkaline-Activated Slag: Influence of the Type of Alkaline Activator. Journal of the American Ceramic Society. 86(8): 1389-1394.

Fernández-Jiménez, A., Palomo, J.G., Puertas, F., (1999). Alkali-Activated Slag Mortars Mechanical Strength Behaviour. Cement and Concrete Research. 29:1313-1321.

Fink, P. J., Miller, J. L. & Konitzer, D. G. Rhenium reduction—alloy design using an economically strategic element. JOM 62, (2010).

Fonseca, R.O.C. Mallmann, G. O'Neil, H. Campbell, I.H. (2007). How chalcophile is rhenium? An experimental study of the solubility of Re in sulphide mattes. Earth and Planetary Science Letters. 260 pp. 537-548. Science Direct.

Friedrich, B. Kalisch, M., Friedmann, D., Degel, R. (2017). The Submerged Arc Furnace (SAF) State of Art in Metal Recovery from Non-Ferrous Slags. Proceedings of the Fifth International Slag Valorisation Symposium. Leuven, Belgium. 139-155.

Fulchiron, R., Belyamani, I., Otaigbe, J. U., Bounor-Legaré, V. (2015). A Simple Method for Tuning the Glass Transition Process in Inorganic Phosphate Glasses. Scientific Reports 5:8369 DOI: 10.1038/srep08369.

García-Lodeiro, I and Fernández-Jiménez, A (2010) Effect of calcium additions on N–A–S–H cementitious gels. Journal of the American Ceramic Society. 93(7):1935-1940.

Geddes, Blaine Leon, Hugo Huang, Xiao (2010). Superalloys - Alloying and Performance. ASM International.

Gomez, E. Amutha Rani, D. Cheeseman, C.R. Deegan, D. Wise, M. Boccaccini, A.R. (2008) Thermal plasma technology for the treatment of wastes: A critical review. Journal of Hazardous Materials, 161: 614-626.

Gonzalez-Velaso J.R., Gutierrez-Ortiz M.A., Marc J.L., Botas J.A., Gonzalez-Marcos M.P., Blanchard G. (2003). $Pt/Ce_{0.68}Zr_{0.32}O_2$ Washcoated Monoliths for Automotive Emission Control. Industrial Engineering and Chemistry Resources. 42:311-317.

Grabezhev, A. I. Rhenium in ores of porphyry copper deposits in the Urals. *Doklady Earth Sciences* 413, (2007).

Hagelüken, C. (2012). Recycling the Platinum Group Metals: A European Perspective. Platinum Metals Review 56 (1) pp 29 – 35. Johnson Matthey.

Haha, B. M. Lothenbach, B. Le Saout, G. Winnefeld, F. (2011) Influence of slag chemistry on the hydration of alkali-activated blast furnace slag – Part I: Effect of MgO. Cement and Concrete Research, 41:955-963.

Haha, B. M., Le Saout, G., Winnefeld, F., Lothenbach, B., (2011). Influence of Activator Type on Hydration Kinetics, Hydrate Assemblage and Microstructural Development of Alkali-Activated Blast Furnace Slags. Cement and Concrete Research. 41:301-310.

Hammer, T. (1999). Applications of Plasma Technology in Environmental Techniques. Contributions to Plasma Physics. 39(5), pp 441-462.

Haque, N. Hughes, A. Lim, S. et al. (2014). Rare Earth Elements: Overview of Mining, Mineralogy, Uses, Sustainability and Environmental Impact. Resources. MDPI, Basel. pp 614 – 635.

He, C., Osbaek, B., Makovicky, E., (1995). Pozzolanic Reactions of Six Principle Clay Minerals: Activation, Reactivity Assessments and Technological Effects. Cement and Concrete Research. 25(8) 1691-1702. Pergamon.

He, P, Wang, M, Fu, S, et al. (2016) Effects of Si/Al ratio on the structure and properties of metakaolin based geopolymer. Ceramics International. 42:14416-14422.

Health and Safety Executive, Man Made Mineral Fibre Airborne Number Concentration by Phase Contrast Light Microscopy. Methods for Determination of Hazardous Substances. (1998)

Hong, S.Y. and Glasser, F.P., (1999). Alkali Binding in Cement Pastes Part I. The C-S-H Phase. Cement and Concrete Research. 29:1893-1903.

Hong, S.Y. and Glasser, F.P., (2002). Alkali-Sorption by C-S-H and C-A-S-H Gels Part II. Role of Alumina. Cement and Concrete Research. 32:1101-1111.

Hu, X, Ren, Z, Zhang, G, et al. (2012), A model for estimating the viscosity of blast furnace slags with optical basicity. International Journal of Minerals, 19(12):1088-1092.

Huaiwei, Z. Fei, S. Xiaoyan, S. Bo, Z. Xin, H. (2012), The Viscous and Conductivity Behaviour of Melts Containing Iron Oxide in the FeO_t-SiO_2-CaO-Cu_2O System for Copper Smelting Slags. Metallurgical and Materials Transactions B 43:1046-1053.

Huczko, A. and Szmański, A. (1984). Thermal Decomposition of Carbon Dioxide in an Argon Plasma Jet. Plasma Chemistry and Plasma Processing. 4(1), pp 59-72.

Isawa, T. (2014) Update of Iron and Steel Slag in Japan and Current Development for Valorisation. Proceedings from 3rd International Slag Valorisation Symposium, Leuven, Belgium 19-20th March 2014 pp. 87-98.

Johnson Matthey (2016). PGM Market Report November 2016. Forcast of Platinum Supply and Demand in 2016. Available online at: http://www.platinum.matthey.com/services/market-research/pgm-market-reports date of access: 18th August 2017.

Johnson Matthey (2016). PGM Market Report November 2016. Forcast of Platinum Supply and Demand in 2016. http://www.platinum.matthey.com/documents/new-item/pgm%20market%20reports/pgm_market_report_november_2016.pdf

Johnson, T. and Deegan, D. (2012) Resource Recovery from Mining Related Wastes using Tetronics' Plasma Arc Technology. Proceedings from 16th International Conference on Tailings and Mine Waste, Keystone Colorado, 14-17 October 2012. Published by University of Colorado British Columbia pp.643-652.

Johnson, T. Deegan, D. (2015) The Recovery of Precious Metals and Platinum Group Metals from Spent Catalysts and other Secondary Sources using Plasma Smelting Technology. Proceedings from Precious Metals '15, Falmouth, UK, 11-12th May 2015.

Jothimurugesan, Nayak, Mehta, et al. (1985) Role of rhenium in Pt-Re-Al2O3 reforming catalysis—An integrated study. AIChE Journal, 31

Kakali, G., Perraki, T., Tsivilis, S., Badogiannis, E. (2001). Thermal Treatment of Kaolin: the Effect of Mineralogy on the Pozzolanic Activity. Applied Clay Science. 20:73-80. Elsevier.

Kanazawa, Y and Kamitani, M (2006). Rare Earth Minerals and Resources in the World. Journal of Alloys and Compounds. pp 1339 -1343. Elsevier.

Kasikov and Petrova (2009) Processing of deactivated platinum-rhenium catalysts. Theoretical Foundations of Chemical Engineering. Vol 43 (4) pp 544-552. Pleiades Publishing.

Kasikov, L. G. & Petrova, A. M. Processing of deactivated platinum-rhenium catalysts. Theoretical Foundations of Chemical Engineering 43, (2009).

Keeley, P.M. Rowson, N.A. Deegan, D.E. Stachowski, T. (2015) Platinum and rhenium recovery from reforming catalysts via plasma arc technology. The Conference of Metallurgists, Toronto Published by the Canadian Institute of Mining, Metallurgy and Petroleum, Montreal.

Kelly, E.G. Spottiswood, D.J. (1989) The Theory of Electrostatic Separations: A Review Part I. Fundamentals. Minerals Engineering, 2(1):33-46.

Kelly, E.G. Spottiswood, D.J. (1989) The Theory of Electrostatic Separations: A Review Part II. Particle Charging. Minerals Engineering, 2(2):193-205.

Kelly, E.G. Spottiswood, D.J. (1989) The Theory of Electrostatic Separations: A Review Part III. The Separation of Particles. Minerals Engineering, 2(3):337-349.

Kim, K.A., Lee, W.K., Kim, J.k., Seo, M.S., Lim, Y., Lee, K.H., Chae, G., Lee, S.H., Chung, Y. (2000). Mechanism of Refractory Ceramic Fiber and Rock Wool Induced Cytotoxicity in Alveolar Macrophages. International Archives of Occupational and Environmental Health. 4(1):9-15.

Kingon, A.I., Davis, R.F. (1991). Engineering Properties of Multicomponent and Multiphase Oxides. Engineering Materials Handbook Volume 4. Ceramics and Glasses. Chapter 11 pp 758-775. ASM International. ISBN: 0-87170-282-7

Kourti, I. Amutha Rani, D. Boccaccini, R. Cheeseman, C.R. (2011) Geopolymers from DC plasma-treated air pollution control residues, metakaolin and granulated blast furnace slag. Journal of Materials in Civil Engineering, 23: 735-740.

Kourti, I., Deegan, D.E., Boccaccini, A.R., Cheeseman, C.R. (2013). Use of DC Plasma Treated Air Pollution Control (APC) Residue Glass as Pozzolanic Additive in Portland Cement. Waste and Biomass Valorization. 4(4):719-728. Springer.

Kuenzel, C., Neville, T.P., Donatello, S., Vandeperre, L., Boccaccini, A.R., Cheeseman, C.R., (2013). Influence of Metakaolin Characteristics on the Mechanical Properties of Geopolymers. Applied Clay Science 83-84:308-314. Elsevier.

Kuo, Y.M., Wang, J.W., Chao, H.R., Wang, C.T., Chang-Chien, G.P. (2008). Effect of Cooling Rate and Basicity During Vitrification of Fly Ash Part 2: On the Chemical Stability and Acid Resistance of Slags. Journal of Hazardous Materials. 52(2):554-562. Elsevier.

Kutchko, B.G., Kim, A.G. (2006). Fly Ash Characterisation by SEM-EDS. Fuel. 85(17-18):2537-2544. Elsevier.

Li, C, Sun, H and Li, L (2010) A review: The comparison between alkali-activated slag (Si+ Ca) and metakaolin (Si+ Al) cements. Cement and Concrete Research. 40:1341-1349.

Li, D. Yakushiji D. Kanazawa, S. Ohkubo, T. Nomoto, Y. (2002). Decomposition of Toluene by Streamer Corona Discharge with Catalyst. Journal of Electrostatics, 55 pp 311-319. Elsevier.

Li, G. Zang, H., Ni, H. Guo, M. (2014) Current Development of Slag Valorisation in China. Proceedings from 3rd International Slag Valorisation Symposium, Leuven, Belgium 19-20th March 2014 pp. 57-67.

Li, X. Fernández Bertos, M., Hills, C.D., Carey, P.J., Simon, S. (2007). Accelerated Carbonation of Municipal Solid Waste Incineration Fly Ashes. Waste Management. 27:1200-1206. Elsevier.

Liang, Y. Wu, Y. Sun, K. Chen, Q. Shen, F. Zhang, J. Yao, M. Zhu, T. Fang, J. (2012). Rapid Investigation of Biological Species in the Air Using Atmospheric Pressure Nonthermal Plasma. Environmental Science and Technology. 46, pp 3360-3368. ACS Publications.

Lisienko, V.G., Chesnokov, Y.N., Lapteva, A.V., Noskov, V.Y., (2016). Types of Greenhouse Gas Emissions in the Production of Cast Iron and Steel. IOP Conference Series Materials Science Engineering. 150, 012023. IOP Science.

Luke, K. Glasser, F.P. (1987), Selective dissolution of hydrated blast furnace slag cements. - Cement and Concrete Research, 17:273-282.

Luoto, K., Holopainen, M., Kangas, J., Kalliokoski, P., Savolainen, K. (1995). The Effect of Fiber Length on the Dissolution by Macrophages of Rockwool and Glasswool Fibers. Environmental Research. 70(1):51-61. Elsevier.

Luoto, K., Holopainen, M., Sarataho, M., Savolainen, K. (1997). Comparison of Cytotoxicity of Man-Made Vitreous Fibres. The Annals of Occupational Health. 41(1):37-50.

Mahajan, S. and Kimerling, L.C. (1992). Concise Encyclopedia of Semiconducting Materials & Related Technologies. Electronic and Optical Minerals pp 143. Pergamon Press. ISBN 0-08-034724-X.

Mallmann, G. O'Neill, H. (2006). The redox control upon the rhenium crystal/silicate-melt partitioning. Goldschmidt Conference, Australia.

Massari, S. and Ruberti, M. (2013). Rare Earth Elements as Critical Raw Materials: Focus on International Markets and Future Strategies. Resources Policy, 38 (1) pp 36–43. Elsevier.

Massazza, F. (1993) Pozzolanic cements. Cement and Concrete research, 15:185-214.

Maughan, T. (2015). The Dystopian Lake Filled by the World's Tech Lust. BBC Future. Available online at http://www.bbc.com/future/story/20150402-the-worst-place-on-earth Date of access: 18/08/2017.

Maxim, D.L., Boymel, P., Chase, G.R., Bernstein, D.M., (2002). Indices of Fiber Biopersistence and Carcinogen Classification for Synthetic Vitreous Fibers (SVFs). Regulatory Toxicology and Pharmacology. 35(3):357-378.

Maxim, D.L., Hadley, J.G., Potter, R.M., Niebo, R. (2006). The Role of Fiber Durability/Biopersistence of Silica Based Synthetic Vitreous Fibers and their Influence on Toxicology. Regulatory Toxicology and Pharmacology. 46(1):42-62.

Mizuno, A. Kisanuki, Y. Noguchi, M. Katsura, S. Lee, S, H. Hong, Y.K. Shin, S.Y. Kang, J.H. (1999). Indoor Air Cleaning Using a Pulsed Discharge Plasma. IEEE Transactions on Industry Applications. 35(6) pp 1284-1288.

Moore, M.A., Boymel, P.M., Maxim, L.D., Turim, J. (2002). Categorization and Nomenclature of Vitreous Silicate Wools. Regulatory Toxicology and Pharmacology. 35(1):1-13.

Motz, H., Ehrenberg, A., Mudersbach, D. (2013). Dry Solidification with Heat Recovery of Ferrous Slag. Proceedings of the Third International Slag Valorisation Symposium. Leuven, Belgium. 37-55

Motz, H., Geiseler, J. (2001). Products of Steel Slags an Opportunity to Save Natural Resources. Waste Management. 21:285-293. Pergamon.

Myers, R.J., Bernal, S,A., Provis, J.L., (2014). A Thermodynamic Model for C-(N-)A-S-H Gel: CASH_ss. Derivation and Validation. Cement and Concrete Research. 66:27-47.

Mysen, B. Virgo, D. Scarfe, C. (1980) Relations between anionic structure and viscosity of silicate melts – a Raman spectroscopic study. American Mineralogist**,** 65:690-710.

N N Greenwood, A Earnshaw (1997) Chemistry of the Elements Second Edition Butterworth Heinemann ISBN 0 7506 3365 4

Najafi Kani, E., Allahverdi, A., Provis, J.L., (2012). Efflorescence Control in Geopolymer Binders Based on Natural Pozzolan. Cement and Concrete Composites. 34:25-33.

Naumov, A. V. Rhythms of rhenium. *Russian Journal of Non-Ferrous Metals* 48, (2007).

Naumov, A.V. Rhythms of Rhenium. (2007), Metallurgy of Rare and Noble Metals. Russian Journal of Non-Ferrous Metals. Vol, 48 (6) pp. 418-423 Allerton Press.

Nishigaki, M. (2000). Producing Permeable Blocks and Pavement Bricks from Molten Slag. Waste Management. 20:185-192. Pergamon.

Novikov, L.K., Patrushev, V .V ., Pashkov, G., (1986) Complex Processing of Aluminum-Platinum Catalysts, Proc. XIII Chemical Congress on Chemistry, Analysis and Technology of Platinum Group Metals, Leningrad, vol. 3. p. 110.

Oberdörster, G. (2000) Determinants of the Pathogenicity of Man-Made Vitreous Fibers (MMVF). International Archives of Occupational and Environmental Health. 73:560-568.

Oelkers, E.H. (2001). General Kinetic Description of Multioxide Silicate Mineral and Glass Dissolution. Geochemica et Cosmochimica Acta. 65(21):3703-3719. Pergamon.

Pacheco-Torgal, F. Castro-Gomes, J, Jalali, S. (2008) Alkali-activated binders: A review: Part 1. Historical background, terminology, reaction mechanisms and hydration products. Construction and Building Materials, 22: 1305-1314.

Piatak, N.M., Parsons, M.B., Seal, R.R. (2015). Characteristics and Environmental Aspects of Slag: A Reivew. Applied Geochemistry. 57:236-266.

Pioro, L.S., Pioro, I.L. (2003). Reprocessing of Metallurgical Slag into Materials for the Building Industry. Waste Management. 24:371-379. Elsevier.

Provis, J.L. (2014). Geopolymers and Other Alkali Activated Materials: Why, How, and What? Materials and Structures. 47:11-25.

Provis, J.L. Palomo, A. Shi, C. (2015) Advances in understanding alkali-activated materials. Cement and Concrete Research

Rani, A., D. Boccaccini, D. Deegan, D. Cheeseman, C.R. (2008) Air pollution control residues from waste incineration: Current UK situation and assessment of alternative technologies. Waste Management, 28: 2279-92.

Rawlings, R.D. Wu, J.P., Boccaccini, A.R. (2006). Glass Ceramics: Their Production from Wastes – A Review. Journal of Material Science. 41:733-761. Springer.

Reforming catalyst compositions Beeckman, J.W. and Mccarthy, S.J. and Cheng, J.C.2013Google Patents WO Patent App. PCT/US2012/055,896 https://www.google.co.uk/patents/WO2013043585A1?cl=en

Reiß, S, Wedemann, M, Moos, R, Rosch, M. (2009) Electrical in situ characterization of three-way catalyst coatings. Topics in Catalysis. 52:1898-1902.

Righter, K. Campbell, A.J. Humayun, M. Hervig, R.L. (2004). Partitioning of Ru, Rh, Pd, Re, Ir, and Au between Cr-bearing spinel, olivine, pyroxene and silicate melts. Geochemica et Cosmochimica Acta, Vol 68(4) pp. 867 – 880. Elsevier.

Righter, K. Drake, M.J. (1997). Metal-silicate equilibrium in a homogenously accreting earth: new results for Re. Earth and Planetary Science Letters. 146 ppg. 541-553. Elsevier.

Roether, J.A., Daniel, D.J., Amutha, Rani, D., Deegan, D.E., Chesseman, C.R., Boccaccini, A.R. (2010). Properties of Sintered Glass-Ceramics Prepared from Plasma Vitrified Air Pollution Control Residues. Journal of Hazardous Materials. 173:563-569. Elsevier.

Saurat, M. and Bringezu, S. (2008). Platinum Group Metal Flows of Europe, Part 1. Journal of Industrial Ecology, 12; 754 – 767. Wiley Blackwell.

Sekiguchi, H. (2001). Catalysis Assisted Plasma Decomposition of Benzene Using Dielectric Barrier Discharge. The Canadian Journal of Chemical Engineering. 79 pp 512 – 516.

Shaffer, P.T.B. (1991) Engineering Properties of Carbides. Engineering Materials Handbook Volume 4. Ceramics and Glasses. Chapter 11 pp 804-812. ASM International. ISBN: 0-87170-282-7.

Shehata, M.H., and Thomas, M.D.A., (2006). Alkali Release Characteristics of Blended Cements. Cement and Concrete Research. 36:1166-1175.

Shi, C. Qian, J. (2000) High performance cementing materials from industrial slags – a review. Resources, Conservation and Recycling 29:195-207.

Simonetti, D., Kunkes, E. & Dumesic, J. Gas-phase conversion of glycerol to synthesis gas over carbon-supported platinum and platinum–rhenium catalysts. Journal of Catalysis 247, (2007).

Singh, R. (2016). Chapter 4 – Structure of Materials. Applied Welding Engineering 2nd Edition. Pp 27-36. Butterworth-Heinemann. ISBN 9780128041765.

Statista (2017). Cement Production Globally and in the U.S. from 2010 to 2016. https://www.statista.com/statistics/219343/cement-production-worldwide/

Steenland, K. and Stayner, L. (1997). Silica, Asbestos, Man-Made Mineral Fibers and Cancer. Cancer Causes and Control.

Sun, W., Bennett, V., Eggins, S., Kamenetsky, V. & Arculus, R. Enhanced mantle-to-crust rhenium transfer in undegassed arc magmas. Nature 422, 294–7 (2003).

Sun, Y. Nie, Y. Wu, A. Ji, D. Yu, F. Ji, J. (2012). Carbon Dioxide Reforming of Methane to Syngas by Thermal Plasma. Plasma Science and Technology. 14(4) pp 253-256. IOP Science.

Taylor, H. (1986) Proposed structure for calcium silicate hydrate gel. Journal of the American Ceramic Society, 69(6):464-67.

Taylor, R., Richardson, I.G., Brydson, R.M.D., (2010). Composition and Microstructure of 20-Year Old Ordinary Portland Cement-Ground Granulated Blast-Furnace Slag Blends Containing 0 to 100% Slag. Cement and Concrete Research. 40(7):981-983. Elsevier

Tchakoute, H.K., Rüscher, C.H., Djobo, J.N.Y., Kenne, B.B.D., Njopwouo, D. (2015). Influence of Gibbsite and Quartz in Kaolin on the Properties of Metakaolin Based Geopolymer Cements. Applied Clay Science. 107:188-194. Elsevier.

Temuujin, J, Riessen, V.A. and Williams, R (2009) Influence of calcium compounds on the mechanical properties of fly Ash geopolymer Pastes. Journal of Hazardous Materials. 167:82-88.

The Intercontinental Exchange (ICE), 2014 http://www.theice.com/marketdata/reports/148

The Society of Motor Manufacturers and Traders (SMMT) (2015). Average Vehicle Age. Automotive Sustainability Report. Available at: https://www.smmt.co.uk/industry-topics/sustainability/average-vehicle-age/

Turkdogan, E.T., (1984). Physicochemical Properties of Molten Slags and Glasses. Chapter 2 Structural Aspects, Section 2.9 Glass Transition Temperatures. Pp 81 – 83. The Metals Society, London. ISBN 0 904357 54 6.

UNEP (2011) Recycling Rates of Metals – A Status Report, A Report of the Working Group on the Global Metal Flows to the International Resource Panel. Graedel, T.E.; Allwood, J; Birat, J.-P.; Reck, B.K.; Sibley, S.F.; Sonnemann, G.; Buchert, M.; Hagelüken, C. ISBN: 978-92-807-3161-3

United Kingdom Debt Management Office, 2012.

http://www.dmo.gov.uk/index.aspx?page=ETS/AuctionInfo

United States Geological Survey (USGS) (2017). 2015 Minerals Yearbook Rhenium.

USGS (2017) 2015 Minerals Yearbook. Rhenium Advanced Release.

https://minerals.usgs.gov/minerals/pubs/commodity/rhenium/myb1-2015-rheni.pdf

Van Durme, J. Dewulf, J. Sysmans, W. Leys, C. Van Langenhove, H. (2007). Abatement and Degradation Pathways of Toluene in Indoor Air by Positive Corona Discharge. Chemosphere 68, 1821-1829. Elsevier.

Wagner, J.C. (1972). The Significant of Asbestos in Tissue. Current Results in Cancer Research. 39:37-46.

Walker, P. and Imperial, G. (1957) Structure of Graphites: Graphitic Character of Kish. *Nature 4596.* 1185.

Walker, R. and Pavía, S. (2011). Physical Properties and Reactivity of Pozzolans, and Their Influence on the Properties of Lime-Pozzolan Pastes. Materials and Structures. 44(6):1139-1150. Springer.

Wang, M. Cheng, J. Li, M. He, F. (2011), Raman spectra of soda-lime-silicate glass doped with rare earth. Physica B, 406:365-3869.

Wang, S.D. and Scrivener, K.L., (1995). Hydration Products of Alkali Activated Slag Cement. Cement and Concrete Research. 25(3):561-571.

Williams, R.P., van Riessen, A. (2010). Determination of the Reactive Component of Fly Ashes for Geopolymer Production Using XRF and XRD. Fuel. 89:3683-3692. Elsevier.

Wöllmer, S., Mack, T. & Glatzel, U. Influence of tungsten and rhenium concentration on creep properties of a second generation superalloy. *Materials Science and Engineering: A* 319-321, (2001).

Working Group on Action to Control Chemicals (WATCH/MIN/2008/20)

Xu, N. Fu, W. He, C. Cao, L. Liu, X. Zhao, J. Pan, H. (2014). Benzene Removal Using Non-Thermal Plasma With CuO/AC Catalyst: Reaction Condition Optimization and Decomposition Mechanism. Plasma Chemistry and Plasma Process, 34 pp 1387-1402. Springer Science.

Xue, G.-M. et al. Fabrication of rhenium Josephson junctions. *Chinese Physics B* 22, (2013).

Yao, S.L. Okumoto, M. Nakayama, A. Suzuki, E. (2001). Plasma Reforming and Coupling of Methane with Carbon Dioxide. Energy and Fuels, 15, pp 1295-1299. American Chemical Society.

Yao, X., Yang, T., Zhang, Z., (2016). Fly Ash-Based Geopolymers: Effect of Slag Addition on Efflorescence. Journal of Wuhan University of Technology-Material Science Edition. 31(3):689-694.

Ye, G., Lindvall, M., Magnusson, M. (2013). Swera Mefos Perspective on Metal Recovery from Slags. Proceedings of the Third International Slag Valorisation Symposium. Leuven, Belgium. 147-156.

Yip, C.K.M Lukey, G.C., van Deventer, J.S.J. (2005). The Coexistence of Geopolymeric Gel and Calcium Silicate Hydrate at the Early Stage of Akaline Activation. Cement and Concrete Research. 35:1688-1697.

Zhang, G. and Chou, K. (2010), Model for Evaluating Density of Molten Slag With Optical Basicity. Journal of Iron and Steel Research, International, 17 (4): 1–4.

Zhang, L. and Lütte, A. (2008). Aluminosilicate Dissolution Kinetics: A General Stochastic Model. Journal of Physical Chemistry B. 112:1736-1742. Elsevier.

Zhang, M., Yang, M., Zhao, M., Yang, K., Shen, R., Zheng, Y., (2017). Immobilization Potential of Cr (VI) in Sodium Hydroxide Activated Slag Pastes. Journal of Hazardous Materials. 321:281-289.

Zhang, Z., Wang, H., Yao, X., Zhu, Y. (2012). Effects of Halloysite in Kaolin on the Formation and Properties of Geopolymers. Cement and Concrete Composites. 34:709-715. Elsevier.

Zhang, Z.Q., Zhang, Y.Z., Yang, A.M., Xing H.W., Tian, T.L., Li, Z.H., (2016) Preparation and Properties of Slag Wool Board Using Modified Polyvinyl Alcohol as Binder. Materials and Manufacturing Processes. 31:168-172. Taylor and Francis.

Zhang. Z., Provis, J.L., Reid, A., Wang, H. (2014). Fly Ash-Based Geopolymers: The Relationship between Composition, Pore Structure and Efflorescence. Cement and Concrete Research. 64:30-41.

Zhao, D., Zhang, Z., Tang, X., Liu, L., Wang, X., (2014). Preparation of Slag Wool by Integrated Waste-Heat Recovery and Resource Recycling of Molten Blast Furnace Slags: From Fundamental to Industrial Application. Energies. 7:3121-3135.

Zheng, K. Junlin, L. Wang, X. Zhang, Z. (2013), Raman spectroscopy of CaO-MgO-SiO_2-TiO_2 slags. Journal of Non-Crystalline solids, 376:209-215.

Appendix A. A Report on the Rhenium Market.

A.1. Introduction.

Named after the river Rhine and undiscovered until 1925, rhenium was the last element to be found occurring naturally. Very rare, being only present at 2ppb in the earth's crust (Sun et al. 2003); its ore is not mined and only produced as a by-product from the mining of porphyry-copper. Nevertheless, rhenium has important applications in modern society lending its properties to enable jet engines to function at increased efficiencies with reduced emissions and high octane petroleum to be produced economically. Most of rhenium's applications take advantage of its high melting point, 3160°C, which is the second highest of all the elements. The annual production of the metal in 2016 was 47 tonnes (USGS, 2016), and currently has a market price of around $2,000 per kg. When the price of rhenium spiked in 2008 at $10400 per kg, companies began to develop ways to lessen their dependence on the primary metal by increasing recycling and recovery rates to reduce the risks of supply from economic and political issues. These increased recycling rates have contributed to a drop in the rhenium price and production since 2008.

A.2. Uses of rhenium.

A.2.1. Superalloys.

Creep is a major problem for the safe operation of turbine blades especially when they are employed at high temperatures. Rhenium offers excellent creep resistance for jet engine turbines at high operating temperatures when present in superalloys at concentrations of either 3 wt% or 6 wt% (Wöllmer et al. 2001). The effect of rhenium in lengthening the creep life of superalloys has been so successful that rhenium containing superalloys have replaced

single crystal turbines and in doing so allows for high performance turbine blades to be produced more cheaply (Geddes et al. 2010).

80% of rhenium produced is used in superalloy manufacture meaning it is by far the most important use for rhenium (USGS, 2012). The main consumers of rhenium are General Electric Aviation, Pratt and Whiteny and Rolls Royce which is unsurprising as these manufacturers produce high performance jet engines. The Minor Metals Trade Association reports these companies consume around 45 tonnes of rhenium per year which is around 80% of the total consumption of rhenium (taking into account the recycling of the metal by these companies which is accounts for 10% of their use).

The demand for aerospace engines for civil aviation is increasing as airlines need to acquire more aeroplanes to meet the increasing passenger demand. This is shown by the 2012 order books for Rolls Royce increasing by 5%. This is due largely to the successful development of the Trent XWB engines designed for the Airbus A350 which have received substantial orders (Rolls Royce, 2013). In 2014, Pratt and Whitney signed a $690 million deal with Molymet to supply them with rhenium for all their engine programmes showing the long term importance of the metal to the aviation industry.

A.2.2. Platinum-Rhenium Catalysts.

The use of rhenium in petrochemical catalysts makes up 10% of the total use of the metal (USGS, 2012). Rhenium has seven valence states and can easily change between them, so coupled with good acidic and high temperature resistance; rhenium has ideal properties to be used as a catalyst (Greenwood and Earnshaw, 1997). Used since the 1960s, platinum-rhenium catalysts are favoured in the petrochemical industry because they can undergo high levels of coking before they are deactivated (Naumov, 2007). The addition of rhenium to platinum

containing catalysts has a number of advantages; the catalysts are more stable and produce a higher yield of heavier hydrocarbons whilst still achieving high selectivity even at high levels of coking. Previously reforming catalysts which just contained platinum needed the addition of chlorine to maintain the catalyst's acidity, but chlorine presented a number of issues including its reduced concentration over time because of its high reactivity and corrosive nature but also it had low coke stability (Beeckman et al. 2012). The rhenium content in these catalysts can vary from producer to producer but is typically in the region of 0.3 wt% (Chen et al. 1994). According to the Minor Metals Trade Association, 15 tonnes per year of rhenium is used for producing platinum rhenium catalysts. However, there is a large closed looped cycle recycling route involved in the catalyst's production where around 80% of the metal is recycled, meaning that only around 3 tonnes of virgin rhenium is required per year to make the catalysts.

Currently Pt-Re catalysts are used to produce lead free, high octane rated petroleum by producing heavier hydrocarbons from naphthas in the reforming process (Kasikov and Petrova 2009). The reforming reactors each contain around 25 tonnes of catalyst and these catalysts have a long life span which can be between one to two years after which they are sent to a refiner to recover the metals for reuse. The major users of these reforming catalysts are the USA and Europe who account for 30 and 21% respectively however there is an increasing trend for the petroleum industry to move production to the Far East and so the major users may become some of the eastern states such as China in the coming years.

Historically Pt-Re catalysts have been used in the past in gas shift Fischer-Tropsch type reactions and gas to liquid applications, which are resurfacing again due to the increased

importance of synthetic natural gas and biofuel production and also because of the increased interest in shale gas extraction especially in the United States, South America and areas of Europe (United States Energy Information Administration, 2013).

A.2.3. Other Applications.

Making up about 10% of the total use of rhenium is an assortment of varied applications in which rhenium's properties are exploited. It can be found in some expensive pen nibs and also in some semiconductor materials. Rhenium's high melting point is ideal to be used in thermocouples and so it is alloyed with another element such as platinum or palladium for this purpose. Like many elements with high electrical resistivity, rhenium when added to other materials becomes superconducting at very low temperatures which may in the future be exploited in the development of quantum computers (Xue et al 2013). There are also medical applications for rhenium where it can be used in anti-cancer treatment.

These applications involve low volumes of rhenium and are highly specialised. An increased demand for rhenium in any of these applications would need to be coupled with an advance in technology in one of these areas the most likely being in the development of quantum computers, however this application would have a low volume output and may not even use rhenium as a material in the future.

A.3. Rhenium Production.

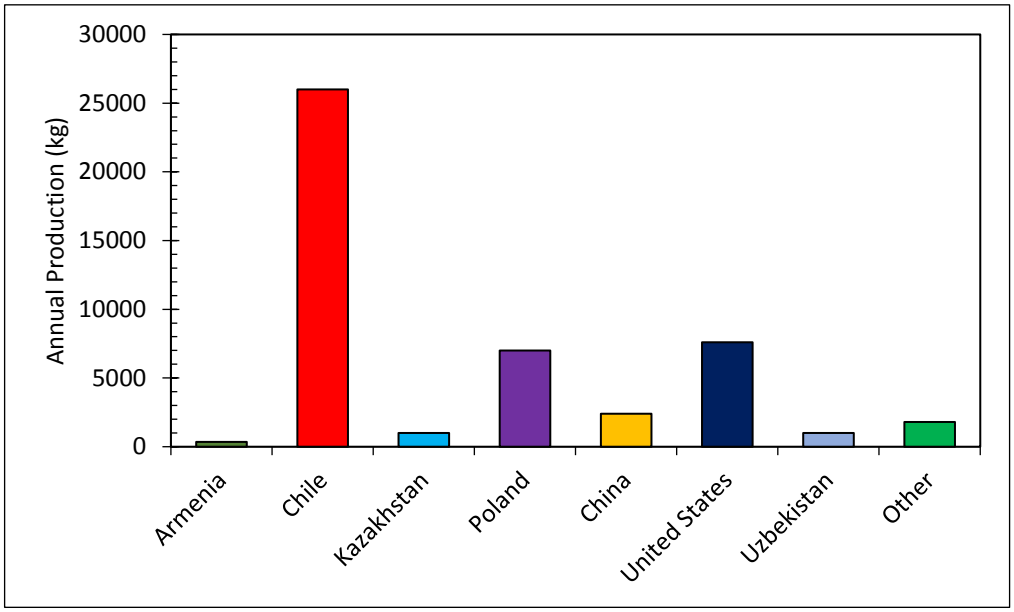

Figure A-1: The annual production of rhenium by country.

According to the USGS, the annual production of rhenium in 2016 was 47,200 kg. The primary source of rhenium is as a by-product of Cu-Mo ores found in porphyry-copper mines as molybdenite (MoS_2) is the only economic primary source of rhenium. The Re content in molybdenite is variable depending on the geographical location and ranges from low concentrations of 0.2ppm to higher concentrations of around 600ppm (Grabezhev, 2007). During the roasting of this sulphide the rhenium becomes oxidised to Re_2O_7 and due to its volatility becomes a gas and is subsequently captured in flue dust and extracted through a wet scrubbing process (Chatteriee, 2007).

Rhenium is sold in two forms; as a highly pure metal and in ammonium perrhenate (NH_4ReO_4), a compound which contains around 69.4% Re. Ammonium perrhenate is the product of the wet scrubbing extraction process of the flue dust captured from molybdenite roasting. Rhenium is recovered from catalysts via hydrometallurgical recycling processes as ammonium

perrhenate and this salt is used to produce Re containing catalysts. These catalysts are produced by impregnating an alumina catalyst support with ammonium perrhenate which is then calcined at a high temperature to produce the final catalyst. Metallic rhenium can also be prepared via the reduction of ammonium perrhenate by hydrogen as shown in the reaction shown in Equation A-1.

$$2NH_4ReO_4 + 7H_2 \rightarrow 2NH_4OH + 6H_2O + 2Re \qquad \text{Equation A-1}$$

Figure A-1 shows the countries which produce rhenium from primary sources. The world's largest rhenium producer is Chile which produced 55 % of the world's rhenium in 2016. The United States of America are the world's largest consumers of rhenium, mainly due to its aviation industry, and the majority of their rhenium is supplied by Chile (USGS, 2016).

The Chilean company Molymet is the world's largest producer of rhenium and has a massive rhenium market share of 70% (Molymet, 2013). This company produces rhenium not only in Chile but also in the United States and Canada under the name of Molycorp. KGHM ECOREN is the only major European producer of primary rhenium who operates in Poland. The company has recently invested in upgrading its facilities and currently supplies around 12% of the world's rhenium supply (KGHM ECOREN, 2010).

The output of rhenium has risen and fallen over the past twenty years coinciding with political and technological events. In the mid-90s there was a significant drop in rhenium production due to the collapse of the Soviet Union and consequently a large amount of stockpiled rhenium was released to the west from former Soviet states such as Kazakhstan. The surplus of rhenium in the mid-90s caused the price to fall to around $1000 per kg. A new generation

of superalloys for turbine blades containing rhenium was developed and so there was a rise in the demand for the metal causing the rhenium price to peak in 2008 at $10400 per kg. The price has fallen steadily to around 2000 per kg today. However, due to the nature of the rhenium market the quoted price is not necessarily reflective of the actual price which is paid by the major consumers due to long term fixed contracts with the suppliers for instance the long term $690 million pound deal between Molymet and Pratt and Whitney.

The price drop of rhenium may be due to an increase in the recycling of the metal by the major users, especially the increase in the recycling of superalloy scrap by the aviation industry. It is estimated that around 10,000 kg rhenium is recovered from recycled superalloy scrap per year which would significantly reduce the demand for the material and so the price naturally drop. This is a trend which has been seen for numerous metals for example in the platinum group metal market where the price of these metals has stagnated due to increased recycling.

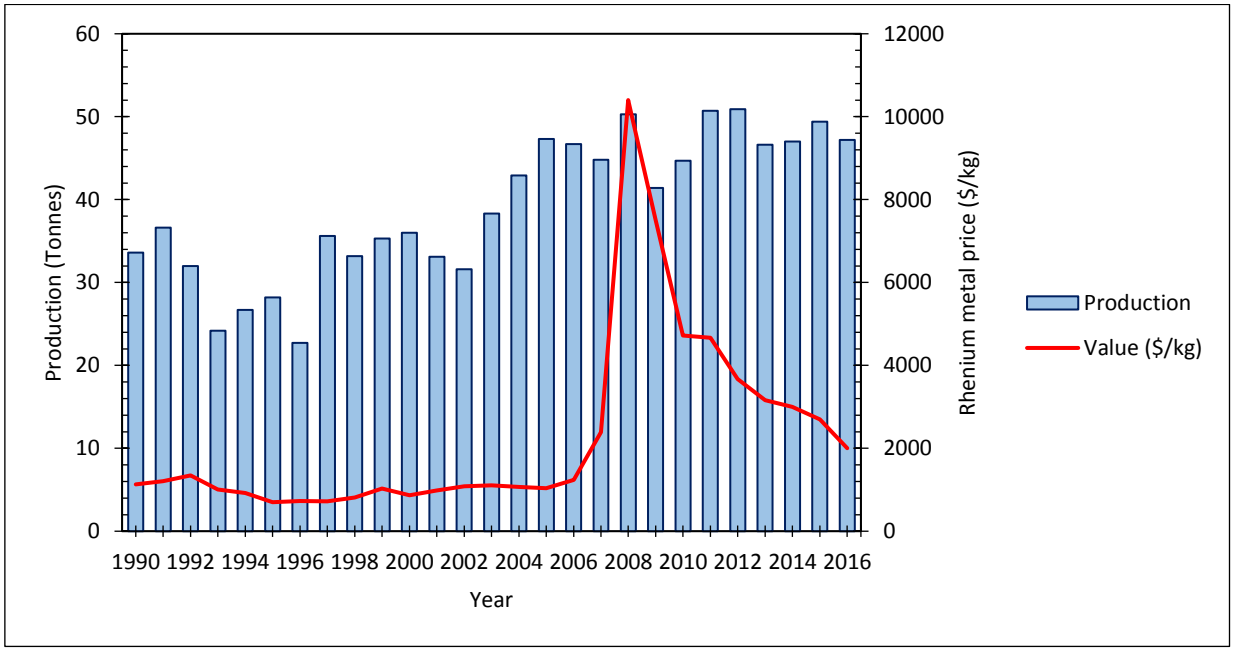

Figure A-2: Rhenium production and metal value (Data obtained from USGS).

As stated above, rhenium is traded in two forms; a metal and as the salt ammonium perrhenate (APR). The form in which the metal is traded depends on its final use. The powdered metal is generally sold for use in superalloys and other minor uses, but the salt is used for catalyst production. The price of the APR compared to the price of the rhenium metal is shown in Figure A-3**.**

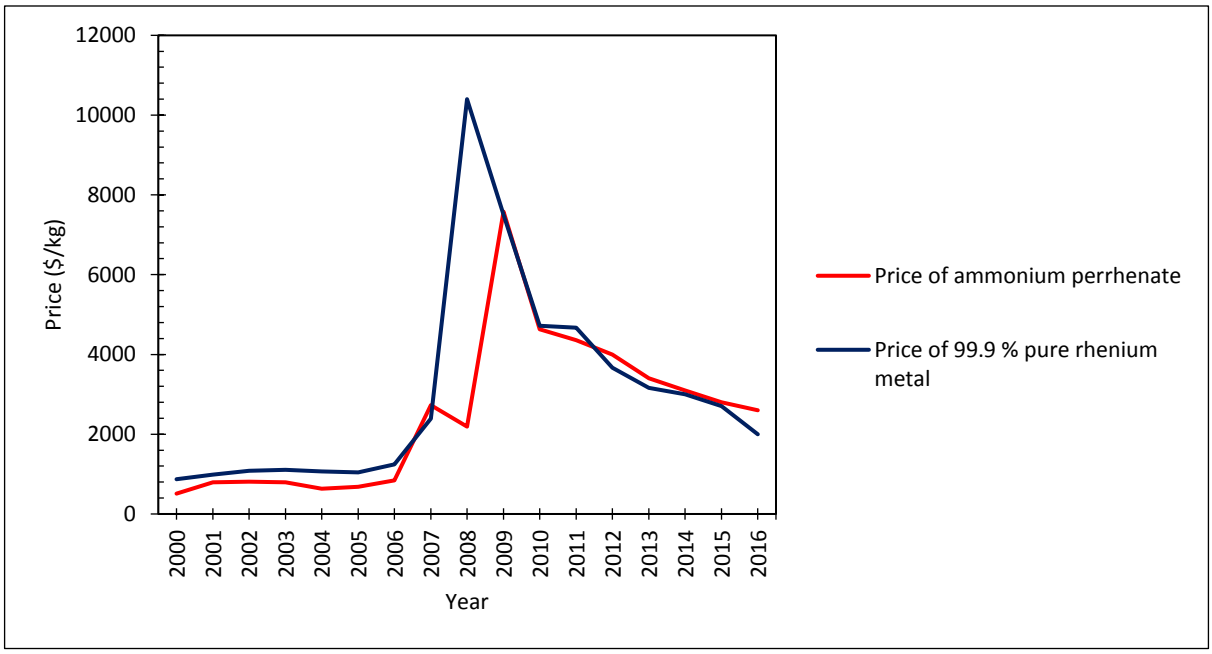

Figure A-3: Rhenium metal and ammonium perrhenate price trends.

The price of APR shows similar trends to the price of the metal but there is also a distinction between the two prices due their ultimate use. The spike in 2008 of the metal price was due to the new generation of superalloys and this was not reflected in the price of the APR due to the demand for the metal and not the salt. The salt's price did spike however in 2009 and this was because of a combination of the increased demand for the salt from the petrochemical industry for catalyst production but also a lagging effect from the increased price of the metal, but this was suppressed due to the semi-closed loop nature of the reforming catalyst market.

Although APR typically contains around 69% Re, this is not reflected in the price of the salt compared to the metal and in some cases the salt has been known to be more expensive than the metal, which is currently the case. The APR market and the metal market can for this reason almost be treated separately due to their distinct uses. Although the price of APR does to some extent rely on the metal price, the amount of metal which is required for the reforming catalyst market is only to cover the losses of the recovery processes. In the aviation industry the recovery of the metal is increasing but it is not as mature and in reality recycled metal only accounts for around 10% of the rhenium used in the components. As the aviation industry accounts for nearly 80% of the rhenium use the metal price could almost be split into the price for the aviation industry (metal) and then the price for the petrochemical industry (salt).

A.4. Rhenium Recovery.

Due to the volatility of the price of rhenium in the past decade and a number of supply chain risks, many large consumers of rhenium for example General Electric Aviation (GE) and Rolls Royce began to research into ways which they could reduce their rhenium dependence. GE unveiled a rhenium reduction programme designed to 'revert, recycle, recover and reduce' rhenium and reduce their dependence on the metal by half year on year (Fink et al. 2010).

The 'revert' process is designed to re-melt and reuse the scrap which is generated during the casting of the superalloys. This includes running systems, in-gates and machine tailings (swarf) which are rhenium containing materials lost from the final casting during production. These pieces of scrap can amount to quite a substantial volume of raw material to be reused. Recycling involves the collection of end of life turbines from engines which are then added to the production process. Recovery involves scraped turbines being sent to specialist recovery

facilities which can extract the rhenium metal from the alloys. In 2011, GE stated that 10% of the rhenium which is used to produce superalloys came from recycled sources. As the scrapped superalloys contain a significant amount of rhenium (3 wt%) they are a valuable secondary source of the valuable metal and so the dependence on primary sourced rhenium is reduced. The success of these revert programmes has been shown in the previous section with a significant price decrease of rhenium from 2008 with today's price being 80% lower.

GE has spent a large amount of time researching and developing superalloys containing significantly reduced or no rhenium content. Superalloys containing 1.5wt% rhenium have shown properties comparable to 3wt% Re containing superalloys, but at lower operating temperatures. The newly developed superalloys cannot perform as well as the 3wt% or 6wt% Re superalloys at high operating temperatures. It is more advantageous for engines to run at higher temperatures because this leads to increased fuel efficiency. In the current climate where fuel efficiency is very important both economically and environmentally, rhenium containing superalloys allow for desirable performances. Rhenium addition is reported to result in a ten-fold increase of the creep to rupture life of superalloys (Mottura et al. 2012) meaning that the operational life of the component is greatly increased which is much more economical and practical for the user. Research is continuing to develop new superalloys with reduced rhenium content which can produce similar performances to the current turbine blades.

Rolls Royce also has a similar 'revert' programme to reduce their dependence on primary rhenium and other rare elements which are used in their components. The recycling programme and methods which are used by the company and the partners means that almost

half of a jet engine can be recycled to either be reused or to recover the raw materials. There is a considerable environmental benefit which is gained from pursuing projects like revert as the energy consumption of obtaining the metal is reduced considerably, Rolls Royce estimates it saves 20000 MWh of energy each year through its revert programme reducing their carbon emissions by 9000 tonnes (Rolls Royce 2013).

The major rhenium recycling companies are Buss and Buss Spezial metalle, Molycorp and Colonial Metals. These companies recycle rhenium containing superalloys. The major processing routes for the recycling of rhenium are hydrometallurgical and the main product produced is ammonium perrhenate. Buss and Buss do produce Re pellets and Colonial Metals produce a variety of rhenium products.

Pt-Re catalysts find themselves in a semi closed-loop recycling process; the spent catalysts are sent to a specialist refiner where the metals are recovered, the only requirement for virgin rhenium is from the losses in the refining process or from any expansion in demand from the user. The most notable companies which recycle rhenium from spent catalysts are Heraeus who dominate the European and Middle Eastern markets, Gemini Industries who control the bulk of the North American market and other companies such as KGHM ECOREN who have recently invested in recovery facilities. These companies refine the metal from the spent catalyst which is then sent to companies such as Johnson Matthey and Umicore who produce the metal salt to be used in the catalyst production. Catalyst producers include Criterion Catalysts, UOP and Axens and the users are generally the large petrochemical companies such as Shell, BP and Exxon Mobil. The life cycle of the reforming catalyst is shown in Figure A-4:

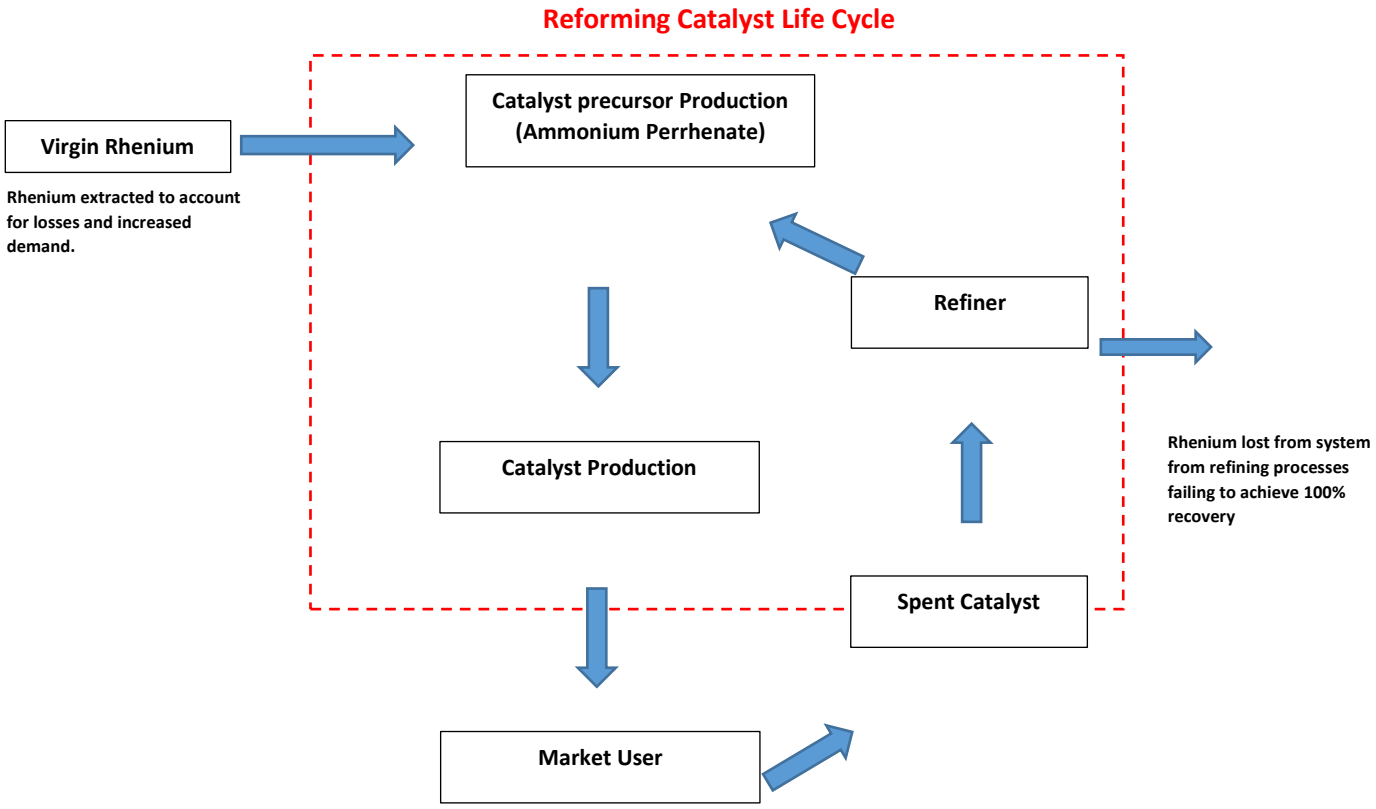

Figure A-4: Rhenium catalyst lifecycle.

The hydrometallurgical processing routes which are employed by companies to recover the metals offer varying yields of recovery. The recovery of rhenium and platinum from spent catalysts via hydrometallurgical routes is a common but complex process. Pt-Re catalysts differ from manufacturer to manufacturer in their composition and as the hydrometallurgical processing route is specific to the catalyst his processing technique is quite inflexible (Drobot et al. 2007). The two main disadvantages of hydrometallurgical processes are the multistage processing steps and the large volumes of aluminate solutions which are produced. The catalysts are composed of >95 wt% alumina which is used as the catalyst support and in most hydrometallurgical processes this needs to be dissolved to recover the metals. The alumina support does not dissolve very easily, in fact only about 90% of reforming catalysts are manufactured on dissolvable alumina (γ-alumina), and without the use of concentrated acids

such as HCl or H_2SO_4, a viscous solution is produced with is very difficult to work with (Kasikov and Petrova 2007). The use of concentrated acids required both specialised chemically resistant equipment and effluent treatment plants which add to capital and operating costs. The recovery rates of the metals from spent catalysts via hydrometallurgical routes are quite variable and can be between 90-95% however it is often the case that the recovery of one metal is higher than the other and is very much dependent on the processing steps during recovery (Drobot et al. 2007). Pyrometallurgical processing routes have an advantage that they are less sensitive to the composition and the metal valence than traditional processing routes. An example being the use of DC plasma arc technology where the catalyst is put into a furnace with fluxing additives which at temperatures at around 1600°C form a slag material which separates from the metals in the catalyst. A distinctive slag and distinctive metal layer are formed which can be easily separated. Any impurities such as chlorine or volatile heavy metals are extracted from the off gas system as either acid or air pollution control residue ensuring the process complies with environmental legislation whilst producing little waste products as the slag can be used as a construction material. Pyrometallurgical routes can be quite energy intensive especially since plasma recovery processes use large amounts of electricity. The refining of rhenium in this process is still quite novel and the even though in theory there can be high recovery rates of the metal from the process they are yet to be proven in a large scale application. The recovery of platinum and other PGMs via this technology has been proven and can achieve high recovery rates of 98%.

The recycling of rhenium from the catalysts is advantageous as long term contracts and relationships between recycler and users means that's the petrochemical industry is not reliant on the market price for the metals which can be, as shown above, quite volatile.

Especially so for the petrochemical industry where so much of the raw materials have volatile market prices and the opportunity to obtain stable supply prices for raw materials is welcomed. Increased efficiency in the recovery of the metals from the catalyst is of interest to this industry which would reduce the need for virgin metal and thus creating an even tighter closed loop production process.

The United Nations Environmental Programme (UNEP) publicised data highlighting the amount of rhenium which is recycled. It gave three factors; end of life recycle rate (EOL-RR), recycled content RC and OSR old scrap ratios which is the share of old scrap in the total scrap flow. The end of life recycling rate it the percentage of the metal containing material which is recycled after discarding. The recycled content gives the percentage of new products which contains recycled metals. The recycling rates for rhenium are shown in Table A-1.

Table A-1: UNEP 2011 Rhenium Recycling Rates.

Old scrap ratio	Recycled content	End of life recycling rate
~50%	10-25%	>55%

The high recycle rates for rhenium is mainly due to the closed loop recycling programmes which are set up. The recycled content of rhenium is lower than the end of life recycle rate is because of the long life span of the products which are made. The catalysts life span is 1-2 years but a superalloy turbine's lifespan is considerably longer at approximately 10 years and as this application accounts for 80% of rhenium's use this is reflected in the statistics.

The recycling of metals is driven by the price of the primary metal but there are also other factors such as spikes in demand or potential risks to supply; which is especially so for metals which are mined in very few countries. Recycling of some precious metals is well established,

an example being platinum and there is a growing trend for the recycling of valuable metals as it is often the case that the concentration of the metal in the end of life products is higher than the concentration in the primary ore making secondary sources.

Platinum and palladium recycling from materials such as end of life automotive catalysts is well established especially in the US is mature cars were required by law to have catalytic converters since the 70s whereas in Europe it was only made a legal requirement for cars to have catalytic converters in the early 90s. Figure A-5 and Figure A-6 show the recycling rates of these metals compared to the metal's price. It can be seen that initially the high metal prices drove an incentive to recycle, but a decoupling of the lines is observed because the high recycling rates began to supress further price rises of the metals. Lower prices can see recycling rates drop, which is shown in 2009 where traders would wait for prices to rise, but now the significant role of recyclers in the PGM industry today may mean that this stockholding will be less common.

The effect of recycling rates on the price of metals is very evident in the rhodium recycling market which can be seen in Figure A-7. Rhodium similarities with rhenium due to the majority of its use is in one application rather than platinum and palladium which have numerous applications. The increase in the recycling rates of rhodium since 2008 has meant that rhodium's price has fallen and remained steady. This is because of the high availability of secondary sourced rhodium in the market which reduces the demand for the primary metal. The rise in the recycling of rhenium has coincided with a drop in its price and so it would be logical to assume that the price trend of rhenium will follow that of the PGMs as the recycling rates of the metals rise. It would be interesting to compare the price trends of the PGMs and

rhenium as both the recycling rates of these metals are increasing, but as the PGMs are also traditional investment metals it may be that recycling of these metals is reduced to allow for the prices to recover. Rhenium on the other hand is essentially just an industrial metal and so it would not be as likely for there to be any economic reason for the recycling rates to decrease as recycling directly benefits the end users.

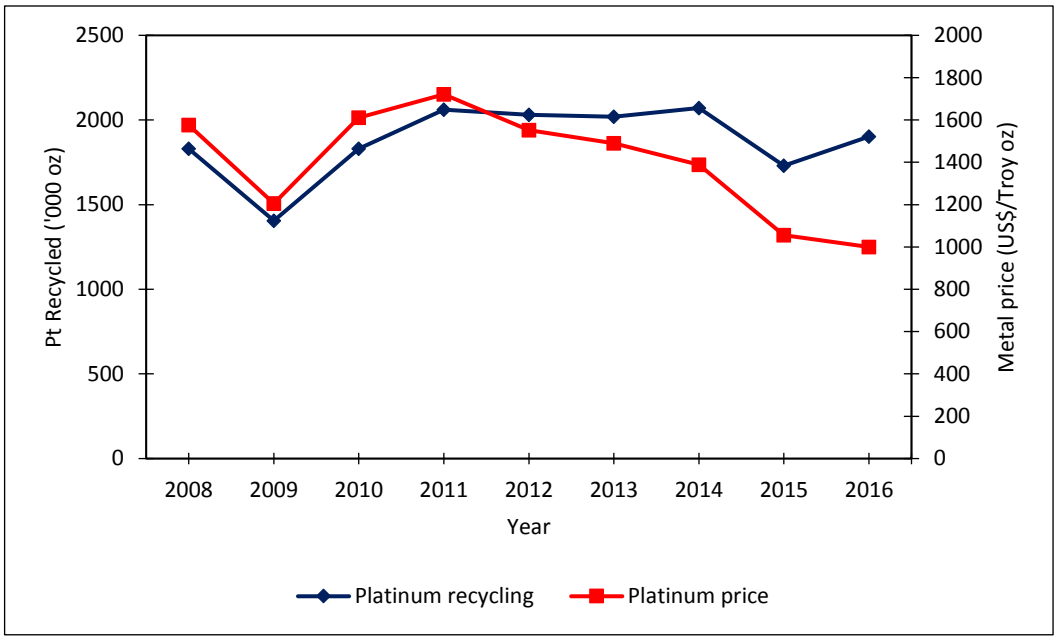

Figure A-5: Recycled amount of platinum and price of the metal,

(Johnson and Matthey , 2016).

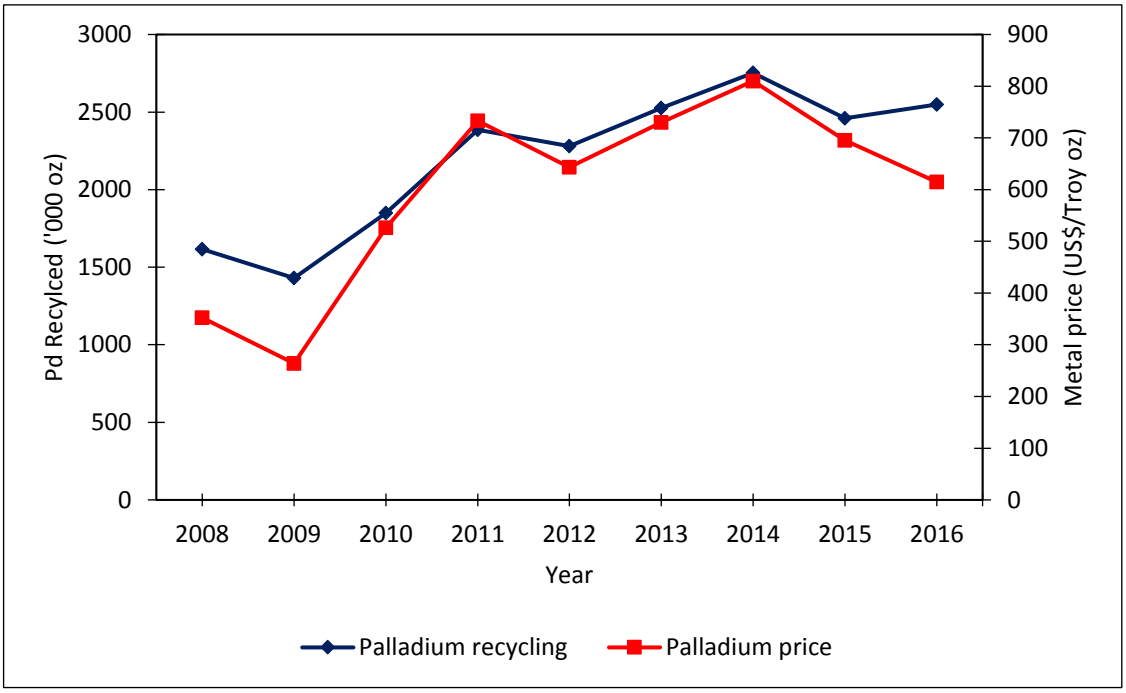

Figure A-6: Palladium recycling amounts and price of the metal (Johnson and Matthey, 2016).

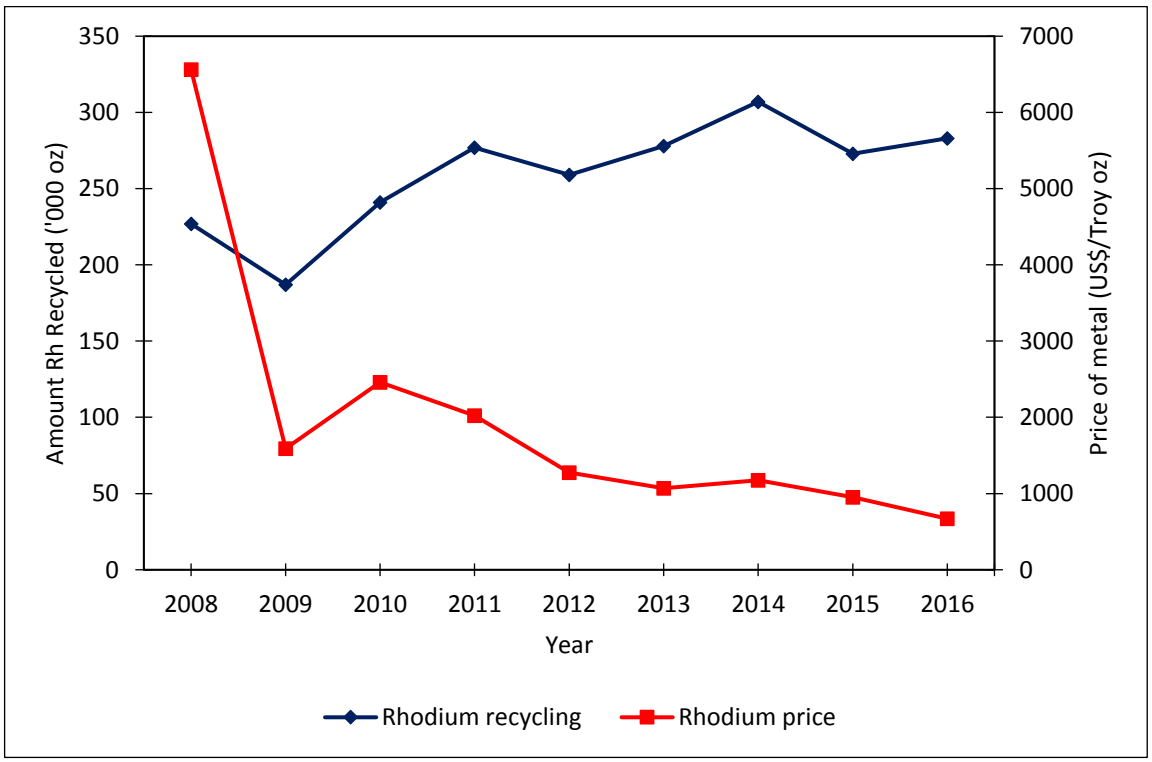

Figure A-7: Rhodium recycling amounts and price of metal (Johnson and Matthey, 2016).

A.5. Foresight.

Although there is research into the potential to substitute less valuable metals for rhenium there are not any real competitors for rhenium in both turbine and catalyst applications. The demand for rhenium is set to increase through-out the next few years to the latter end of the decade due to the rise in the orders for the large commercial aeroplanes which require their engines to function at high efficiencies and reduced emissions meaning rhenium's role in these materials will not be diminished. Replacement materials in turbines are not able to reproduce the performance which rhenium containing superalloys can achieve and with the increase in environmental legislation in aviation and the need to reduce fuel consumption there is a need to keep rhenium in these turbine blades. It is more likely that these companies will develop turbines which contain less rhenium than what is currently used rather than replacing the metal altogether however the demand for rhenium is still expected to remain strong in the aviation industry.

In the chemical industry there have also been investigations into the replacement of rhenium with other metals in catalysts, which was driven by past price increases. Iridium and tin have been proven to be just as effective as rhenium in one commercial application (USGS, 2013). The advantage of rhenium however, is that it can be applied to a number of catalytic operations and so is more durable in industries such as the petrochemical industry which is quite diverse. The physical characteristics of rhenium and PGMs make them ideal for catalysts and although these metals are expensive, they are by far the most efficient materials to be used in catalysts. Therefore catalyst producers are reducing the metal loading on the catalysts rather than replacing them with a base metal. There will be a growth in the gas to liquid operations especially in fields such as shale gas production and the exploitation of biofuels.

Therefore the demand for platinum rhenium catalysts will remain strong in the coming years keeping a strong demand for APR.

There is however a move in industry for the reliance on primary sourced metals to be cut and a more heavy emphasis in on the recovery and recycling of these metals. This can be seen from the revert processes from GE and Rolls Royce but also from the initiatives from the European Community in projects such as Horizon 2020 in which the EC want to reduce the industrial risks involved with dependence on what it deems to be 'critical metals'. This initiative involves the potential replacement and increased recycling rates of these metals. Although rhenium does not fall into the 'Critical 14', the push towards a more circular economy in the future is clear to see. Therefore the role of recycling of materials most importantly metals in the future will be of prime industrial importance and it does seem that there is a large incentive, both economically and environmentally to achieve a higher proportion of supply of materials will be met from recycled sources.

The eventual rise of recycling of rhenium may take many years to achieve a situation where the majority of supply is met from recycled sources and so the price of rhenium is not likely to be affected from this increased recycling rate in the near future. The major factor in determining the price of the metal at the moment is the demand for it in the aviation industry. Due to the increased orders for jet engines for the major aviation companies it is very likely that the demand for rhenium will increase in the coming years and this may have an effect in raising the price of the metal. As the aviation companies increase their recycling programmes, the demand for the primary sourced rhenium may being to drop and this may begin to take

shape towards the end of the decade as currently in service turbines begin to reach the end of their lives causing the price of the metal to decrease.

As rhenium is produced as a by-product its rate of production can easily be controlled as it is copper not rhenium which creates the largest revenue from the overall process. Therefore if the price of rhenium drops due to the increased recycling rates, primary producers may very likely reduce the output of rhenium thus increasing or stabilising the price. Similarly if the demand for the primary metal falls then the price of the metal could increase due to producing it at low volumes, this may cause low output producers to cease extracting rhenium and eliminating the competition for the larger extractors who are able to react to changes in the market more easily. Due to the long life of the components in jet engines and the increased passenger and aeroplane demand it is likely that a balance between the demand for primary rhenium and the rhenium recycled will be achieved since it is not likely that the recycling of the metal will meet the demands of the market and only become more significant over time.

The future of rhenium like many other rare and precious metals will be in recycling. The economic benefits of recycling rare metals from their secondary sources are very clear but it has a number of environmental benefits. Rhenium, like other rare and precious metals, enables transportation to reduce their emissions, but it is rather ironic that the production of these metals from primary sources can be very carbon and energy intensive. Reduction of a company's carbon footprint is very topical in the current industrial climate and with added political pressure and the bonus of good PR, recycling of the metals does offer great advantages, but with the extraction of primary rhenium being so dependent on single areas in the globe, there are real risks to the supply which may come from political or natural

occurrences therefore supplying the metal from secondary sources reduces these risks significantly.

Markets are constantly changing systems which can be at times difficult to predict, when the introduction of a brand new technology can cause a rush for the material unexpected spikes can occur. As the aviation industry like many other industries enters an age of recycling and reuse of valuable metals the rhenium market will begin to change accordingly and it will have to react to these new times in a way in which it hasn't had to before in its relatively short time span.

Appendix B. Road Map for the Commercialisation of Plasmarok® as a Cement Replacement.

B.1. Introduction.

Increasing the value of Plasmarok has the potential to be able to significantly improve the economics of the plasma process. The vast majority of the current applications of plasma produce large volumes of slag especially metal recovery processes and the treatment of hazardous materials such as air pollution control residue (APCr).

Plasmarok is the major product from hazardous waste treatment processes and it is in these processes where increasing the value of the slag will have the most important impact, significantly changing the operational costs of the process making them more economically attractive.

The use of Plasmarok® as a cement replacement shows great potential for the material to be used in industry and demand a higher value than it currently can achieve. Currently Plasmarok is typically valued around £6 per tonne, but as a cement replacement it could be valued between £50 to 80 per tonne.

The work presented in chapter 6 of this thesis has shown that the slag does show pozzolanic properties and could be used as a cement replacement, but there are issues which will need to be addressed before it would be able to become commercialised. These issues are centred on the material being able to conform to construction materials regulations and for it to be CE marked for the market. This chapter outlines a 'road map' for the commercialisation of the Plasmarok as a pozzolanic material which would lead to Tetronics being able to CE mark the material.

The commercialisation route would include the generation of data (both in house and third party) comparing the slag against current regulatory standards and then the generation of a European Assessment Document issued by a technical assessment body which would allow for the CE marking of the slag.

B.2. British and European Standards and CE Marking.

B.2.1. Relevant Standards.

The relevant standards which are used to assess cement and pozzolanic materials and which adopted throughout the European Union are:

- BS EN 197-1:2011 *Cement. Composition, specifications and conformity criteria for common cements.*
- BS EN 197-2:2011 *Cement. Conformity evaluation.*
- BS EN 196 *(1-9 various testing methods).*
- BS EN 15167-1:2006 *Ground granulated blast furnace slag for use in concrete, mortar and grout. Definitions, specifications and conformity criteria.*
- BS EN 15167-2:2006 *Ground granulated blast furnace slag for use in concrete, mortar and grout. Conformity evaluation.*

B.2.2. BS EN 197-1:2011.

Understandably there are a large number of standards for the construction industry and for construction materials. The most important British Standard which defines cement and its constituents is BS EN 197-1-2011 *Cement composition, specifications and conformity criteria for common cements.* The scope of this standard is to define and give specifications of the common, but distinctly different, cements which are available for use within Europe. The definition of each cement includes the proportions in which the constituents are to be

combined to produce the different cements of varying strength classes as well as the performance requirements of these cements (mechanical properties, chemical characteristics and durability performance).

There are 27 distinct types of cements and they are categorised into cement classes which are based firstly on their constituents and then the loading of these constituents. Figure B-1 shows the different cement classifications which are described in BS EN 196.

Figure B-1: Cement classifications (BS EN 197-1:2011).

B.2.3. Pozzolanic materials.

BS EN 197 defines the different types of pozzolana which can be used in cements. There are quite narrow specifications for some of the pozzolanic materials and some rather vague definitions for others.

Ground granulated blast furnace slag has the following definition:

5.2.2 "*Granulated blast furnace slag is made by rapid cooling of a slag melt of suitable composition, as obtained by smelting iron ore in a blast furnace and contains at least two-thirds of glassy slag and possesses hydraulic properties when suitably activated.*

Granulated blast furnace slag shall consist of at least two-thirds by mass of the sum of calcium oxide (CaO), magnesium oxide (MgO) and silicon dioxide (SiO_2). The remainder contains aluminium oxide (Al_2O_3) together with small amounts of other components. The ratio by mass $(CaO + MgO)/(SiO_2)$ shall exceed 1.0."

Although Plasmarok is a close relation to the blast furnace slag, the narrow definition of the GGBFS means that Plasmarok would not be able to conform to the specifications due to its origin and the narrow compositional range which is specified for GGBFS. The results from this thesis indicate that this compositional range is not due to any performance related properties of the material.

However, there is a "general definition" of a pozzolanic material which is vaguer and is as follows:

5.2.3.1 *"Pozzolanic materials are natural substances of siliceous or silico-aluminous composition or a combination thereof. Although fly ash and silica fume have pozzolanic properties, they are specified in separate sub-clauses…*

…Pozzolanic materials do not harden in themselves when mixed with water but, when finely ground and in the presence of water, they react at normal ambient temperature with dissolved calcium hydroxide ($Ca(OH)_2$) to form strength-developing calcium silicate and calcium aluminate compounds. These compounds are similar to those which are formed in the hardening of hydraulic materials. Pozzolans consist essentially of reactive silicon dioxide (SiO_2) and aluminium oxide (Al_2O_3). The remainder contains iron oxide (Fe_2O_3) and other oxides. The proportion of reactive calcium oxide for hardening is negligible. The reactive silicon dioxide content shall be not less than 25.0% by mass."

Other definitions of pozzolanic materials in BS EN 197-1 are very specific to other pozzolanic materials such as fly ash. From the definitions above it seems that Plasmarok is a material which has pozzolanic properties, but does not quit fit wholly into any standard definition of a pozzolanic material.

Plasmarok mostly fits the definition of a general pozzolanic material however it is not a "natural substance" and there is not a British Standard test for reactive silica making this definition quite vague. This means that it is difficult to place a Plasmarok-blended cement in any of the cement classifications shown in Figure B-1 directly.

B.2.4. Performance Requirements of Cements.

The British Standards do very clearly outline the performance requirements for the cements and so being able to show that the pozzolanic blended cements are compliant with these specifications will be key to moving the material to the market.

There are a number of testing methods which are used to determine the mechanical performance, chemical characteristics and durability properties of the cements and these are

outlined in the series of British Standards under BS EN 196. Figure B-2 and Figure B-3 show the strength and chemical specifications for cements which determine which class the cement can be classified as, i.e. high strength cement. The chemical specifications strict as these have a serious effect on the durability of the cement if they are not met for example the effect of chlorine content on the corrosion of steel bars.

Figure B-2: Strength classes for cements (BS EN 196-1:2011).

Figure B-3: Chemical specifications for cements (BS EN 196-1:2011).

Depending on what the application of the cement would be or where the cement would be placed there would be a requirement for the cement to have certain durability properties. These properties are not essential for all cements but they can include:

- Frost resistance.
- Chemical resistance.
- Protection of reinforcement.
- Alkali-silica reaction.
- Carbonation.
- Sulphate resistance.

B.2.5. BS EN 15167.

This standard is the European Standard which specifies the chemical and physical requirements and also quality control procedures for ground granulated blast furnace slag for use as an addition for type II cement.

The chemical composition requirements defined in BS EN 197 and described above as well as the chloride, sulphide and sulphate content which must be less than 0.1%, 2.0% and 2.5% respectively.

The physical requirements include the fineness, setting time, activity index and durability. The setting time and durability are dependent on the final use of the concrete and so are to be reported in line with the guidelines set in BS EN 197. The fineness and activity index are more specific and they are as follows:

- Fineness – not less than 275 m^2/kg.
- Activity index – activity index at 7 days and at 28 days should not be less than 0.45 and 0.7 respectively. (Note this is when 50% of the cement has been substituted with GGBFS and with a solid liquid ratio of 0.5).

The standard also details which information needs to be supplied to a user of the material on request. This information is as follows:

a) 7 and 28 day activity index of at least 0.45 and 0.7 respectively for a 50% combination of the ground granulated blast furnace slag with 50% of test cement determined in accordance with 5.3.2.3.
b) Initial setting time of a 50% combination of the ground granulated blast furnace slag with 50% test cement.

c) Initial setting time and 7- and 28- day strength of the test cement.

d) Chemical oxide composition of the ground granulated blast furnace slag, comprising the contents of calcium oxide (CaO), silicon dioxide (SiO_2), aluminium oxide (Al_2O_3), magnesium oxide (MgO), titanium dioxide (TiO_2) and manganese (Mn_2O_3).

e) Total content of alkalis determined in accordance with EN 196-2 or other method agreed between manufacturer and user, and expressed as equivalent sodium oxide.

f) Fineness value determined in accordance with the air permeability method in EN 196-6.

g) Relative density determined in accordance with EN 196-6.

h) Glass content and the method used for its determination.

i) The method(s) of rapid cooling used to produce the granulated blast furnace slag(s) used in the manufacture of the ground granulated blast furnace slag.

The above is the information and the data which is required to show the performance characteristics of the Plasmarok. Comparing the Plasmarok against GGBFS would be beneficial as it would hopefully show that the material will perform as a good as a widely used industrial material. Where the material does not conform to the requirements which are specified for GGBFS, for example the compositional requirements, further data can be used to demonstrate that there is no detrimental effect due to the Plasmarok differing from the standards.

B.3. CE Marking.

The CE marking of a product enables customers and end users to be able to check the performance of a product and compare it to others. A CE mark contains essential information about the product and provides a link to other additional documents containing important and more detailed information.

CE marking Plasmarok would give an end user confidence of using the material because there would be certain performance criteria to which the material would need to conform to and it would allow end users to compare Plasmarok to another pozzolan for use in their concrete mixes.

CE marking in the EU is compulsory for some products and voluntary for others. When there is a harmonised standard to which a product must conform, CE marking is compulsory. As there is a harmonised standard for blast furnace slag for use as a pozzolan (BS EN 15167), GGBFS must be CE marked to demonstrate its conformity to this standard.

There are no harmonised standards for any pozzolanic materials other than blast furnace slag or fly ash. This means that it is not compulsory for Plasmarok to be CE marked for it to be used in cement, however for customer confidence and competitiveness against GGBFS it may be strategically important for the material to be voluntarily CE marked and a set of performance characteristics for the material to be defined.

Without a harmonised standard, to CE mark a material there must be some sort of performance criteria for the material to be assessed against. This performance criteria can be generated in what is called a European Assessment Document (EAD). There are various EADs for materials but if none exist for a specific product then one can be created by requesting a Technical Assessment Body (TAB) to develop one.

There is no existing EAD for pozzolanic materials which Plasmarok could be categorized with and so one would have to be generated by a TAB.

An EAD is document which is a technical specification for a material. The documents contains:

- A general description of the construction product.
- The list of essential characteristics agreed between the manufacturer and the European Organisation for Technical Assessment (EOTA).
- The methods and criteria for assessing the performance of the product in relation to these essential characteristics.
- Principles for factory production control to be applied.

The EAD is essentially a harmonised standard for the material and it is the basis for which the properties of the material would be tested against before a European Technical Assessment (ETA) can be issued which is issued by the Technical Assessment Body to show that the material conforms to the EAD.

For the ETA to be issued it would have to be demonstrated that Plasmarok has the "essential characteristics" required by generating data for the material and also ensure that there is sufficient quality control during Plasmarok's production so that it maintains a consistent performance.

How the material is assessed and what is required for each essential characteristic would be defined in the EAD. Each essential characteristic will require what is known as an assessment and verification of constancy of performance system (AVPC system) and this will be defined in the EAD by the TAB.

The AVPC system will include the method of testing and the data required to ensure that material is performing as required as well as process control demonstration. Depending on how it is defined in the EAD the assessment would either have to be carried out by the

manufacturer or by a notified body which could be a third party laboratory with the necessary accreditation.

The TAB would then issue a European Technical Assessment document which shows the conformity of the material to the EAD.

As well as the European Technical Assessment there is a requirement for a number of supporting documents to be able to support the CE marking of the material which are:

- Initial testing of the product including the list of essential characteristics and the results of the assessment (testing, tabulated values, etc).
- European Technical Assessment.
- Documented factory production control procedure.
- Certificate or certificates from the Notified Body or Bodies, if required.
- Appropriate technical documentation where necessary.
- Specific technical documents where necessary.

These documents are required and can be requested by Trading Standards who are the UKs market surveillance authority and who can also audit the company.

The CE marking of the product and the quality control requirements of the product will vary from application to application and would be defined by the TAB. The potential issue for Tetronics in this regard would be the changing composition or the changing plasma process from which the Plasmarok is derived.

To combat this the initial testing and the initial research into the use of Plasmarok should define the compositional boundaries for which Plasmarok shows good pozzolanic activity and

try to ensure that these boundaries cover the types of slags which the plasma process would produce. As previously discussed there is a good flexibility in the allowed composition for the Plasmarok which is a positive indication. This would hopefully enable Tetronics to CE mark "Plasmarok" in general rather than a specific slag from a specific composition.

The process controls required could be built into the processes for example appropriate cooling methods of the slag would be similar for most processes and the grinding/milling techniques for the processes would also be similar and so the same process control would be able to be established across a number of different plasma applications.

With the information which would be generated from the initial testing, control procedures etc. a CE mark would be able to be made and presented to a customer along with the following documents;

- Declaration of performance (DoP) of the product.
- CE marking and accompanying information of the product.
- Instructions and safety information.
- REACH information.

The declaration of performance is a document which is produced from all the testing of the material and specification data which was generated during the assessment of the material's properties. This document is as important as the CE marking because it is a more detailed description of the performance of the material and the CE marking is essentially there to summarise this document.

The declaration of performance is as follows:

- Number of the declaration of performance.
- Unique identification code of the product type.
- Intended use.
- Manufacturer.
- System(s) of AVCP.
- Notified bodies.
- European Assessment Document.
- European Technical Assessment.
- Technical Assessment Body.
- Declared performance.
- Appropriate technical documentation.
- Link to online copy of the declaration of performance.

The CE mark is developed based on this declaration of performance. A typical layout of a CE label is shown in Figure B-4.

The REACH information is the safety data sheet of the material and is required for end users for health and safety purposes plus to make aware of any potential hazards of using the material.

The CE mark can then be associated with the product. Trading standards or the notified bodies are allowed to audit the material to ensure that the performance or the essential characteristics of the material have not changed over time. This means that constant sampling and internal data acquisition would be required.

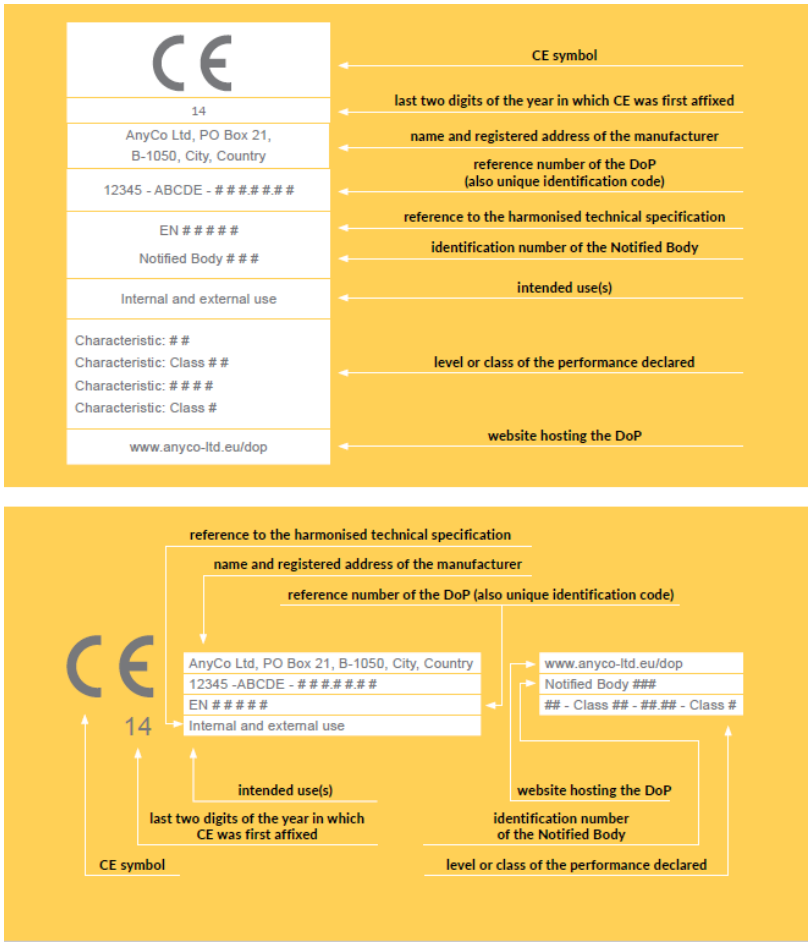

Figure B-4: Typical layout of a CE label.

B.4. Road Map Plan for the Commercialisation Plasmarok.

The goal of the road map would be to get Plasmarok a CE marking which would generate confidence for end users to use the material.

The regulations and processes which have been discussed in the previous sections have outlined the requirements for CE marking. It is clear that there are a number of stages which need to be completed before a CE mark can be applied to a product.

As there are no harmonised standards for Plasmarok, the process is more complex and so requires the appointment of a Technical Assessment Body to develop an EAD for Plasmarok.

The British Research Establishment (BRE) are able to act as a TAB for the material and be commissioned to develop an EAD for Plasmarok. This group is a specialist in research in the construction industry and so have good experience in dealing with the movement of materials towards the market.

The stages which are required for the Plasmarok to be commercialised are as follows and are summarized in Table B-1.

- Creation of a dossier containing data from the initial testing of the material.
- Presentation of the dossier to BRE and a scoping study into options for standardisation and conformity.
- Development of an EAD for the material (or other route depending on the outcome of the scoping study).

Table B-1: Summary of project tasks and deliverables.

Activity	Time required	Deliverables
Initial Testing	8 weeks	Dossier of initial data to be presented to BRE.
BRE Scoping study	5 weeks	Report by BRE to Tetronics and the discussion of the best route forward for commercialisation of Plasmarok.
EAD Development	60 weeks	EAD for Plasmarok as a pozzolan.
Additional R&D	30 weeks	Dossier to demonstrate the process control and process requirements to produce Plasmarok to the correct specifications.

B.4.1. Initial testing of the material.

The initial testing of the material needs to be completed to show a full range of the characteristics of the material which would allow for a full assessment of the material against the current specifications and standards which then would lead to the requirements and essential characteristics for any EAD which may be produced.

The initial testing of the material would include any work which has been done so far which has been presented in this thesis and should also be supported by third party laboratory testing to ensure that the results which have already been obtained are consistent and reliable.

The testing which will be required would be the tests which are relevant for the material but required and defined in the current cement standards BS EN 197 (the tests being outlined in BS EN 196) and those which are defined in BS EN 15167.

The dossier should include the following data:

- Activity index 28 day strength EN 196-1.
- Activity index 90 day strength EN 196-1.
- Soundness EN 196-3.
- Fineness EN 451-2.
- Loss on ignition EN 196-2.
- Particle density EN 1097-7.
- Initial setting time EN 196-3.
- Water requirement EN 450-1.
- Chemical analysis EN 196-2.

- Chloride content EN 196-2.
- Relationship between compressive strength and proportions EN 196-1.
- Sulphide content EN 196-2.
- Sulphate content EN 196-2.
- Additional supporting data (pozzolanicity tests for example EN 196-5, microstructural analysis).

The results of some of this test data would be dependent on the composition of the Plasmarok and others would be dependent on the processing of the material. It is important to understand which aspects of the performance of the Plasmarok can be controlled from an initial composition design and which can be controlled from a mechanical/processing perspective.

The properties which would be most likely be effected by the composition of the material would be:

- Activity index.
- Setting time.
- Particle density.
- Water requirements.

Those which would be affected by the processing route would be:

- Fineness.
- Microstructure.
- Activity index.

There would be an overlap between a number of the characteristics i.e. the activity index would be affected by both the composition of the Plasmarok and also its fineness. Understanding these parameters and relationships would be very important in determining what essential characteristics the material can have.

Therefore for some of these tests it would be beneficial to obtain data for a range of Plasmarok compositions to demonstrate if there are any changes in the performance of the material depending on the source or the process from which the Plasmarok was derived.

This should lead to the ability to CE mark Plasmarok as a whole and not have too much of a restriction on its composition.

Some of the tests would not require an external laboratory to perform them for example compositional analysis of the slags. It is the tests which are more specific to concrete/cement manufacture where the external testing would be beneficial i.e. activity index, water requirements etc.

On completion of these tests the data would be analysed and a dossier created which would then be presented to BRE.

The initial testing of the material would take one month to complete (28 days are required for the activity index, the 90 days test would be supplementary). With an additional month to analyse the data and then creating the document, two months would be required for the first stage of this work.

B.4.2. BRE Scoping Study.

After the completion of the initial assessment the data would be presented to BRE who will look through the information and evaluate it. The evaluation will be to determine what steps are actually required for the material to get to market. It may be that with the data which is obtained, BRE might be able to advise that CE marking isn't necessary or that there is an already existing EAD which would be able to be used to assess the material.

The outcomes of this study would be to identify if there are any gaps in the initial data which would need to be dealt with before the project progresses. BRE will take the information available and compare it to the existing standards and see where the material conforms and where it doesn't. By doing this BRE will then be able to advise on what are the next steps to take.

From discussions with BRE the outcomes from the study would lead to one of these options:

- Demonstration of full or partial alignment of the Plasmarok with existing harmonised standards (EN 197 or EN 15167-1&2:2006).
- An independent BRE report on the material to show to third parties (including independent confirmatory testing).
- Third party certification.
- A BRE product standard.
- An EAD.

The deliverables from the study would be:

- A brief BRE report on the scoping study.
- A face to face meeting at BRE to overview above options and routes to standardisation.

The decision of the next stage of the work would be dependent on the advice from BRE but also the strategy which to take. It may be so that the material does partly conform to the current harmonised standards and BRE would be able to issue an independent report which may be similar to a declaration of performance of the material. This may be a cheaper option than perusing an EAD route however it may not result in being able to CE mark the material.

Commissioning an EAD to be able to CE mark Plasmarok against may give the material a better market advantage than if it wasn't CE marked. Given the choice between a material which is CE marked and one which isn't a customer may be more likely to choose the CE marked material, depending on price. If the Plasmarok was CE marked it may also demand a higher material value and so would have a greater effect on the business models of the processes from which it is derived from.

The benefit of the scoping study would enable Tetronics to make a decision on these questions based on the expert advice from a technical body.

B.4.3. European Assessment Document.

The development of an EAD would be longest process in this work. The work would include defining and carrying out research to identify the key performance characteristics of the Plasmarok, although much of this work may have already been done in the initial assessment stage. It may be that large collections of data would be needed to determine the standard deviation of the strengths or activity indexes for example to accurately define that characteristic.

The scoping study and the initial assessment would direct exactly what work would be required but the general outline of the work would be as follows:

- Researching the key performance characteristics of Plasmarok and supporting tests likely to be required. (Week 0-5).
- Develop draft content and properties/limits for an EAD. (Week 5-15).
- Carry out independent confirmatory durability and performance tests in support of an EAD (in addition to test data provided by Tetronics). (Week 15-60).
- Final report to BRE global on performance/durability in support of EAD preparation. (week 60)

B.4.4. European Technical Assessment.

Upon the completion of the EAD the technical body would then have to issue a European technical assessment by assessing the performance against the requirements of the EAD. Most of this work should have already been completed by this stage but it would require the demonstration of process control during the manufacturing of the Plasmarok.

There has been no budget set for the cost of an ETA due to it being out of the scope with the discussions with BRE and it being quite far down the line.

It would be important to highlight the process control requirements that can be envisaged for the Plasmarok during its production. This would be the basis for further in-house research activities for Tetronics which could take place during the EAD process to facilitate the issuing of an ETA.

B.4.5. Further R&D work.

The chlorine content of the slag would be of vital importance in determining its potential applications in cement. The allowed chlorine content in reinforced cement is 0.1% and the presence of chlorine above this level would mean that there would be a danger of unacceptable corrosion of the steel bars in concrete. As most construction concrete is

reinforced, having high chlorine levels in the slag would limit the applications of the material and so reduce its attractiveness in the market.

The chlorine levels in PGM recovery slags are not usually very high and generally are below 0.1% however it is the slags which are derived from hazardous waste treatment and in particular APCr which may contain very high chlorine levels.

APCr can contain from 25 to 30% chlorine and even though most of the chlorine is removed to the off gas the slag can contain levels of chlorine of around 2%; a comparison between the slags can be seen in Table B-2.

Table B-2: Chlorine content of APCr slag and chemical catalyst slag.

Slag Origin	Chlorine content (wt%)
Chemical Catalyst	0.1
APCr	1.8

Research would have to be conducted to determine a method of removing the chlorine from the slag. This may result in a further processing stage for the material after it has been removed from the furnace. Vacuum degassing of the slag as it is molten may well be the most effective way of removing the chlorine from the slag as opposed to other methods such as a washing stage.

During degassing of the slag the molten slag is removed from the furnace and held at a temperature where it is molten. If a vacuum is applied to the slag then the volatile components in the slag may be removed.

The research should also look into potential design of the degassing equipment and its feasibility in the process. Adding a degassing step may also have an effect on the vitrification

of the glass on cooling. It is important that the formation of a glassy slag is not compromised during this process as there would be a significant negative effect on the pozzolanic activity of the material.

As discussed in chapter 6, the presence of crystalline phases in the slag significantly reduces the pozzolanic activity of the slag and so it is important that the slag is cooled quickly to ensure that a glassy structure is produced. Tapping the slag into a ladle will cause the generation of a semi-crystalline slag material which will not have the required pozzolanic activity required for its use as a cement replacement. Generally on a trial basis where small volumes of slag is produced (in the pilot plant for example), as the mass of the slag is small the cooling rates are higher so the need for fast quenching is not always necessary but at the volume of the slag increases it becomes more important to control the cooling of the slag.

Therefore cooling rates required for the slag and the cooling techniques for the slag to be defined to engineer a solution to generate a glassy slag. The cooling of the slag needs to be fast enough to not allow crystal growth and there are technologies which are used in industry to achieve this.

Water quenching is typically used in industry to generate glassy slag, this is where the slag is tapped into a water bath. This is an effective technique however there are health and safety risks associated with this due to the large amounts of steam which are produced.

Air quenching is also a potential application of cooling the slag however this technology is not as well used in industry and so could potentially be expensive.

The work for looking at slag quenching would therefore be experimental work to determine the cooling rates required for molten slag i.e. cooling rate vs glass fraction data could be generated. This would help to design a solution for quenching the slag in a plasma plant.

Quenching the slag in water produces a granulated substance and there may also be high residual stress in the material, both of these characteristics may improve grinding efficiency when preparing the powdered slag.

One of the most critical factors of the pozzolanic activity and the strength development of a cement-pozzolan blend is the particle size. The finer the particle size the greater the activity. The crushing and the grinding of the material will therefore be one of the most important process stages in the preparation of the material. The current grinding techniques which are used on site may not be suitable in being able to produce a slag which is fine enough to display the required characteristics.

An initial investigation into the particle sizes achieved during the crushing of the material should be performed to understand whether any addition milling units would be required to achieve the correct particle size. This may just mean that an extra small, but intense, mill be added onto the end of the current set up.

Milling time vs particle size yield data can then be collected to attempt to optimise and control the particle size. The effect of quenching on the material may also be investigated plus the addition of any milling aids which may be added to the system.

Conducting the above R&D would allow for the development of the process controls which are required to produce a consistent material and demonstrate the plant process controls which would be necessary for the issuing of an ETA.

A timeline 10 weeks for the work on each of the stages in the additional R&D work has been allocated as it is likely that there would have to be some sort of hot work involved in this work using either the muffle furnace or if there were any trials taking place then to attach some of the work to these trials. An example would be if there was a PGM trial or a trial which involved tapping of material from the furnace then it may be a good idea to explore quenching process experiments. This would therefore involve planning and health and safety risk assessment so increasing the timeframe of the work. As the timeline of an EAD development is so long, there would be plenty of time for this research and so this means there is good flexibility in being able to plan and carry out the work.

B.4.6. Timeline and cost breakdown.

The total time required from the initial research stage to the production of an EAD is estimated to be 73 weeks. The majority of the time taken is by the EAD development. To get to the stage where the decision would be made to actually undertake the development of an EAD (after the completion of the BRE scoping study) is 13 weeks. The time line is shown in the form of a Gantt chart in Figure B-5.

Table B-3: Cost summary for the project.

Activity	Cost	Resources
Initial Testing	£5,000	Process engineering
BRE Scoping study	£5,000	Process engineering
EAD Development	£50,000	Process engineering
Additional R&D	£10,000	Process + workshop
Total	£70,000	

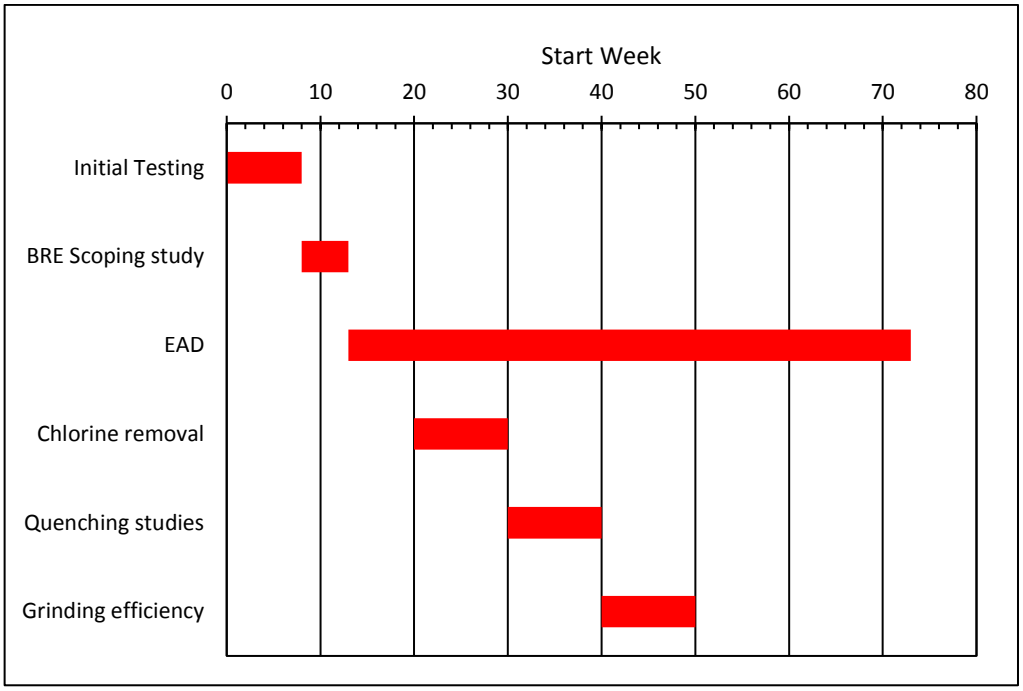

Figure B-5: Gantt chart showing project timeline.

The total cost of the project is estimated to be £70,000 and like the timeline, the major cost of this project would be the development of the EAD. A summary of the costs is shown in Table B-3. It must be noted that the cost breakdown represents a worst case cost. BRE have quoted the cost of the EAD may be between £30,000 and £40,000 but with additional work which would push up the price (BRE estimated that the extra work would be in the region of £7,000) therefore it may be that the cost of the EAD would be close to £50,000.

The costs of process engineering time and the costs of workshop time may be more accurately defined in a PCB. The additional R&D requirements may also become clearer after discussions with BRE about how Tetronics would need to demonstrate process control for an ETA to be issued.

The commercialisation of Plasmarok as a pozzolan would enable the material to demand a value of around £50 per tonne. For the material to command this sum it is likely that it would be the ability to CE mark the material which gives it a defined and accepted performance as use as a cement replacement.

Having a CE mark for the material would be attractive to be able to present to clients with a very real application for the material. Finding end users of the material would also be a big step for Plasmarok however it is more likely that an end user would trust using it, in a traditionally conservative industry, with the specifications and certifications accompanying it.

To get the material to market would most likely require the production of an EAD and some plant/processing modifications to ensure that the material has the right characteristics for use as a pozzolan. The market for pozzolanic materials is strong and so there would be great potential for the use of the material in this application.

End of Document.